

Electrophoretic and Electrolytic Deposition of Ceramic Particles on Porous Substrates

L. Gal-Or, S. Haber, S. Liubovich

Israel Institute of Metals
Technion Research and Development Foundation

Final Scientific Report
March 1, 1988 – November 30, 1992
AFOSR Grant 89-0474

Prepared for
EOARD – England, London
AFOSR – Bolling, Washington, D.C., 20332, U.S.A.

Approved for public release;
distribution unlimited.

Electrophoretic and Electrolytic Deposition of Ceramic Particles on Porous Substrates

L. Gal-Or, S. Haber, S. Liubovich

Israel Institute of Metals
Technion Research and Development Foundation

Final Scientific Report
March 1, 1988 — November 30, 1992
AFOSR Grant 89-0474

Prepared for
EOARD — England, London
AFOSR — Bolling, Washington, D.C., 20332, U.S.A.

REPORT DOCUMENTATION PAGE			Form Approved OMB No 0704-0188	
<small>Public reporting burden for this collection of information is estimated to average 1 hour per response, including the time for reviewing instructions, searching existing data sources, gathering and maintaining the data needed, and completing and reviewing the collection of information. Send comments regarding this burden estimate or any other aspect of this collection of information, including suggestions for reducing this burden, to Washington Headquarters Services, Directorate for Information Operations and Reports, 1215 Jefferson Davis Highway, Suite 1204, Arlington, VA 22202-4302 and to the Office of Management and Budget, Paperwork Reduction Project (0704-0188), Washington, DC 20503</small>				
1. AGENCY USE ONLY (Leave blank)		2. REPORT DATE		3. REPORT TYPE AND DATES COVERED Final Report March 1, 1988 - Sept. 30, 1992
4. TITLE AND SUBTITLE Electrophoretic and Electrolytic Deposition of Ceramic Particles on Porous Substrates			5. FUNDING NUMBERS AFOSR-89-0474	
6. AUTHOR(S) L. Gal-Or, S. Liubovich, S. Haber				
7. PERFORMING ORGANIZATION NAME(S) AND ADDRESS(ES) Technion R&D Foundation Technion City, Haifa, 32000, Israel			8. PERFORMING ORGANIZATION REPORT NUMBER	
9. SPONSORING/MONITORING AGENCY NAME(S) AND ADDRESS(ES) - EOARD 223/231 Old Marylebone Rd. London NW1 5TH UK - AFOSR/NE, Lt.Col. L. Burggraf, Bolling AFB DC 20332-6448			10. SPONSORING/MONITORING AGENCY REPORT NUMBER	
11. SUPPLEMENTARY NOTES				
12a. DISTRIBUTION/AVAILABILITY STATEMENT Unlimited Approved for public release; distribution unlimited.			12b. DISTRIBUTION CODE	
13. ABSTRACT (Maximum 200 words) Electrophoretic deposition of ceramic particles and their penetration into the pores of graphite and a 2D C-C composite were demonstrated and studied theoretically and experimentally for colloidal SiO ₂ , SiC, Si ₃ N ₄ , Al ₂ TiO ₅ and HfTiO ₄ . The effect of deposition parameters (field intensity, particle concentration, ratio of dielectric constant/viscosity of fluid) on the amount of induced material was experimentally studied. Penetration depth of particles as function of above parameters was analyzed theoretically. Penetration is enhanced by large Peclet numbers and is therefore higher in aqueous suspensions, while coating morphology is better in propanol suspensions. Optimal conditions for coverage and penetration in a two-stage process were therefore determined. Subsequent deposition of two layers was demonstrated and studied for Si ₃ N ₄ on Al ₂ TiO ₅ and SiC on a glass ceramic. Single (Si ₃ N ₄ , Al ₂ TiO ₅ , HfTiO ₄) and multilayer (Si ₃ N ₄ on Al ₂ TiO ₅ , and Si ₃ N ₄ on fused SiO ₂) coatings were deposited, sintered in a N ₂ atmosphere and their phase composition, and morphology studied. Oxidation resistance of coated specimens was studied at 830°C in continuous and intermittent exposures. Graphite exhaust nozzles were coated and tested in an air breathing engine simulation. Very efficient protection was achieved. Electrolytic deposition of ZrO ₂ , Al ₂ O ₃ and Al ₂ O ₃ -ZrO ₂ was achieved from aqueous solutions of ZrO(NO ₃) ₂ and Al(NO ₃) ₃ . The deposition kinetics and microstructure of the deposits were studied. The initial amorphous deposits transformed into crystalline phases with nanocrystalline dimensions after heat treatment.				
14. SUBJECT TERMS Electrophoresis, Ceramics, Impregnation, Coating, Electrolytic Deposition			15. NUMBER OF PAGES	
			16. PRICE CODE	
17. SECURITY CLASSIFICATION OF REPORT Unclassified	18. SECURITY CLASSIFICATION OF THIS PAGE Unclassified	19. SECURITY CLASSIFICATION OF ABSTRACT Unclassified	20. LIMITATION OF ABSTRACT Unlimited	

List of Personnel

Dr. L. Gal-Or - Principal Investigator
S. Liubovich - Research Associate
Prof. S. Haber - Consultant on Analytical Investigation

G. Starck
S. Almaleh-Rockman
I. Silberman
S. Sharon

} Graduate students

Dr. R. Chaim - Co-supervisor of graduate students

R. Cohen
Y. Robes

} Workshop staff

DTIC TAB 1 UNCLASSIFIED 3

Accession For	
NTIS GRA&I	<input checked="checked" type="checkbox"/>
DTIC TAB	<input type="checkbox"/>
Unannounced	<input type="checkbox"/>
Justification	
By	
Distribution/	
Availability Codes	
Avail and/or	
Dist	Special
A-1	

List of Publications and Presentations

1. L. Gal-Or, I. Silberman, R. Chaim "Electrolytic ZrO_2 Coatings – I. Electrochemical Aspects", Journ. Electrochem. Soc. Vol. 138, No. 7, July 1991, p. 1939.
2. R. Chaim, I. Silberman, L. Gal-Or "Electrolytic ZrO_2 Coatings – II. Microstructural Aspects". *ibid.*, p. 1942.
3. S. Haber, L. Gal-Or "Deep Electrophoretic Penetration and Deposition of Ceramic Particles Inside Porous Substrates – I. Analytical Model," Journ. Electrochem Soc. Vol. 139, No. 4, April 1992, p. 1071.
4. L. Gal-Or, L. Liubovich, S. Haber "Deep Electrophoretic Penetration and Deposition of Ceramic Particles Inside Porous Substrates – II. Experimental Model", *ibid.*, p. 1078.
5. L. Gal-Or, S. Liubovich "Single and Multilayer Electrophoretic Deposition and Penetration of Low-Expansion Ceramics on Porous Substrates", submitted to Journ. Electrochem. Soc.
6. L. Gal-Or, A. Sharon, "Electrophoretic Deposition of Alumina and Co-deposition of Alumina Zirconia" submitted to Journ. Electrochem. Soc.
7. S. Haber "Deep Electrophoretic Penetration and Deposition of Ceramic Particles Inside Impermeable Porous Substrates", submitted to Journ. Electrochem. Soc.

List of Theses -- Technion, Israel Institute of Technology

1. I. Silberman "Synthesis and Coatings of Ceramic Oxides by Electrodeposition," March 1991.
2. A Sharon "Electrolytic Deposition of Alumina and Alumina-Zirconia on Graphite Substrates," April 1992.
3. G. Starck "Electrolytic Deposition of Alumina on Non-Oxide Conductive Ceramics" in preparation.
4. S. Almaleh-Rockman "Electrolytic Deposition of Chromia on Non-Oxide Conductive Ceramics" in preparation.

Summary of Final Report

The objectives of this research project were:

- To study experimentally and theoretically the mechanism and kinetics of deposition and penetration of ceramic particles into porous substrates by electrophoresis.
- To study formation of ceramic oxide coatings from ionic solutions by electroreduction.
- To apply the results in order to develop a method for coating and impregnation of graphite and carbon-carbon composites with oxidation resistant materials.

The approach adopted in order to achieve these objects was based on:

- Application of an electric field for deposition and penetration of ceramic oxides from ionic aqueous solutions by electroreduction.
- Solve Fokker-Planck probability functions to predict theoretically particle penetration into pores as a function of physical parameters.

Electrophoretic deposition is obtained by the movement of electrically charged ceramic particles suspended in a fluid under the influence of a relatively high electric field. The charging of the particles takes place by the absorption of ions from the medium or by dissociation of the particle itself. The mobility of the particles in an unbounded medium is a function of the field strength, the dielectric constant and viscosity of the fluid and of the zeta potential and radius of the particle.

The phenomenon of electrophoresis can be utilized also for the induction of ceramic particles into the pores of a porous substrate. The particle penetration is facilitated by the electrophoretic force exerted on it and the electroosmotic flow of the fluid into the pores.

The electrolytic deposition of ceramic oxides from aqueous ionic solutions is based on the generation of hydroxyl ions (OH^-) by cathodic reduction of ions such as NO_3^- and the subsequent interaction between OH^- and appropriate cations, such as Al^{3+} , ZrO^{++} to form insoluble hydroxides of $\text{Al}(\text{OH})_3$, or $\text{Zr}(\text{OH})_4$ for example. Decomposition of the hydroxide upon thermal treatment renders the oxides. Co-deposition of two or more oxides is possible provided the different appropriate cations are present in the electrolyte.

The research program consisted of the following stages.

1. Investigation of the possibility to charge and deposit electrophoretically various oxide and non-oxide ceramics which have the potential to protect carbon materials.
2. Testing of the concept that ceramic particles can be induced into the pores of a porous substrate due to the effect of the electric field.
3. Investigation of the possibility to deposit ceramic coatings on graphite and C-C from aqueous ionic solutions by electrochemical reactions.
4. Theoretical analysis of the penetration of a single ceramic particle under the effect of an electric potential gradient into an open pore in order to:
 - gain an insight on the mechanisms governing the penetration;
 - derive the non-dimensional parameters that characterize the motion of the ceramic particle;
 - predict the penetration depth of the particle.
5. Study the effect of electrophoretic deposition and fluid parameters on the quantitative penetration of ceramic particles into the porous substrate.

6. Study of electrochemical and microstructural aspects of the electrolytic deposition of a ceramic oxide (ZrO_2) from an ionic aqueous electrolyte.
7. Study of electrophoretic surface deposition and penetration of low-expansion ceramic materials such as Al_2TiO_5 and HfTiO_4 . The interest in these coating materials stems from their anticipated compatibility with graphite and C-C substrates from the point of view of thermal expansion. However, the anisotropy of the expansion of these materials results in microcracking.
8. Study of multilayer electrophoretic deposition of ceramic coatings. It has been realized that the complicated problem of C-C protection may demand application of more than one coating. Therefore the sequential deposition of a protective coating on a low-expansion microcracked underlayer was studied.
9. Study of the co-deposition of two oxides by the electrolytic method ($\text{Al}_2\text{O}_3 + \text{ZrO}_2$). The effect of deposition parameters on the kinetics, morphology and composition of the coatings was studied.
10. Theoretical analysis of the penetration of a ceramic particle into a closed pore.
11. Single and multilayer coating of graphite and C-C specimens, sintering of coatings and study of oxidation protection afforded in continuous and sequential exposure to high-temperature oxidizing conditions.
12. Coating of shaped objects (exhaust nozzles) and testing of their oxidation and wear resistance.

Experimental

Deposition and impregnation experiments were carried out on two kinds of substrates:

- Porous graphite UCAR Grade 45 with a 48% volume porosity and 60μ average pore size. This material served as a model material for C-C and has the benefit of more accurate characterization and therefore better reproducibility of results is expected.
- A 2D carbon-carbon composite received from the Philips Lab. at Edwards Base. The ceramic powders used in the electrophoretic deposition studies were:
 - A submicron colloidal SiO_2 - Pyrogenic Aerosol with a specific area of $450 \text{ m}^2/\text{g}$.
 - Si_3N_4 with a particle size in the range of $0.2-0.7\mu$ supplied by the Israel Ceramics Institute. This powder contains a sintering additions of 6% Y_2O_3 .
 - SiC with a particle size of $< 40 \mu$ supplied by the Israel Ceramics Institute.
 - Fused SiO_2 , $1-40\mu$ supplied by the Israel Ceramics Institute.
 - Al_2TiO_5 of two kinds was used. One was supplied and prepared by the Israel Ceramics Institute with a 5% BaCO_3 additive and an average particle size of 1.4μ . The second kind was supplied by the Institute für Gesteinshüttenkunde, Aachen with a 5% additive of SiO_2 .
 - HfTiO_4 was acquired from Cerac Corp. with an average particle size of 70μ .
 - BN Grade B-50, H. Starck, Berlin

Specimens were $20 \times 20 \times 7 \text{ mm}$ and $16 \times 9 \times 7 \text{ mm}$. They were ultrasonically

cleaned in ethanol for 5 min prior to coating. After deposition the specimens were dried in air for 5 min and then at 200° C for 1/2–1 hr.

Most electrophoretic deposition experiments were carried out from suspensions in isopropanol and water. For the study of the effect of solvent properties on penetration, ethanol and pentanol were also used. The deposition was carried out at constant voltage with the electric field intensity varying between 5–300 v/cm. Particle concentrations were 3–250 g/l and deposition times varied between 30 sec – 120 min.

The amount of impregnated material was determined by weight change after removal of the external deposit. In some cases this was determined by weighing the residue after burn-off of the graphite at 900° C for 20 hrs.

The composition and morphology of the deposits were studied in cross-sections of the coated specimens in a Jeol-840 SEM equipped with an EDS analysis unit. In case of "green" deposits specimens were infiltrated with an epoxy resin (Epofix-Struers) and cured for 10 hrs prior to sectioning. Cross-sections were prepared by cutting with a lathe at 800 rpm. In some experiments the cross-sections were polished. X-ray diffraction of the coatings was carried out with a diffractometer Philips Model RW-1820, 40 kv, 40 mA, scanning rate 0.45°/min.

Sintering of coatings was done in air, nitrogen or argon, for 15 min – 4 hrs at 1100° C – 1650° C.

The electrolytic deposition studies included deposition of ZrO_2 from a 0.1M $\text{ZrO}(\text{NO}_3)_2$ aqueous solution. The co-deposition of $\text{ZrO}_2 + \text{Al}_2\text{O}_3$ was carried out from solutions containing both $\text{ZrO}(\text{NO}_3)_2$ and $\text{Al}(\text{NO}_3)_3$ of varying concentrations. The deposition was done at constant current with

c.d.'s in the range of 15–100 mA/cm² and durations of 20 sec–60 min. The deposits were heat treated at 400, 600 and 900°C for 1 hr while the co-deposits were treated for 1 hr at 1200°C. The microstructure was characterized by optical and scanning electron microscopy and the phase content was determined by x-ray diffraction.

The oxidation experiments were carried out with single (Al₂TiO₅, Si₃N₄) as well as with multilayer coatings (Al₂TiO₅ + Si₃N₄, SiO₂ + Si₃N₄, BN + Si₃N₄).

The coated specimens after sintering of the deposits were exposed in an oven at 830°C. In some experiments the exposure was continuous for 7 hrs while in others sequential 1 hr exposures up to a total of 7 hrs were repeated. In each case cooling was in the air. Weight losses were recorded and metallographic cross-sections prepared before and after exposure and studied in the SEM.

Results

– Electrophoretic deposition of all the ceramic materials studied so far, both on graphite and C–C was obtained following the charging of the particles and their displacement under the influence of the electric field. Some particles (e.g., SiO₂, SiC) acquired negative charges in isopropanol and therefore deposited on the anode while others (Si₃N₄, Al₂TiO₅) deposited on the cathode.

– In addition to surface deposition, the induction of the ceramic particles into the pores of porous graphite was demonstrated qualitatively for all the materials and was studied quantitatively for colloidal SiO₂. The penetration of the SiO₂ into the substrate was demonstrated by x-ray mapping of Si on cross-sections of coated specimens. It was found that in

the specimen with higher SiO_2 contents, a skeleton of SiO_2 of the same shape and dimensions as the original specimen remained after gasification of the graphite. The cross-section of this skeleton showed that the whole cross-section of the graphite was impregnated.

— The existence of an electroosmotic effect was demonstrated by the enhancement of pore filling by water and propanol in the presence of the electric field.

The theoretical analysis enables to predict the penetration depth of a ceramic particle inside the porous substrate under the influence of the electric potential gradient. It also enabled to derive the non-dimensional parameters that affect the particle motion. It was thus deduced that the parameters which affect most the particle penetration are the Peclet number (Pe) and the Damkohler number (λ):

$$\text{Pe} = \frac{U b}{D} = \left(\frac{U' + U''}{D} \right) b$$

$$\lambda = \frac{k b}{D}$$

where

U' — electrophoretic velocity

U'' — electroosmotic velocity

b — pore mean radius

D — diffusion coefficient

k — local deposition rate

Large Peclet numbers and small Damkohler numbers enhance penetration. Thus, deep penetration (over hundred pore diameters) can be achieved for very low deposition rates ($\lambda < 0.1$) and for very high Peclet numbers ($\text{Pe} > 100$). Deepest penetration is obtained for $\lambda = 0$ which can be achieved if a

repelling force between particles and pore walls would exist. Electroosmosis increases the Peclet number and thus penetration. The diffusion coefficient of the particle has a dual effect: its decrease increases the Peclet number, but it also increases the deposition rate. The theoretical analysis also indicates how the penetration can be controlled by selection of solvent properties, particle size and concentration and electric field strength.

The dispersion around the mean penetration depth is large for small Damkohler numbers and grows almost linearly with Peclet numbers. Thus, an almost even spread can be achieved for the same values which will bring about deep penetration. This result is a very favorable outcome for electrophoretic coating methods.

Comparison with the result we obtained for the open pore structure of the substrate reveals that penetration depths for closed pores is smaller whereas dispersion in the latter is larger provided electroosmosis exists.

Experimental studies of the effect of solvent and deposition parameters on particles carried out with colloidal SiO_2 showed that as predicted theoretically, an increase in the ϵ/η ratio of the fluid enhances penetration. Thus, it was found that the amount of induced SiO_2 was 10 times larger for water ($\epsilon/\eta = 81$) than for pentanol ($\epsilon/\eta = 4.2$).

It was found that the electric field has a dual effect on the extent of particle penetration. Due to increase of the particle velocity and Peclet number with field strength, penetration is enhanced by it. However, the field also enhances the buildup of an external deposit on the substrate, which blocks penetration. Therefore, there exists an optimal field strength, its value decreasing with increased particle concentration, because of faster buildup of the external coating at higher concentrations.

Penetration increases with particle concentration both in water and

propanol. At low field strengths (5 V/cm) the relationship is linear for the range of concentrations studied.

Penetration increases with deposition time, but reaches a plateau after a period which depends on solvent concentration and field strength. The fact that the plateau is reached before full impregnation of the pores is probably due to the blockage by the external coating. Thus, the extent of penetration could be increased if a way is found to prevent surface deposition.

Impregnation and coating with low-expansion ceramics was studied with Al_2TiO_5 and HfTiO_4 particles. In contrast to SiO_2 particles, it was found that both Al_2TiO_5 and HfTiO_4 deposit on the cathode both from water and propanol suspensions. The positive charge on the particles indicates a high isoelectric point since the pH of these suspensions was determined as 8.1 in water and 6.2 in propanol. As in the study of SiO_2 deposition, it was found that penetration of Al_2TiO_5 into the porous substrate is higher in water than in propanol. However, the addition of $\approx 20\%$ propanol to the water leads to a maximal penetration probably due to better wetting of the graphite as demonstrated in simple wetting experiments. About 6% of substrate weight of Al_2TiO_5 were induced into the pores at 100 V/cm, 30 g/l after 60 min. The surface deposition, however, is both higher and morphologically better in propanol due to a lower fraction of penetrated material and lower H_2 formation on the cathode.

It was thus concluded that for optimal coverage and penetration a two stage process would be employed: impregnation from an aqueous solvent with 20% propanol for relatively long duration (60 min, 75–100 V/cm) and coating in propanol at higher field (200 V/cm) and shorter duration (≈ 2

min.) It was shown that impregnation increases with field intensity and deposition time.

The feasibility of subsequent deposition of two different layers of materials with zeta potentials of the same polarity was shown for Si_3N_4 on Al_2TiO_5 (cathodic deposits) and SiC on glass ceramic (anodic deposits). The deposition is carried out by transferring the coated substrate from the first suspension into the second to continue the deposition of the second material. Cross-sections of the two layers were prepared after impregnation. Elemental analysis and Si and Ti x-ray images were performed in the SEM and the existence of the two layers shown. However, penetration of the Si_3N_4 and SiC into the first layer was observed. The layer thicknesses obtained in these experiments were in the range of 150–300 μ .

The sintering and oxidation experiments gave the following results:

HfTiO_4 coatings disintegrated after sintering and no viable undercoating was obtained.

Sintering Al_2TiO_5 coatings at 1650°C in N_2 resulted in adherent coatings which, however, decomposed partially into Al_2O_3 and TiO_2 .

Si_3N_4 coatings were obtained by sintering at 1650°C in N_2 . Uniform and adherent coatings were obtained with extensive anchoring in the pores and voids of the substrate. Interaction with the substrate took place resulting in SiC and Si formation.

Sintering of Si_3N_4 coatings deposited on an underlayer of Al_2TiO_5 resulted in dense Si_3N_4 layers reaching the substrate through a discontinuous layer containing Ti. An even distribution of Al was seen in the entire cross-section.

Adherent coatings of Si_3N_4 on fused SiO_2 were obtained with anchoring in the substrate. Horizontal and vertical microcracks are seen in

the coatings after sintering.

Impregnation of BN into the pores prior to Si_3N_4 coating was attempted. Since both B and N are not visible in the EDS-SEM no evidence of penetration was seen except for weight gain after impregnation.

Shaped objects, exhaust nozzles and casting crucibles, were coated with $\text{Si}_3\text{N}_4 + \text{Al}_2\text{TiO}_5$ and $\text{Si}_3\text{N}_4 + \text{SiO}_2$. Uniform internal and external coatings were obtained using shaped electrodes.

Oxidation experiments were carried out by recording the weight loss during continuous and repeated exposures of 830°C . Best results with graphite specimens were obtained with the $\text{Si}_3\text{N}_4 + \text{Al}_2\text{TiO}_5$ system where in some cases nil weight loss was recorded after 7 repeated 1-hr exposures, a regime that exposed the specimens to repeated thermal shock. No beneficial effect of an underlayer of fused SiO_2 or BN was found in laboratory specimens when compared with Si_3N_4 only. However, very good results were obtained with an underlayer of SiO_2 on exhaust graphite nozzles under specific testing conditions.

On C-C specimens low weight losses were obtained with Si_3N_4 and Si_3N_4 on Al_2TiO_5 in continuous exposure experiments. In most repeated exposure tests high weight losses were recorded. However, in some experiments Si_3N_4 coatings gave low weight loss. The irreproducibility of the results in both materials and in particular in the case of C-C may stem from a major defect in the coating formed on the location of the holder during deposition. Although repeated depositions were made this problem may not have been solved completely and should be elaborated in further experiments.

The electrolytic route of obtaining ceramic oxide coatings on graphite and C-C was studied for deposits of ZrO_2 and co-deposits of ZrO_2 and Al_2O_3 .

ZrO₂ coatings were deposited from an aqueous solution of ZrO(NO₃)₂. A two-step mechanism is suggested for the ZrO₂ formation; generation of hydroxyl ions (OH⁻) at the cathodic substrate by reduction of NO₃⁻ and dissolved O₂, and then reaction of the hydroxyl ions with zirconyl ions present in the solution to form the hydroxide Zr(OH)₄, which in turn decomposes on drying to yield zirconia (ZrO₂). Faradaic efficiencies of 20–50% were found, attributable to reduction reactions that do not produce hydroxyl ions, as well as to formation of the hydroxide at sites removed from the cathodic substrate due to diffusion of the hydroxyl ions. The effects of current density, time, and hydrodynamic conditions on coating weight, cell voltage, temperature, and pH of the solution were studied.

As expected, it was found that coating weight increases with c.d. and time, while stirring of the electrolyte caused a significant reduction of deposition rate, probably by facilitating migration of OH⁻ from the cathode into the bulk of the solution so that the hydroxide formed does not accumulate on the cathode. Cell voltage and temperature of the solution increased with increase in c.d. and time, as a result of the formation of the non-conductive deposit characterized by a high ohmic resistance. pH of the solution as measured in the bulk is reduced at high c.d. due to the generation of H⁺ by the anodic reaction and use of the OH⁻ formed at the cathode in the Zr(OH)₄ formation.

The initial coating is a zirconium hydroxide gel with an amorphous character. Microcracks develop in the coating during drying due to tensile stresses associated with non-uniform contraction. Firing of the coating led to its crystallization into fine, equiaxed submicron particles of monoclinic and tetragonal polymorphs of zirconia. Calculation of crystallite sizes by reflection broadening, indicated them to be 2 nm after treatment at 400°C and 12 nm when fired at 600°C for 1 hour. Under these conditions the

polymorphs were undistinguishable. Firing for 1 hr at 900°C resulted in distinct crystallites of both phases, 20–25 nm in size. The volume fractions were 15% and 85% for the tetragonal and monoclinic phases respectively.

The co-deposition of two oxides by an electrolytic process from aqueous solutions containing salts of both cations $\text{Al}(\text{NO}_3)_3 + \text{ZrO}(\text{NO}_3)_2$ was demonstrated and studied for $\text{Al}_2\text{O}_3 + \text{ZrO}_2$ deposits. Prior to that the deposition of Al_2O_3 was studied.

During deposition of Al_2O_3 the cell voltage rises steeply as a result of the build-up of the hydroxide with a high ohmic resistance. At a certain stage further growth of the deposit is enabled by local breakdown of the film creating new sites of reduction. A more gradual rise in cell voltage takes place when Al_2O_3 and ZrO_2 are co-deposited indicating a change in the dielectric properties of the co-deposit.

The as-deposited coatings are amorphous and after a heat-treatment at 1200°C for 1 hr became crystalline exhibiting phases of $\alpha\text{Al}_2\text{O}_3$ and tetragonal ZrO_2 . It was shown that the atomic ratio of Al/Zr in the deposit can be varied by varying this ratio in the solution. The $\text{Al}(\text{OH})_3$ is, however, preferentially deposited probably due to the higher diffusion coefficient of Al^{3+} as compared to that of ZrO_2^{2+} .

Improved coating morphology and maximum thickness was obtained by applying a pulsed current for deposition. This effect can be explained by the creation of new nucleation sites for deposit formation during current intermission decreasing thus the cluster size.

The present work demonstrated the potentialities of the electrolytic method for production of single ceramic oxide deposits as well as co-deposits of two oxides. Control of thickness as well as of composition can be achieved by control of deposition and solution parameters. However, further studies of the drying stage are necessary in order to achieve sound and crack-free coatings.

Summary and Future Work

The present project has laid the experimental and theoretical foundations for a technology aimed at protecting carbon-based porous materials from oxidation at elevated temperatures. This is achieved by electrophoretic impregnation and deposition of an unlimited variety of ceramic materials. The basic advantages of this technology as compared with existing ones are:

- The possibility to deposit any type of ceramic material including materials that cannot be deposited by other coating techniques such as CVD.
- The possibility to induce the ceramic material into pores and cracks of the substrate to improve adhesion of coating and overall protection.
- High coating rate
- The possibility to coat complex shapes.
- Low cost of equipment and operation.

Two specific coating systems were studied in specimens and demonstrated on shaped products — exhaust nozzles and crucibles. These systems are coatings of Si_3N_4 on Al_2TiO_5 and on fused SiO_2 . Also coatings of Si_3N_4 only were studied on specimens. The coatings were sintered and their oxidation protection studied at one set of conditions.

The feasibility of producing single and multi-layer coatings and impregnation, their sintering and achieving oxidation protection has been proven.

However, more experimental work should be done to optimize and finalize this technology. This work should include the following investigation:

- Testing of additional single and multi-layer coating systems for further optimization of the oxidation protection.
- Optimization of coating thicknesses.
- Study of geometrical parameters for shaped body coating.
- Procedures for preventing defects in coating due to use of holder.
- Scale-up of process.

Sintering and Oxidation Experiments

Report for the period 1.6.91 – 30.9.92

L. Gal-Or

S. Liubovich

Israel Institute of Metals

Technion Research and Development Foundation

REPORT DOCUMENTATION PAGE

Form Approved

OMB No. 0704-0188

Public reporting burden for this collection of information is estimated to average 1 hour per response, including the time for reviewing instructions, searching existing data sources, gathering and maintaining the data needed, and completing and reviewing the collection of information. Send comments regarding this burden estimate or any other aspect of this collection of information, including suggestions for reducing this burden, to Washington Headquarters Services, Directorate for Information Operations and Reports, 1215 Jefferson Davis Highway, Suite 1204, Arlington, VA 22202-4302, and to the Office of Management and Budget, Paperwork Reduction Project (0704-0188), Washington, DC 20503.

1. AGENCY USE ONLY (Leave blank)	2. REPORT DATE November 30, 1992	3. REPORT TYPE AND DATES COVERED Annual Report 1 July 91-30 Sept. 92	
4. TITLE AND SUBTITLE Electrophoretic and Electrolytic deposition of ceramic particles on porous substrates.		5. FUNDING NUMBERS AFOSR-89-0474	
6. AUTHOR(S) L. Gal-Or, S. Liubovich			
7. PERFORMING ORGANIZATION NAME(S) AND ADDRESS(ES) Technion Research and Development Foundation Technion City, Haifa 32000, Israel		8. PERFORMING ORGANIZATION REPORT NUMBER	
9. SPONSORING / MONITORING AGENCY NAME(S) AND ADDRESS(ES) - EOARD 223/231 Old Marylbone Rd. London NW1, 5th UK - AFOSR/NE Lt. Col. L. Burggraf, Bolling AFB Washington DC 20332-6448, USA		10. SPONSORING / MONITORING AGENCY REPORT NUMBER	
11. SUPPLEMENTARY NOTES			
12a. DISTRIBUTION / AVAILABILITY STATEMENT Unlimited		12b. DISTRIBUTION CODE	
13. ABSTRACT (Maximum 200 words) The sintering and protective properties of electrophoretically deposited and impregnated coatings on graphite and C-C were investigated. Coating systems studied were: Al_2TiO_5 , $HfTiO_4$, Si_3N_4 , Si_3N_4 on Al_2TiO_5 , Si_3N_4 on fused SiO_2 and on BN. Adherent coatings of Al_2TiO_5 were obtained after sintering at $1650^\circ C$ in N_2 . Partial decomposition into TiO_2 and Al_2O_3 took place. No viable coatings of $HfTiO_4$ were obtained. Si_3N_4 coatings were deposited on the Al_2TiO_5 in view of the microcracking of the latter. After sintering uniform dense coatings anchored in the pores and cracks of the substrate were obtained. Zero weight loss was recorded for this system on graphite after seven 1-hr exposures at $830^\circ C$ with rapid intermittent cooling. On C-C single layers of Si_3N_4 gave good results at continuous exposures. Higher weight losses were recorded for coatings with SiO_2 and BN underlayers. Exhaust nozzles of graphite were coated and tested in conditions simulating the air breathing engine. Complete protection of the nozzle was recorded.			
14. SUBJECT TERMS Electrophoresis, Ceramics, Penetration, Sintering, Oxidation Resistance, Electrolytic Deposition		15. NUMBER OF PAGES	
		16. PRICE CODE	
17. SECURITY CLASSIFICATION OF REPORT Unclassified	18. SECURITY CLASSIFICATION OF THIS PAGE Unclassified	19. SECURITY CLASSIFICATION OF ABSTRACT Unclassified	20. LIMITATION OF ABSTRACT Unlimited

NSN 7540-01-280-5500

Standard Form 298 (Rev. 2-89)
Prescribed by ANSI Std. Z39-18
298-102

Table of Contents

	Page
1. Introduction.....	1
2. Materials and Methods.....	1
3. Results and Discussion.....	4
3.1 HfTiO ₄ Coatings.....	4
3.2 Al ₂ TiO ₅ Coatings.....	7
3.3 Si ₃ N ₄ Coatings.....	11
3.4 Si ₃ N ₄ on Al ₂ TiO ₅ Coatings.....	26
3.5 Si ₃ N ₄ on Fused SiO ₂ Coatings.....	29
3.6 Si ₃ N ₄ coating after impregnation with BN.....	39
3.7 Coating of exhaust nozzles and crucibles.....	39
3.8 Oxidation Experiments.....	43
4. Summary and Conclusions.....	64

1. Introduction

This report covers the last research period of this project which concentrated on the sintering of coatings and testing of the oxidation resistance of the coated specimens. Experiments were carried out on graphite and C-C specimens and in the final stage, deposition on shaped objects was carried out. Those were graphite exhaust nozzles and crucibles.

2. Materials and Methods

a) Substrates

Two kinds of substrates were used, a porous graphite and carbon-carbon composite:

- Porous Graphite UCAR Grade 45. Porosity 48% and an average pore size of 60μ .
- 2D Carbon-Carbon (received from the Phillips Lab. at Edwards Base)

b) Ceramic Materials

- Al_2TiO_5 prepared at the Israel Ceramics Institute with 5% BaCO_3 added for sintering enhancement. After attrition milling the average particle size was 1.4μ .
- Al_2TiO_5 - bioceramic submicron powder with 5% SiO_2 from Institut für Gesteinshüttenkunde, Germany.
- Si_3N_4 LC12 was acquired from Alfa Corp. and prepared at the Israel Ceramics Institute with 6% Y_2O_3 added for sintering enhancement. The average particle size was $<0.7\mu$.
- HfTiO_4 was acquired from Cerac Corp. and had originally an average size of 70μ .

- Fused SiO_2 (1–40 μ) supplied by the Israel Ceramics Institute.
- BN – Grade B–50, Hermann C. Starck, Berlin.

c. Specimens

Specimen dimensions were 16 × 9 × 7mm.

Nozzles: ϕ 60mm, height – 60 mm.

Crucibles: ϕ 60 mm, height – 80 mm.

d. Deposition parameters

Electrophoresis was carried out from suspensions of respective particles in aqueous and non–aqueous solvents, and mixtures of the two solvents. Suspensions were prepared by wet milling for 3 hours in a ball mill, sonicating for 5 min. Stirring was applied during deposition and penetration.

Deposition electric field was – 5v/cm – 300v/cm.

Particle concentration – 30 g/l – 100 g/l

Solvents – isopropanol and water after deionizing

Temperature – room

Current – 0.1 – 100 mA (current fell during experiments due to build–up of deposit)

Deposition time – 15 sec – 60 min

Counter electrodes – stainless steel

Distance between electrodes – 15 mm

Specimen Preparation

The specimens were cleaned ultrasonically in ethanol for 4 min prior to coating and twice for 4 min after sintering of coating.

Sintering

Sintering was carried out at temperatures 1400°C – 1650°C for

45 min — 4 hours in an Ar or N₂ atmosphere. Cooling was in the furnace. The specimens were immersed in a powder of Si₃N₄ during the sintering. Prior to sintering the deposits were dried at 200° C for 20 min.

Testing of Deposits

For quantitative determination of the deposited material, specimens were weighed before deposition, after deposition and after sintering of the deposit. The amount of impregnated material was determined by weight change after removal of the external deposit. The oxidation experiments were carried out with Si₃N₄ as well as with multi-layer coatings (Al₂TiO₅ + Si₃N₄, BN + Si₃N₄ ; SiO₂ + Si₃N₄). The coated specimens, after sintering of the deposit, were exposed in a furnace at 830° C. In some experiments the exposure was continuous for 7 hours while in others sequential 1 hr exposures up to a total of 7 hrs were repeated. In each case cooling was in the air. Weight losses were recorded and metallographic cross-sections prepared before and after exposure.

The morphology and composition of deposit were studied by optical and electron microscopy with a JEOL 840 SEM and the phase content was determined by X-ray diffraction. For study of cross-sections, the coated specimens after sintering and oxidation were covered with an Epofix (Struers) resin and cured for 10 hrs at room temperature. Then the cross-section was prepared by cutting with a lathe at 800 rpm. The cross-sections of some specimens were polished.

3. Results and Discussion

The first steps of this research period concentrated on the deposition of ceramic materials with low expansion coefficients — HfTiO_4 and Al_2TiO_5 (see Fig. 1). This property is important to minimize crack formation during sintering and use. It was clear that an additional coating will have to be applied later since both materials have anisotropic expansion properties and therefore microcracking will take place.

The deposition conditions were defined on the basis of the previous work.

3.1 HfTiO_4 Coatings

The HfTiO_4 powder was deposited on the cathode at the following conditions:

particle conc. — 30 g/l

field intensity — 300 v/cm

time — 30 min

fluid — propanol

Following deposition the coatings were dried and sintered. In order to determine the sintering conditions a dilatometric test was performed on the HfTiO_4 powder (Fig. 2). This test showed a strong shrinkage (18%) in the temperature range 1000–1550°C. A body was prepared, sintered at 1550°C for 3 hrs and tested. The density was found to be 5.6 gr/cm³, open porosity — 0.3% and water absorption — 0.05%. An X-ray diffraction test showed the characteristic peaks of the HfTiO_4 with a small concentration of other crystalline phases. In view of the above results it was decided to sinter the HfTiO_4 coatings at 1650°C for 1.5 hrs in N_2 so as to ensure complete sintering. However in all experiments the HfTiO_4 coatings disintegrated and fell off the substrate. X-ray diffraction of the coated surface after sintering did not show any evidence of HfTiO_4 , HfO_2 or TiO_2 .

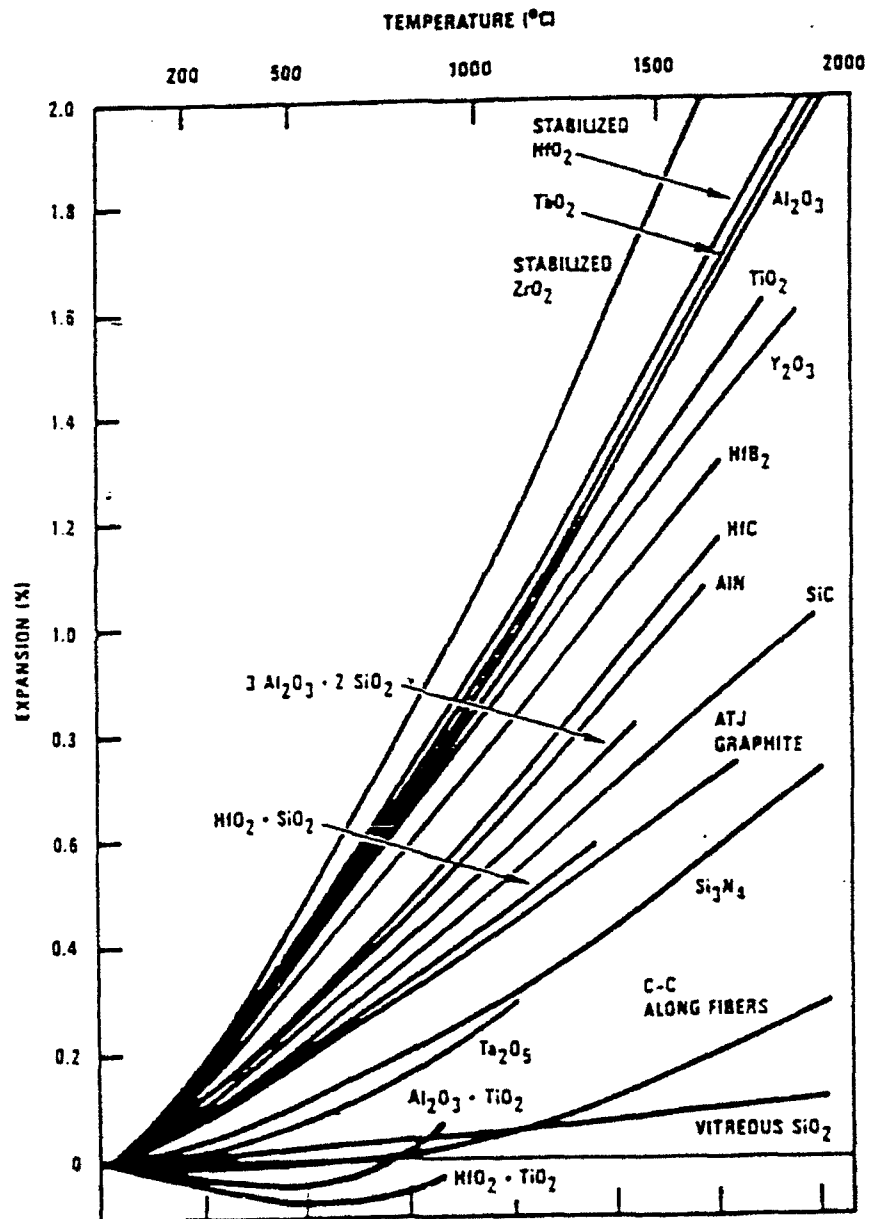


Fig. 1: Ceramic thermal expansion characteristics

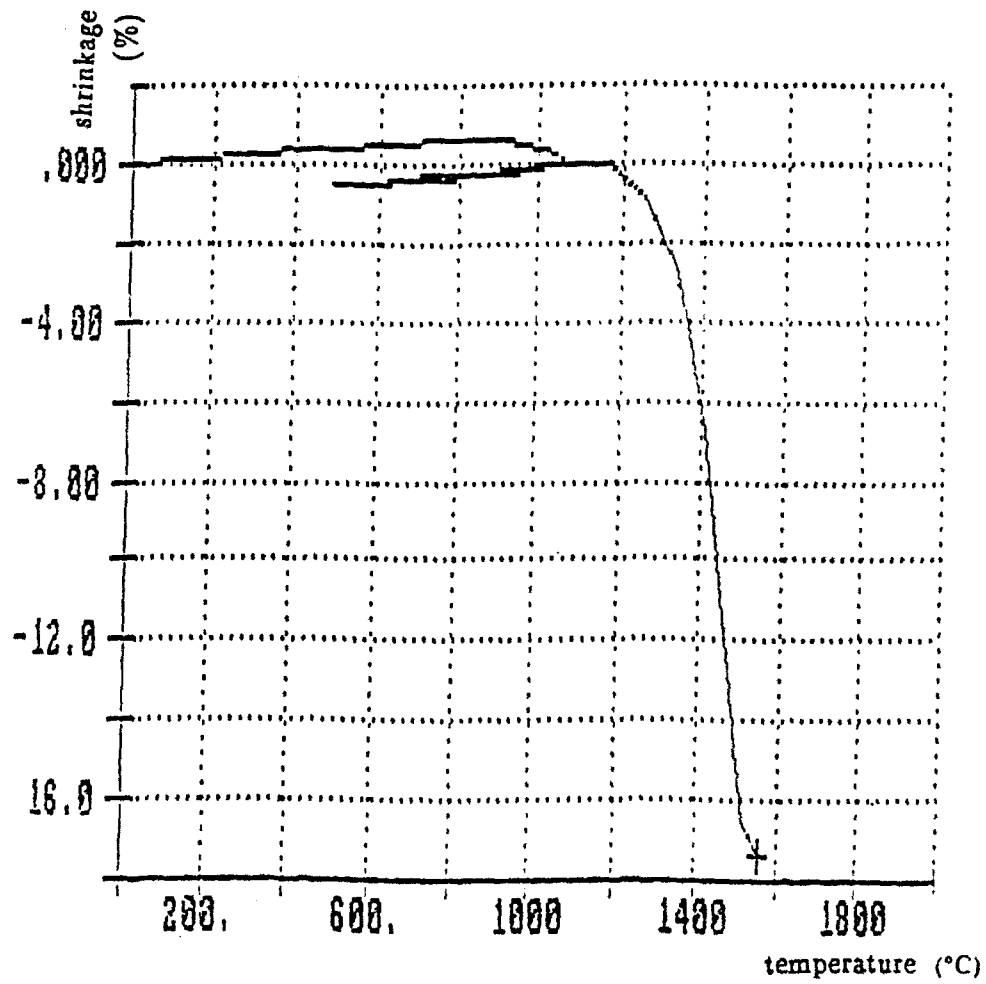


Fig. 2: Dilatometric curve of HfTiO_4 body (sintering)

3.2 Al₂TiO₅ Coatings

Al₂TiO₅ was deposited both on graphite and C-C specimens (Fig. 3). The cathodic deposition was carried out in two stages based on the previous work. The first stage was performed so as to secure impregnation of the pores and the second for surface coating.

First stage:

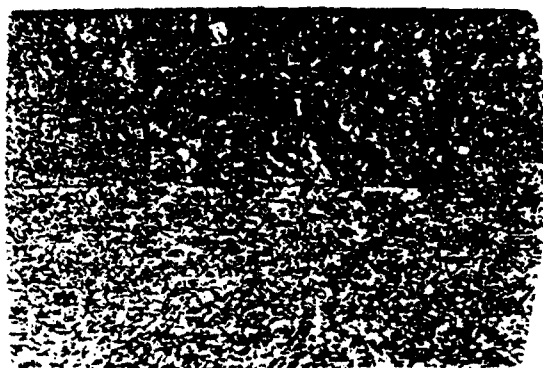
particle concentration — 30 g/l
field intensity — 75 v/cm
deposition time — 60 min
fluid — water with 20% propanol

Second stage:

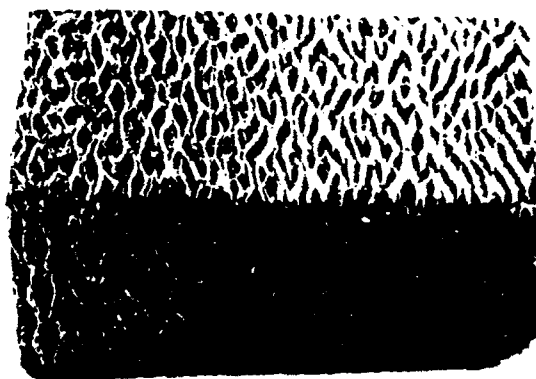
particle concentration — 30 g/l
field intensity — 100 v/cm
deposition time — 15 sec + 15 sec (change of holder position)
fluid — propanol

Fig. 4a shows a coated specimen after deposition and 4b shows the cross-section of an uncoated and coated porous graphite specimen. An even external coating is obtained and impregnation of the cross-section is seen. Results of a dilatometric test of the Al₂TiO₅ powder is seen in Fig. 5. Shrinkage of the specimen which indicate sintering, took place in the temperature range of 1100 — 1400°C and it was ~ 18%.

Coatings were sintered at first at 1400°C for 3.5 hrs in Ar. However, they did not adhere to the surface, their color was nonuniform and X-ray diffraction indicated partial decomposition into Al₂O₃ and TiO₂. Sintering at 1650°C for 1.5 hr in N₂ resulted in an adherent coating with dark and light gray areas. X-ray diffraction patterns of the light and dark areas are given in Figs. 6 and 7 respectively. Partial decomposition is seen in both

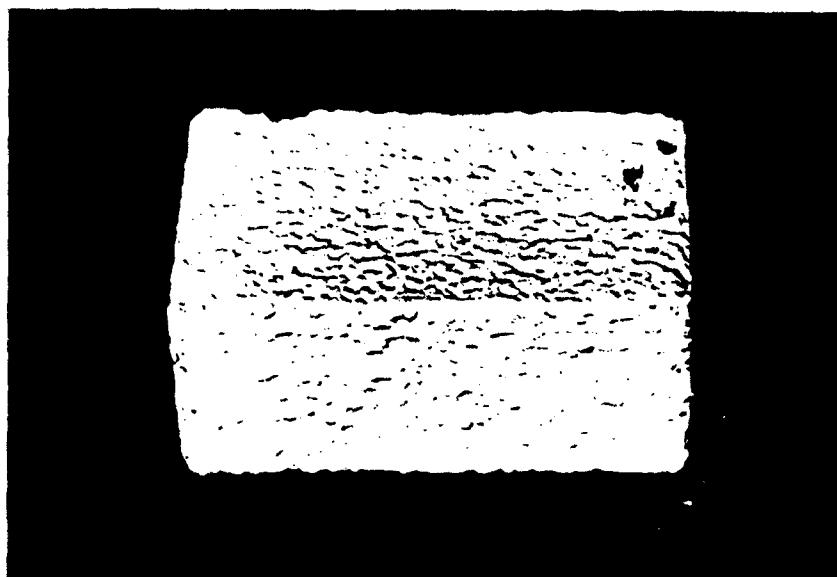


a) graphite

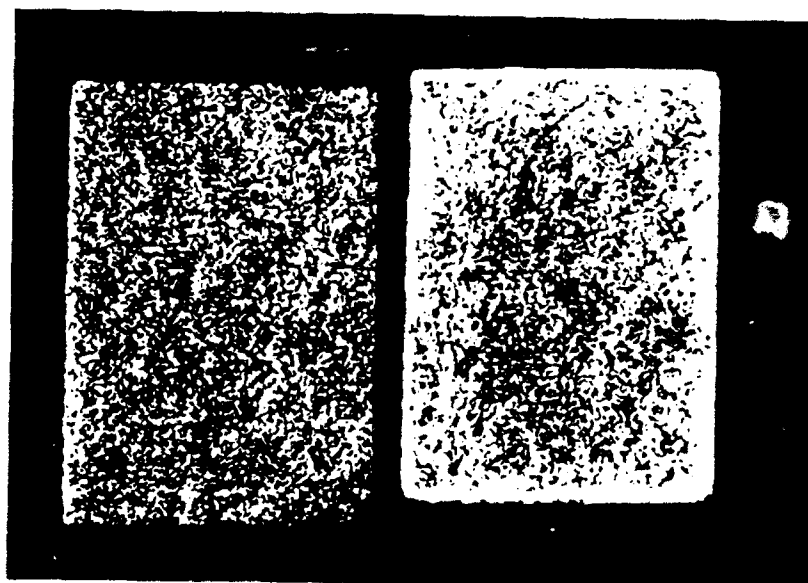


b) C-C 2D-composite

Fig. 3: Uncoated specimens



a) coated specimen



b) Cross-sections of uncoated (left) and coated specimen

Fig. 4: Al_2TiO_5 coating on graphite before sintering

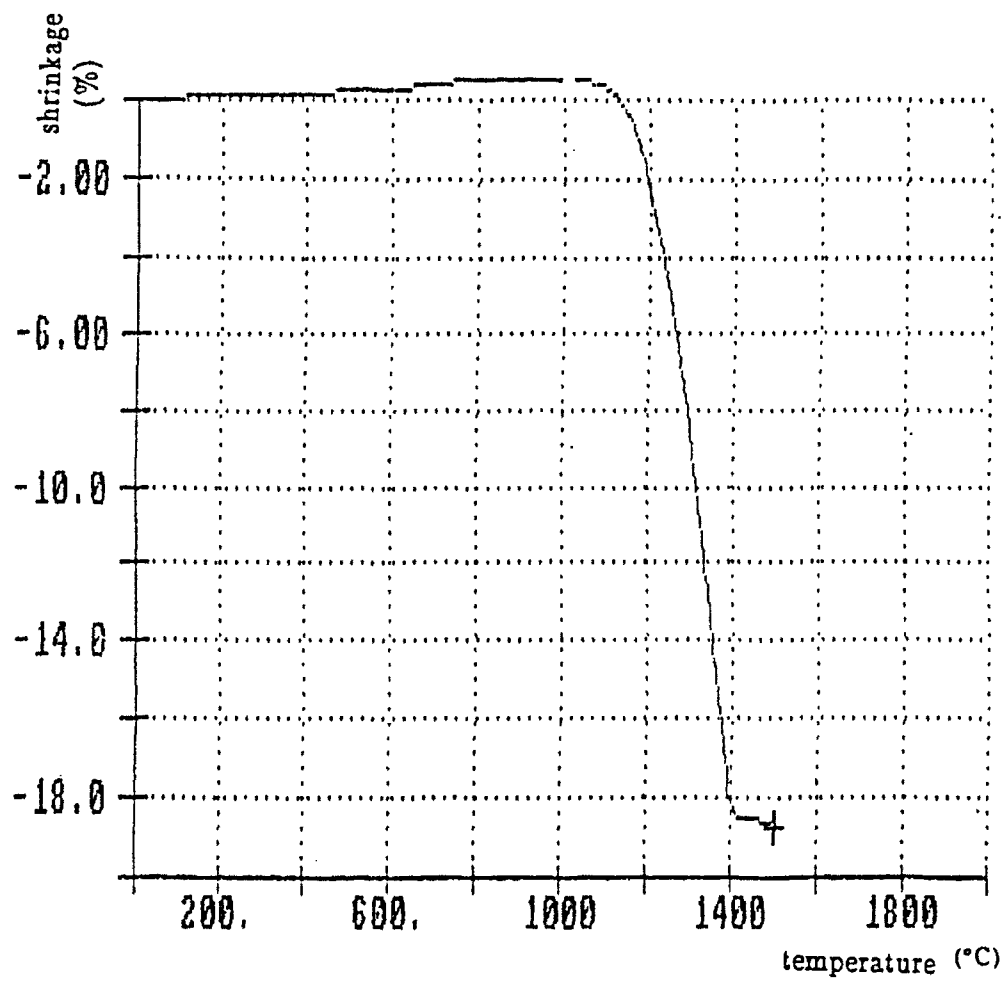


Fig. 5: Dilatometric curve of Al_2TiO_5 body

cases with stronger decomposition in the dark areas where in addition to TiO_2 , also TiO and Ti_2O_3 appeared. According to the literature Al_2TiO_5 is unstable in the range of $700\text{--}1300^\circ\text{C}$. But additions such as MgO reduce significantly the degree of decomposition. Attempts to deposit Al_2TiO_5 with 5% MgO failed. No electrophoretic deposition took place. Therefore, all experiments were carried out with $\text{Al}_2\text{TiO}_5 + 5\% \text{BaCO}_3$ as a sintering additive. In the last stages a powder with 5% SiO_2 was obtained from Germany and deposited.

3.3 Si_3N_4 Coatings

The coatings were obtained on the cathode at the following conditions:

particle concentration — 100 g/l

field intensity — 100 v/cm and 50 v/cm

deposition time — 15–60 sec.

Coatings were obtained in single and multi-layers with and without drying in between layers (Fig. 8). Initial sintering was done at 1600°C for 2.5 hrs in N_2 . The coatings did not adhere to the substrate (Fig. 9a). Therefore sintering temperature was raised to 1650°C and time shortened to 1.5 hrs. These coatings were adherent (Fig. 9b); however, their color varied from dark grey to green and black. X-ray diffraction of these coatings is given in Fig. 10. In addition to $\beta\text{Si}_3\text{N}_4$, αSiC , βSiC and Si were found. These results indicate an interaction between the coating and substrate to form SiC and formation of Si .

Cross-sections through a graphite specimen coated with two layers (50 v/cm, 15 + 15 sec) of Si_3N_4 after sintering are seen in Fig. 11 and at larger magnifications in Fig. 12. The coating is relatively uniform and anchoring in the pores is seen.

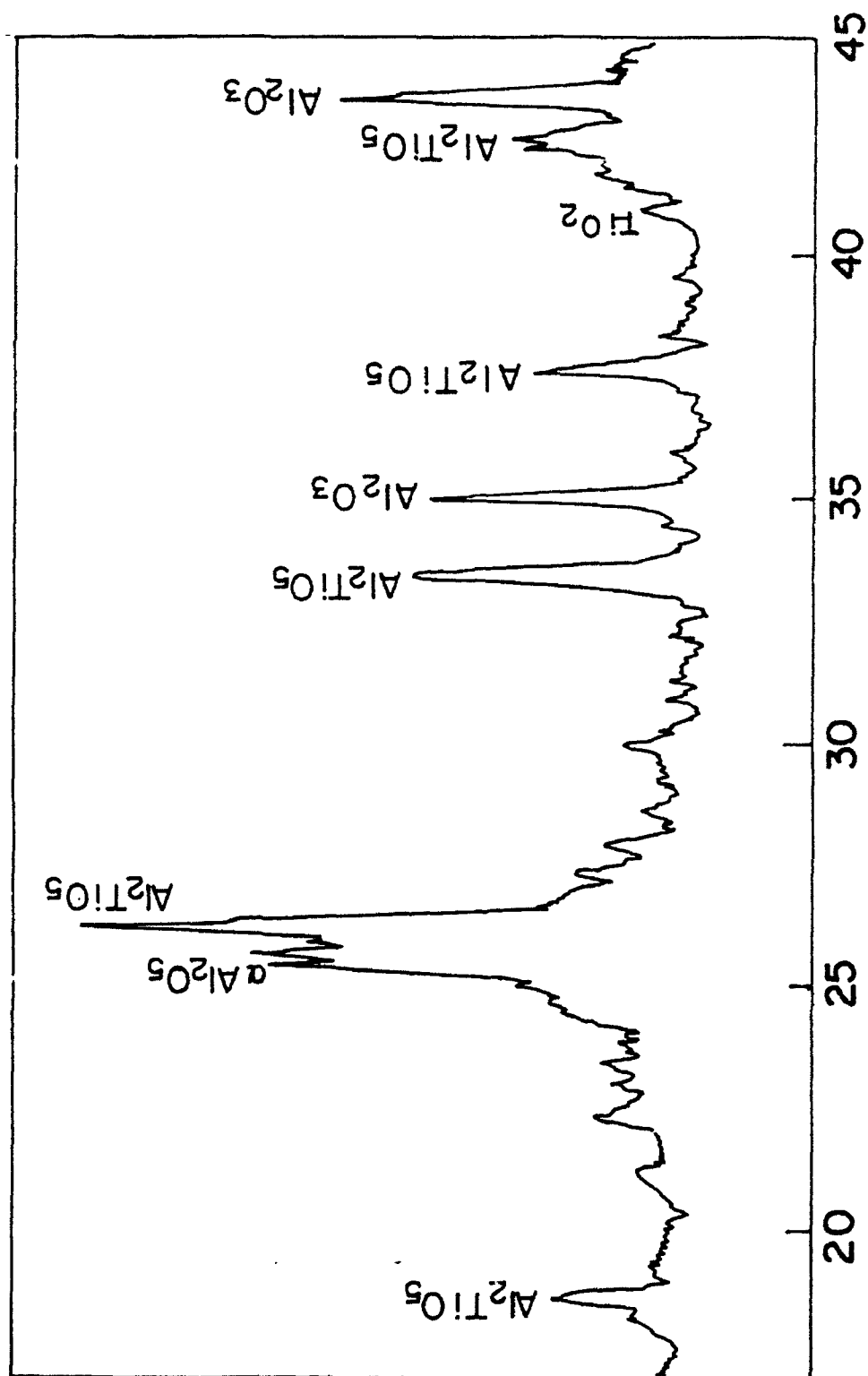


Fig. 6: X-Ray diffraction of Al_2TiO_5 coating (in light gray area) sintered at 1650°C for 1.5 hours in N_2

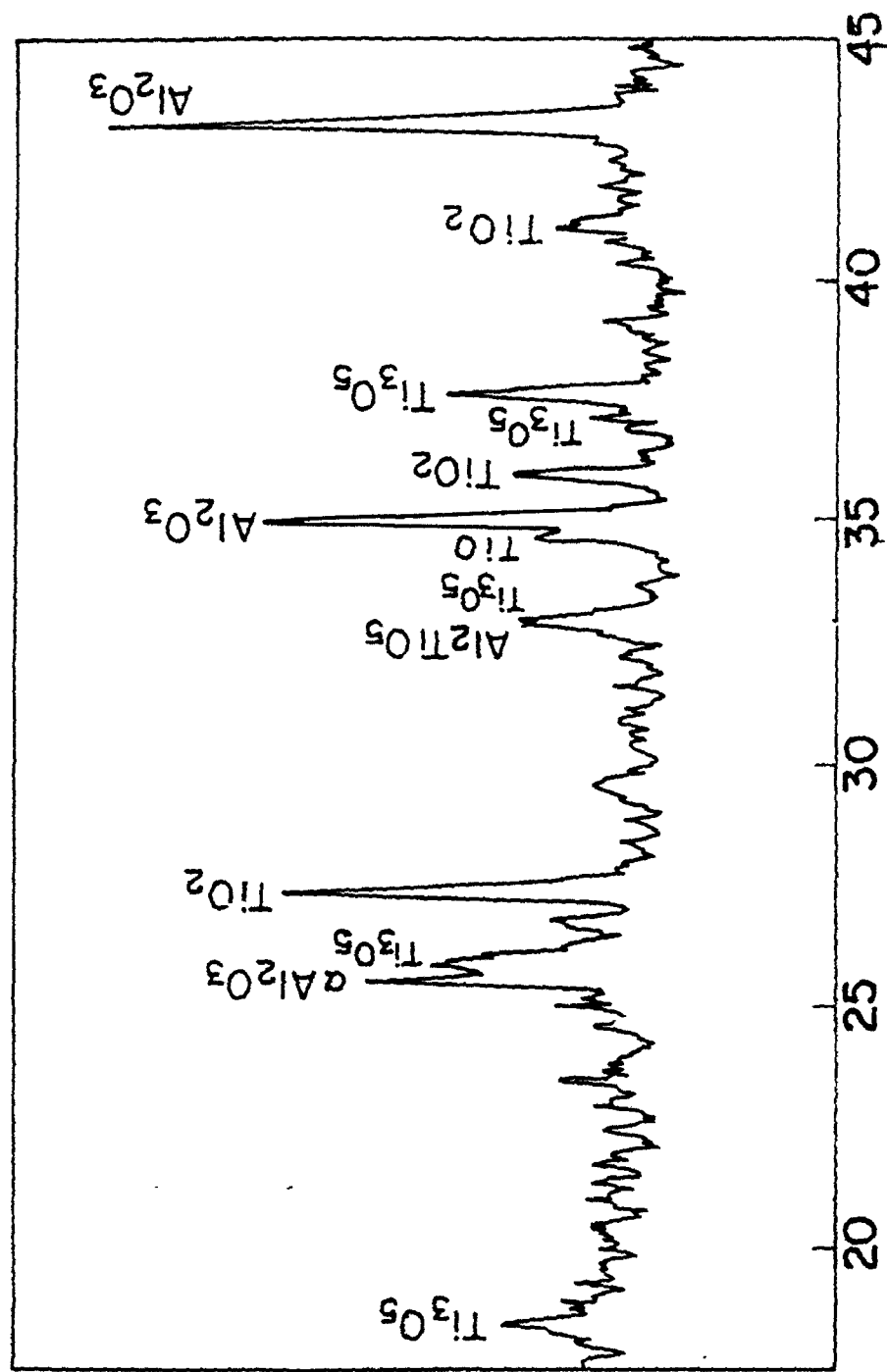


Fig. 7: X-Ray diffraction of Al_7TiO_5 coating as in Fig. 6, but in dark grey area

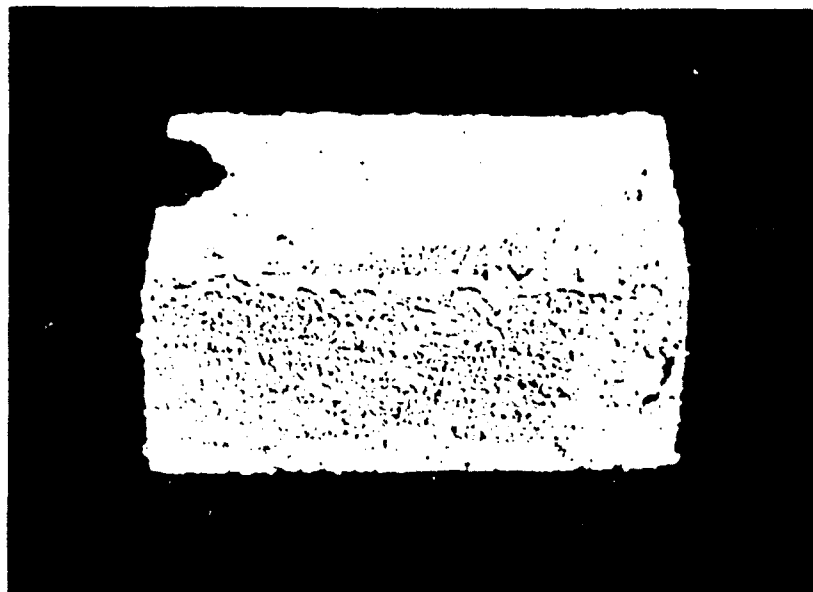
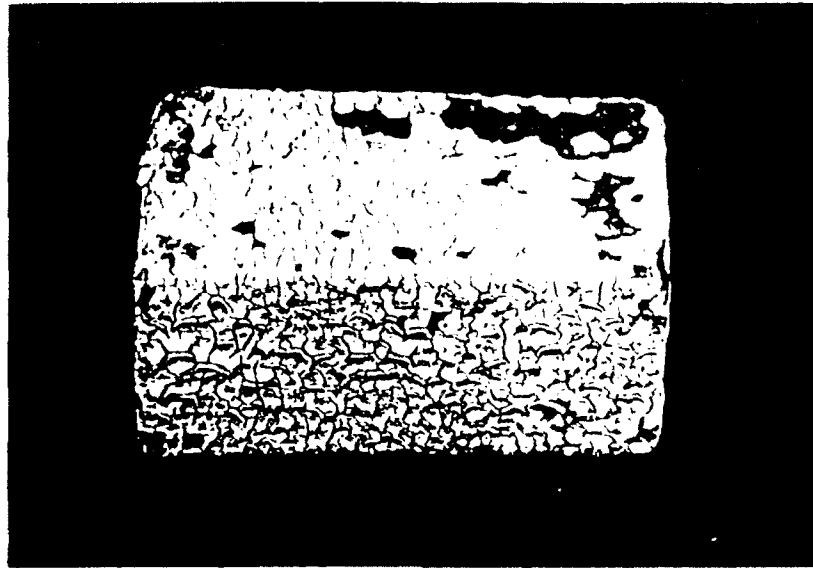
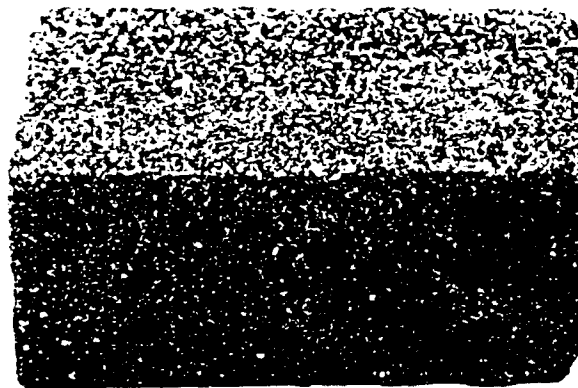


Fig. 8: Si₃N₄ Coating on C-C before sintering



a. at 1600° C for 2,5 hr



b. at 1650° for 1,5 hr

Fig. 9: Si_3N_4 Coating on C-C after sintering at different temperatures and time in N_2

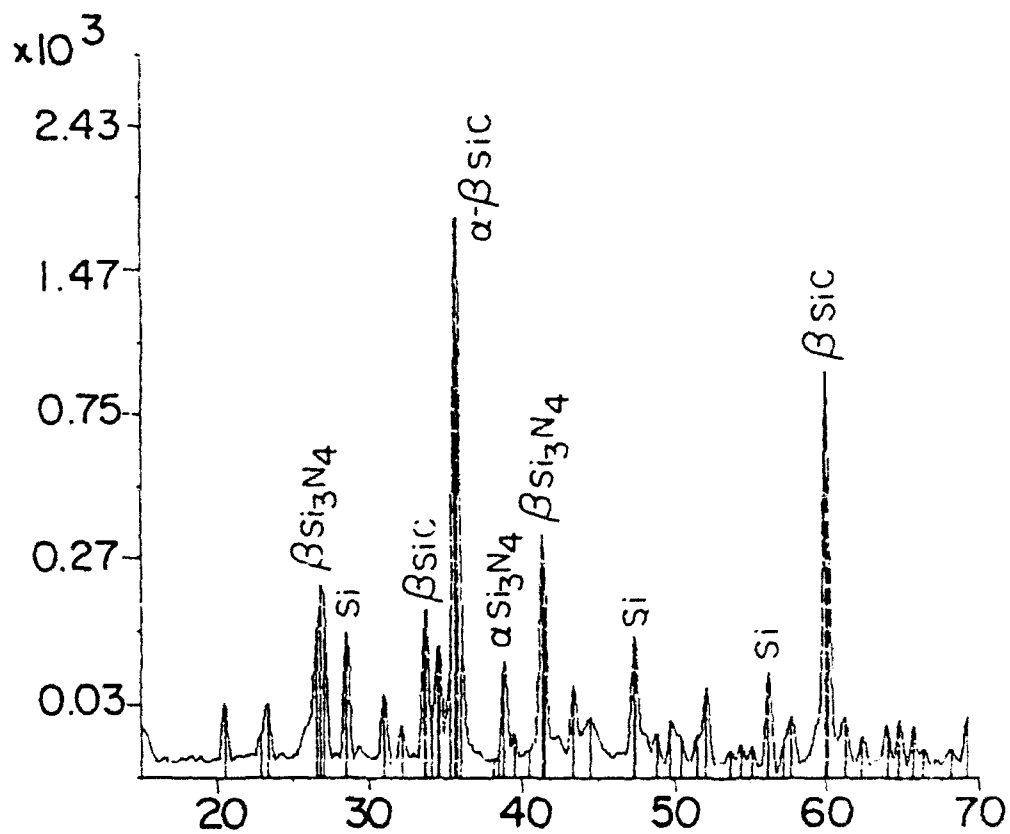
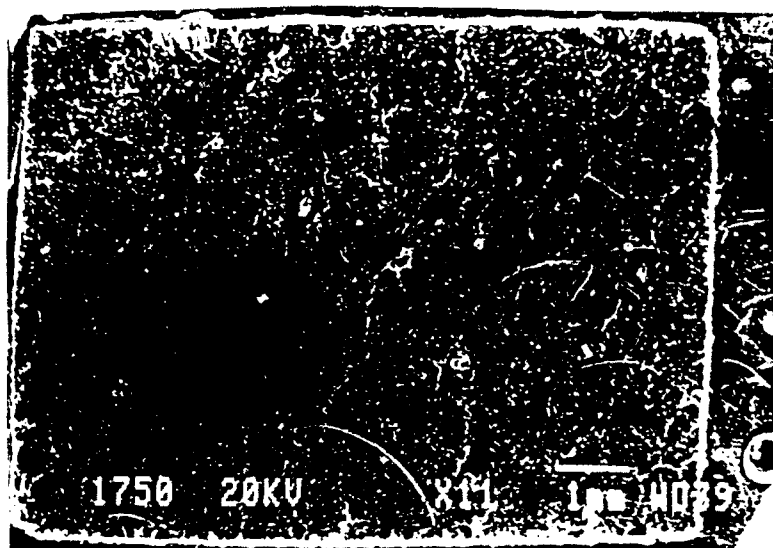
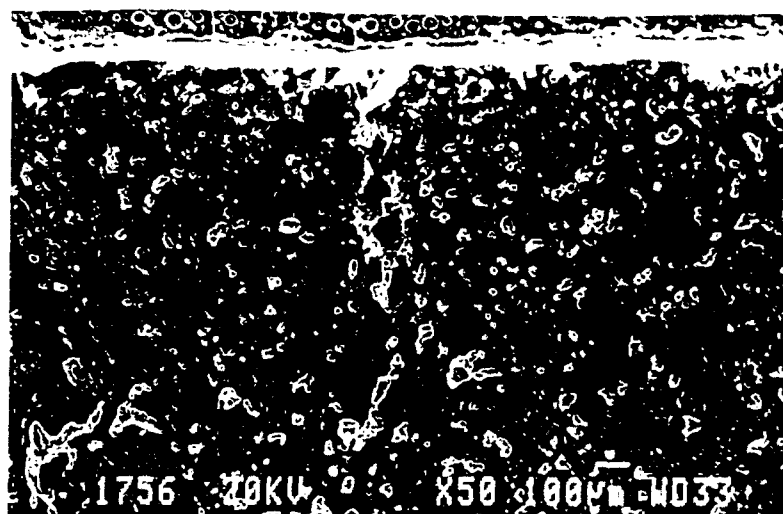


Fig. 10: X-Ray diffraction of Si_3N_4 coating sintered at 1650°C for 1.5 hrs in N_2

a



b



c

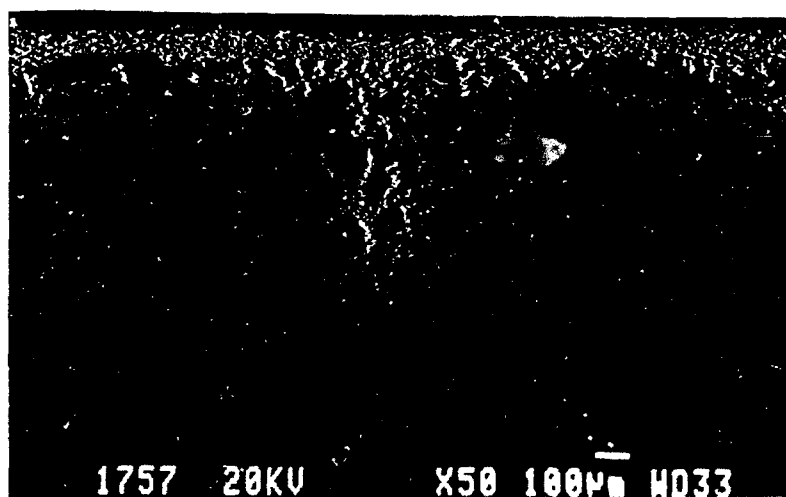


Fig. 11: Cross-sections of graphite specimen coated with Si_3N_4 at 50 v/cm, 15 + 15 sec

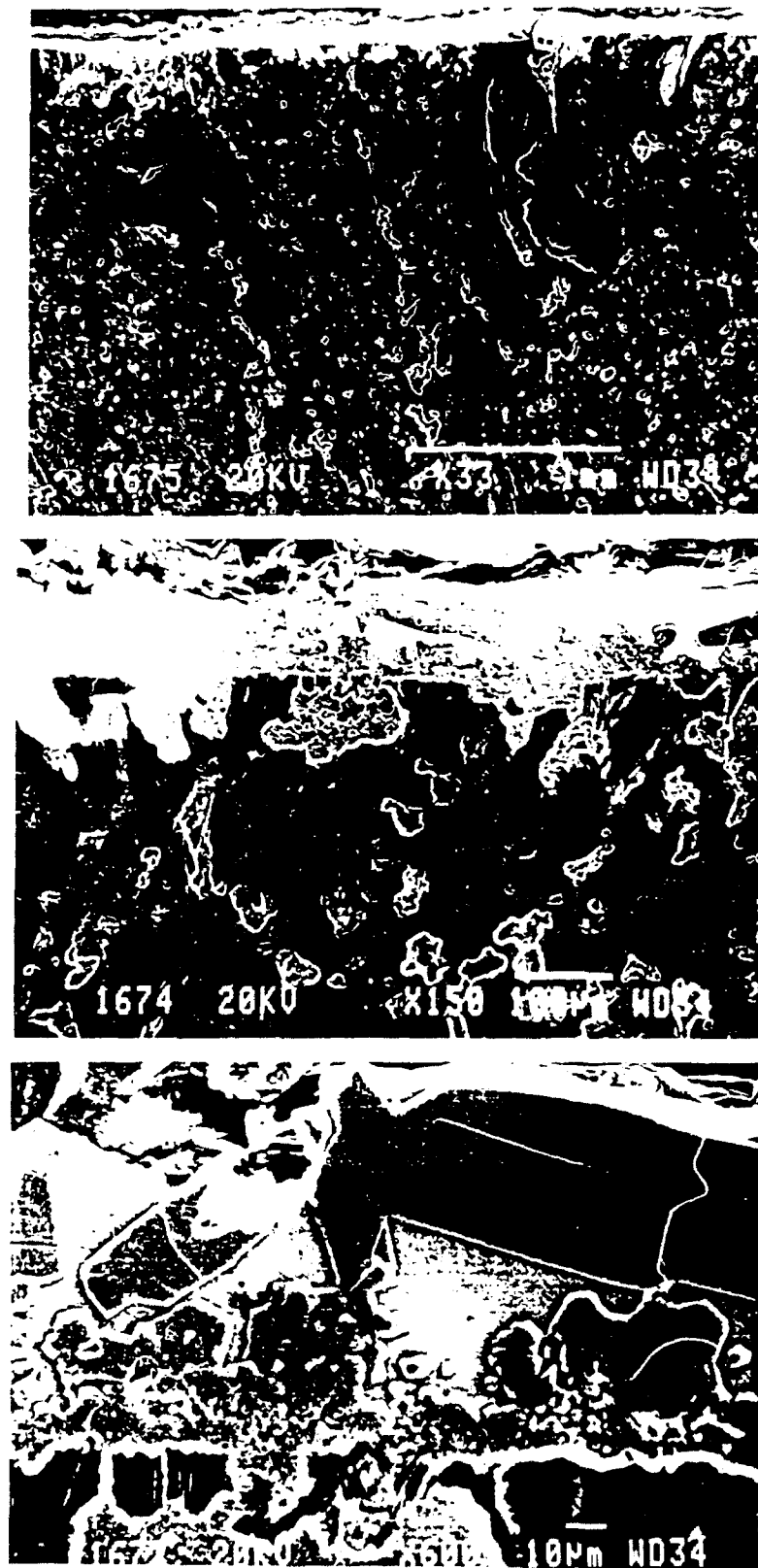
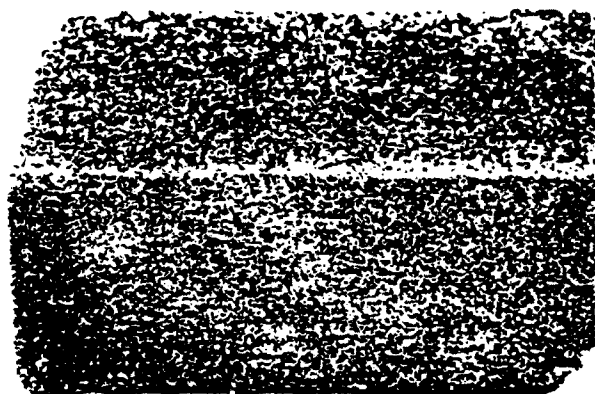


Fig. 12: Cross-sections of graphite specimen, coating conditions as in Fig. 11

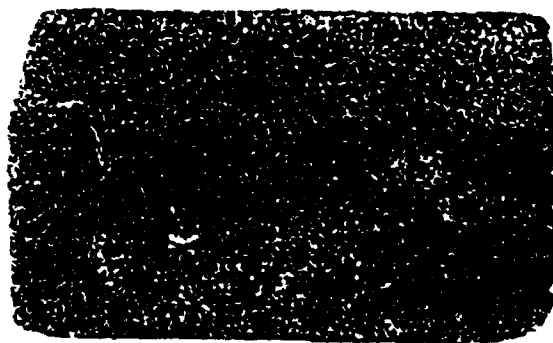
A specimen coated with six layers (50 v/cm, 15 sec each coating) after sintering before and after oxidation for seven 1-hr repeated exposures at 830°C is seen in Fig. 13. A cross-section through the specimen after oxidation and Si mapping of the cross-section are seen in Fig. 14. The coated specimen which had a coating of a total thickness of 80 μ lost 6.1% of its weight during the oxidation.

The cross-section of a C-C specimen coated with Si₃N₄ at 50 v/cm by two layers (15 sec each) after exposure at 830°C for seven 1 hr exposures is seen in Fig. 15. This specimen lost 7.5% during the exposure. A dense coating which penetrated into cracks and voids of the substrate is seen. Another C-C specimen coated and sintered is seen in Fig. 16. A longitudinal crack in the coating is seen.

In some cases catastrophic oxidation of the coated specimen took place and caused weight loss up to 38% within 7 × 1 hr exposures at 830°C. This was caused by flaws in the coating such as cracks (Fig. 17e) and discontinuity (Fig. 17 b and c). This specimen had 6 layers 15 sec. each. Thus the increase in number of layers and overall thickness was not beneficial.

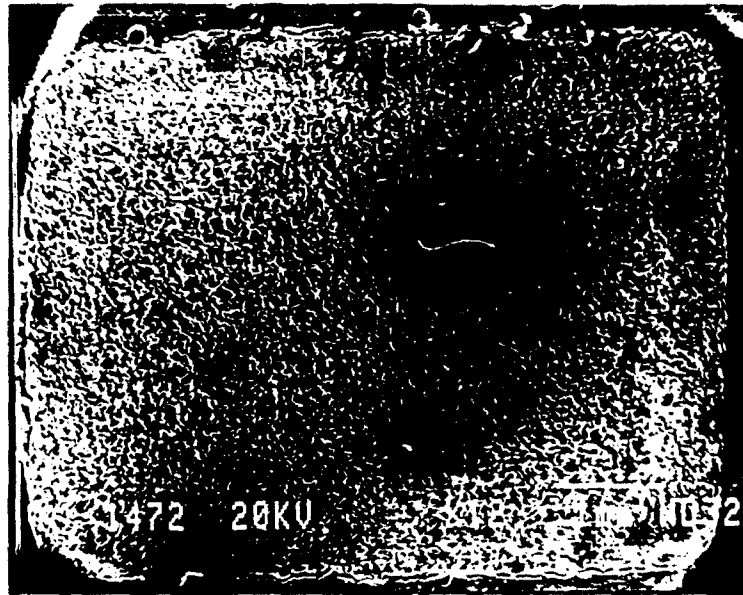


a. Si_3N_4 coating, six layers on graphite — 50 v/cm, 15 sec.

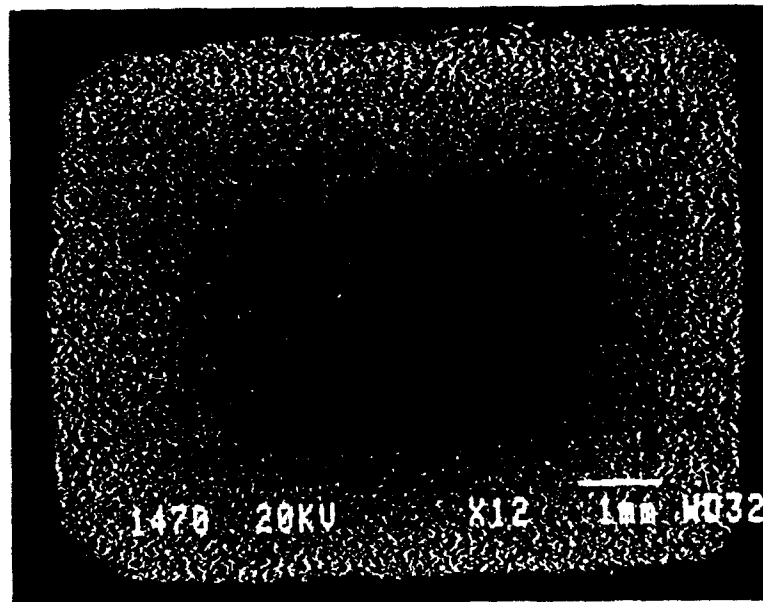


b. Above specimen after 7 hrs of repeated 1-hr exposures at 830° C. Weight loss 6.1%

Fig. 13: Si_3N_4 coating after sintering



a. Morphology



b. X-ray mapping of Si on area seen in a.

Fig. 14: Cross-section of specimen seen in Fig. 13b.



Fig. 15a: Cross-section through C-C coated with Si_3N_4 at 50 v/cm, 15 + 15 sec after oxidation

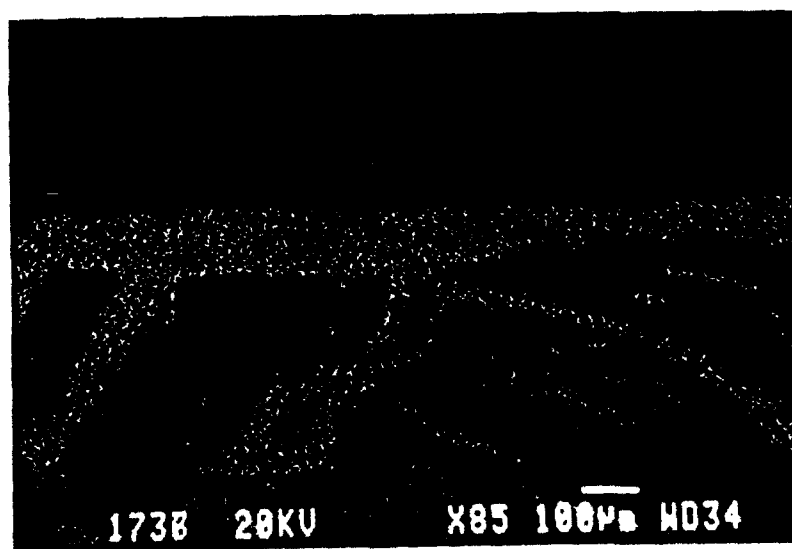
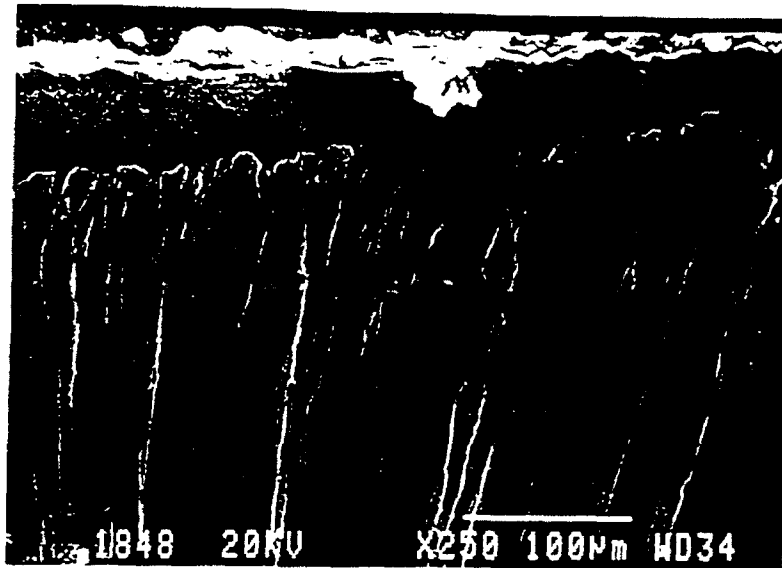
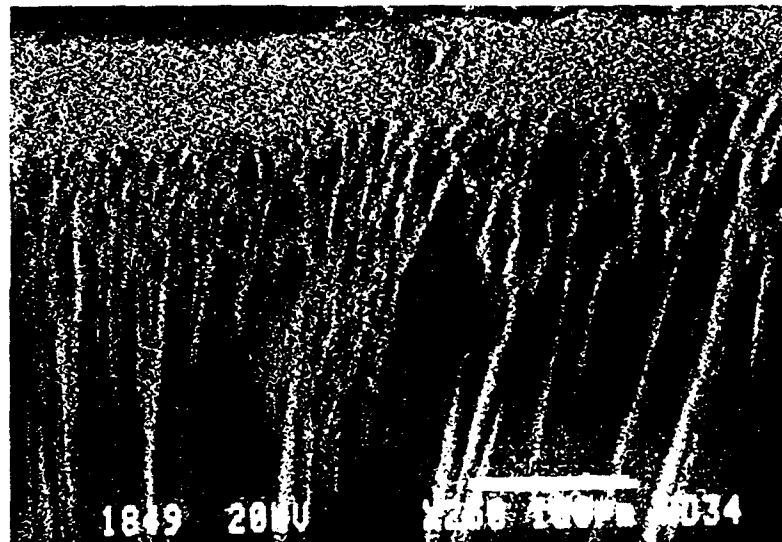


Fig. 15b: X-ray mapping of area seen in 15a.

a



b
X-ray mapping of
Si on area a



c

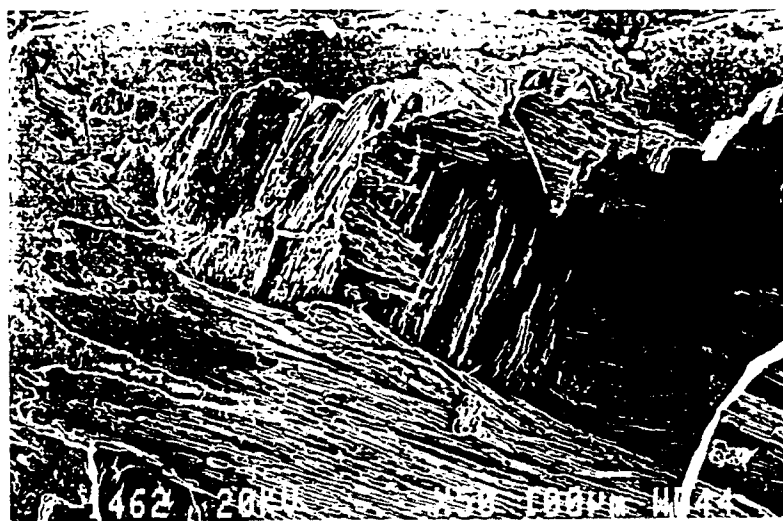


Fig. 16: Cross-sections of C-C composite specimen coated with Si₃N₄ after sintering

a



b



c

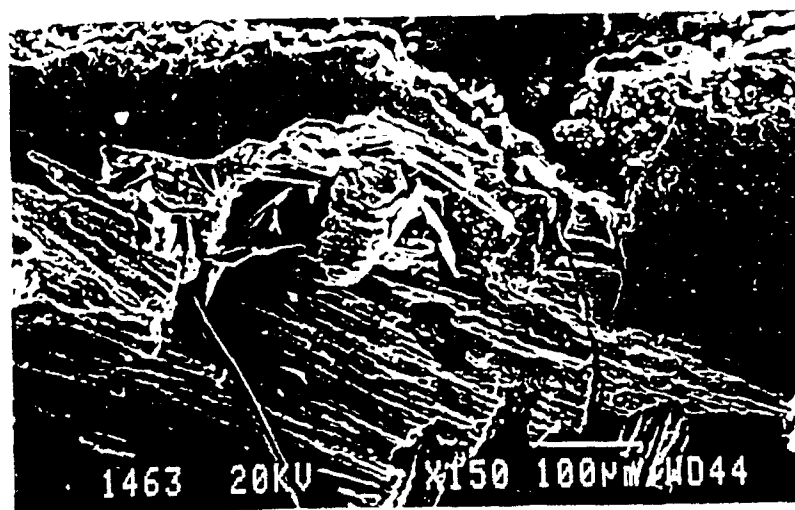
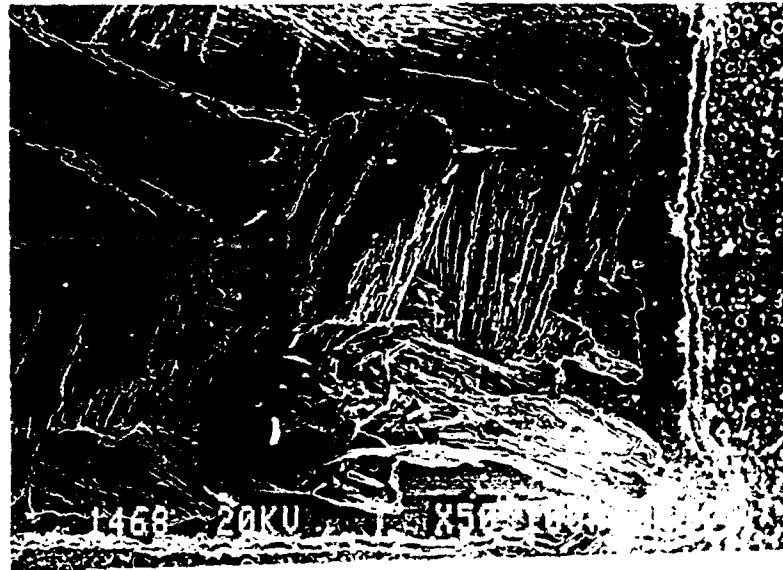
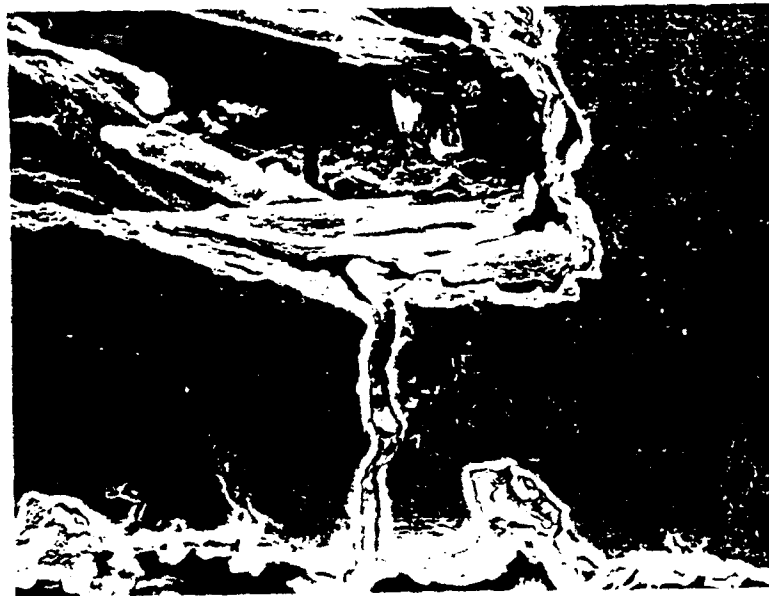


Fig. 17: Cross-sections of C-C composite specimen coated with Si_3N_4 after repeated 1-hr exposures at 830°C for 7 hrs. Weight loss 38,0%

d



e



Continuation of Fig. 17

3.4 Si₃N₄ on Al₂TiO₅ Coatings

Si₃N₄ was deposited on an underlayer of Al₂TiO₅. The condition for deposition of Al₂TiO₅ (with two kinds of sintering additions – 5% BaCO₃ or 5% SiO₂) were as follows:

– stage I (impregnation):

fluid – 20% propanol in water

concentration – 30 g/l

field intensity – 75 v/cm

time – 60 min

Stage II (external coating)

fluid – propanol

concentration – 30 g/l

field intensity – 100 v/cm – 200 v/cm

time – twice 1–2 min (change of holder position)

In some experiments 20 ml/l of 85% H₃PO₄ were added to the propanol in order to obtain cementation of the Al₂TiO₅ deposit. This helped to maintain the integrity of this layer during the deposition of the Si₃N₄. Under these conditions the deposit formed on the anode indicating absorption of PO₄⁻ ions on the particles.

Stage III – Si₃N₄ coating:

fluid – propanol

concentration – 100 g/l

field intensity – 50–100 v/cm

time – twice 15–30 sec

A macro view of C–C and graphite specimens coated with Si₃N₄ on top of Al₂TiO₅ is seen in Figs. 18 and 19. A cross-section through coated graphite in the "green" state is seen in Fig. 20. X-ray mapping of Ti shows its

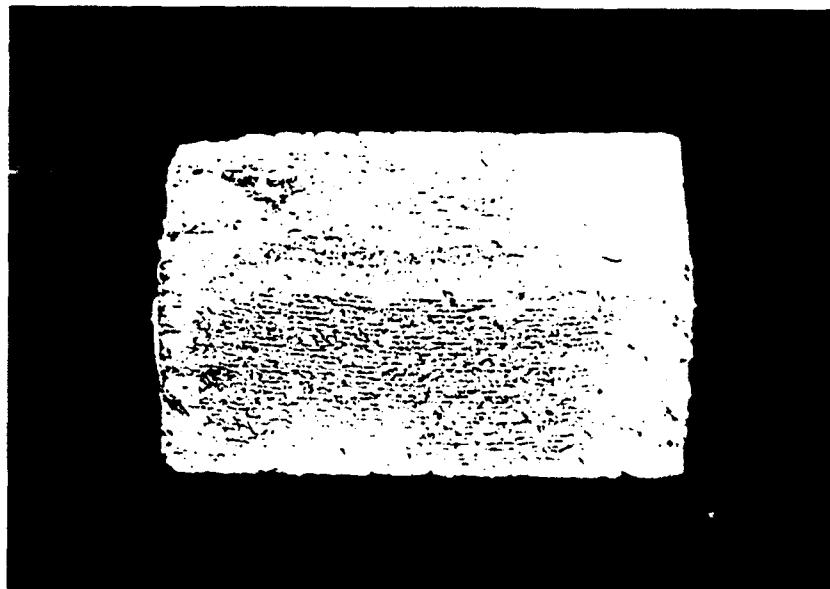


Fig. 18: C—C specimen coated with $\text{Si}_3\text{N}_4 + \text{Al}_2\text{TiO}_5$ before sintering

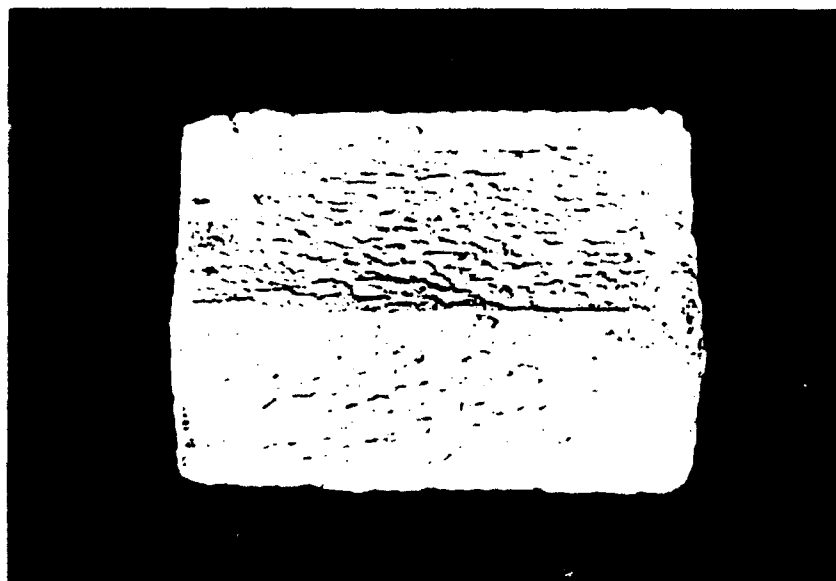
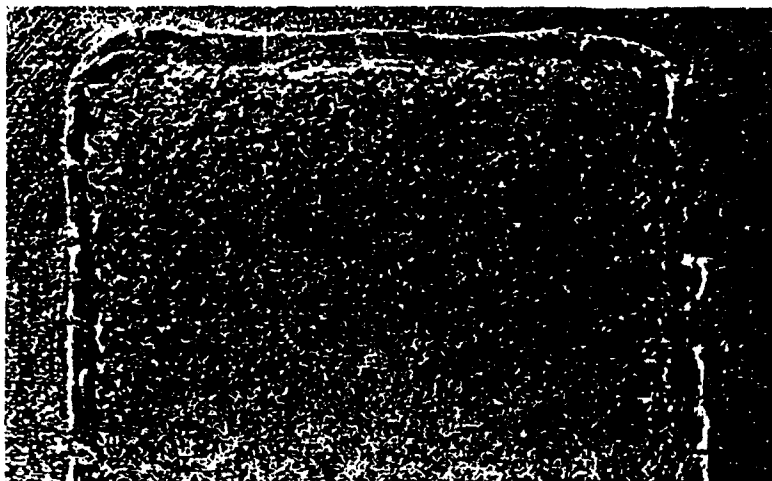
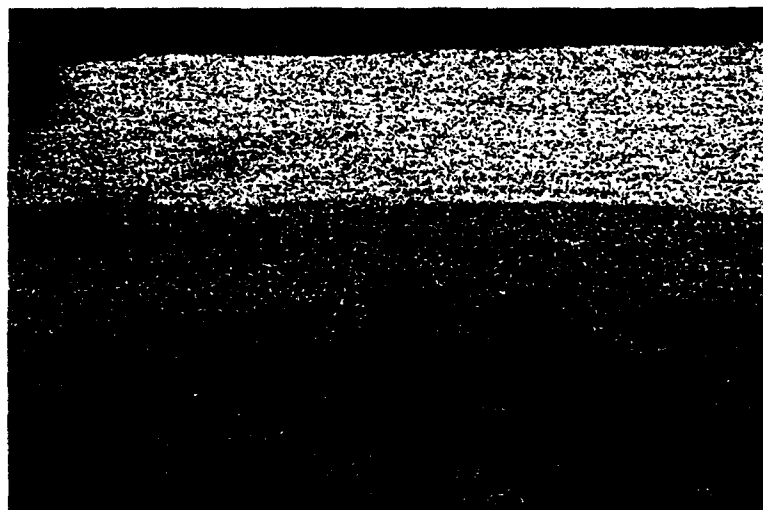


Fig. 19: Graphite specimen coated with $\text{Si}_3\text{N}_4 + \text{Al}_2\text{TiO}_5$ before sintering



Si_3N_4 on
 Al_2TiO_5



X-ray Si



X-ray Ti

Fig. 20: Cross-section of double layer deposit of Si_3N_4
($\times 10$) (100 g/l isopropanol, 50 v/cm, 2 min) and Al_2TiO_5
(30 g/l isopropanol 200 v/cm, 90 sec) and X-ray images
($\times 100$)

presence in a uniform underlayer with "pegging" into the pores of the substrate. Si-mapping shows its massive presence in the upper layer but also a smaller amount is present in the underlayer indicating the penetration of Si_3N_4 particles into the pores of the Al_2TiO_5 layer.

Sintering of the coating was performed as before at 1650°C 1.5 hrs in N_2 . The sintered coating has an uneven dark grey color. Figs. 21 and 22 show sintered specimens. X-ray diffraction pattern of the sintered coating is seen in Fig. 23 indicating formation of SiC through interaction of Si_3N_4 with the substrate and decomposition of the Al_2TiO_5 . Cross-sections through the sintered coating in graphite are seen in Figs. 24 and 25. A dense layer of Si_3N_4 reaching the substrate is on top of a Ti containing layer (TiO_2 ?). X-ray mapping of Al shows it to be distributed through the entire coating. Cross-section through a C-C coated specimen and its mapping are seen in Figs. 26 and 27. The distribution of the elements is similar to that in the coating on graphite. Local microanalyses in the middle of the coatings and near the substrate are seen in Fig. 28 a and b, respectively. Cross-sections through a graphite coated specimen after oxidation at 830°C for 7×1 -hr exposures are seen in Fig. 29. An adherent intact coating is seen on the whole periphery of the specimen. Indeed the weight loss of this specimen was nil. The presence of Ti in the pores of the substrate is shown by microanalysis in Fig. 30.

3.5 Si_3N_4 on Fused SiO_2 Coatings

The underlayer of fused SiO_2 was obtained at the following conditions:

particle concentration — 100 g/l

field intensity — 5 v/cm

time — twice 2 min (in between drying at 200°C for 30 min)

fluid — water

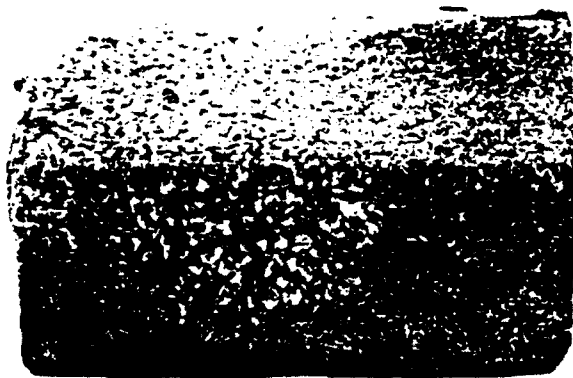


Fig. 21: $\text{Si}_3\text{N}_4 + \text{Al}_2\text{TiO}_5$ coating on C-C after sintering at 1650°C for 1.5 hr in N_2



Fig. 22: $\text{Si}_3\text{N}_4 + \text{Al}_2\text{TiO}_5$ coating on graphite after sintering at 1600°C for 2.5 hrs in N_2

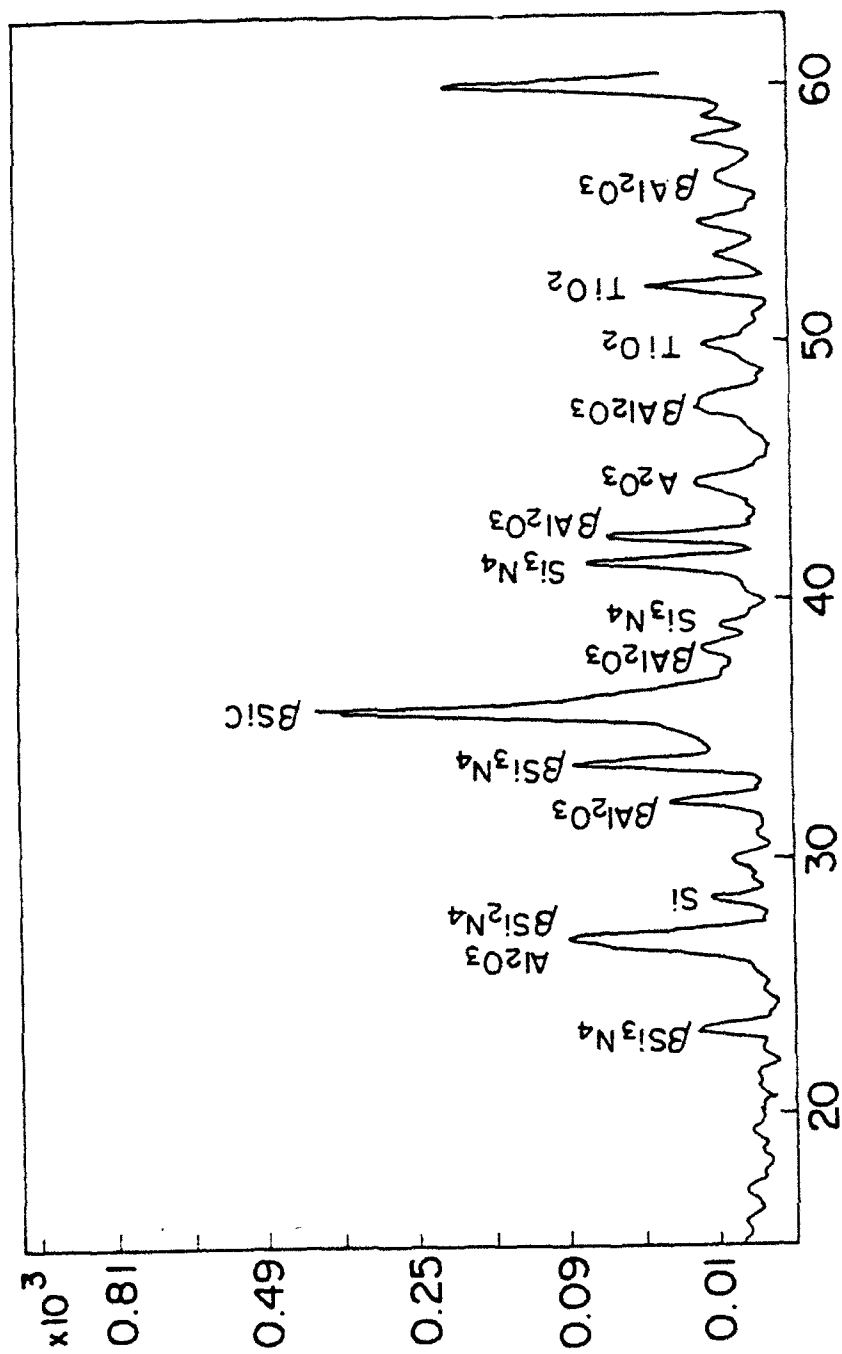
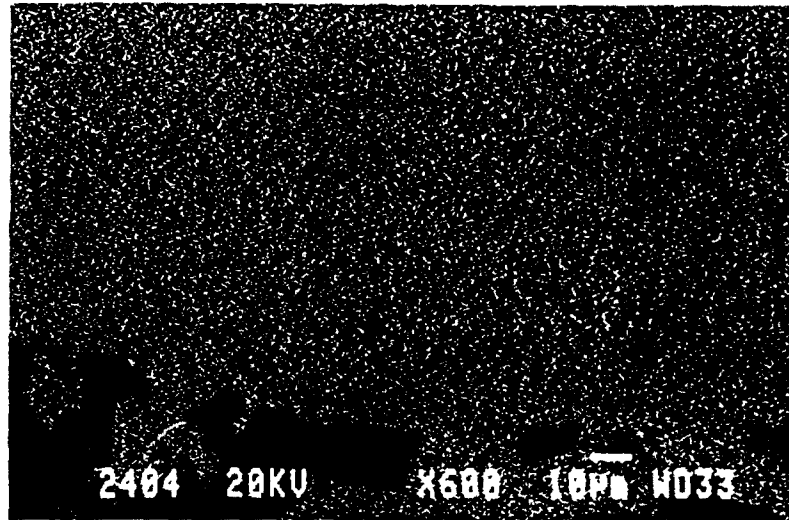


Fig. 23: X-ray diffraction of sintered Si_3N_4 on Al_2TiO_5 coating



Fig. 24 Cross-section of double layer deposit of $\text{Si}_3\text{N}_4 + \text{Al}_2\text{TiO}_5$ on graphite on different areas and different magnification

a.
x-ray mapping
of Si



b.
x-ray mapping
of Ti



c.
X-ray mapping
of Al

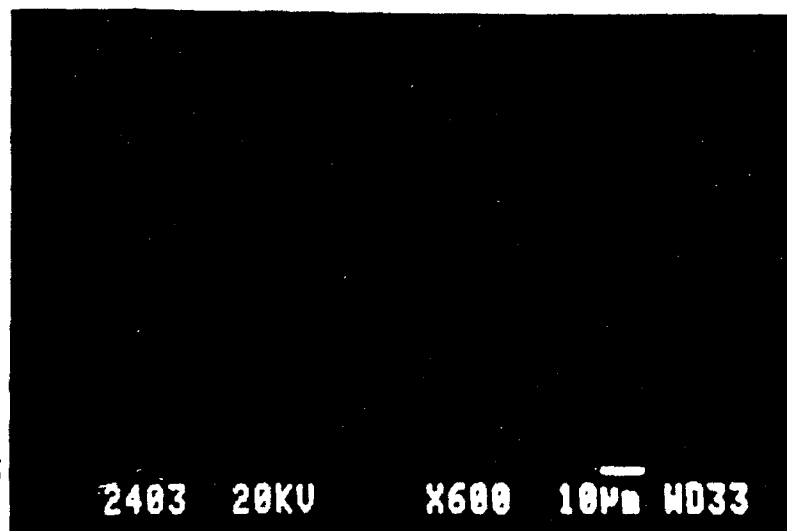


Fig. 25: X-ray mapping of area seen in Fig. 24b

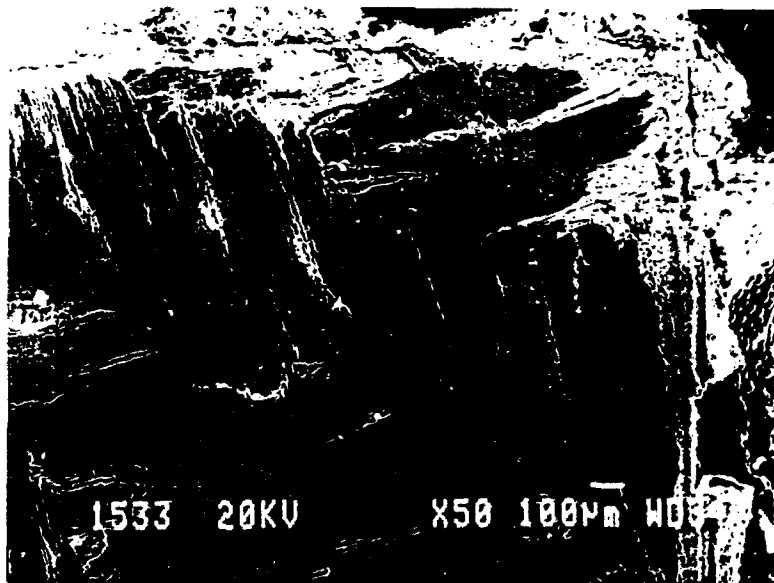
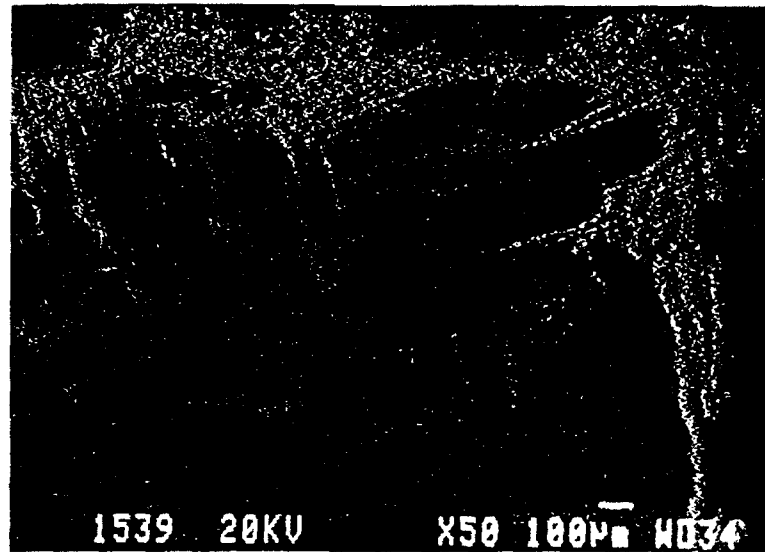


Fig. 26: Cross-section of C-C composite specimen coated with $\text{Si}_3\text{N}_4 + \text{Al}_2\text{TiO}_5$ after sintering

a.
x-ray mapping
of Si



b.
x-ray mapping
of Ti



c.
X-ray mapping
of Al

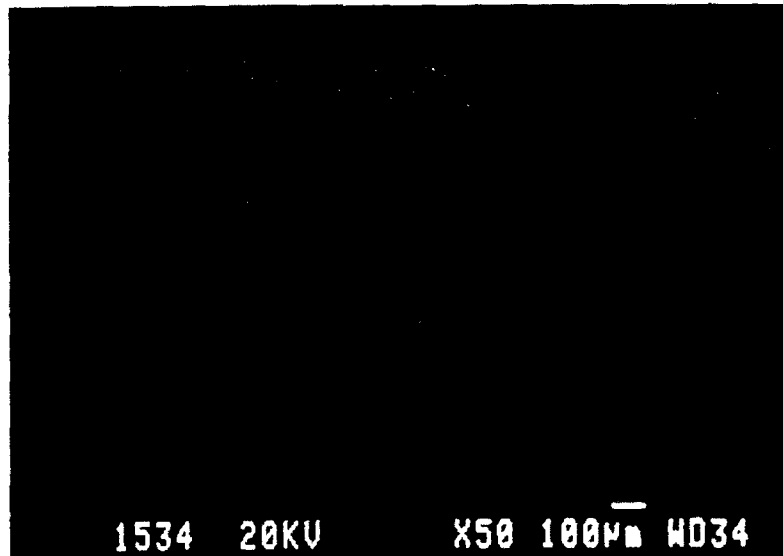


Fig. 27: X-ray mapping of area seen in Fig. 26

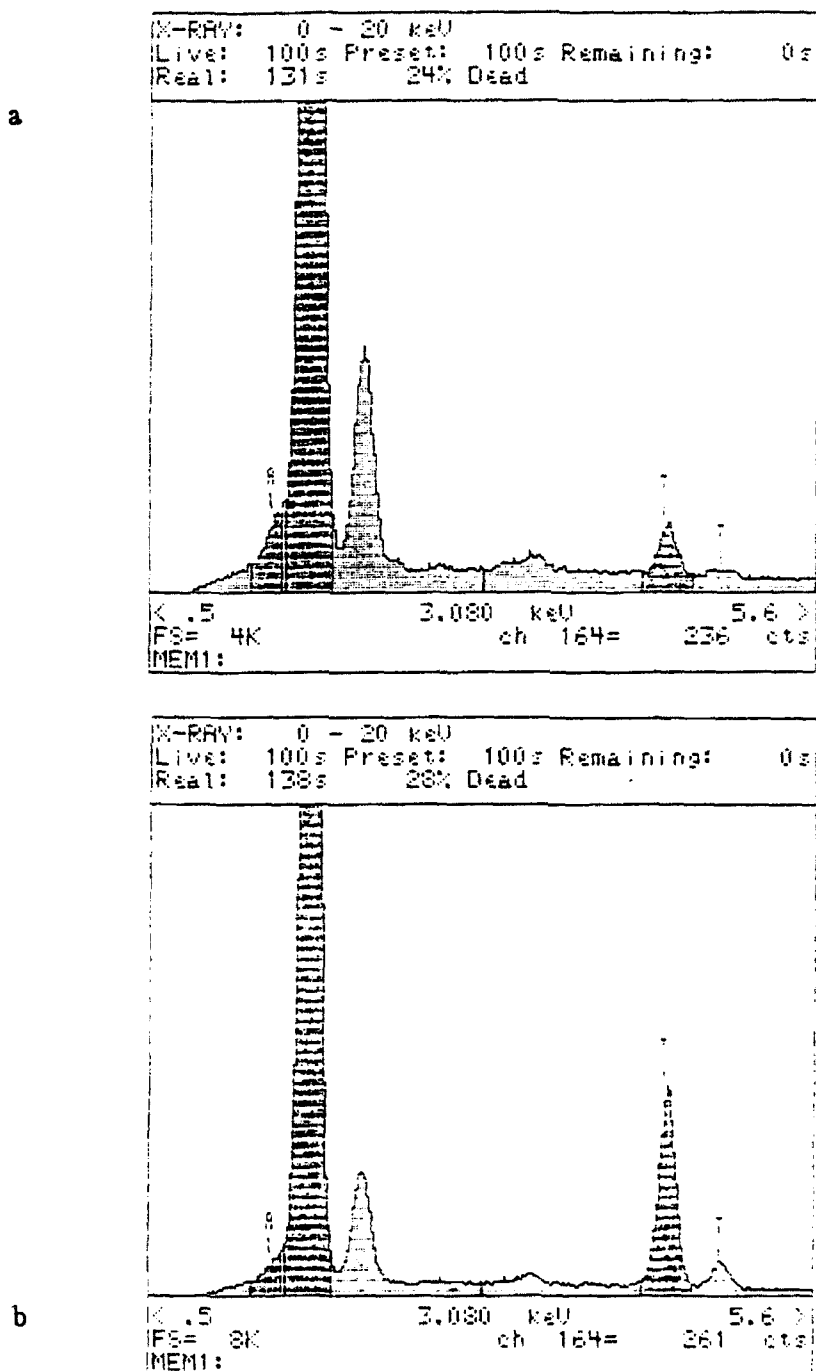


Fig. 28: EDS spectrum of area seen in fig. 26

- a) Center of coating
- b) Near substrate

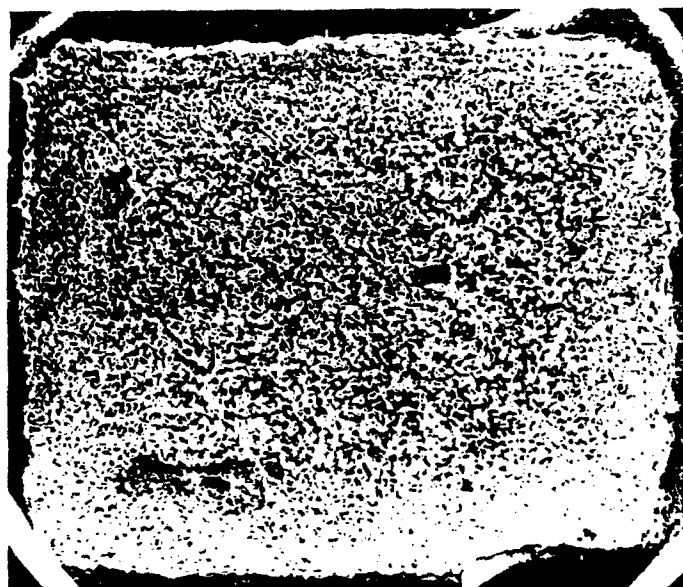


Fig. 29: Cross-section of graphite specimen coated with $\text{Si}_3\text{N}_4 + \text{Al}_2\text{TiO}_5$ ($\text{Al}_2\text{TiO}_5 + 5\% \text{SiO}_2$) after sintering and repeated 1 hr exposures at 830°C for 7 hrs (weight loss zero)

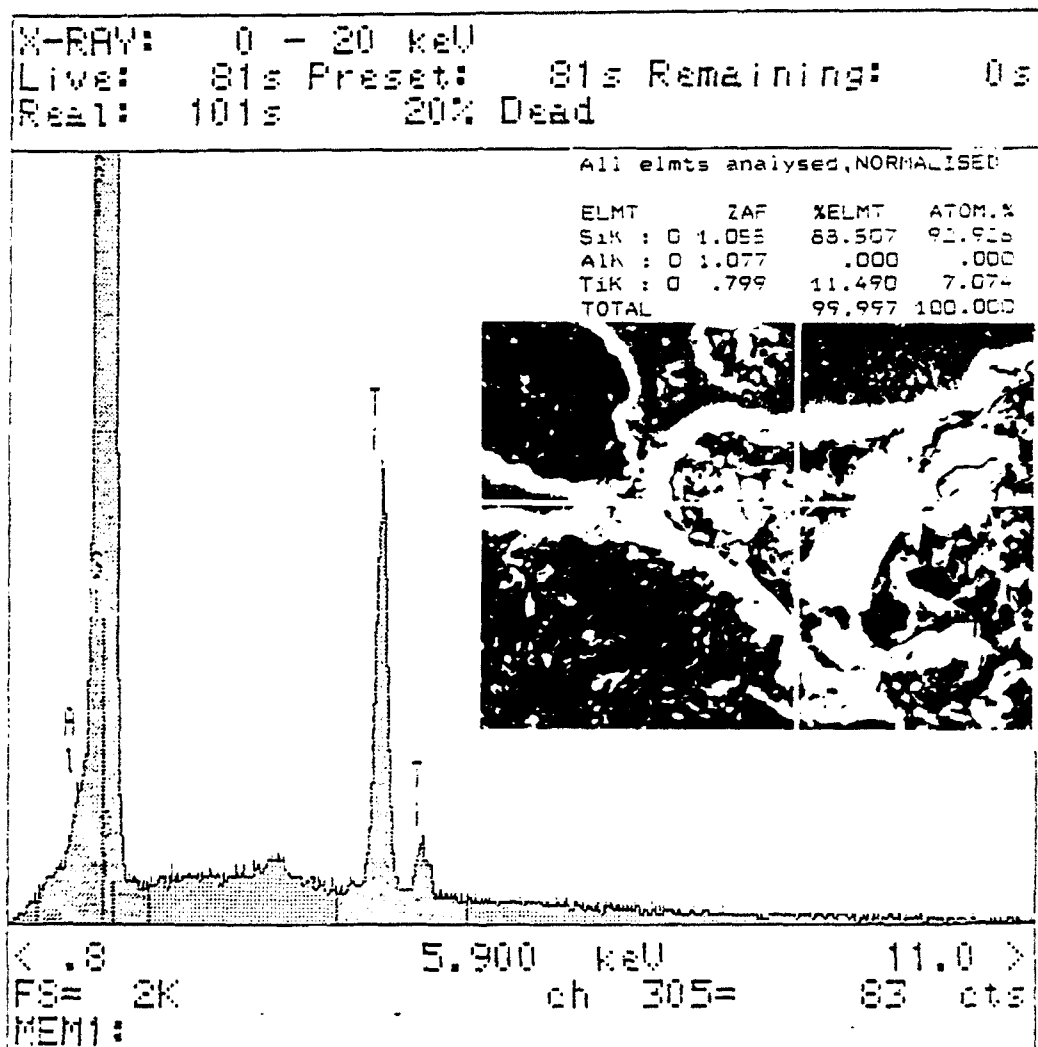


Fig. 30: EDS spectrum of particle in pore, coating
 $\text{Si}_3\text{N}_4 + \text{Al}_2\text{TiO}_5$

The Si_3N_4 coating was deposited at 50 v/cm for 15 + 15 sec. Sintering of the coating was as mentioned before. The overall thickness of the coatings was 110–150 μ . The X-ray diffraction pattern after sintering is seen in Fig. 31. As in the system $\text{Si}_3\text{N}_4 + \text{Al}_2\text{TiO}_5$ interaction with the substrate resulted in SiC formation as well as metallic Si is formed. As expected peaks of SiO_2 and Si_3N_4 are seen. Fig. 32 shows a cross-section through the sintered coating. Fig. 33 shows cross-sections through the coating after a 4-hr exposure at 830°C. Anchoring of the coating in the pores is seen, however. Horizontal and vertical cracks through the coating are seen which indeed impaired the oxidation resistance (see further). Another example of anchoring of the coating in the porous substrate is seen in Fig. 34.

3.6 Si_3N_4 coatings after impregnation with BN

BN particles were induced into the pores of graphite at 5 v/cm, for 60 min at a concentration of 30 g/l in water + 20% propanol. Si_3N_4 was then deposited at 50 v/cm, 15 + 15 sec. Sintering was performed as before. No SEM-EDS photos are available due to the fact that both B and N are not detected in it. As shown later, no improvement in oxidation resistance was found.

3.7 Coatings of exhaust nozzles and crucibles

Following the sintering and oxidation experiments a "real" system was coated and tested. The test was performed on a set of graphite exhaust nozzles which were coated with Si_3N_4 and underlayers of fused SiO_2 and Al_2TiO_5 respectively. Prior to the coating of the nozzles experiments were carried out with the same shapes made of brass. The purpose of this stage was to determine the deposition conditions and shape of electrodes so as to

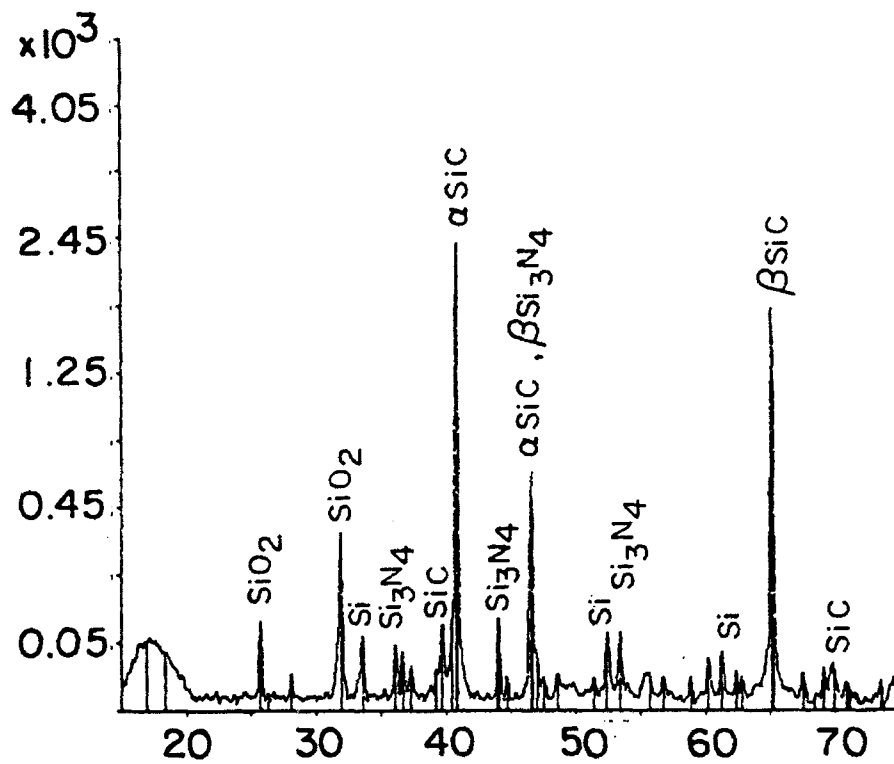


Fig. 31: X-ray diffraction pattern of sintered $\text{Si}_3\text{N}_4 + \text{SiO}_2$ coating

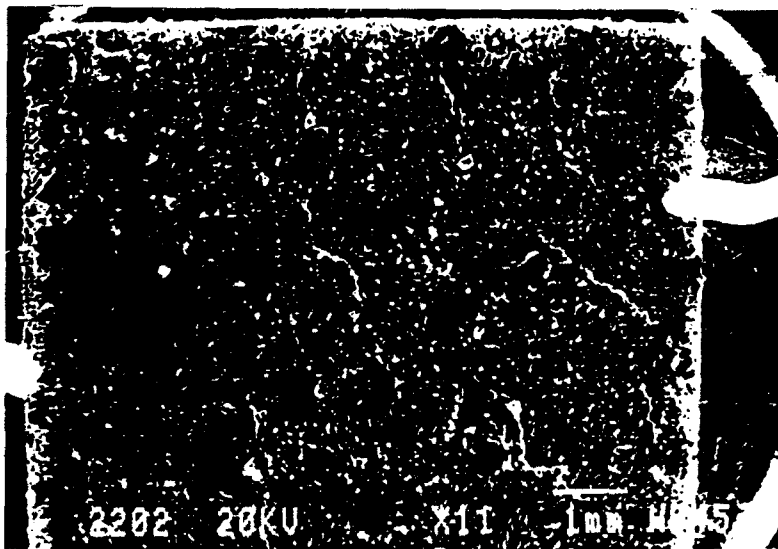


Fig. 32: Cross-section of graphite specimen coated with Si_3N_4 on Fused SiO_2 after sintering

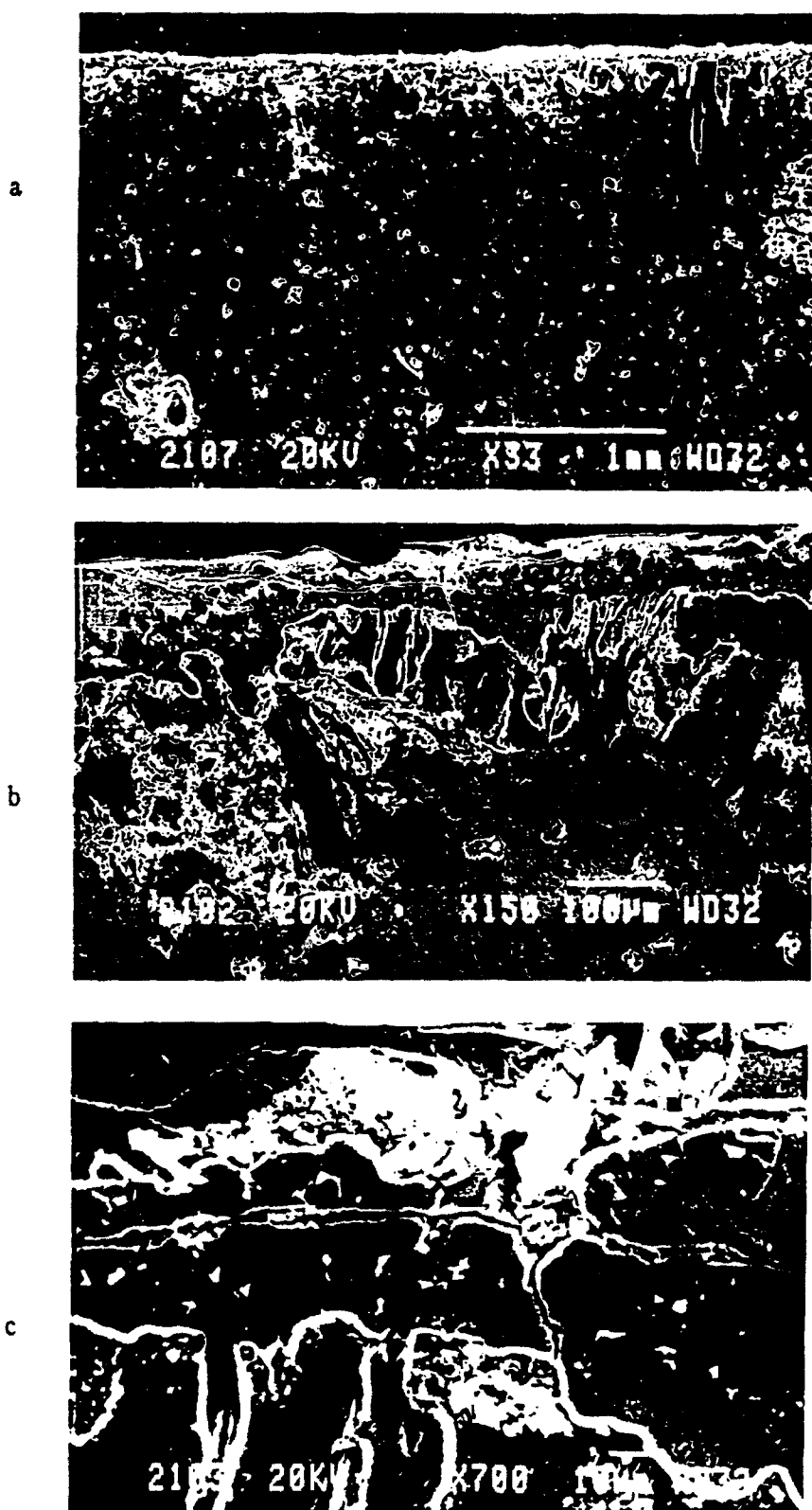
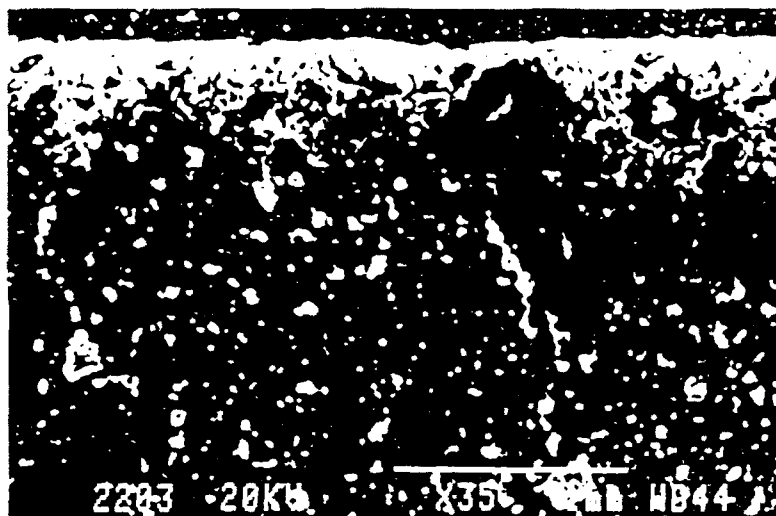
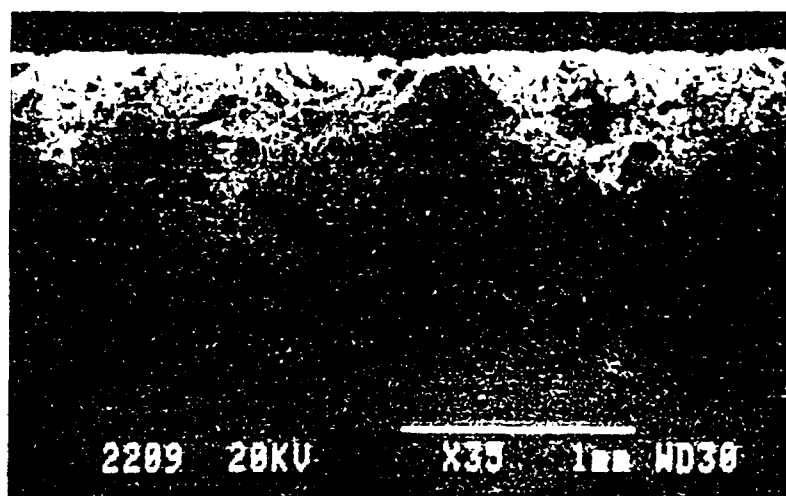


Fig. 33: Cross-section of coated graphite specimen
but after 4 hrs at 830°C (Si_3N_4 on fused SiO_2)

a

X-ray mapping
of Si

b



c

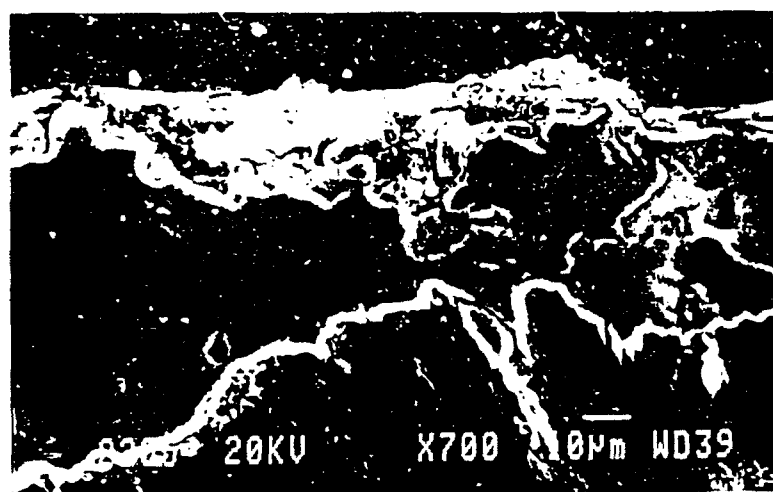


Fig. 34: Cross-section of graphite specimen coated with $\text{Si}_3\text{N}_4 + \text{SiO}_2$ and sintered

obtain an internal uniform coating. The inner electrode was a shaped electrode with a shape that copied the inner space of the nozzle. The coated brass models are seen in Fig. 35. Following this experiment the graphite nozzles were coated, sintered, and tested.

Figs. 36 and 37 show the graphite nozzles after sintering. The graphite nozzles were tested under conditions that simulate an air-breathing engine that operates at high temperature (2000°C) at an absolute pressure of 6 atm. with an excess of oxygen — equivalent ratio of fuel/oxygen = 0.75. The performance was compared to that of nozzles coated with CVD SiC. The conclusion of the experiment that lasted 100 sec were that no effect whatsoever is seen on the nozzles with the electrophoretic deposit. The SiC coated nozzles performed the same but were exposed for 50 sec only.

Another application was the inner and outer coating of a graphite crucible used for metal casting. Fig. 38 shows the coated crucible (Si_3N_4 on Al_2TiO_5) prior to sintering. An uniform coating was obtained using shaped electrodes. Sintering was performed later and soon the crucible will be sent for testing.

3.8 Oxidation Experiments

The last stage of this work was dedicated to the testing of the oxidation resistance of coated graphite and C-C specimens. These experiments led to some interesting results, however, there were some limitations that did not allow a full assessment of the oxidation protection in some cases. The main limitation is in the discontinuity of the coating formed as a result of the contact with the holder during the deposition. Although efforts were made to remedy this by repeating the coating while changing the holder position, this did not always eliminate the defect. Further elaboration of this coating

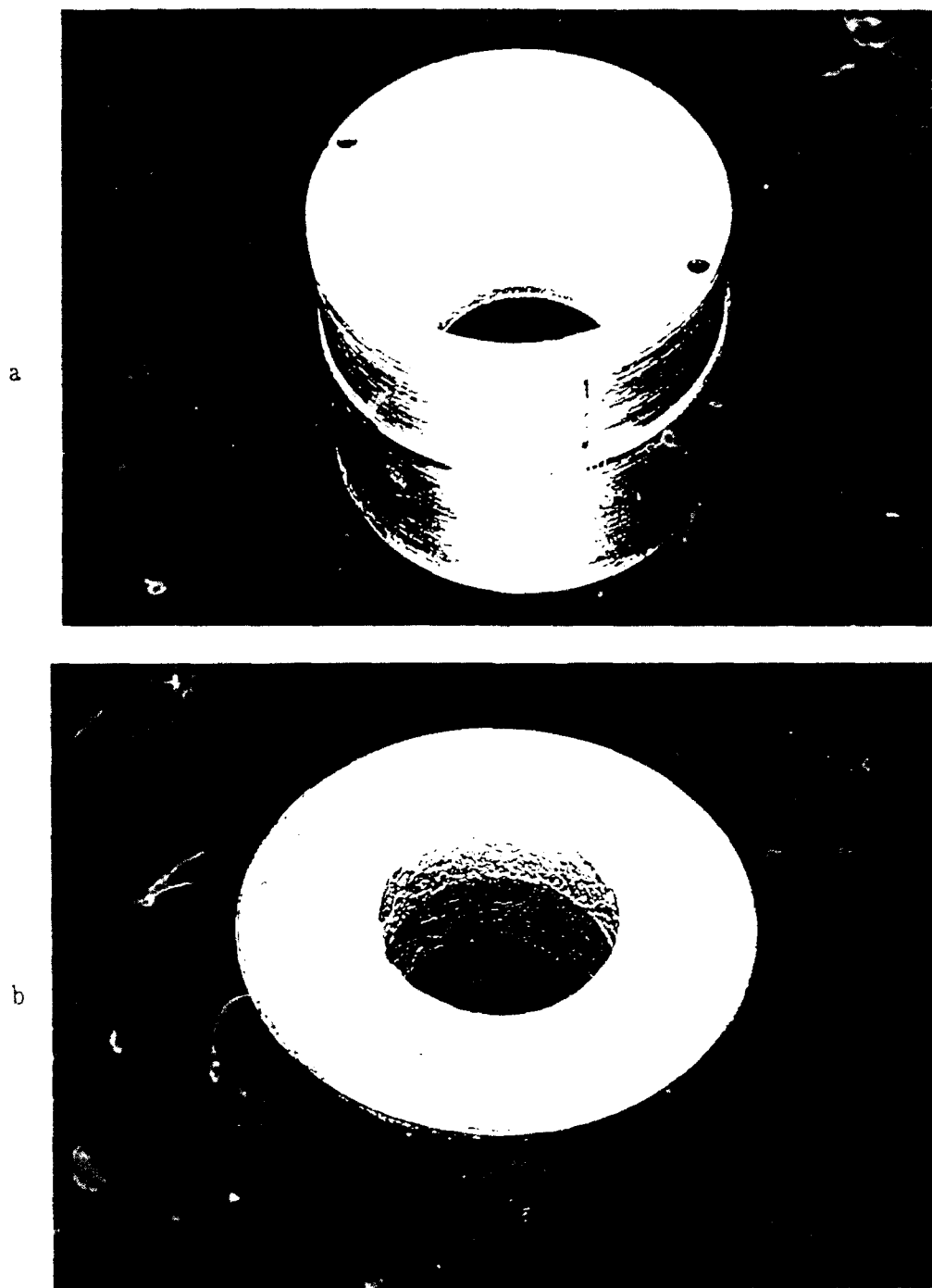


Fig. 35: Brass model coated with:

- a. Si_3N_4 on SiO_2
 SiO_2 - 100 g/l, 5v/cm, 2 min * 2,
 Si_3N_4 - 100 g/l, 50 v/cm, 30 sec
- b. Si_3N_4 on Al_2TiO_5
 Al_2TiO_5 - 30 g/l, 200 v/cm, 1.5 min
 Si_3N_4 - 100 g/l, 50 v/cm, 30 sec

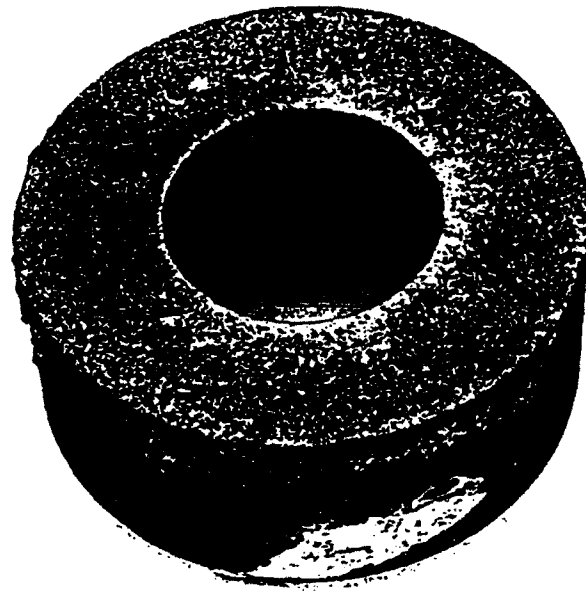


Fig. 36: Coated graphite nozzles after sintering
Coating Si_3N_4 on Al_2TiO_5
 Al_2TiO_5 - 30 g/l, 200 v/cm, 1,5 min
 Si_3N_4 - 100 g/l, 50 v/cm, 30 sec

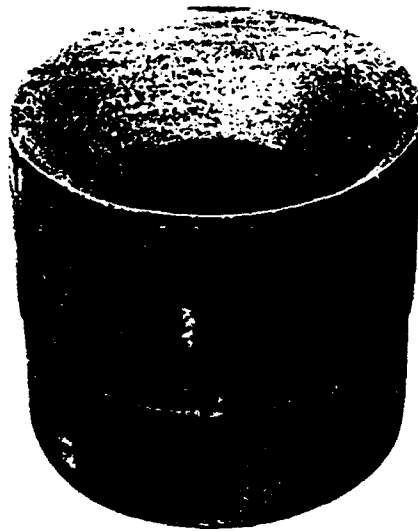


Fig. 37: Coated graphite nozzles after sintering
Coating Si_3N_4 on SiO_2
 SiO_2 - 100 g/l, 5 v/cm, 2 min \times 2
 Si_3N_4 - 100 g/l, 50 v/cm, 30 sec \times 2

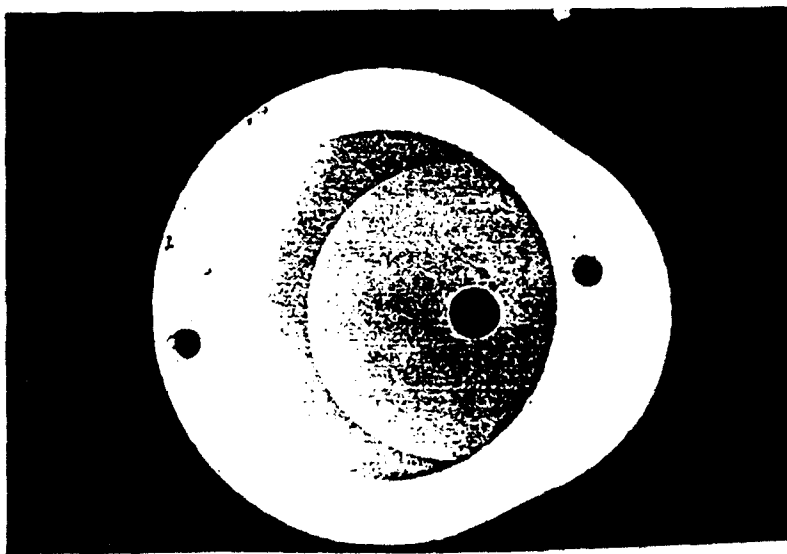
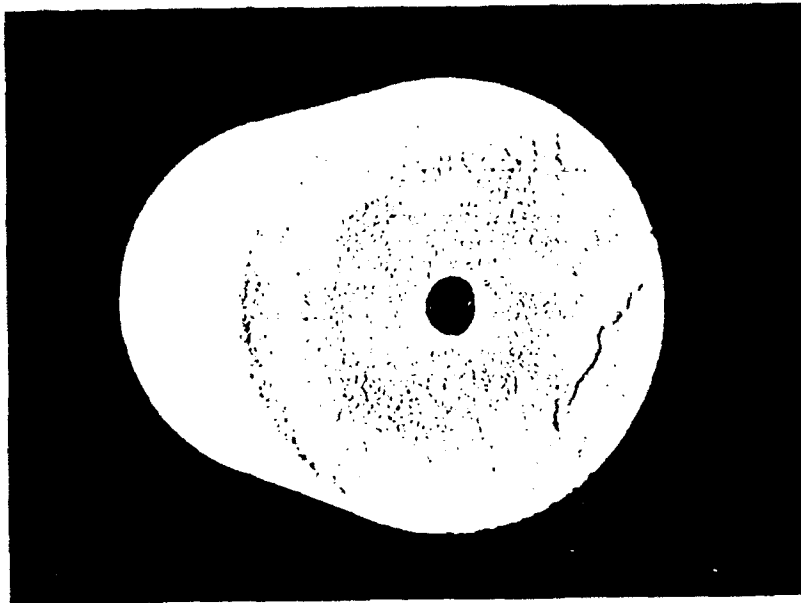


Fig. 38: Coated graphite crucible before sintering
Coating: Si_3N_4 on Al_2TiO_5
 Al_2TiO_5 - 30 g/l, 100 v/cm, 30 min
 Si_3N_4 - 100 g/l, 50 v/cm, 30 sec

method will have to put emphasis on this issue. As a result of this very rapid failure occurred in some cases while in others including duplicate specimens very good performance was exhibited. Therefore, only a relatively small selection of results is presented, while many more were omitted. Due to the limit in time the number of experiments with C-C specimens was smaller after exhaustive experiments with graphite specimens. The oxidation conditions at this initial stage, were relatively mild and were determined in consulting with experts of Wright-Patterson Laboratories.

Tables 1 and 2 summarize the weight losses of the specimens, expressed in weight percentages, during exposure at 830°C in air. When repeated exposures were done they included cooling to room temperature in air and re-exposure to the oven maintained at the testing temperature. As reference, uncoated graphite specimens were used. Their complete gasification took place after 3 repeated exposures. Specimens 4.69 and 4.70 present duplicates of a Si_3N_4 coating following BN impregnation. The large difference in weight loss is probably due to the defect in the coating continuity. The same explanation may hold for the high loss of specimen 4.83 which differs from specimens 4.81, 4.82 and 4.85 in field intensity only. The high weight losses of specimens 4.86, 4.89 and 4.90 may be attributed to the fact that the holder position was not changed during deposition. While this was done, as in specimen 3.147, a significantly better result was obtained. Si_3N_4 coatings on fused SiO_2 gave very high weight losses in all specimens tested. However, in the nozzle coating tested at different conditions good results were obtained. Therefore, it is suggested to further test the merit of this system.

The best results with graphite specimens were obtained with the $\text{Si}_3\text{N}_4 + \text{Al}_2\text{TiO}_6$ system where in some conditions almost nil weight loss was recorded after seven (1-hr) repeated exposures which included an element of repeated thermal shock.

On C—C specimens only Si_3N_4 and $\text{Si}_3\text{N}_4 + \text{Al}_2\text{TiO}_5$ coatings were tested in view of the poor behavior of $\text{Si}_3\text{N}_4 + \text{SiO}_2$ on graphite specimens. The irreproducibility on these specimens was higher than on the graphite specimens (see specimens 4.79 and 3.173). However, relatively good protection was obtained in continued exposure by both coating systems by two consecutive 15 sec coatings (while changing holder position) both at 50 and 100 v/cm for the Si_3N_4 coating and (specimen 4.104, 4.110 — 4.111) and same coating conditions for Si_3N_4 on top of a Al_2TiO_5 layer (specimens 4.118 and 4.119). No benefit of the Al_2TiO_5 presence was seen in case of the C—C substrate. However, this result should be re-evaluated before drawing final conclusions.

Figs. 39—47 present the weight losses graphically by histograms and graphs. It should be noted that these curves were drawn on the basis of the specimen with best performance in each group, which it is believed to represent the potential of the respective coatings. Figs. 39—40 show the performance of the different coatings on graphite. The drastic difference in the coated vs. uncoated specimens is seen, as well as the excellent performance of the $\text{Si}_3\text{N}_4 + \text{Al}_2\text{TiO}_5$ system and the limited performance of the $\text{Si}_3\text{N}_4 + \text{SiO}_2$ system.

Figs. 41 and 42 show the behavior of Si_3N_4 coatings obtained at different deposition conditions. They show that the best protection is obtained by two consecutive depositions (while changing holder positions) at the higher field intensity (100 v/cm). The beneficial effect of the Al_2TiO_5 under the Si_3N_4 on graphite specimens is seen in Figs. 43 and 44. The seemingly detrimental effect of the SiO_2 underlayer is seen in Figs. 45. Fig. 46 shows the effect of deposition conditions of Si_3N_4 on C—C on oxidation protection. The coatings were obtained at two field intensities (50 and 100 v/cm) during 15 + 15 sec. Fig. 47 shows the lack of positive effect of the presence of an underlayer of Al_2TiO_5 on C—C based on specimens 4.93 and 4.95 from Table 2.

Table No. 1: % Weight loss as a function of exposure time at 830°C. Graphite specimens (cont.)

Spec. No.	4.77	4.78	4.94	4.96	4.98	4.60	4.100	4.102	4.69	4.70
Deposit	Si ₃ N ₄ on Al ₂ TiO ₅ with impreg-nation Al ₂ TiO ₅	Si ₃ N ₄ on Al ₂ TiO ₅ with impreg-nation Al ₂ TiO ₅	Si ₃ N ₄ on Al ₂ TiO ₅	Si ₃ N ₄ on Al ₂ TiO ₅	Si ₃ N ₄ on Al ₂ TiO ₅	Si ₃ N ₄ on Al ₂ TiO ₅ with 5% SiO ₂	Si ₃ N ₄ on Fused SiO ₂	Si ₃ N ₄ on Fused SiO ₂	Si ₃ N ₄ after BN impreg-nation	Si ₃ N ₄ after BN impreg-nation
Deposit- ion con- ditions	Si ₃ N ₄ 50v/cm 15+15sec Al ₂ TiO ₅ 100v/cm 1+1 min 75v/cm 60min	Si ₃ N ₄ 50v/cm 15+15sec Al ₂ TiO ₅ 100v/cm 1,5+1,5min 75v/cm 60min	Si ₃ N ₄ 50v/cm 30sec Al ₂ TiO ₅ 100v/cm 1+1 min	Si ₃ N ₄ 50v/cm 60sec Al ₂ TiO ₅ 100v/cm 1,5+1,5 min	Si ₃ N ₄ 50v/cm 60sec Al ₂ TiO ₅ 100v/cm 1,5+1,5 min	Si ₃ N ₄ 50v/cm 30sec 50v/cm 30 sec Al ₂ TiO ₅ 200v/cm 2+2min	Si ₃ N ₄ 50v/cm 15+15sec Fused SiO ₂ 5v/cm 2min 5v/cm 2min	Si ₃ N ₄ 50v/cm 15+15sec Fused SiO ₂ 5v/cm 2min 5v/cm 2min	Si ₃ N ₄ 50v/cm 15+15sec BN 5v/cm 60 min	Si ₃ N ₄ 50v/cm 15+15sec BN 5v/cm 60 min
Deposit thick- ness, μ	32 29	16 59	36 36	32 53	45 53	15 185	33 114	32 108	38 —	58 —
First ex- posure, 1h	+0,01	0,33	0,02	+0,02	+0,02	+0,03	10,5	16,6	0,17	4,2
2nd expo- sure, 1hr	+0,01	0,9	0,11	+0,03	+0,01	+0,05	21,1	27,2	0,42	9,3
3rd expo- sure, 1hr	0	1,4	0,23	+0,02	+0,01	+0,08	28,1	33,2	0,77	13,7
4th expo- sure, 1hr	0	2,0	0,37	+0,02	0	+0,11	31,3	34,4	1,3	18,5
5th expo- sure, 1hr	0	2,7	0,53	+0,02	0,1	+0,15	32,0	34,7	2,0	22,8

[illegible][illegible]

Table No. 2: % Weight loss as a function of exposure time at 830° C. C-C specimens

Specimen No.	3.173	4.79	4.104	4.105	4.101	4.108	4.80	3.179	3.146	Uncoated Specimen	Uncoated Specimen
Deposit	Si ₃ N ₄	Si ₃ N ₄	Si ₃ N ₄	Si ₃ N ₄	Si ₃ N ₄	Si ₃ N ₄	Si ₃ N ₄	Si ₃ N ₄	Si ₃ N ₄	—	—
Deposit— ion con- ditions	Si ₃ N ₄ 50v/cm 15+15 sec	Si ₃ N ₄ 50v/cm 15+15 sec	Si ₃ N ₄ 50v/cm 15+15 sec	Si ₃ N ₄ 50v/cm 15+15 sec	Si ₃ N ₄ 50v/cm 15+15 sec	Si ₃ N ₄ 50v/cm 15+15 sec	Si ₃ N ₄ 50v/cm 15+15 sec	Si ₃ N ₄ 50v/cm 15sec 50v/cm 50sec	Si ₃ N ₄ 50v/cm 15+15sec 50v/cm 15+15sec 50v/cm 15+15sec	—	—
Deposit thickness, μ	21	27	29	28	28	28	27	21	62	—	—
First exposure 1hr	0,26	3,26	—	—	—	—	8,8	3,84	3,24	41,3	—
Second exposure 1hr	0,7	8,2	—	—	—	—	15,8	8,95	8,3	74,4	—
3rd exposure 1hr	1,52	13,6	—	—	—	—	23,9	15,0	14,6	99,2	—
4th exposure 1hr	2,84	20,5	—	—	—	—	28,4	22,0	20,8	99,4	—
5th exposure 1hr	4,63	26,2	—	—	—	—	30,7	31,0	27,0	—	—
6th exposure 1hr	5,77	32	—	—	—	—	31,6	36,5	33,0	—	—
7th exposure 1hr	7,5	38,2	—	—	—	—	31,8	43,8	38,0	—	—
continuous exposure for 7 hrs	—	—	5,6	10,7	23	15	—	—	—	—	99,97

Table No. 2: % Weight loss as a function of exposure time at 830°C. C-C specimens (cont.)

Specimen No	4.84	4.110	4.111	4.93	4.95	4.116	4.117	4.118	4.119
Deposit	Si ₃ N ₄	Si ₃ N ₄	Si ₃ N ₄	Si ₃ N ₄ on Al ₂ TiO ₅	Si ₃ N ₄ on Al ₂ TiO ₅	Si ₃ N ₄ or Al ₂ TiO ₅	Si ₃ N ₄ on Al ₂ TiO ₅	Si ₃ N ₄ on Al ₂ TiO ₅	Si ₃ N ₄ on Al ₂ TiO ₅
Deposit conditions	Si ₃ N ₄ 100v/cm 15+15sec	Si ₃ N ₄ 100v/cm 15+15sec	Si ₃ N ₄ 100v/cm 15+15sec	Si ₃ N ₄ 50v/cm 15+15sec Al ₂ TiO ₅ 100v/cm 1+1 min	Si ₃ N ₄ 50v/cm 15+15sec Al ₂ TiO ₅ 100v/cm 1,5+1,5 min	Si ₃ N ₄ 100v/cm 15+15sec Al ₂ TiO ₅ 100v/cm 1,5+1,5 min	Si ₃ N ₄ 100v/cm 15+15sec Al ₂ TiO ₅ 100v/cm 1,5+1,5 min	Si ₃ N ₄ 100v/cm 15+15sec Al ₂ TiO ₅ 100v/cm 1,5+1,5 min	Si ₃ N ₄ 100v/cm 15+15sec Al ₂ TiO ₅ 100v/cm 1,5+1,5 min
Deposit thickness, μ	42	51	46	19	15	15	13	11	17
First exposure, 1hr	2,3	—	—	1,31	4,26	—	—	—	—
2nd exposure, 1hr	6,1	—	—	3,74	10,23	—	—	—	—
3rd exposure, 1hr	10,8	—	—	6,62	17,8	—	—	—	—
4th exposure, 1hr	16,1	—	—	10,2	24,9	—	—	—	—
5th exposure, 1hr	22,3	—	—	16,0	31,9	—	—	—	—
6th exposure, 1hr	27,2	—	—	23,5	40	—	—	—	—
7th exposure, 1hr	32,8	—	—	24,8	47	—	—	—	—
continuous exposure for 7 hrs	—	4,4	4,6	—	—	16,4	18,1	5,8	7,4

Weight loss (%) as function of repeated 1hr exposures at 830°C.
Different coatings on graphite.

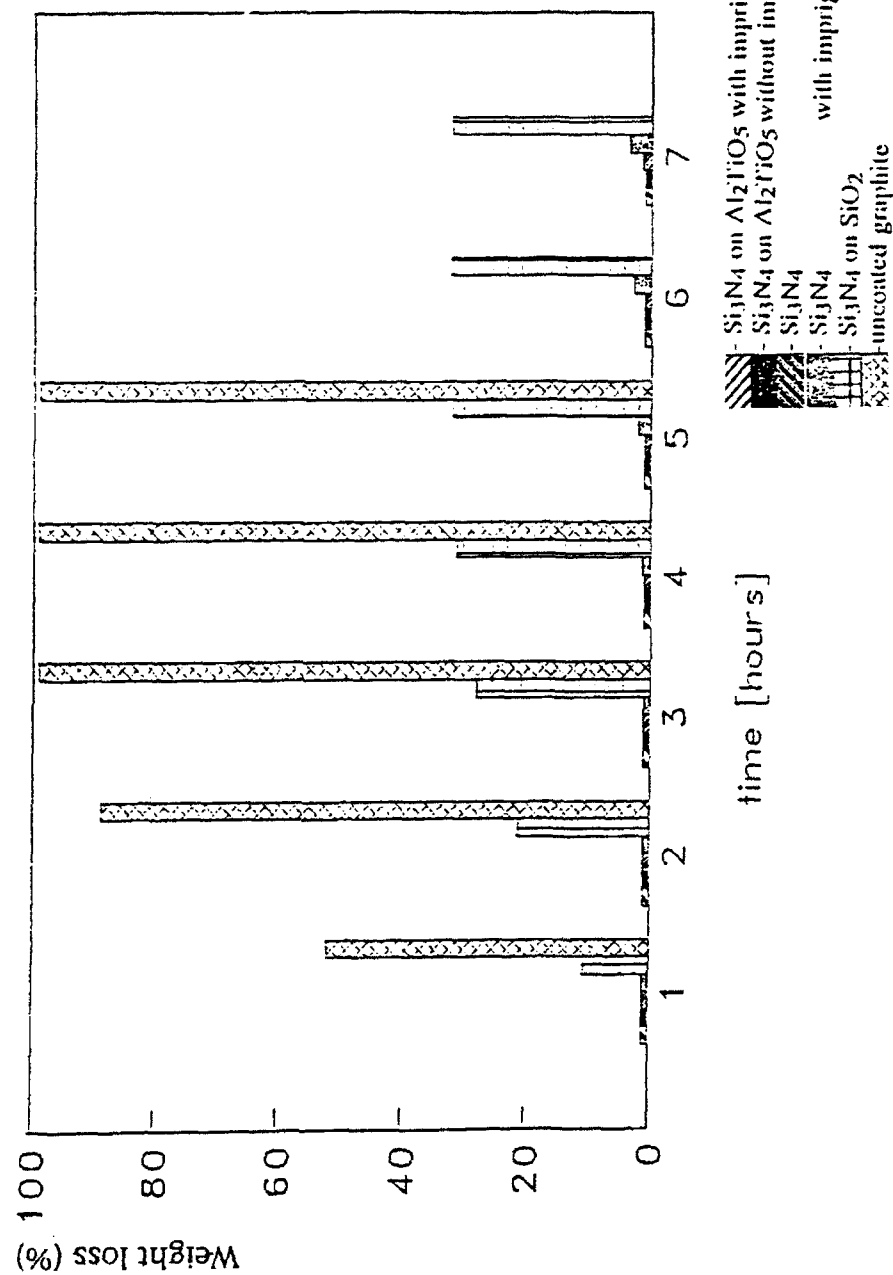


Fig. 39

Weight loss (%) as function of repeated 1hr exposures at 830°C.

Different coatings on graphite.

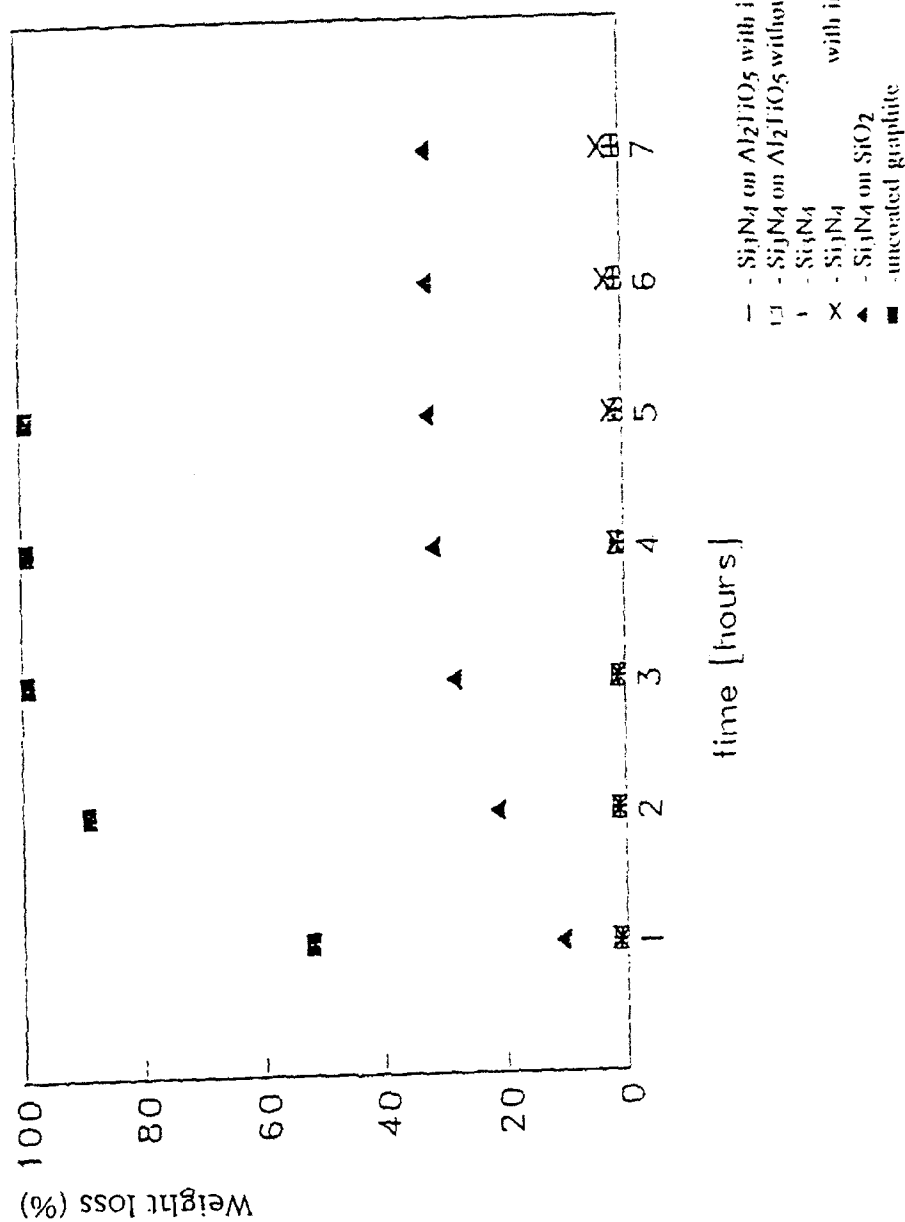


Fig. 40

Weight loss (%) as function of repeated 1 hr exposures at 830°C.
Graphite coated with Si_3N_4 at different conditions.

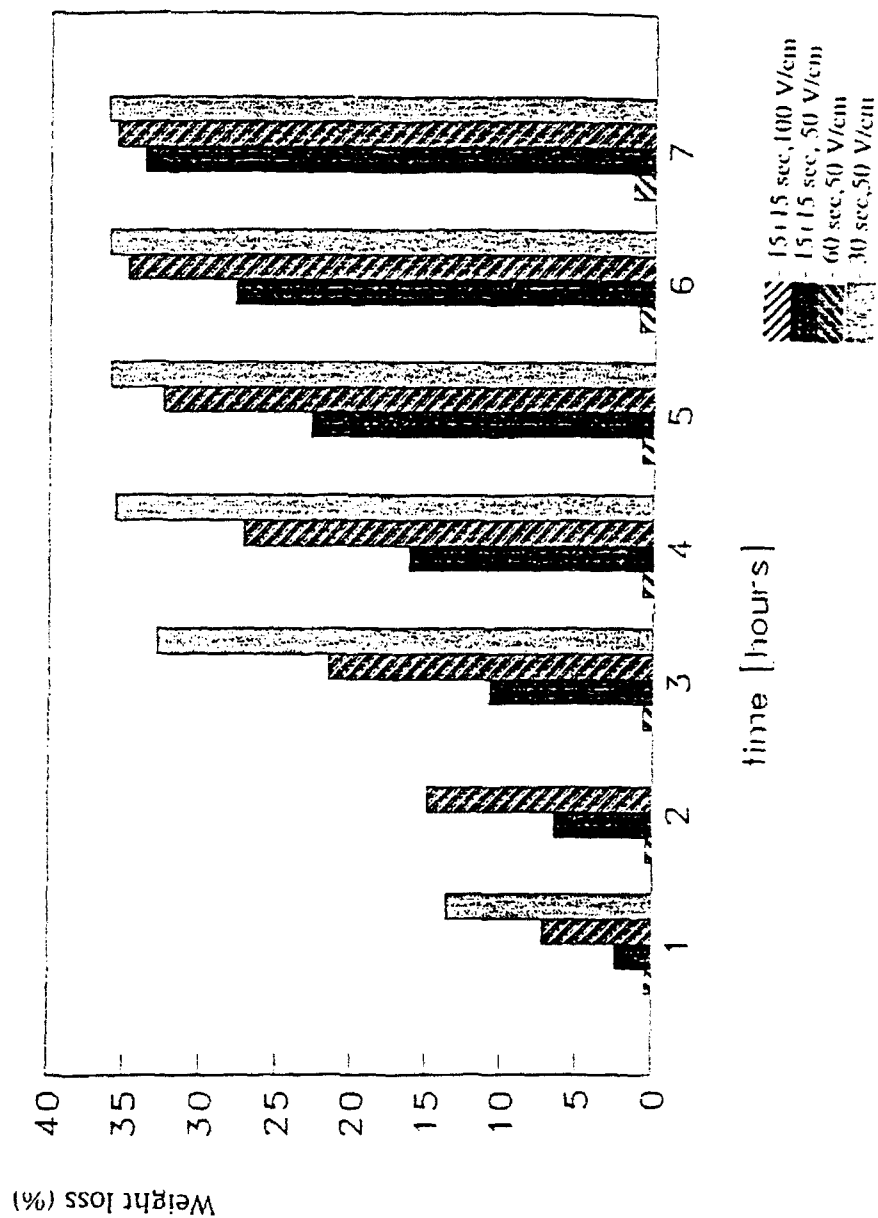


Fig. 41

Weight loss (%) as function of repeated 1hr exposures at 830°C.
 Graphite coated with Si_3N_4 at different conditions.

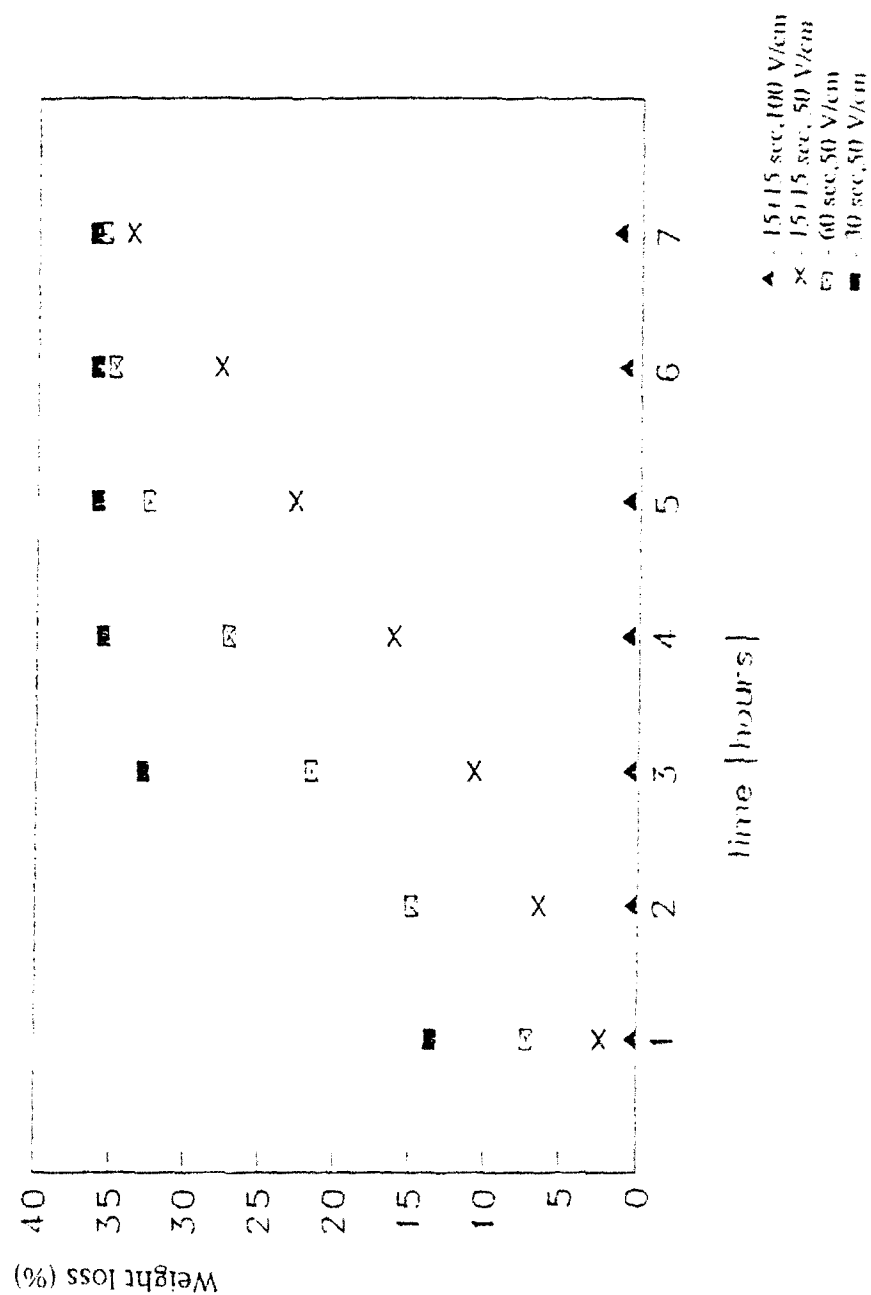


Fig. 42

Weight loss (%) as function of repeated 1hr exposures at 830°C.

Si_3N_4 coated graphite with and without Al_2TiO_5 underlayer.

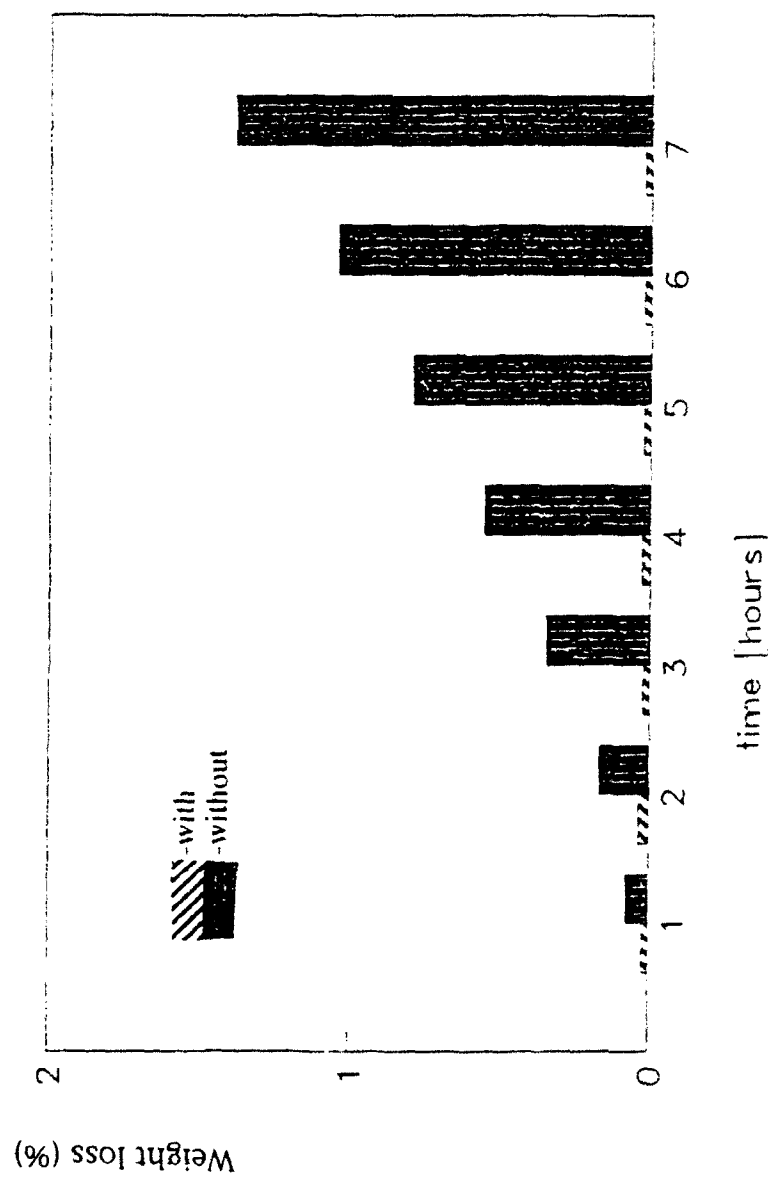


Fig. 43

Weight loss (%) as function of repeated 1hr exposures at 830°C.
Si₃N₄ coated graphite with and without Al₂TiO₅ underlayer.

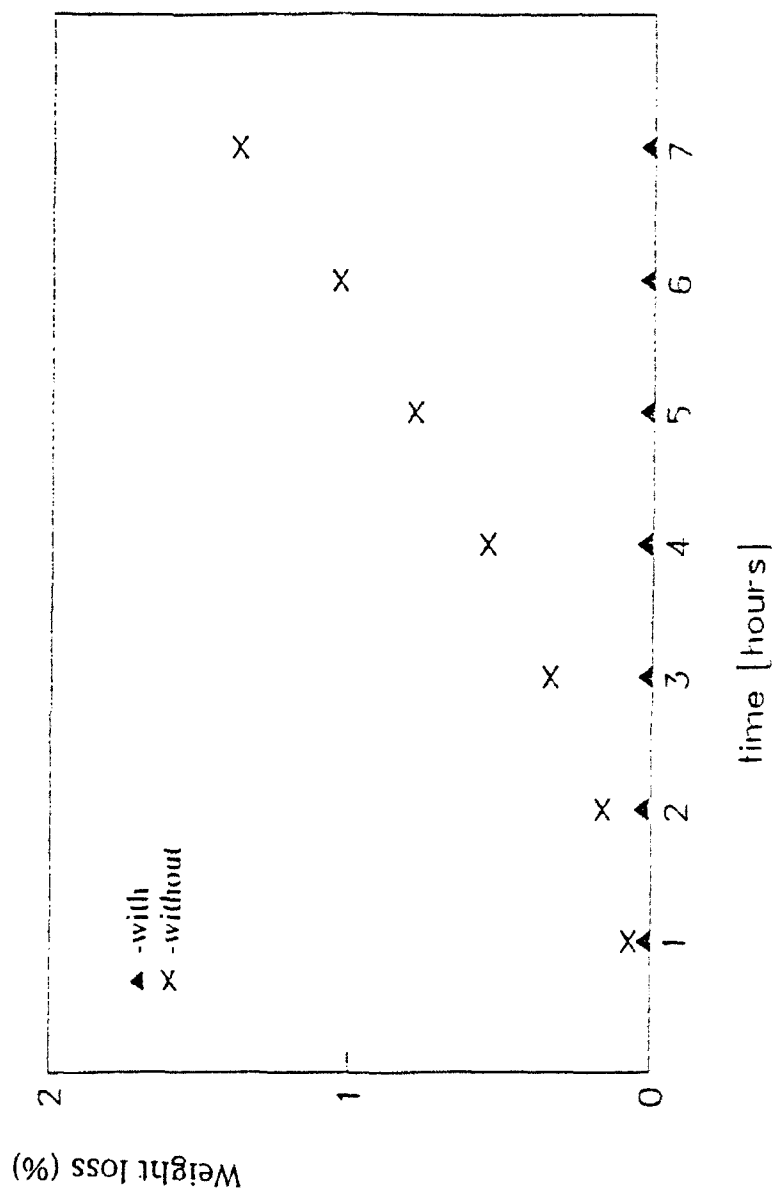


Fig. 44

Weight loss (%) as function of repeated 1hr exposures at 830°C.
Si₃N₄ with and without SiO₂ on graphite.

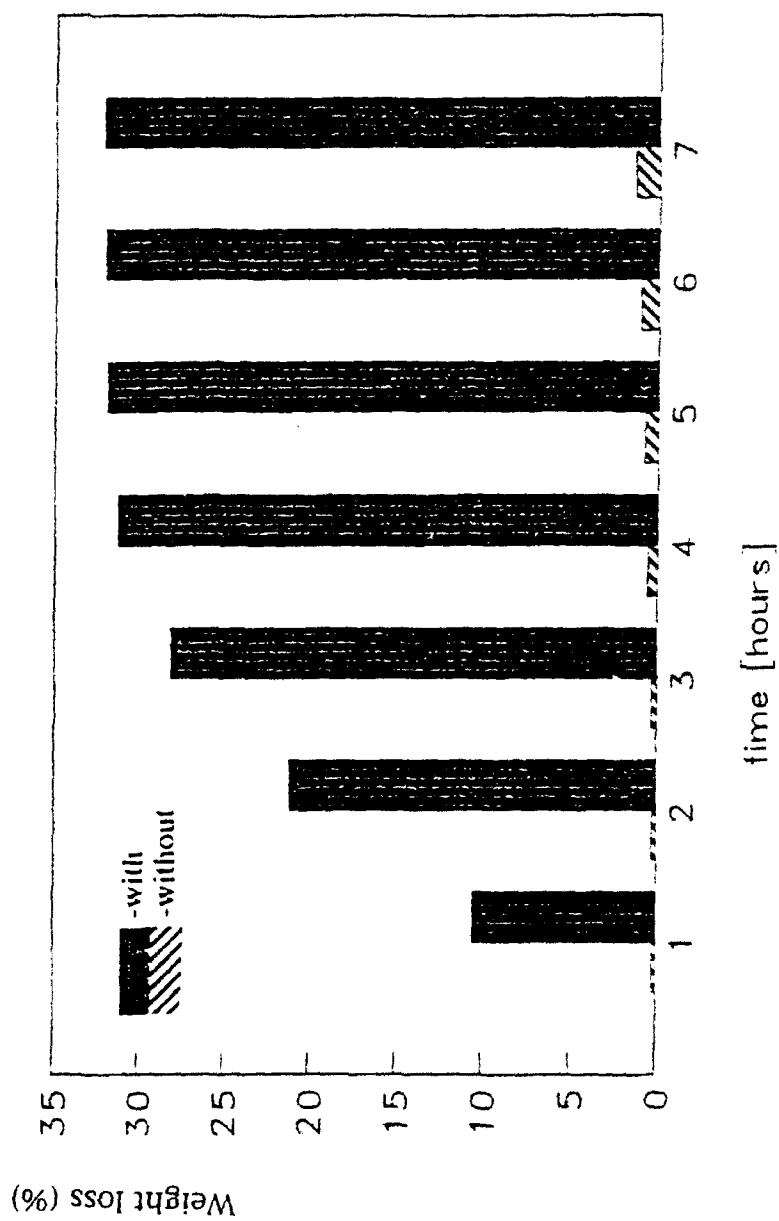


Fig. 45

Weight loss (%) as function of repeated 1hr exposures at 830°C.

C-C composites coated with Si_3N_4 at different conditions.

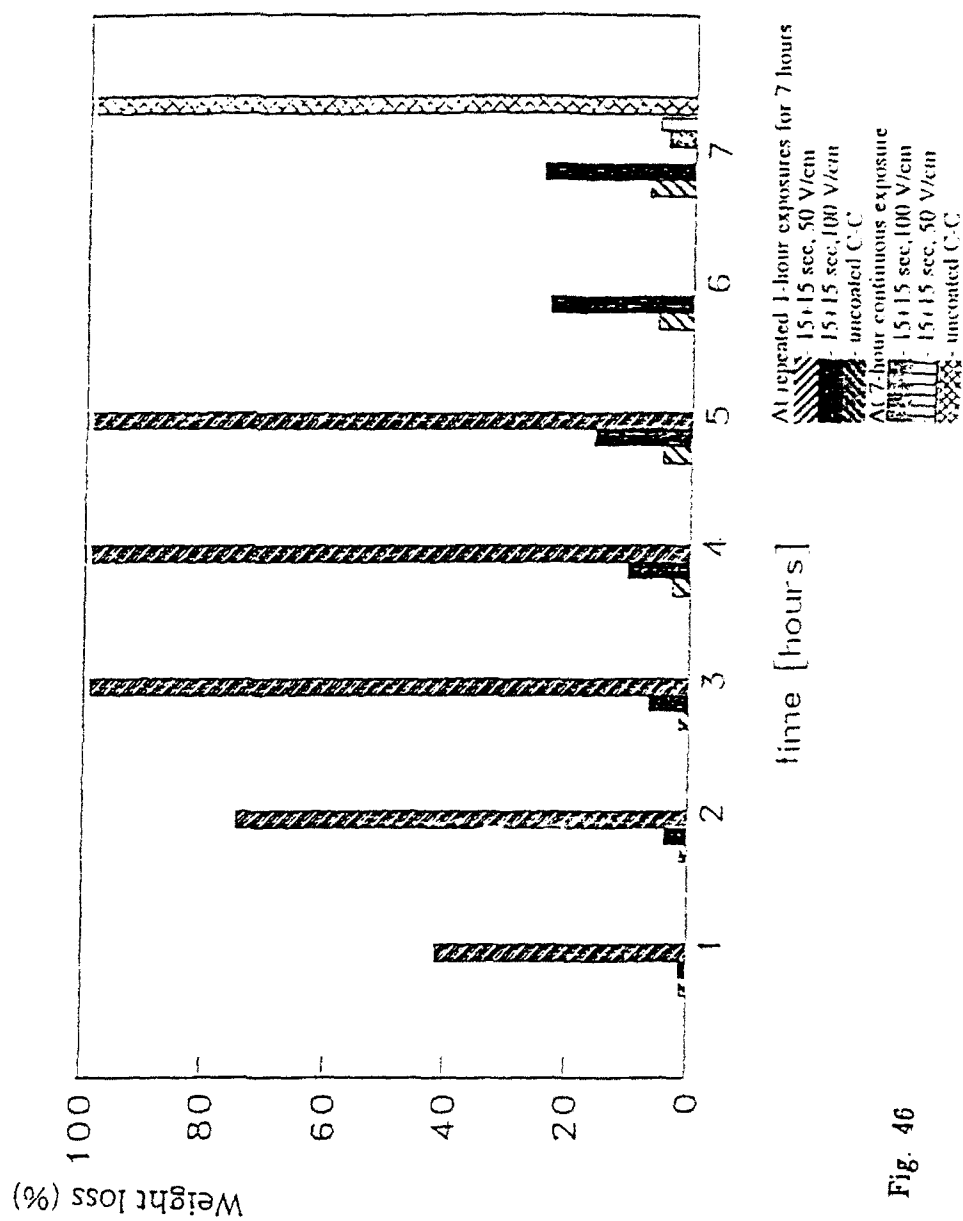


Fig. 46

Weight loss (%) as function of repeated 1hr exposures at 830°C.

Si₃N₄ coated C-C composites with and without Al₂TiO₅ underlayer

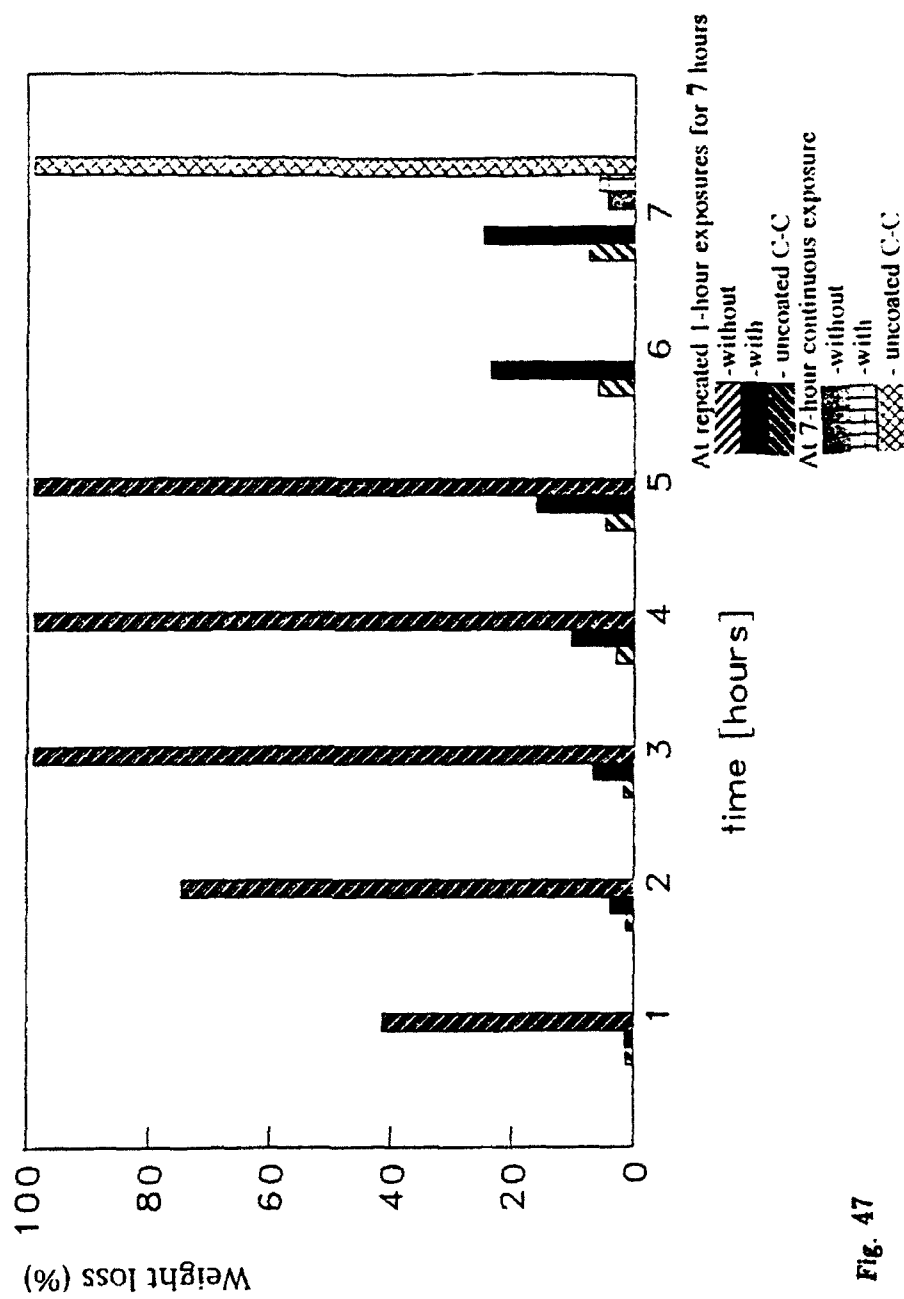


Fig. 47

4. Summary and Conclusions

The work presented in this report concentrated on the final steps of the development of electrophoretic protective coatings for graphite and carbon-carbon composites. The emphasis was therefore on the sintering of these coatings and the testing of their protective properties. The deposition conditions were determined in the previous stages of this project.

The coating systems studied were: Al_2TiO_5 , HfTiO_4 , Si_3N_4 , Si_3N_4 on Al_2TiO_5 , Si_3N_4 on fused SiO_2 and Si_3N_4 on BN. The Al_2TiO_5 and HfTiO_4 coatings were selected due to their compatibility with graphite and C-C in terms of thermal expansion. However, it was expected that due to the anisotropy of the thermal expansion coefficient microcracking will take place and therefore additional overcoating will be needed for oxidation protection.

The HfTiO_4 disintegrated after sintering and no viable undercoating could be obtained. Al_2TiO_5 was impregnated and uniformly deposited. Sintering at 1650°C in N_2 resulted in adherent coatings which however decomposed partially into Al_2O_3 and TiO_2 as shown by the X-ray diffraction pattern.

Si_3N_4 coatings were obtained both in single and multiple deposition stages. Multiple deposition was done primarily in order to change the holder position to minimize defects in the coatings. After sintering at 1650°C in N_2 uniform, adherent coatings were obtained with extensive anchoring in the pores and voids of the substrate. Interaction with the substrate took place as indicated by diffraction peaks of SiC and Si .

Si_3N_4 coatings with underlayers of Al_2TiO_5 were obtained. Uniform layers of Si_3N_4 with penetration into the Al_2TiO_5 underlayer formed in the "green" state. After sintering cross-sections showed dense layers of Si_3N_4

anchored in the substrate with a discontinuous layer of a Ti containing component below the Si_3N_4 and an even distribution of the element Al in the entire coating. Very extensive anchoring of the Si_3N_4 coating is seen both in graphite and C-C specimens. Overall coating thicknesses were up to 88μ . Adherent coatings of Si_3N_4 on fused SiO_2 were obtained with anchoring in the substrate. Horizontal and vertical microcracks are seen in the coatings after sintering.

Impregnation of BN into the pores prior to Si_3N_4 coating was attempted. Since both B and N are not visible in the EDS-SEM no evidence of penetration was seen except for weight gain after impregnation.

Shaped objects, exhaust nozzles and casting crucibles, were coated with $\text{Si}_3\text{N}_4 + \text{Al}_2\text{TiO}_5$ and $\text{Si}_3\text{N}_4 + \text{SiO}_2$. Uniform internal and external coatings were obtained using shaped electrodes.

Oxidation experiments were carried out by recording the weight loss during continuous and repeated exposures of 830°C . Best results with graphite specimens were obtained with the $\text{Si}_3\text{N}_4 + \text{Al}_2\text{TiO}_5$ system where in some cases nil weight loss was recorded after 7 repeated 1-hr exposures, a regime that exposed the specimens to repeated thermal shock. No beneficial effect of an underlayer of fused SiO_2 or BN was found in laboratory specimens when compared with Si_3N_4 only. However, very good results were obtained with an underlayer of SiO_2 on exhaust graphite nozzles under specific testing conditions.

On C-C specimens low weight losses were obtained with Si_3N_4 and Si_3N_4 on Al_2TiO_5 in continuous exposure experiments. In most repeated exposure tests high weight losses were recorded. However, in some experiments Si_3N_4 coatings gave low weight loss. The irreproducibility of the results in both

materials and in particular in the case of C-C may stem from a major defect in the coating formed on the location of the holder during deposition. Although repeated depositions were made this problem may not have been solved completely and should be elaborated in further experiments.

REPORT DOCUMENTATION PAGE			Form Approved OMB No 0704-0188	
<small>Public reporting burden for this collection of information is estimated to average 1 hour per response, including the time for reviewing instructions, searching existing data sources, gathering and maintaining the data needed, and completing and reviewing the collection of information. Send comments regarding this burden estimate or any other aspect of this collection of information, including suggestions for reducing this burden, to Washington Headquarters Services, Directorate for Information Operations and Reports, 1215 Jefferson Davis Highway, Suite 1204, Arlington, VA 22202-4302, and to the Office of Management and Budget, Paperwork Reduction Project (0704-0188), Washington, DC 20503.</small>				
1. AGENCY USE ONLY (Leave blank)	2. REPORT DATE August 30, 1991	3. REPORT TYPE AND DATES COVERED Annual report 1 July 90-30 June 91		
4. TITLE AND SUBTITLE Electrophoretic and electrolytic deposition of ceramic particles on porous substrates		5. FUNDING NUMBERS AFOSR-89-0474		
6. AUTHOR(S) L. Gal-Or, S. Haber, S. Liubovich				
7. PERFORMING ORGANIZATION NAME(S) AND ADDRESS(ES) Technion Research and Development Foundation Technion City, Haifa 32000, Israel		8. PERFORMING ORGANIZATION REPORT NUMBER		
9. SPONSORING/MONITORING AGENCY NAME(S) AND ADDRESS(ES) - EOARD 223/231 Old Marylebone Rd., London NW1 5TH UK - AFOSR/NE, Lt.Col. L. Burggraf, Bolling AFB DC 20332-6448		10. SPONSORING/MONITORING AGENCY REPORT NUMBER		
11. SUPPLEMENTARY NOTES				
12a. DISTRIBUTION/AVAILABILITY STATEMENT Unlimited.		12b. DISTRIBUTION CODE		
13. ABSTRACT (Maximum 200 words) The electrophoretic deposition of low expansion ceramic materials (Al_2TiO_5 and $HfTiO_4$) on porous graphite and their penetration into the pores was studied. Penetration is enhanced by large Pe numbers and is therefore higher in aqueous suspensions while coating morphology is improved in ipropanol suspensions. Optimal conditions for coverage and penetration in a two-stage process were determined. The feasibility of subsequent electrophoretic deposition of two different layers of materials with zeta potentials of the same polarity was demonstrated for Si_3N_4 on Al_2TiO_5 (cathodic deposits) and SiC on glass ceramic (anodic deposits). Layer thicknesses in these experiments were in the range of 100-300 μ . In parallel studies on electrolytic deposition from ionic aqueous solutions the deposition of Al_2O_3 and co-deposition of $Al_2O_3+ZrO_2$ from solutions of $Al(NO_3)_3$ and $ZrO(NO_3)_2$ were demonstrated and studied. It was shown that the atomic ratio of Al/Zr in the deposit can be varied by varying this ratio in the solution. The as-deposited coatings are amorphous and became crystalline after heat treatment.				
14. SUBJECT TERMS Electrophoresis, Ceramics, Penetration, Electrolytic Deposition, Zirconia, Alumina		15. NUMBER OF PAGES		
		16. PRICE CODE		
17. SECURITY CLASSIFICATION OF REPORT Unclassified	18. SECURITY CLASSIFICATION OF THIS PAGE Unclassified	19. SECURITY CLASSIFICATION OF ABSTRACT Unclassified	20. LIMITATION OF ABSTRACT Unlimited	

ELECTROPHORETIC AND ELECTROLYTIC DEPOSITION OF CERAMIC PARTICLES ON POROUS SUBSTRATES

L. Gal-Or, S. Haber, S. Liubovich

Summary of Annual Report

1 July 1990 - 30 June 1991

INTRODUCTION

The present phase of the research project concentrated on the following aspects:

- Surface deposition and penetration of low-expansion ceramic materials such as Al_2TiO_5 and HfTiO_4 on porous graphite.
- Multilayer electrophoretic deposition of two different ceramic materials: Al_2TiO_5 and S_3N_4 as well as glass ceramic and SiC .
- Electrolytic deposition of a single oxide (Al_2O_3) and co-deposition of two oxides ($\text{Al}_2\text{O}_3 + \text{ZrO}_2$) from aqueous ionic solutions.
- Theoretical analysis of particle penetration into pores

The interest in the deposition of low-expansion ceramics stems from the intention to apply electrophoretic deposition for the coverage and impregnation of carbon-carbon composites with appropriate ceramic materials so as to prevent its oxidation at elevated temperatures. Al_2TiO_5 and HfTiO_4 are characterized by low thermal expansion coefficients similar to that of carbon-carbon. Therefore, their use as coating materials may provide the necessary compatibility with the

substrate from the point of view of thermal expansion. However, it is known that the expansion of these materials is anisotropic and therefore microcracking of the coating takes place upon sintering. It has been realized for some time that the complicated problem of carbon-carbon protection will have to be solved by the application of several different coatings. It was thus considered of great importance to study sequential electrophoretic deposition of another ceramic material such as Si_3N_4 on the Al_2TiO_5 as a remedy of the detrimental effect of microcracking.

The above mentioned studies were performed on the basis of the conclusions from the previous basic experimental and theoretical studies of the deposition of colloidal SiO_2 .

The electrolytic deposition of ZrO_2 , studied in the previous year, was now extended to its codeposition with another oxide- Al_2O_3 . Thus the deposition of Al_2O_3 only was first studied and then the feasibility of co-deposition was demonstrated. The effect of deposition parameters on the kinetics, morphology and composition of the coatings was studied.

The penetration of particles into a porous substrate assuming it consists of pores which are closed at the far end was analyzed theoretically (an open interconnected porous structure was considered previously).

EXPERIMENTAL

The electrophoretic and electrolytic deposition was carried out on porous graphite substrates (UCAR grade 45, 48% volume porosity average pore size 60 μ). Initial experiments with C-C were performed on a 2-D composite supplied by the USAF.

Al_2TiO_5 , prepared at the Israel Ceramics Institute, had a 5% BaCO_3 addition and an average particle size of 1.4 μ . The HfTiO_4 was acquired from Cerac Corp. and had originally an average size of 70 μ .

Si_3N_4 particles were in the range of 0.5-1.0 μ and that of SiC 40 μ . Suspensions of the ceramic particles were prepared in isopropanol, water and mixtures of the two solvents. Particle concentrations were 30, 100 and 250 g/l, the electric field was in the range of 5-300 V/cm and deposition times were 30 sec-60 min.

The amount of impregnated material was determined by weight change after removal of the external deposit.

The multilayer deposition was carried out by immersion of the substrate, coated with the first layer in the suspension of the second material while still wet.

The composition and morphology of the multilayer deposits were studied on crosssections obtained by cutting coated specimens that were infiltrated with an epoxy resin and cured for 10 hrs. These studies were performed with a JEOL 840 SEM equipped with an EDS unit.

The electrolytic deposition was carried out from solutions of 0.02-0.2M $\text{Al}(\text{NO}_3)_3$ with and without 0.01-0.05M $\text{ZrO}(\text{NO}_3)_2$. The deposition was done at constant current with c.d.'s in the range of 15-60 mA/cm² and deposition times of 20 sec - 40 min.

Some deposits were heat-treated at 1200°C for 1 hr. Morphology and microanalysis were studied in the JEOL 840 SEM and phase content with an x-ray diffractometer Phillips Model PW-1730.

SUMMARY OF RESULTS

In contrast to the SiO_2 particles deposited in previous studies it was found that both Al_2TiO_5 and HfTiO_4 deposit on the cathode both from water and ipropanol suspensions. The positive charge on the particles indicates a high isoelectric point since the pH of these suspensions was determined as 8.1

in water and 6.2 in propanol. As in the previous study of SiO_2 deposition, it was found that penetration of Al_2TiO_5 into the porous substrate is higher in water than in ipropanol. However, the addition of $\approx 20\%$ ipropanol to the water lead to a maximal penetration probably due to better wetting of the graphite as demonstrated in simple wetting experiments. About 6% of substrate weight of Al_2TiO_5 were induced into the pores at 100 V/cm, 30 g/l after 60 min. The surface deposition, however, is both higher and morphologically better in propanol due to a lower fraction of penetrated material and lower H_2 formation on the cathode.

It was thus concluded that for optimal coverage and penetration a two stage process would be employed: impregnation from an aqueous solvent with 20% ipropanol for relatively low duration (60 min, 75-100 V/cm) and coating in ipropanol at higher field (200 V/cm) and shorter duration (≈ 2 min). It was shown that impregnation increases with field intensity and deposition time. The morphology of surface deposits and impregnated crossections were studied.

The feasibility of subsequent deposition of two different layers of materials with zeta potentials of the same polarity was shown for Si_3N_4 on Al_2TiO_5 (cathodic deposits) and SiC on glass ceramic (anodic deposits). The deposition is carried out by transferring the coated substrate from the first suspension into the second to continue the deposition of the second material. Crossections of the two layers were prepared after impregnation of the specimens with an Epoxy resin and its curing. Elemental analysis and Si and Ti x-ray images were performed in the SEM and the existence of the two layers shown. However, penetration of the Si_3N_4 and SiC into the first layer was observed. The layer thicknesses obtained in these experiments were in the range of 150-300 μ .

The co-deposition of two oxides by an electrolytic process from aqueous solutions containing salts of both cations $\text{Al}(\text{NO}_3)_3 + \text{ZrO}(\text{NO}_3)_2$ was demonstrated and studied for $\text{Al}_2\text{O}_3 + \text{ZrO}_2$ deposits. Prior to that the deposition of Al_2O_3 was studied.

The effect of field intensity on the penetration in the optimal solvent is seen in Fig. 4. The penetration increases with field intensity in the range tested (further increase in field intensity caused excessive heating of the suspension and was therefore not studied). A decelerating effect of deposition time on penetration is seen in Fig. 5.

Figs. 6 & 7 describe the morphology of the coating and penetration. The surface deposit of Al_2TiO_5 is seen in Fig. 6. The coverage is uniform on a macroscale with a high degree of roughness reflecting the porous surface of the substrate. It was found that a denser and more uniform deposit is obtained in isopropanol at high field intensities and short deposition times.

A crosssection of a penetrated specimen obtained at optimal penetration conditions compared with a reference untreated specimen is seen in Fig. 7.

b) Multilayer Deposition

A schematic description of the multilayer deposition is given in Fig. 8. A deposit of particles A is formed in suspension A, the coated specimen is removed from the suspension and while still wet introduced in suspension B. A deposit of particles B is formed. A more thorough study of this two-stage deposition process should be done in the future. So far, two systems were deposited: Si_3N_4 on top of Al_2TiO_5 and SiC on a glass ceramic deposit. In each system the zeta potential of the different materials had the same sign, Si_3N_4 and Al_2TiO_5 deposited both on the cathode, while SiC and the glass ceramic migrated to the anode. When couples of materials with opposite zeta potential were studied, the first deposit migrated away from the substrate when its polarity was changed so as to deposit the next layer. Yet conditions can be envisaged where such two-layer deposition can still be performed and these will be studied in a future work.

Crosssections of the two layer deposits are seen in Figs. 9-12. Fig. 9 shows an optical micrograph of the layer of Al_2TiO_5 and Si_3N_4 as well as an SEM x-ray image of Si and Ti at a higher magnification. The overall layer thickness is $\approx 350 \mu\text{m}$. The element Si is seen in both layers with a

much higher density in the outer layer (the Si_3N_4). Its existence in the inner layer (the Al_2TiO_5) is explained by penetration of some Si_3N_4 into the initial porous ("green") Al_2TiO_5 layer. The element Ti, however, exists as expected only in the inner layer. An interesting feature is the "pegging" of the inner layer in the pores of the substrate. The thickness of the Si_3N_4 is $\approx 200 \mu\text{m}$ and that of Al_2TiO_5 $\approx 150 \mu\text{m}$. Composition graphs of the the two layers are seen in Fig. 11 showing again the penetration of Si into the underlying Al_2TiO_5 layer.

Two anodic deposits are shown in Figs. 11, 12. An inner glass ceramic layer ($\approx 300 \mu$) with an elemental composition seen in Fig. 11a and an x-ray image characterized by the element K. An outer layer of SiC ($\approx 150 \mu$) with traces of Fe (from the anode). The x-ray image (Fig. 12b) shows again the penetration of SiC (characterized by the element Si) into the underlying layer of the glass-ceramic. The amount of Si_3N_4 deposited on Al_2TiO_5 as function of deposition time was determined with the intention to study the effect of the underlying Al_2TiO_5 layer on the deposition of Si_3N_4 (see Fig. 13). It is seen that the existence of the underlying layer does not affect the deposition kinetics probably due to the high porosity of the first layer which is still in the "green state".

CONCLUSIONS

A low expansion ceramic material-aluminium titanate (Al_2TiO_5) was electrophoretically deposited and penetrated into porous graphite. The Al_2TiO_5 which is positively charged deposits on a cathodic substrate at a $\text{pH}=8.1$ indicating a relatively high isoelectric point. The amount of material that penetrated was maximal in an aqueous solution of 20% ipropanol. This composition is an outcome of the balance between the high ϵ/η ratio of water and the improved wetting of the substrate in the presence of ipropanol.

Penetration increases with electric field intensity in the range studied and with deposition time. For optimal coverage and penetration a two stage process should be applied:

- impregnation in a 20% ipropanol solution in water (at 100 V/cm, 30 g/l about 6% of substrate weight of Al_2TiO_5 is penetrated after 60 min.).

- Surface coating in ipropanol at a high field strength (200 V/cm) and short duration (2 min.).

At optimal penetration conditions the whole crossection of a 7 mm thick substrate of porous graphite was penetrated.

Multilayer deposition of different ceramic materials is possible by subsequent deposition from different suspensions of materials with zeta potential of the same polarity. This was demonstrated by forming an inner layer of Al_2TiO_3 and an outer layer of Si_3N_4 (cathodic deposits) as well as an inner layer of a glass ceramic and an outer layer of SiC (anodic deposits). The individual layer thicknesses were in the range of 150-300 μ .

In the range of thickness discussed, the existence of the underlying "green" layer did not affect the kinetics of deposition of the external layer.

ACKNOWLEDGEMENT

Research sponsored by the Air Force Office of Scientific Research, Air Force Systems Command, U.S.A., under Grant No. 89-0474.

The U.S. Goevernment is authorized to reproduce and distribute reprints for Governmental purposes not withstanding any copyright notation thereon.

LIST OF FIGURES

- Fig. 1: Ceramic thermal expansion characteristics [4].
- Fig. 2: Amounts of Al_2TiO_5 deposited and penetrated in porous graphite as function of ipropanol concentration in water.
- Fig. 3: Model for a two-stage deposition process.
- Fig. 4: Amount of Al_2TiO_5 penetrated as function of field intensity (20% ipropanol in H_2O , 60 min, 30 g/l).
- Fig. 5: Amount of Al_2TiO_5 penetrated as function of deposition time (20% ipropanol, 50 V/cm, 30 g/l).
- Fig. 6: Surface deposit on graphite obtained in ipropanol at 200 V/cm, 2 min, 30 g/l.
- Fig. 7: Crossections of treated (20% ipropanol, 100 V/cm, 60 min) and untreated specimens.
- Fig. 8: Schematic description of multilayer formation.
- Fig. 9: Crossection of a double layer deposit of Si_3N_4 (x10) (100 g/l, ipropanol, 50 V/cm, 2 min) and Al_2TiO_5 (30 g/l, ipropanol, 200 V/cm, 90 sec) and x-ray images (x100).
- Fig. 10: Elemental composition of the two layers
a) Si_3N_4 ; b) Al_2TiO_5
- Fig. 11: Crossection of a double layer deposit of SiC on glass ceramic (x10). SiC (100 g/l, ipropanol, 50 V/cm, 15 sec), glass ceramic (250 g/l, ipropanol, 200 V/cm, 10 sec).
- Fig. 12: Elemental composition of the two layers a) SiC
b) glass ceramic (x100).
- Fig. 13: Amount of Si_3N_4 deposited on Al_2TiO_5 (70 μ) as function of deposition time.

BIBLIOGRAPHY

1. L. Gal-Or, S. Liubovich, S. Haber, "Deep Electrophoretic Penetration and Deposition of Ceramic Particles Inside Porous Substrates - Experimental", J. Electrochem. Soc., in press.
2. L. Gal-Or, S. Liubovich, S. Haber, "Deep Electrophoretic Penetration and Deposition of Ceramic Particles Inside Porous Substrates - An Analytical Model", J. Electrochem. Soc., in press.
3. D.W. McKee, Carbon, 24, 737(1986).
4. I. Jawed, D.C. Nagle, Mat. Res. Bull., 21,1391(1986).
5. K.L. Luthra, Carbon, 26,217(1988).
6. J.R. Strife, J.E. Sheenan, Ceramic Bulletin, 67, 369 (1988).
7. R.W. Lynch, B. Morosin, J. Am. Ceram. Soc., 55, 409 (1972).
8. G.A. Parks, Chem. Rev., 65,177(1985).

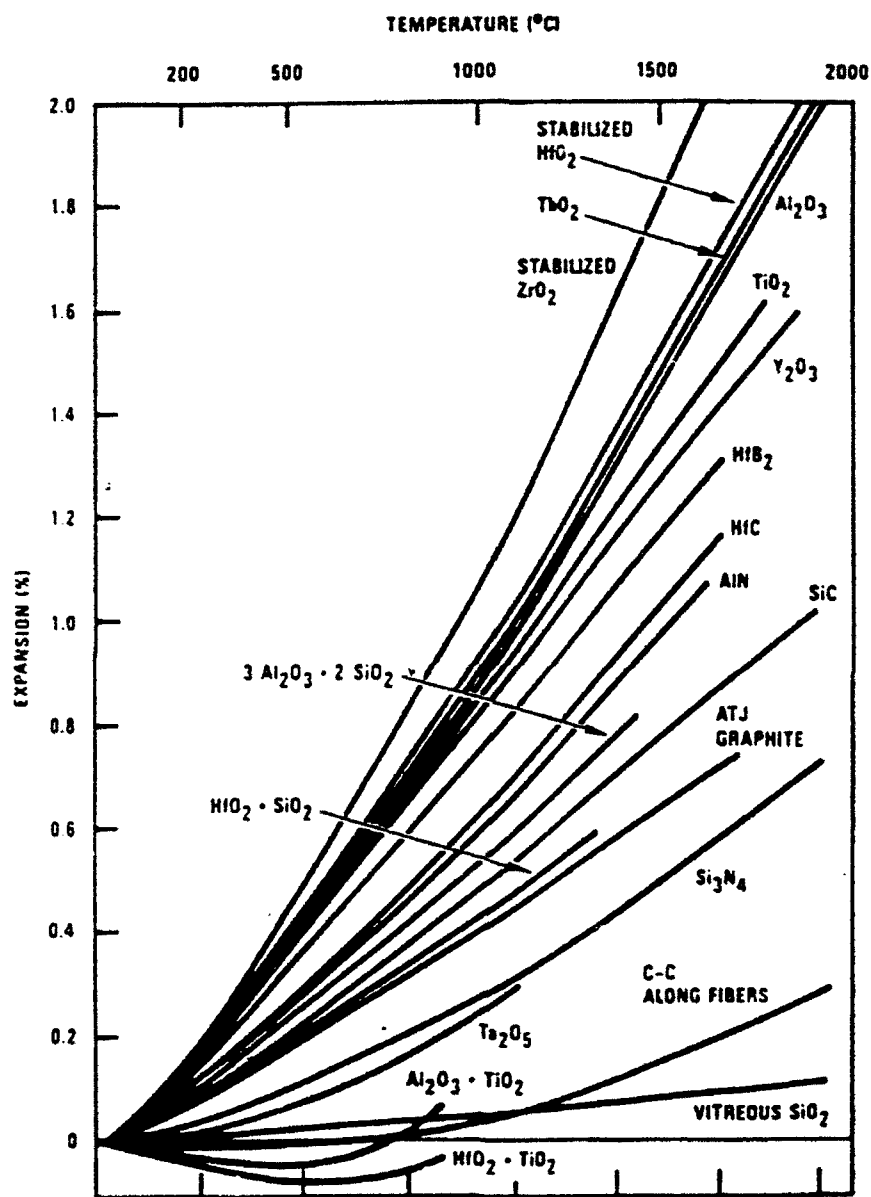


Fig. 1

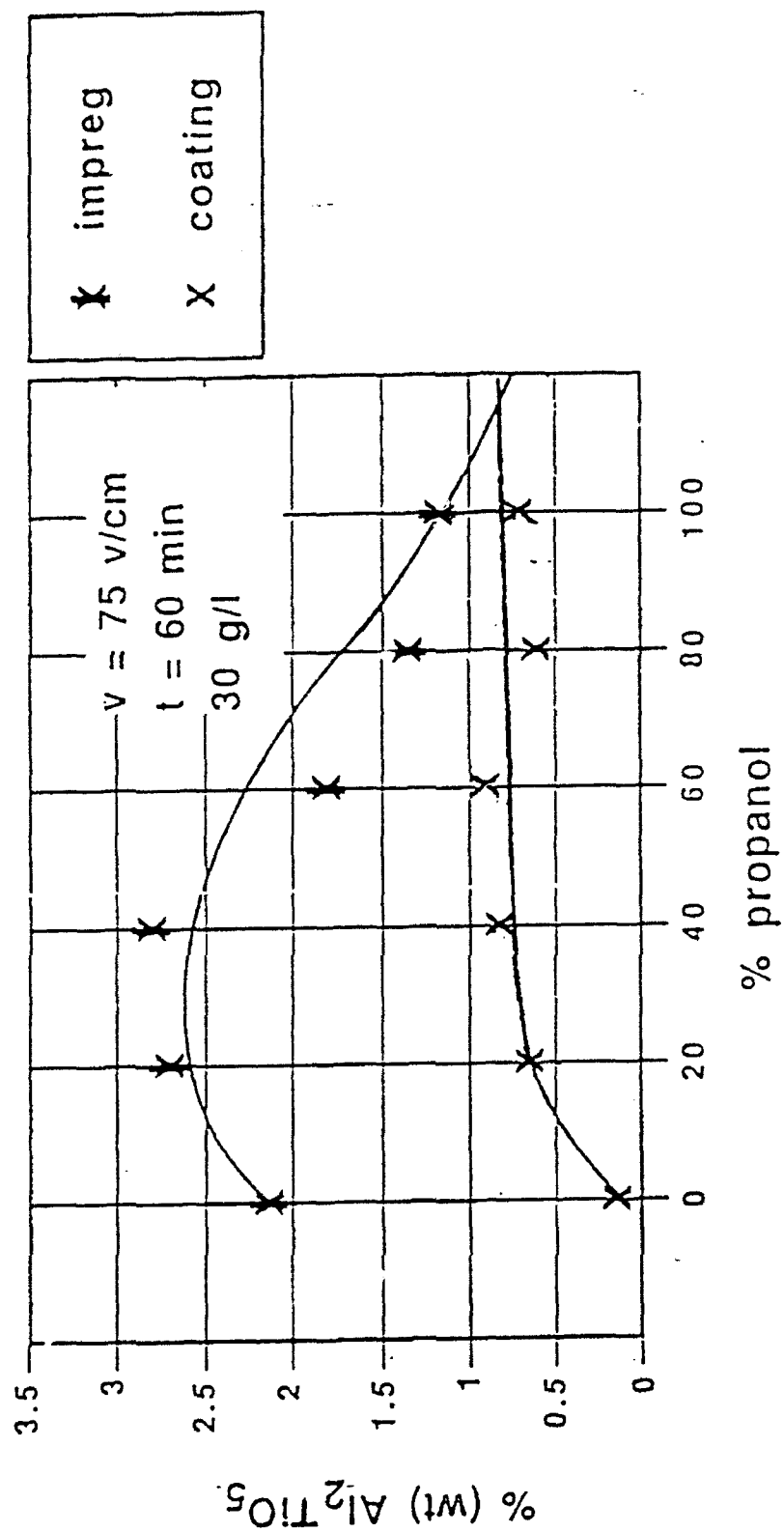
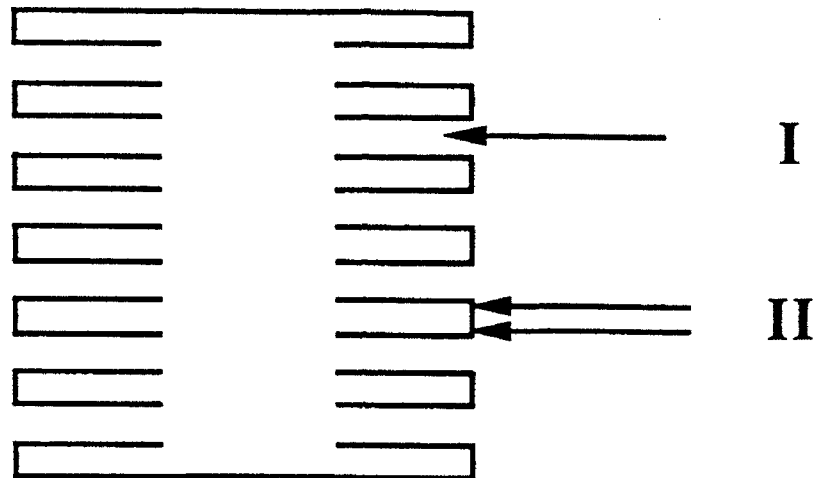


Fig. 2

TWO STAGE PROCESS:



I) OPTIMAL CONDITIONS FOR IMPREGNATION:

$$Pe \gg Pe = \left(\frac{u' + u''}{D} \right) \cdot r \quad U' = \frac{\varepsilon \cdot \zeta_p E}{4 \pi \eta}$$

$$\varepsilon_{H_2O} = 81 \quad \varepsilon_{prop} = 18.3$$

$$\eta_{H_2O} = 1 \text{ cp} \quad \eta_{prop} = 2 \text{ cp}$$

20% propanol in H_2O

II) OPTIMAL CONDITIONS FOR COATING:

100% propanol

• less penetration of particles

Fig. 3

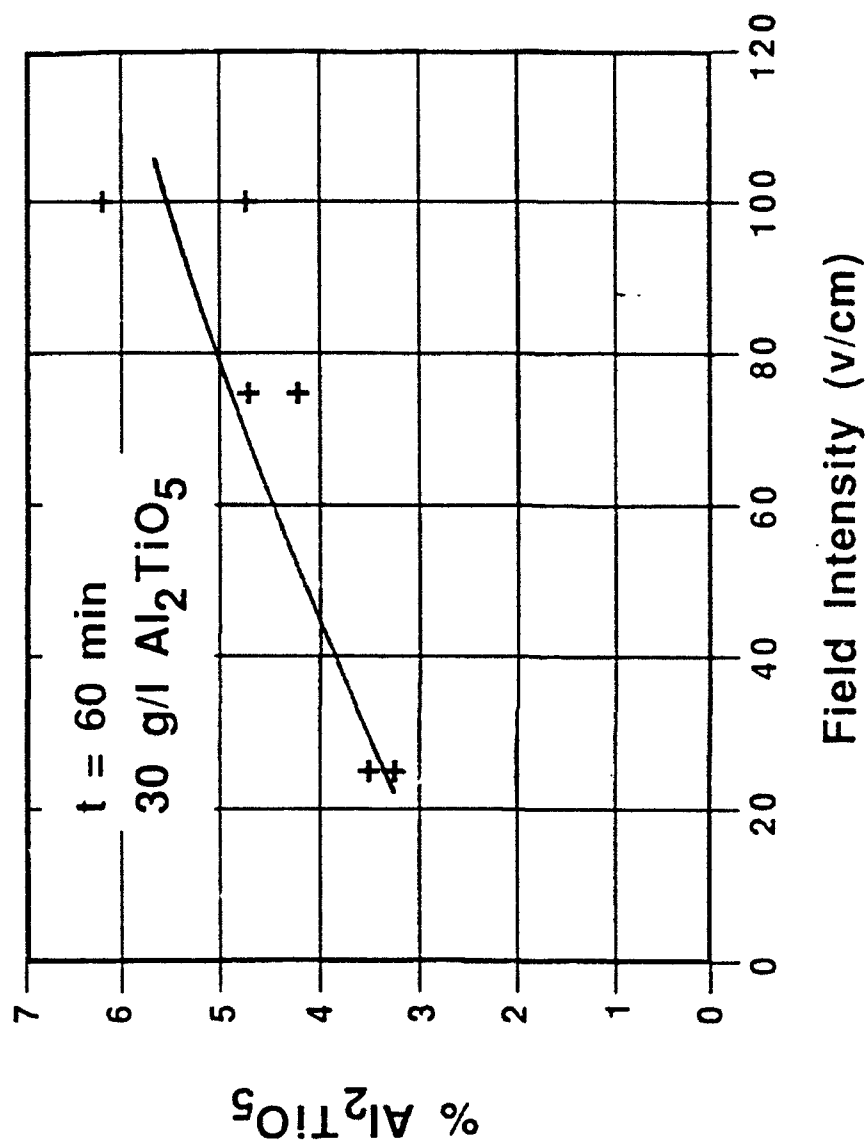


Fig. 4

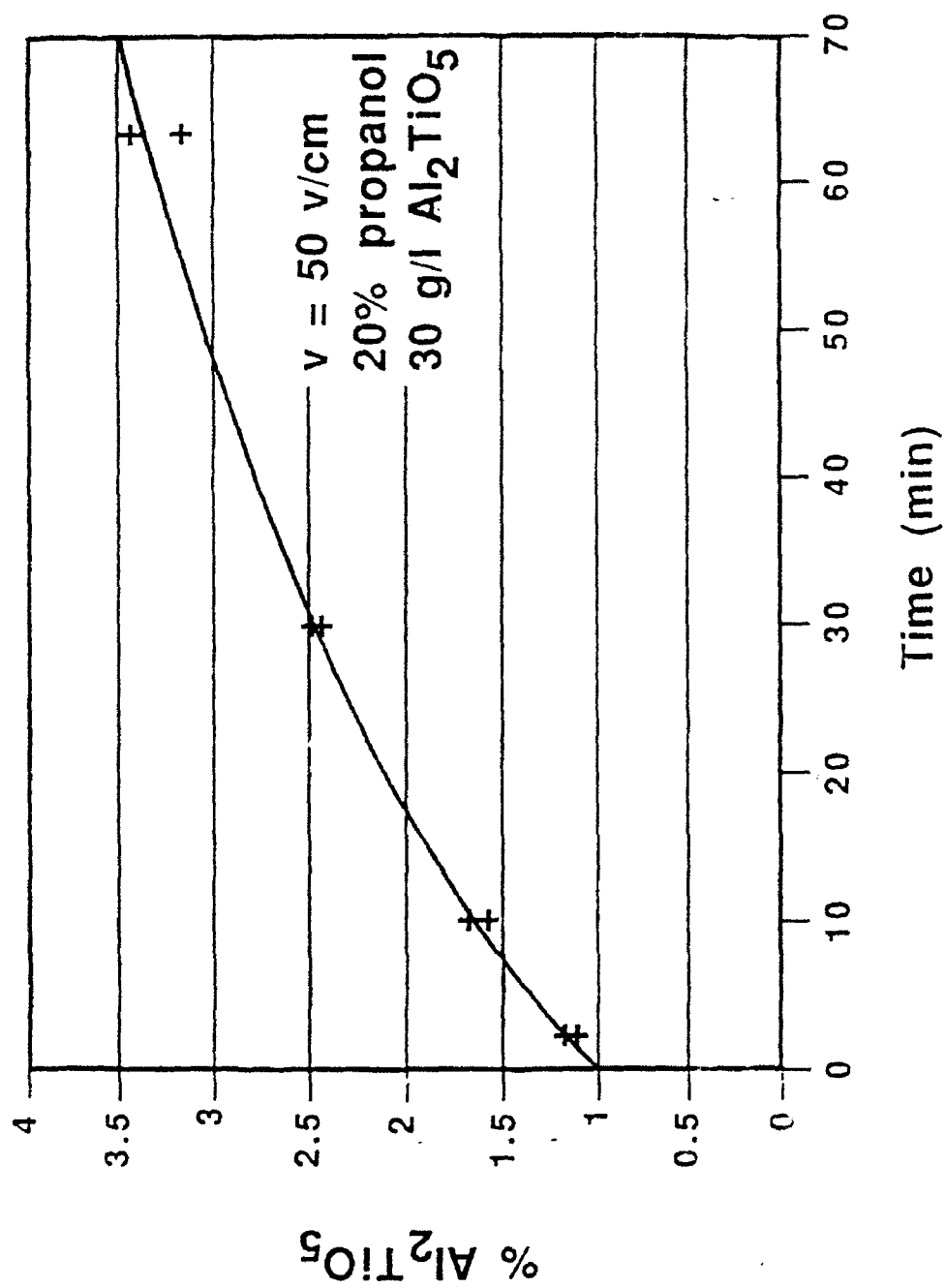


Fig 5

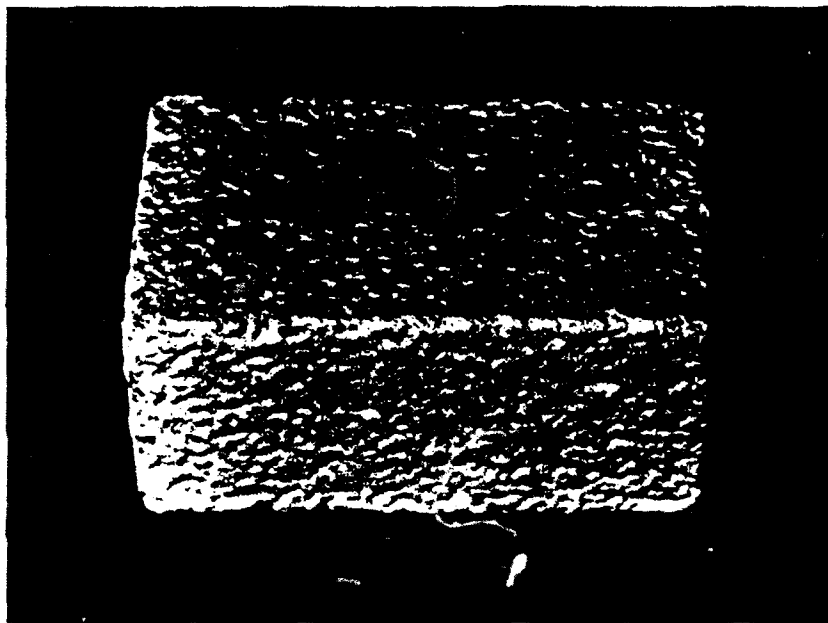


Fig 6

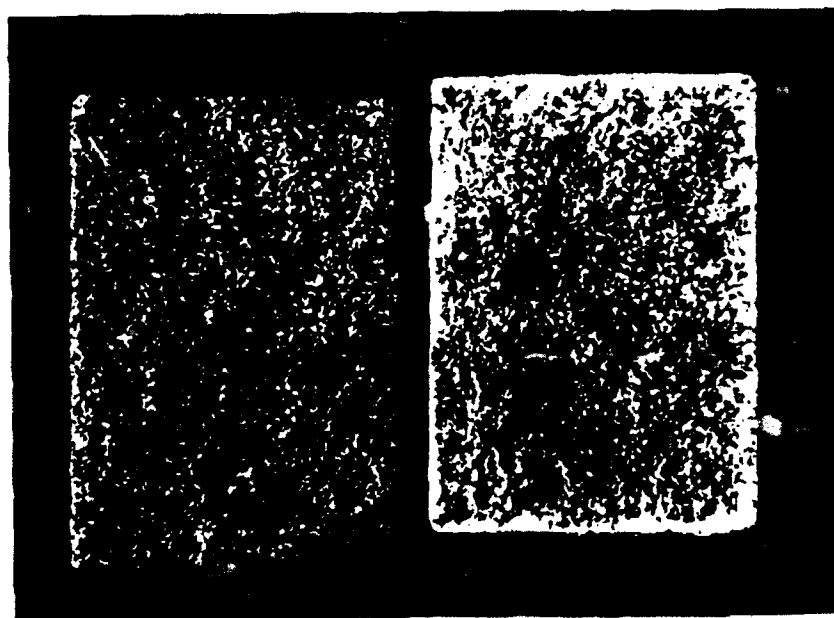


Fig 7

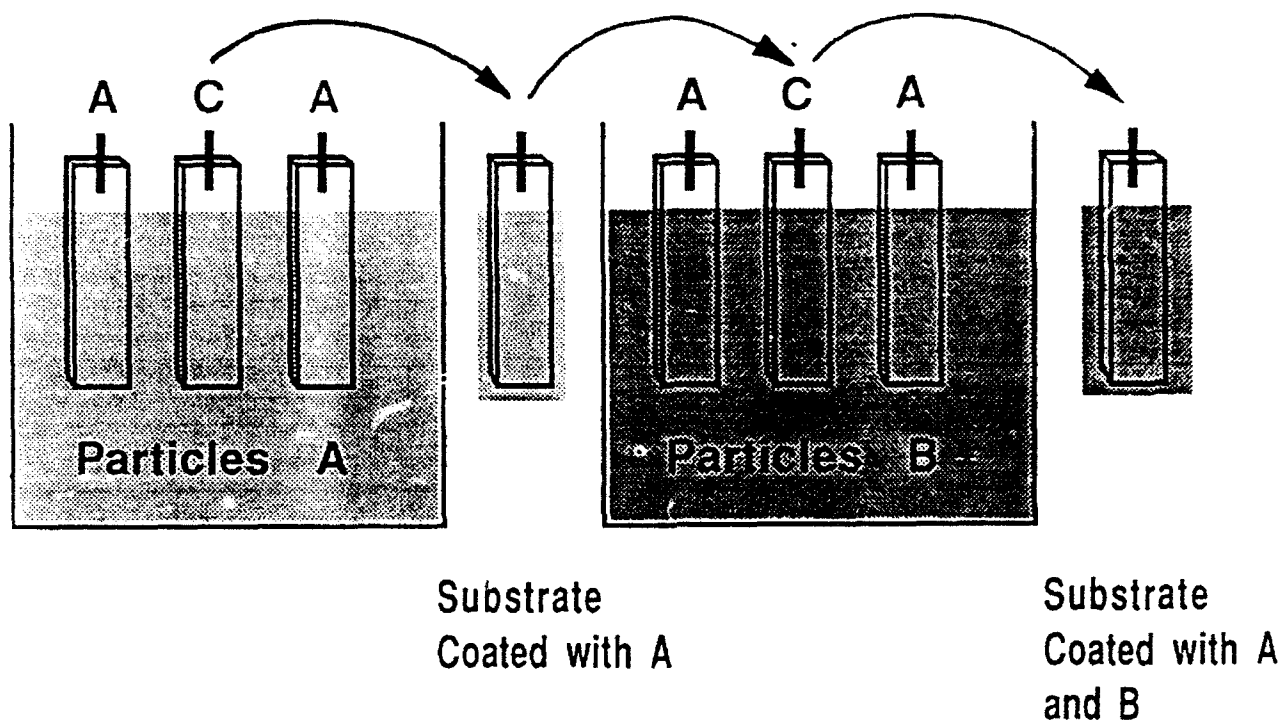
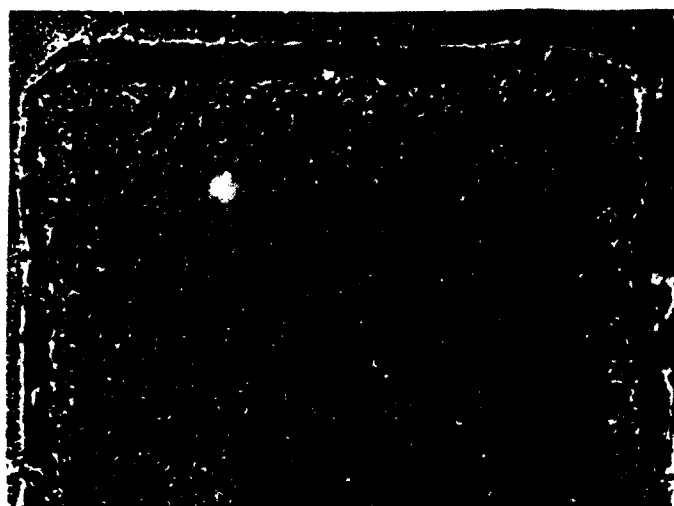


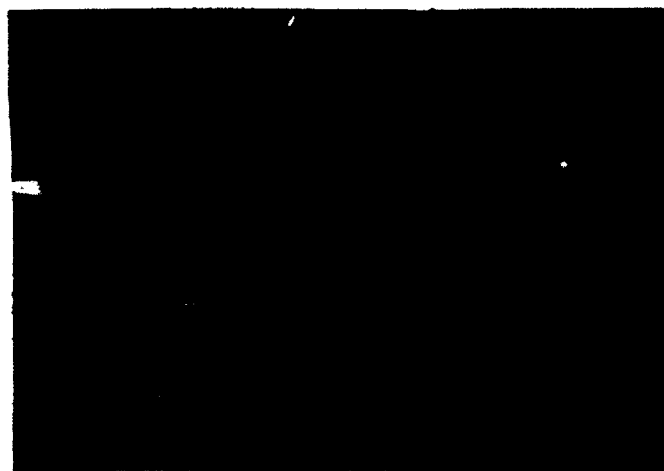
Fig 8



Si_3N_4 on
 Al_2TiO_5



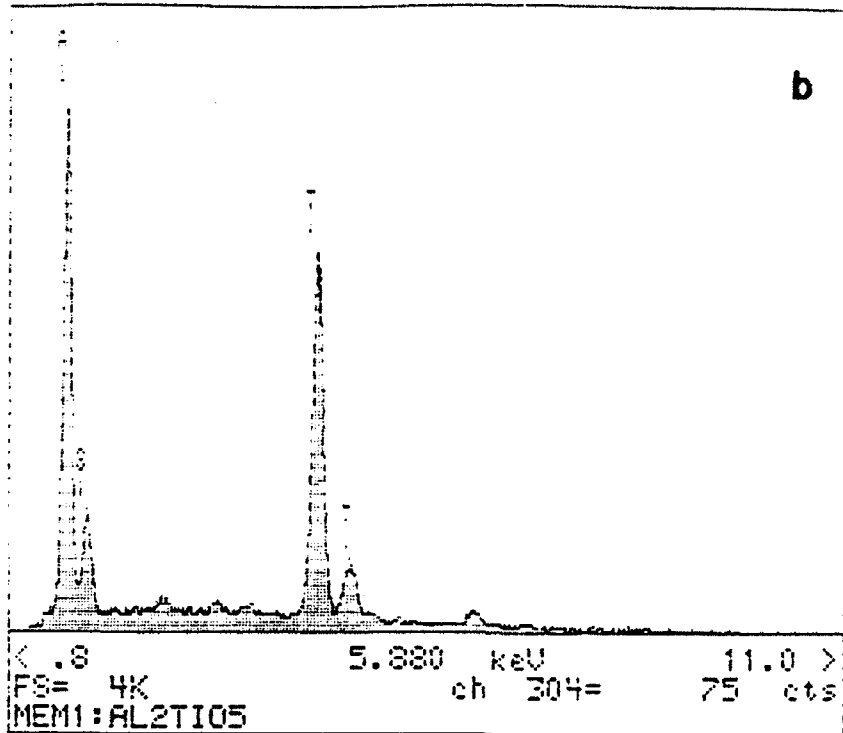
X-ray Si



X-ray Ti

Fig 9

X-RAY: 0 - 20 keV
Live: 97s Preset: 100s Remaining: 3s
Real: 110s 12% Dead



X-RAY: 0 - 20 keV
Live: 100s Preset: 100s Remaining: 0s
Real: 115s 13% Dead

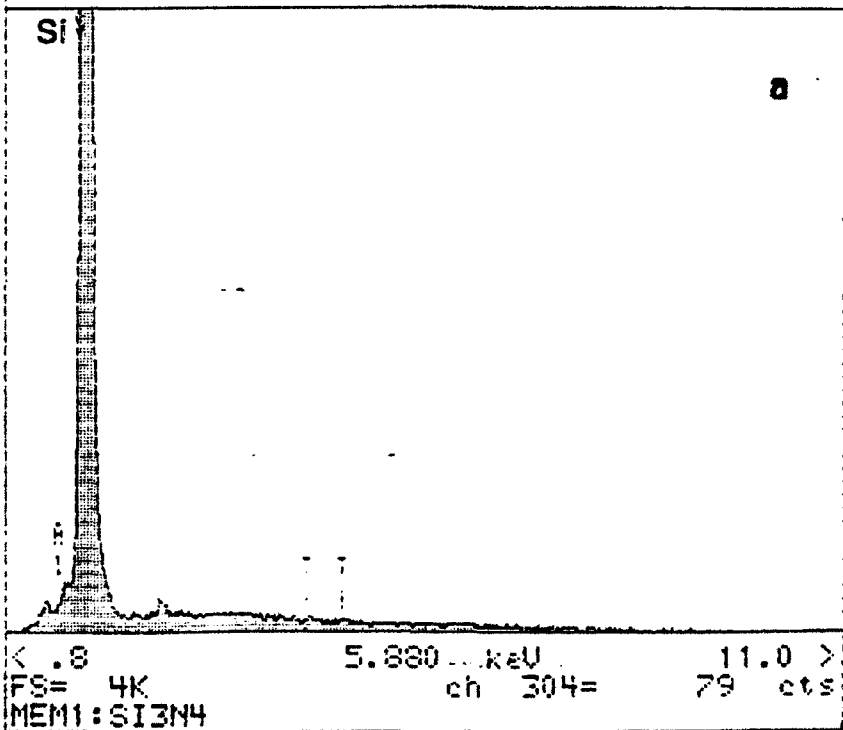


Fig 10

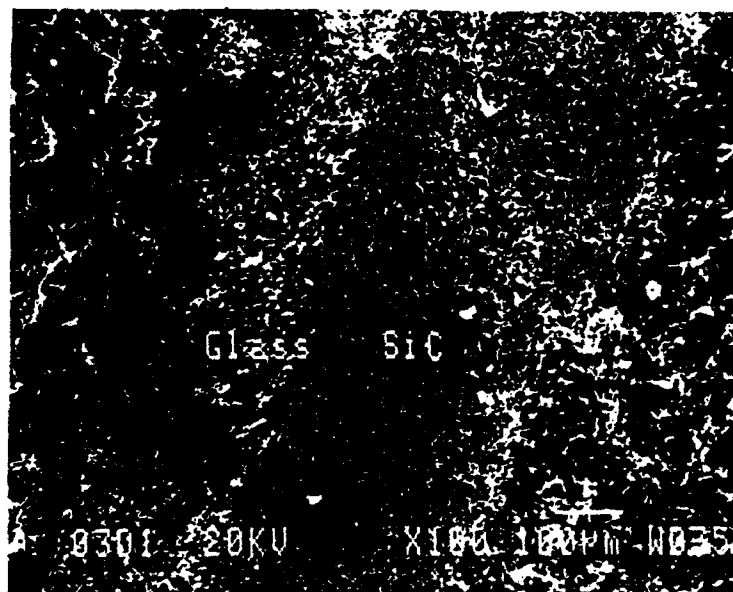
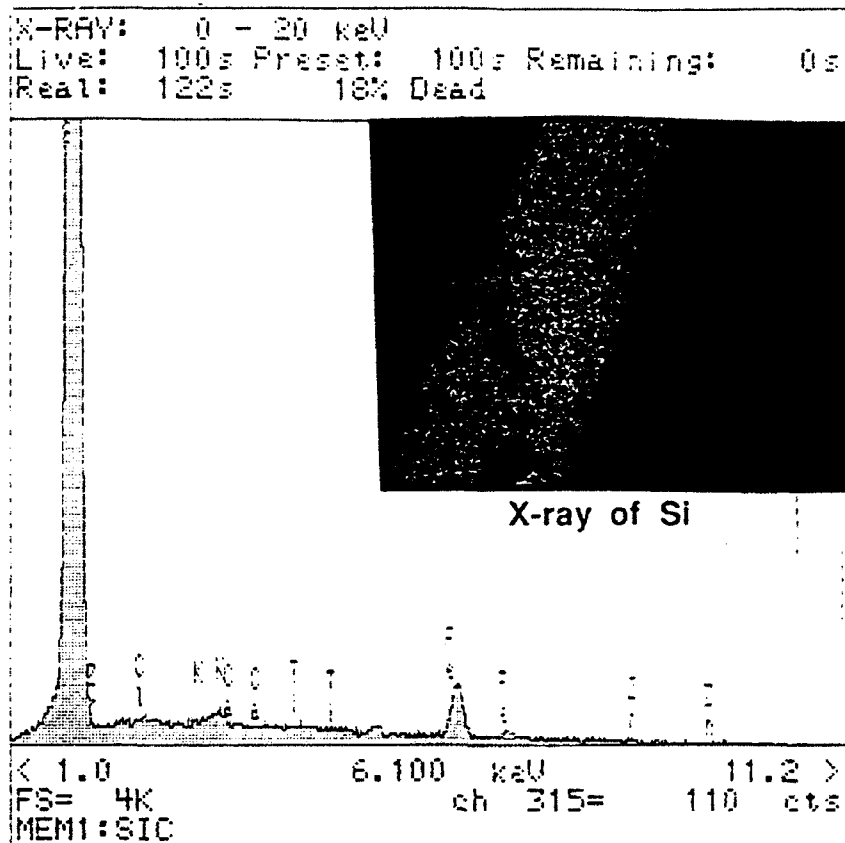
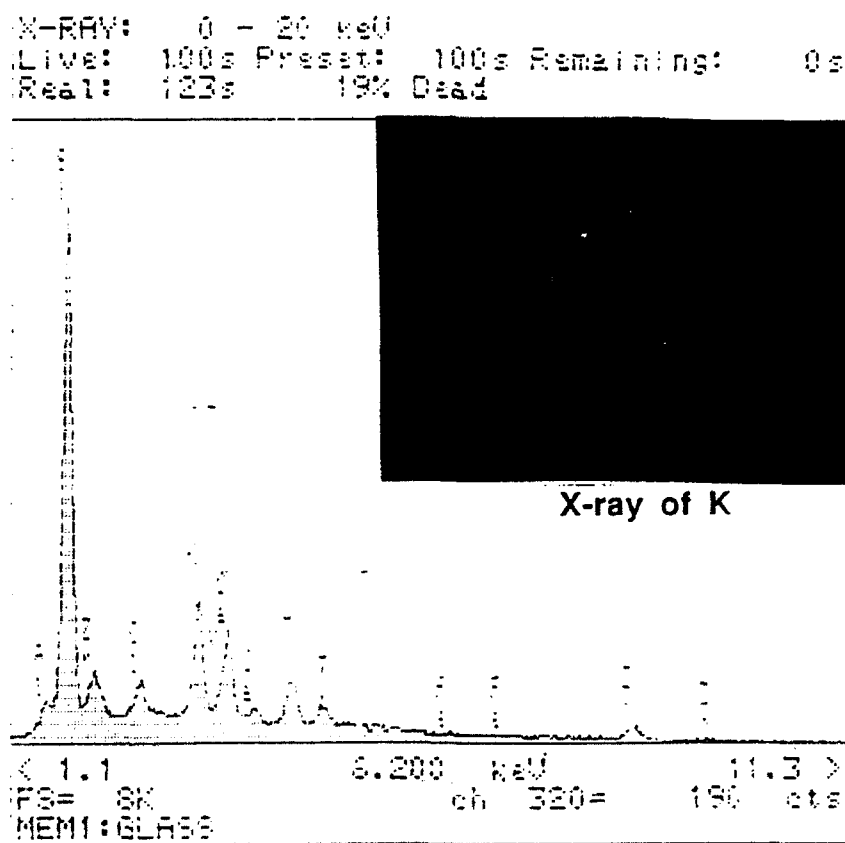


Fig 11



a



b

Fig 12

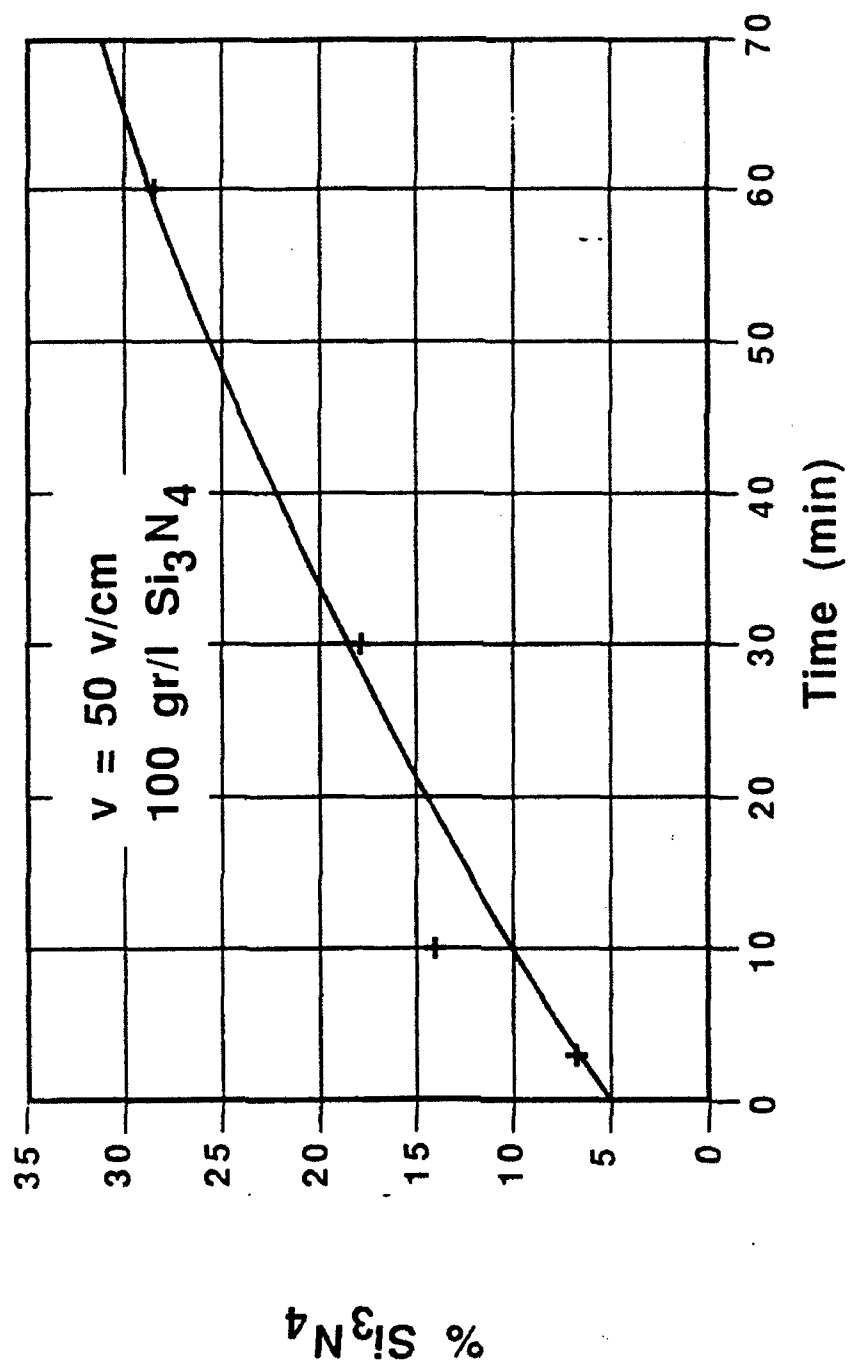


Fig 13

**SINGLE AND MULTILAYER ELECTROPHORETIC DEPOSITION
AND PENETRATION OF LOW-EXPANSION CERAMICS ON
POROUS SUBSTRATES**

L. Gal-Or, S. Liubovich

**Institute of Metals - Technion, Israel Institute
of Technology**

ABSTRACT

Previous electrophoretic deposition and penetration studies were further extended to the deposition of a low expansion ceramic material - Al_2TiO_5 - on porous graphite and to multilayer deposition. It was found that the penetration of Al_2TiO_5 into the pores is higher in water than in propanol. However, maximum penetration is obtained in a 20% mixture of propanol in water probably due to enhanced wetting of the graphite surface. The surface deposition is both more efficient and morphologically better in propanol. Thus, for optimal average and penetration a two stage process should be employed.

The feasibility of subsequent deposition of two different layers of materials with zeta potentials of the same polarity was shown for deposition of Si_3N_4 on Al_2TiO_5 (cathodic deposits) and of SiC on a glass ceramic layer (anodic deposits). Crosssections of the two layers in the order of hundreds of microns were prepared and elemental analysis and x-ray images are shown.

INTRODUCTION

Basic principles and parameters of electrophoretic deposition of ceramic particles in the pores of a conductive porous substrate, were described in two previous publications [1,2].

These reports summarized studies of deposition of colloidal SiO_2 from aqueous and nonaqueous suspensions on porous graphite. It was shown, experimentally [1], that penetration is enhanced by a high ratio of dielectric constant to viscosity of the solvent as well as by increased particle concentration and electric field. At optimal conditions the whole crosssection of the porous graphite substrate was penetrated and a skeleton of SiO_2 with the same shape and dimensions as the original graphite specimen was obtained after burning off of the graphite. A theoretical analysis [2] of the penetration enables to predict the penetration depth as function of two non-dimensional parameters, the Peclet number (Pe) and the deposition rate (λ).

Large Pe and low λ enhance the penetration. In addition to the above mentioned results the feasibility of deposition of a variety of other oxide and non oxide ceramic materials (fused SiO_2 , SiC , SiN) was demonstrated.

The present report is an extension of these studies concentrating on the following two aspects:

- Surface deposition and penetration of a low expansion ceramic material - Al_2TiO_5 - aluminium titanate on porous graphite.
- Multilayer electrophoretic deposition which includes deposition of two consecutive layers of different composition: Al_2TiO_5 and Si_3N_4 as well as a glass ceramic and SiC .

The interest in the low expansion ceramic and the multilayer deposits stems from the intention to apply electrophoretic deposition for the coverage and impregnation of carbon-carbon composites with ceramic materials so as to prevent oxidation at elevated temperatures. Carbon-carbon (C-C) composites are of great interest for aerospace applications since they exhibit excellent high-temperature mechanical stability and low weight. However, they are characterized by a residual porosity and low oxidation resistance in air at temperatures above 500°C [3-5]. Another feature of these composites is their low thermal expansion coefficient ($1-3 \times 10^{-6}/^\circ\text{C}$). The ceramic protective coating should therefore be characterized

by a low expansion coefficient so as to prevent its cracking during use.

$\text{Al}_2\text{O}_3 \cdot \text{TiO}_2$ (Al_2TiO_5) has one of the lowest thermal expansion coefficients as seen in Fig. 1 [6]. Therefore, it is a plausible candidate for the application mentioned above. However, the expansion of this material is anisotropic and therefore microcracking will occur when applied as a coating [7]. The detrimental effect of the microcracking on the oxidation protection can be remedied by another coating deposited on the Al_2TiO_5 such as Si_3N_4 .

In addition to the practical interest described above the study of sequential electrophoretic deposition of different ceramic materials is of interest for understanding the process and widening its scope. Thus another system (glass ceramic and SiC) was also deposited.

EXPERIMENTAL PROCEDURE

The deposition and impregnation were performed on porous graphite - UCAR grade 45 with a 48% volume porosity and an average pore size of 60μ . (The porous graphite serves as a model material for the C-C composite). The specimens were $20 \times 20 \times 7$ mm. The ceramic materials deposited were:

- Al_2TiO_5 prepared at the Israel Ceramics Institute with 5% BaCO_3 added for sintering enhancement. After attrition milling the average particle size was 1.42μ .
- Si_3N_4 - 0.5μ .
- SiC - 600 mesh ($<40\mu$)
- glass ceramic, Ferro-Electronic Grade, 1μ average size

Suspensions of the ceramic materials in water, isopropanol and mixtures of the two solvents were prepared, followed by wet milling for 3 hrs in a ball mill.

The graphite specimens were cleaned ultrasonically in ethanol for 4 min and then dried at 200°C for 30 min.

Deposition was carried out at constant voltage in an experimental set-up described in [1]. The electric field was in the range of 5-300 V/cm, the deposition time 30 sec - 60 min and particle concentration was 30, 100 and 250 gr/l.

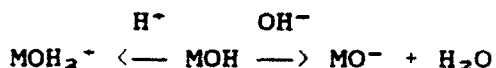
For quantitative determination of deposited material, specimens were weighted after drying in air for 24 hrs to 0.1 mg. For determination of impregnated material the external deposit was removed with a gentle brush prior to the weighing of the specimen. The morphology and composition of the deposit were studied by optical and electron microscopy with a JEOL 840 SEM.

For study of crosssections the coated specimens were first impregnated with an Epofix (Struers) resin and cured for 10 hrs at room temp. Then the crosssection was prepared by cutting with a lathe at 800 rpm.

RESULTS AND DISCUSSION

a) Aluminium Titanate Deposition

Preliminary experiments of Al_2TiO_5 deposition both from water and isopropanol showed that the particles are deposited on the cathode as opposed to SiO_2 which deposits on the anode. The surface charge of oxides forms by the adsorption of protons or hydroxyls to hydroxyl groups existing on the oxide surface and which act as amphoteric sites:



The surface charge, ζ , is given by:

$$\zeta = e(V_+ - V_-) \text{ where}$$

e - electronic charge

V_+ - numbers of positive sites per unit area

V_- - numbers of negative sites

At a pH lower than the isoelectric point (i.e.p., the point at which the zeta potential is zero) the surface charge is usually positive and at a higher pH the charge is negative.

The deposition of Al_2TiO_5 on the cathode indicates that the particles are positively charged and that the isoelectric point is at a relatively high pH. The pH of the suspension of Al_2TiO_5 in water was measured as 8.1 and that in isopropanol as 6.2. From literature [8] it is known that the isoelectric point of SiO_2 is at pH=2.5 and that

of Al_2O_3 is at $\text{pH}=9.1$. The i.e.p. of Al_2TiO_5 is probably similar to that of Al_2O_3 and this explains the difference in polarity of SiO_2 and Al_2TiO_5 .

From previous studies [1,2] we know that particle penetration is enhanced by higher Pe numbers:

$$\text{Pe} = \frac{U^1 b}{D} = \frac{(U^1 + U^u) b}{D} \quad \lambda = \frac{k b}{D} \quad \text{where}$$

U^1 - electrophoretic velocity

U^u - electroosmotic velocity

b - mean pore radius

D - diffusion coefficient

k - local deposition rate

The electrophoretic velocity $u^1 = \epsilon pE/4\pi\eta$.

Therefore in solvents with a higher ratio of ϵ/η the penetration is enhanced. For water this ratio is 81/1 while for ipropanol it is 18.3/2. As expected, the amount of Al_2TiO_5 that penetrated into the porous graphite in water is higher than that in ipropanol. However, when mixtures of H_2O and ipropanol are considered a maximal penetration is obtained at a *20% concentration of ipropanol in water (Fig. 2). Fig. 2 describes the amount of Al_2TiO_5 (expressed in percentage of specimen weight) as function of ipropanol concentration in H_2O at a field strength of 75 V/cm after 60 min in a suspension of 30 g/l of Al_2TiO_5 . The maximum at 20% ipropanol is explained by better wetting of the graphite as compared to pure H_2O as was demonstrated in primitive wetting experiments performed in different H_2O : ipropanol solutions. The surface deposition, however, is both higher and morphologically better in ipropanol. This can be explained by the lower fraction of penetrated material as well as by lower parallel H_2 formation on the cathode during deposition from the nonaqueous solvent.

From these experiments it may be concluded that optimization of coverage and penetration of a porous substrate by electrophoretic deposition, as described in Fig. 3, should be performed in two stages. Impregnation of the substrate in an aqueous suspension with 20% ipropanol and coating in a suspension of ipropanol.

The mechanism of deposition is based on the formation of OH^- by a cathodic reduction of NO_3^- and O_2 and its subsequent reaction with Al^{3+} and ZrO_2^{2-} to form $\text{Al}(\text{OH})_3$ and $\text{Zr}(\text{OH})_4$.

The as-deposited coatings are amorphous and after a heat-treatment at 1200°C for 1 hr became crystalline exhibiting phases of $\alpha\text{Al}_2\text{O}_3$ and tetragonal ZrO_2 . It was shown that the atomic ratio of Al/Zr in the deposit can be varied by varying this ratio in the solution. The $\text{Al}(\text{OH})_3$ is, however, preferentially deposited probably due to the higher diffusion coefficient of Al^{3+} as compared to that of ZrO_2^{2-} .

An improvement of coating morphology and maximum thickness was obtained by applying a pulsed current for deposition. This effect can be explained by the creation of new nucleation sites for deposit formation during current intermission decreasing thus the cluster size.

During deposition of Al_2O_3 the cell voltage rises steeply as a result of the build-up of the hydroxide with a high ohmic resistance. At a certain stage further growth of the deposit is enabled by local breakdown of the film creating new sites of reduction. A more gradual rise in cell voltage takes place when Al_2O_3 and ZrO_2 are co-deposited indicating a change in the dielectric properties of the co-deposit.

The theoretical analysis shows that deep electrophoretic penetration (more than hundred pore diameters) can be achieved only for small Damkohler numbers λ ($\lambda < 0.2$) and for high Peclet numbers ($\text{Pe} > 10$) where:

$$\lambda = \frac{kb}{D} \quad \text{Pe} = \frac{U_{\infty}xb}{D}$$

k - local deposition rate;

b - mean pore radius;

D - diffusion coefficient;

U_w - electroosmotic velocity adjacent to the pore wall.

The dispersion around the mean penetration depth is large for small Damkohler numbers and grows almost linearly with Peclet number. Thus, an almost even spread can be achieved for the same values which will bring about deep penetration. This result is a very favorable outcome for electrophoretic coating methods.

Comparison with the results we obtained for the open pore structure of the substrate reveals that penetration depths for closed pores is smaller whereas dispersion in the latter is larger provided electroosmosis exists.

REPORT DOCUMENTATION PAGE			Form Approved OMB No. 0704-0188	
<small>Public reporting burden for this collection of information is estimated to average 1 hour per response, including the time for reviewing instructions, searching existing data sources, gathering and maintaining the data needed, and completing and reviewing the collection of information. Send comments regarding this burden estimate or any other aspect of this collection of information, including suggestions for reducing this burden, to Washington Headquarters Services, Directorate for Information Operations and Reports, 1215 Jefferson Davis Highway, Suite 1204, Arlington, VA 22202-4302, and to the Office of Management and Budget, Paperwork Reduction Project (0704-0188), Washington, DC 20503.</small>				
1. AGENCY USE ONLY (Leave blank)		2. REPORT DATE August 30, 1990	3. REPORT TYPE AND DATES COVERED Annual Report 1 July/89-30 June/90	
4. TITLE AND SUBTITLE Electrophoretic and Electrolytic Deposition of Ceramic Particles on Porous Substrates			5. FUNDING NUMBERS AFOSR-89-0474	
6. AUTHOR(S) L. Gal-Or, S. Haber, S. Liubovich				
7. PERFORMING ORGANIZATION NAME(S) AND ADDRESS(ES) Technion Research and Development Foundation Technion City, Haifa 32000, Israel			8. PERFORMING ORGANIZATION REPORT NUMBER	
9. SPONSORING / MONITORING AGENCY NAME(S) AND ADDRESS(ES) -BOARD 223/231 Old Marylebone Rd. London NW1 5TH UK -AFOSR/NE, Dr. L. Schioler, Bolling AFB DC 20332-6448			10. SPONSORING / MONITORING AGENCY REPORT NUMBER	
11. SUPPLEMENTARY NOTES				
12a. DISTRIBUTION / AVAILABILITY STATEMENT Unlimited			12b. DISTRIBUTION CODE	
13. ABSTRACT (Maximum 200 words) Electrophoretic deposition of ceramic particles on porous graphite and their penetration into the pores was demonstrated and studied both theoretically and experimentally. The theoretical analysis enables to predict the penetration depth of the particles as function of two non-dimensional parameters based on solvent properties, field strength and particle size and concentration. In the experimental studies the amount of induced material was found to increase with the ratio of dielectric constant to viscosity of the solvent, as well as with particle concentration and field intensity. However, due to simultaneous buildup of an overlying deposit penetration as function of deposition time reaches a plateau. In parallel studies on electrolytic deposition, ZrO ₂ coatings were deposited on porous graphite from an aqueous solution of ZrO(NO ₃) ₂ . The deposition kinetics and microstructure of the deposit were studied. The initial amorphous deposits transformed into crystalline ZrO ₂ polymorphs with nanocrystalline dimensions following heat treatment.				
14. SUBJECT TERMS Electrophoresis, Ceramics, Penetration, Electrolytic Deposition, Zirconia			15. NUMBER OF PAGES	
			16. PRICE CODE	
17. SECURITY CLASSIFICATION OF REPORT Unclassified	18. SECURITY CLASSIFICATION OF THIS PAGE Unclassified	19. SECURITY CLASSIFICATION OF ABSTRACT Unclassified	20. LIMITATION OF ABSTRACT Unlimited	

Electrophoretic and Electrolytic Deposition of Ceramic Particles on Porous Substrates

L. Gal-Or, S. Haber, S. Liubovich

Summary of Annual Report

1 July/89 ~ 30 June/90

Introduction

The present phase of the research project concentrated on quantitative evaluation of the ceramic particles induced into the porous substrate as a function of deposition and solvent parameters. This evaluation was carried out both experimentally and theoretically based on an analytical model for deep electrophoretic penetration of particles into porous substrates. In parallel to the electrophoretic studies, the electrolytic deposition of ceramic coatings from aqueous solutions was studied from the electrochemical and microstructural aspects. The four enclosed manuscripts describe in detail the above mentioned studies. Following, therefore, is a concise description of the studies and their results.

Experimental

The experimental studies were carried out on porous graphite substrates - UCAR Grade 45. This substrate has a 48% volume porosity with an average pore size of 60μ . The ceramic particles deposited and induced by electrophoresis were submicron colloidal SiO_2 (Pyrogenic Aerosil) with a specific area of $450 \text{ m}^2/\text{g}$. The concentrations of the ceramic material in the solvent were 3, 13 and 30 g/l . The solvents in most experiments were water and isopropanol. For the study of the effect of solvent properties on penetration ethanol and pentanol were also used. The field intensity was varied between $0\text{--}300\text{v/cm}$ and the deposition time between $5\text{--}120 \text{ min}$.

For quantitative determination of the impregnated SiO_2 , the weight change of the specimen was recorded, after removal of the external deposit. The amount of induced SiO_2 was also determined, in some cases, by weighing the residue after burn-off of the graphite at 900°C for 20 hrs.

The electrolytic deposition studies concentrated on the deposition of ZrO_2 from a $0.1\text{M ZrO}(\text{NO}_3)_2 \cdot n\text{H}_2\text{O}$ aqueous solution. The deposits were obtained at current densities ranging from $15\text{--}100\text{ mA/cm}^2$ and durations of $10\text{--}60\text{ min}$. For kinetic studies the coating weights were determined with an accuracy of 0.05 mg . During deposition the variation of cell voltage, pH and temperature of the solution were measured.

The microstructure of the ZrO_2 coatings was characterized by optical and scanning electron microscopy and the phase content was determined by X-ray diffraction. The microstructural studies were carried out on deposits that were fired at $400, 600$ and 900°C for 1 hr .

Theoretical

The theoretical analysis, at this stage, relates to a single particle travelling in a pore described as a long circular tube of mean pore diameter. Three driving mechanisms are considered: the hydrodynamic drag force exerted on the particle due to the electroosmotic flow of the solvent inside the pore, the electrophoretic force exerted on the particle and the stochastic Brownian force due to thermal fluctuations of the solvent molecules.

Summary of Results

In addition to the formation of surface deposits, electrophoretic induction of ceramic particles into the porous substrate was demonstrated.

It was found that solvent properties such as the ratio between the dielectric constant and the viscosity (ϵ/η) have a significant effect on penetration. Thus the amount of induced SiO_2 is ten times larger for water ($\epsilon/\eta = 81$) than for pentanol ($\epsilon/\eta = 420$). Penetration increases with particle concentration and with deposition time. However, a plateau is reached for the dependence of induced SiO_2 on deposition time due to the build-up of an external coating. Thus the extent of penetration could be enhanced if the external deposit were constantly removed or prevented. An optimal field strength exists for particle penetration due to its dual effect. Increase in field strength increases the particle velocity but it also enhances the build-up of the external deposit which blocks penetration.

The theoretical analysis enables to predict the penetration depth of a ceramic particle inside the porous substrate under the influence of the electric potential gradient. It also enabled to derive the non-dimensional

parameters that affect the particle motion. It was thus deduced that the parameters which affect most the particle penetration are the Peclet number (Pe) and the deposition rate (λ):

$$Pe = \frac{Ub}{D} = \left(\frac{U' + U''}{D} \right) b$$

$$\lambda = \frac{kb}{D}$$

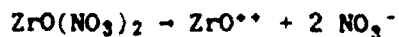
where:

- U' - electrophoretic velocity
- U'' - electroosmotic velocity
- b - pore mean radius
- D - diffusion coefficient
- k - local deposition rate

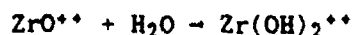
Large Peclet numbers and small deposition rates enhance penetration. Thus, deep penetration (over hundred pore diameters) can be achieved for very low deposition rates ($\lambda < 0.1$) and for very high Peclet numbers ($Pe > 100$). Deepest penetration is obtained for $\lambda = 0$ which can be achieved if a repelling force between particles and pore walls would exist. Electroosmosis increases the Peclet number and thus penetration. The diffusion coefficient of the particle has a dual effect: its decrease increases the Peclet number, but it also increases the deposition rate. The theoretical analysis also indicates how the penetration can be controlled by selection of solvent properties, particle size and concentration and electric field strength.

The electrolytic deposition of ZrO_2 is obtained through the following reactions:

- a) dissociation of the zirconyl salt:



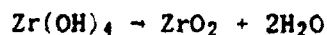
- b) hydrolysis of the zirconyl ion:



- c) interaction of the hydrated cation with OH^- ions generated at the cathode by reduction reactions described further on:



- d) dehydration of the hydroxide:



Several cathodic reactions are possible; however, the cathodic polarization curve indicates that the reduction of NO_3^- is the predominant OH^- producing reaction. The rate of deposit formation increases with current density the dependence reflecting the rate of OH^- generation. Faradaic efficiencies of 40-80% only were obtained attributable to reduction reactions that do not produce OH^- (such as reduction of H^+) as well as to the formation of the hydroxide at sites removed from the substrate. Cell voltage and solution temperature increase as the coating process progresses. This is due to the formation of the deposit characterized by a high electric resistance.

The initial coating is a Zirconium hydroxide gel with an amorphous character. Microcracks develop in the coating during drying due to tensile stresses associated with non-uniform contraction. Firing of the coating led to its crystallization into fine, equiaxed submicron particles of monoclinic and tetragonal polymorphs of zirconia. Calculation of crystallite sizes by reflection broadening, indicated them to be 2 nm after treatment at 400°C and 12 nm when fired at 600°C for 1 hr. Under these conditions the polymorphs were undistinguishable. Firing for 1 hr at 900°C resulted in distinct crystallites of both phases, 20-25 nm in size. The volume fractions were 15% and 85% for the tetragonal and monoclinic phases respectively.

Future electrophoretic studies will include further optimization of penetration by inhibition of surface deposition. One approach will be the application of a low cathodic bias voltage to the specimen.

Following the derivation of optimal process conditions for penetration, experiments with lower expansion ceramics such as HfTiO_4 will be performed.

Further studies on the electrolytic deposition will concentrate on prevention of cracking of the surface deposit during drying and study and optimization of in-pore deposition.

ELECTROLYTIC DEPOSITION OF ALUMINA AND CODEPOSITION OF ALUMINA-ZIRCONIA

L. Gal-Or, A. Sharon

Institute of Metals, Technion - Israel Institute
of Technology

ABSTRACT

Al_2O_3 and $\text{Al}_2\text{O}_3+\text{ZrO}_2$ coatings were deposited on graphite from aqueous solutions containing $\text{Al}(\text{NO}_3)_3$ and $\text{Al}(\text{NO}_3)_3+\text{ZrO}(\text{NO}_3)_2$ salts. The probable mechanism of deposit formation is based on the generation of OH^- by cathodic reduction of NO_3^- and O_2 and its subsequent reaction with Al^{+3} and ZrO^{2+} to form $\text{Al}(\text{OH})_3$ and $\text{Zr}(\text{OH})_4$. Dehydration of the latter compounds results in the formation of Al_2O_3 and ZrO_2 .

Deposition at constant current results in an increase of cell voltage due to ohmic resistance of the deposit. After an initial steep rise in the voltage the slope decreases significantly in spite of further increase in deposit weight. The latter phenomenon is explained by local breakdown of the deposit creating sites of reduction which enable the deposition to proceed.

The co-deposition of $\text{Al}_2\text{O}_3+\text{ZrO}_2$ was demonstrated and it was shown that the ratio of Al/Zr in the deposit varied with the same ratio in the solution.

Deposit weight, phase content and morphology as function of deposition parameters were studied.

INTRODUCTION

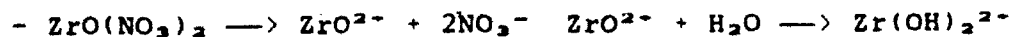
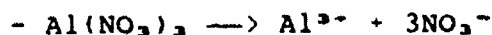
The formation of ceramic coatings by an electrolytic process has been first demonstrated by Switzer for CeO_2 (1,2). The deposition of ZrO_2 from an aqueous zirconyl nitrate solution was studied in detail from the electrochemical (3) and microstructural aspects (4). A two-step mechanism was suggested for the ZrO_2 formation: generation of hydroxyl (OH^-) ions on the cathodic substrate by reduction of NO_3^- and dissolved O_2 and the reaction of the hydroxyl ions with the zirconyl cation to form Zr(OH)_4 , which decomposes upon drying to form ZrO_2 .

Based on the above mentioned concept of oxide formation, the deposition of other insoluble oxides and the co-deposition of different oxides was envisaged. The present study describes the deposition of Al_2O_3 from an $\text{Al(NO}_3)_3$ solution and the co-deposition of Al_2O_3 and ZrO_2 from a solution containing both $\text{Al(NO}_3)_3$ and $\text{ZrO(NO}_3)_2$. The sequence of reactions for the co-deposition is expected to be the following:

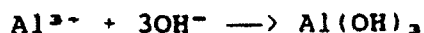
1) Generation of OH^- :



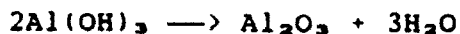
2) Dissociation of the salts:



3) Interaction of hydroxyls with the cations:



4) Dehydration of the hydroxides:



The hydroxides form thus in two successive steps: electrochemical generation of OH^- and a chemical reaction between the cations and the hydroxyls. A schematic description of the co-deposition is given in Fig. 1.

The yield of the deposit depends on the faradaic efficiency of OH^- formation (affected by reduction reactions that do not result in OH^- formation such as $\text{H}^+ + e \longrightarrow \text{H}$ and $\text{H} + \text{H} \longrightarrow \text{H}_2$) and the fraction of hydroxide formed at sites removed from the substrate. The latter parameter depends on the relative diffusion coefficients of OH^- on one hand and that of Al^{3+} and $\text{Zr}(\text{OH})_2^{2+}$ on the other. The ratio of Al_2O_3 and ZrO_2 in the deposit will depend on the relative diffusion coefficients of Al^{3+} and $\text{Zr}(\text{OH})_2^{2+}$ cations which compete for the OH^- ions generated at the cathode, and the solubility constants (K_{sp}) of the two hydroxides formed. A quantitative analysis of the kinetics of deposit formation and its composition will have to take into account all these factors assuming that the diffusion phenomena are the rate determining steps in the hydroxide formation. The present paper describes the effect of electrochemical deposition parameters on the rate, morphology and composition of the Al_2O_3 and $\text{Al}_2\text{O}_3 + \text{ZrO}_2$ deposits.

EXPERIMENTAL

Deposits were obtained on graphite specimens (UCAR45) 2 x 10 x 20 mm. They were polished with a 1000 grit SiC abrasive paper, then rinsed with ethanol in an ultrasonic bath, washed with distilled water and dried in air. Electrolytes were:

0.02M - 0.2M $\text{Al}(\text{NO}_3)_3$ with and without

0.01M - 0.05M $\text{ZrO}(\text{NO}_3)_2$

Deposition was carried out at constant current with a Horizon Model SR-365 d.c. power supply. Two counter anodes made of Pt 14 x 28 mm were used. Cell voltages and currents were measured with AVO meters. A schematic drawing of the experimental set-up is seen in Fig. 2. Current densities were varied in the range of 15-60 mA/cm² and deposition times were in the range of 20 sec - 40 min. Mild stirring was applied with a magnetic stirrer during deposition. Polarization curves were obtained with a PAR Model 270 potentiostat. Deposits were dried in air and their weight determined within an accuracy of 0.05 mg. Some deposits were heat treated at 1200°C for 1 hr in argon. Morphology and microanalysis were studied with a JEOL SEM Model JSM 840. X-ray diffraction was performed with a diffractometer Model PW-1730 operated at 40 KV and 40 mA using Cu k-alpha radiation and scanning speed of 1.2 deg/min.

RESULTS AND DISCUSSION

Cathodic polarization curves in an Al(NO₃)₃ solution and in a solution of Al(NO₃)₃ and ZrO(NO₃)₂ are given in Fig. 3a,b. In both curves a Tafel region is seen (down to -800 mV SCE in the first and -1000 mV SCE in the second solution respectively). A limiting current of ≈10 mA/cm² is seen in both curves setting in at the same potential of -2000 mV SCE. The similarity in the two curves is a result of the same cathodic reaction taking place in both systems with the limiting current being determined by the hydroxide deposit rather than by the concentration of the NO₃⁻ which is higher in the combined solution.

Fig. 4 presents the variation in cell voltage with deposition time for two current densities. At the higher c.d. (25 mA/cm²) the voltage increases steeply for the first 3.5 min as a result of the build-up of the hydroxide deposit and then levels off. Yet, as seen in Fig. 5 for the same c.d., the weight of the deposit continues to rise slowly after 3.5 min.

The cell voltage stability is explained by the formation of local breakdowns in the film creating sites of reduction which enable the deposition process to continue without further significant increase in the cell voltage. The slope of the deposition curve is very high for the first 20 secs (≈ 0.3 mg/cm²/10sec) and then slows down to about 1/10 of that. The change in deposits rate is explained by the fact that at the beginning the whole substrate is conductive and the OH⁻ ions form on the entire surface. As the nonconductive deposit covers the substrate its further build-up depends on the availability of reduction sites created by the deposit breakdown. The behaviour of the voltage/time curve at the lower c.d. (20 mA/cm²) is different, a monotonic increase in voltage takes place for the entire time interval (10 min). The morphology of the Al₂O₃ as-deposited, is seen in Figs. 6a & b. A relatively close-packed deposit consisting of individual clusters is seen in Fig. 6a. A very dense structure of the individual clusters is seen in Fig. 6b. Two kinds of defects are also seen: microcracks that formed during the drying stage due to non-uniform contraction of the wet coating and bubbles attributed to H₂ formation as a result of H⁺ reduction. In preliminary studies (to be published later) with the aim of controlling the drying rate it was shown that the density of cracks can be reduced significantly when the drying rate is lowered.

An attempt to overcome the formation of defects and yet to obtain a thick deposit was made by the use of a pulsed current. Pulses of 2 min duration at 25 cA/cm² were applied with intermissions of 5 sec (see Fig. 7). A relatively smooth increase in voltage up to a much higher voltage than that reached when applying a continuous current (25V vs. ≈ 8 V) was obtained. Accordingly, the deposit was thicker and smoother. This effect can be explained by the possibility of creation of new nucleation sites for deposit formation during the current intermission.

X-ray diffraction patterns of dry as-deposited coatings and deposits fired at 1200°C for 1 hr, according to the

recommendation of (5), are seen in Fig. 8. The as-deposited (dried in air) coating does not show any diffraction pattern except that of the graphite.

Crystallization of the deposit takes place during the heat treatment with the formation of a $\alpha\text{Al}_2\text{O}_3$. The crystallite size, as calculated with the Scherrer equation (6) from the line broadening of the 110 reflection, assuming no strain effects exist due to the substrate, was found to be about 16nm.

Deposition from solutions containing both $\text{Al}(\text{NO}_3)_3$ and $\text{ZrO}(\text{NO}_3)_2$ was carried out at two c.d. (30 and 60 mA/cm² at 14°C. The dependence of cell voltage on deposition time is seen in Fig. 9. A more gradual rise in the voltage takes place in spite of the higher c.d.s when compared with the deposition of Al_2O_3 only (see Fig. 4). A possible explanation is the difference in deposit properties as a result of the presence of $\text{Zr}(\text{OH})_4$. From our previous work (3) it can be inferred that the voltage reached prior to breakdown onset is much higher for $\text{Zr}(\text{OH})_4$, at the same c.d. and so is the deposit weight per unit area. The $\text{Al}(\text{OH})_3$ forms probably a denser film at lower thicknesses and thus is modified when $\text{Zr}(\text{OH})_4$ is codeposited.

The phase structure of a combined deposit was studied after forming at 1200°C for 1 hr. The x-ray diffraction spectrum shows the presence of two phases: tetragonal ZrO_2 and $\alpha\text{Al}_2\text{O}_3$ (Fig. 10). The morphology of the deposit and microanalysis were studied in the SEM by x-ray imaging of Al and Zr and local elemental semiquantitative analyses. Fig. 11-12 shows the x-ray image of Al and Zr in a combined deposit along with the spectrum and semiquantitative results of the Al and Zr content.

The relative concentration of the Al^{3+} and ZrO^{2+} ions in the solution is expected to affect the deposit composition. The latter was therefore studied (in terms of Al/Zr atomic ratios as function of the same ratio in the solution). Fig. 12 shows

this dependence. It is seen that the relative Al concentrations in the deposit is much higher than in the solution, hence the Al(OH)_3 is preferentially deposited. This can be explained by the differences in diffusion coefficients of the two ions Al^{3+} and ZrO_2^{4+} with the Al^{3+} having a higher diffusion rate and, therefore, being more available for the hydroxide formation.

LIST OF FIGURES

- Fig. 1: Schematic description of the co-deposition of $\text{ZrO}_2 + \text{Al}_2\text{O}_3$.
- Fig. 2: Experimental set-up for deposition.
- Fig. 3: Cathodic polarization curves in
 a. 0.05M $\text{ZrO}(\text{NO}_3)_2$
 b. 0.05M $\text{Al}(\text{NO}_3)_3 + 0.05\text{M } \text{ZrO}(\text{NO}_3)_2$
 25°C, 3 mV/sec, vs. SCE.
- Fig. 4: Cell voltage as function of time for two current densities (0.05M $\text{Al}(\text{NO}_3)_3$, 10 min, 25°C).
- Fig. 5: Deposit weight as function of time (0.05M $\text{Al}(\text{NO}_3)_3$, 25 mA/cm², 25°C).
- Fig. 6: Al_2O_3 deposit from 0.05M $\text{Al}(\text{NO}_3)_3$, at 25 mA/cm², 10 min.
 a) X75
 b) X750
- Fig. 7: Voltage/time curves for deposition of Al_2O_3 with pulsed current: 0.05M $\text{Al}(\text{NO}_3)_3$, 25 mA/cm², $t_{\text{on}} = 2$ min toff - 5 sec, 25°C.
- Fig. 8: X-ray diffraction spectra from:
 a) as-deposited Al_2O_3
 b) after firing at 1200°C for 1 hr.
- Fig. 9: Cell voltage as function of time for two current densities for deposit formed from 0.05M $\text{Al}(\text{NO}_3)_3 + 0.05\text{M } \text{ZrO}(\text{NO}_3)_2$ at 14°C, $t = 5$ min c.d. 60 and 30 mA/cm².

Fig. 10: X-ray diffraction pattern of co-deposit.

Fig. 11: X-ray image and local analysis of a deposit formed from a 0.05M $\text{Al}(\text{NO}_3)_3$ +0.05M $\text{Al}(\text{NO}_3)_2$ solution.

Fig. 12: Atomic ratio of Al/Zr in deposit as function of this ratio in solution.

ACKNOWLEDGEMENT

Research sponsored by the Air Force Office of Scientific Research, Air Force Systems Command, U.S.A., under Grant No. 89-0474.

The U.S. Government is authorized to reproduce and distribute reprints for Governmental purposes not withstanding any copyright notation thereon.

BIBLIOGRAPHY

1. J.A. Switzer, Am. Ceram. Soc. Bull. 66, 1521(1987).
2. J.A. Switzer, R.J. Phillips, MRS Symp. Proc. 121, 111(1988).
3. L. Gal-Or, I. Silberman, R. Chaim, Jour. Electrochem. Soc. In press.
4. R. Chaim, I. Silberman, L. Gal-Or, *ibid*.
5. A. Ayrat, J.C. Droguet, Jour. Mat. Res. 4, 970, 1984.
6. B.D. Cullity, "Elements of X-ray Diffraction", p. 254 Addison-Wesley Pub. Co., Reading, Mass., 1978.

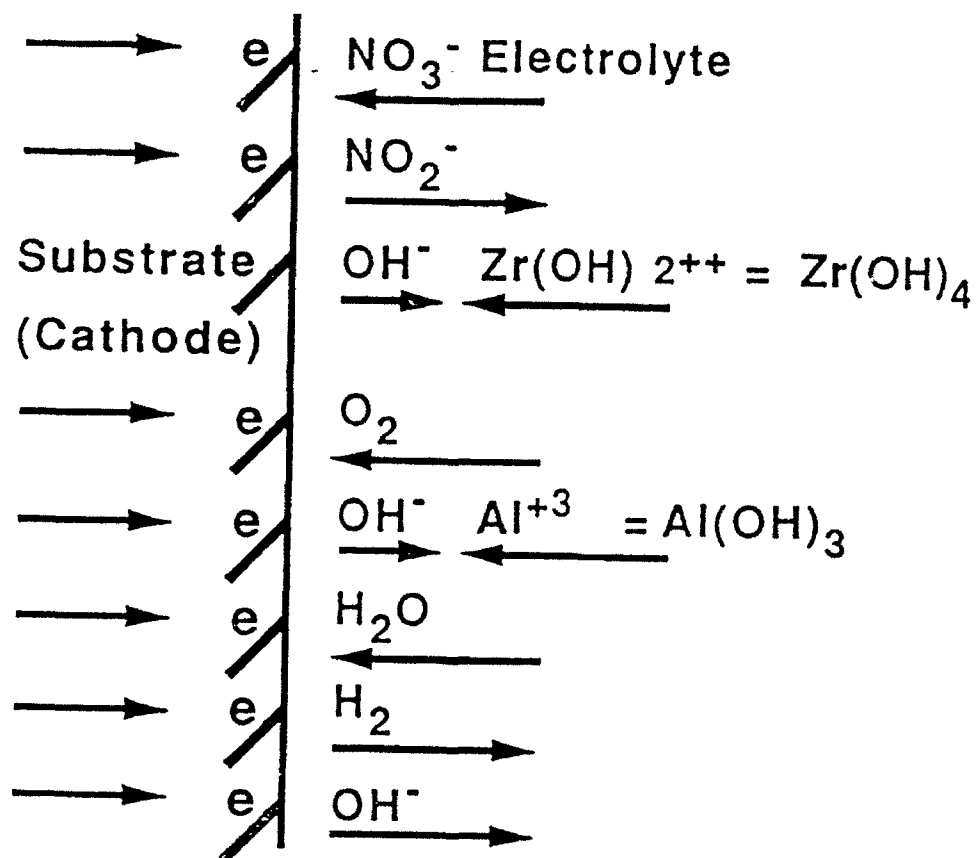


Fig 1

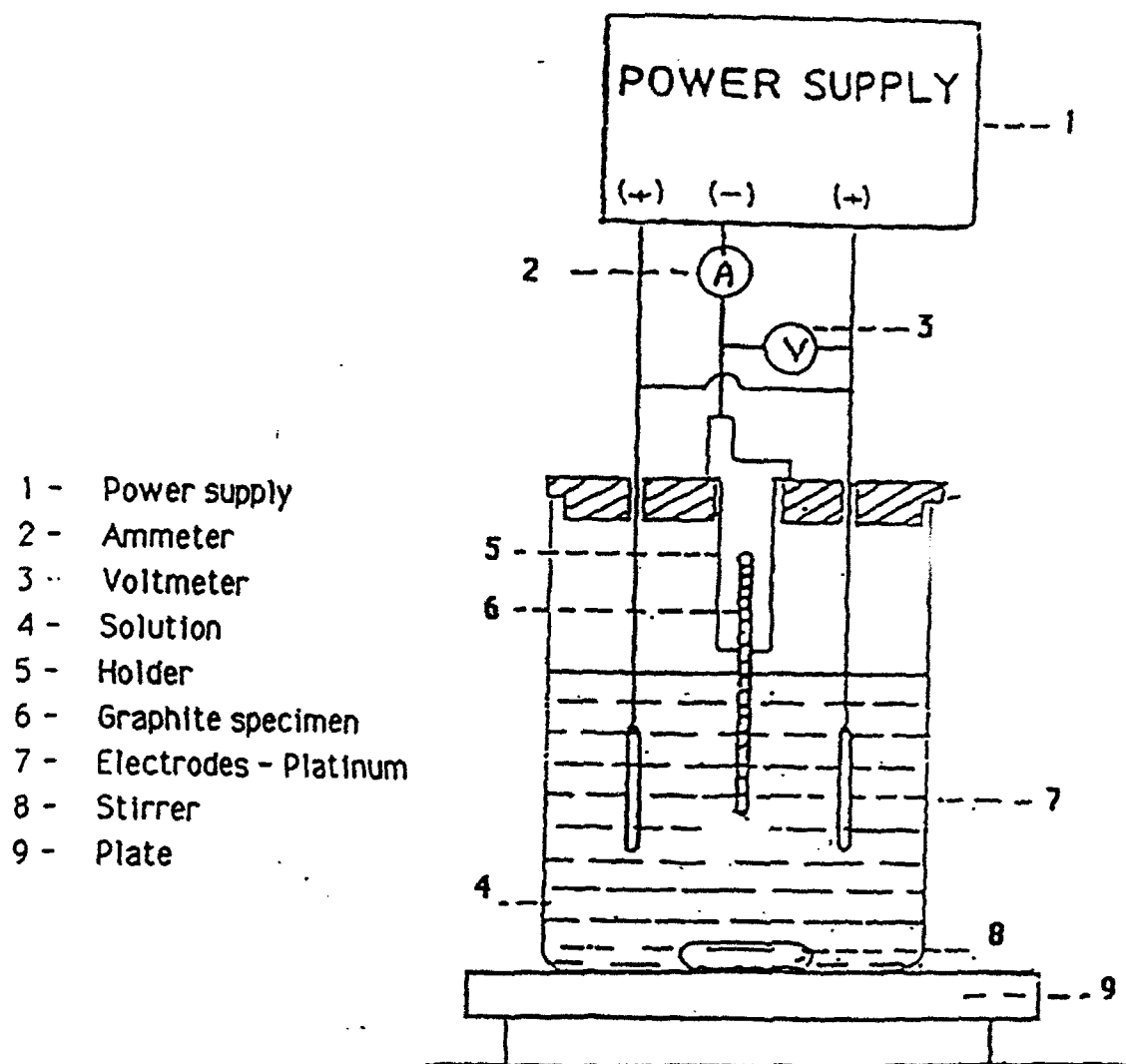


Fig 2: Experimental Set-up For
 Electrolytic Deposition

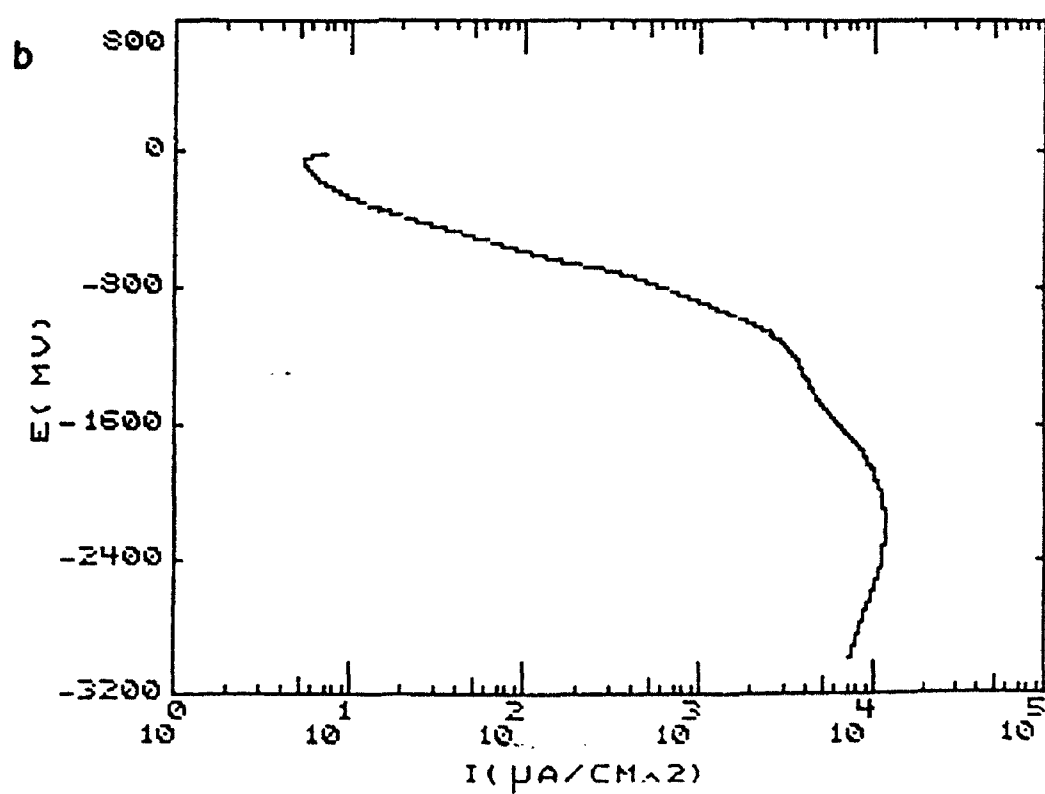
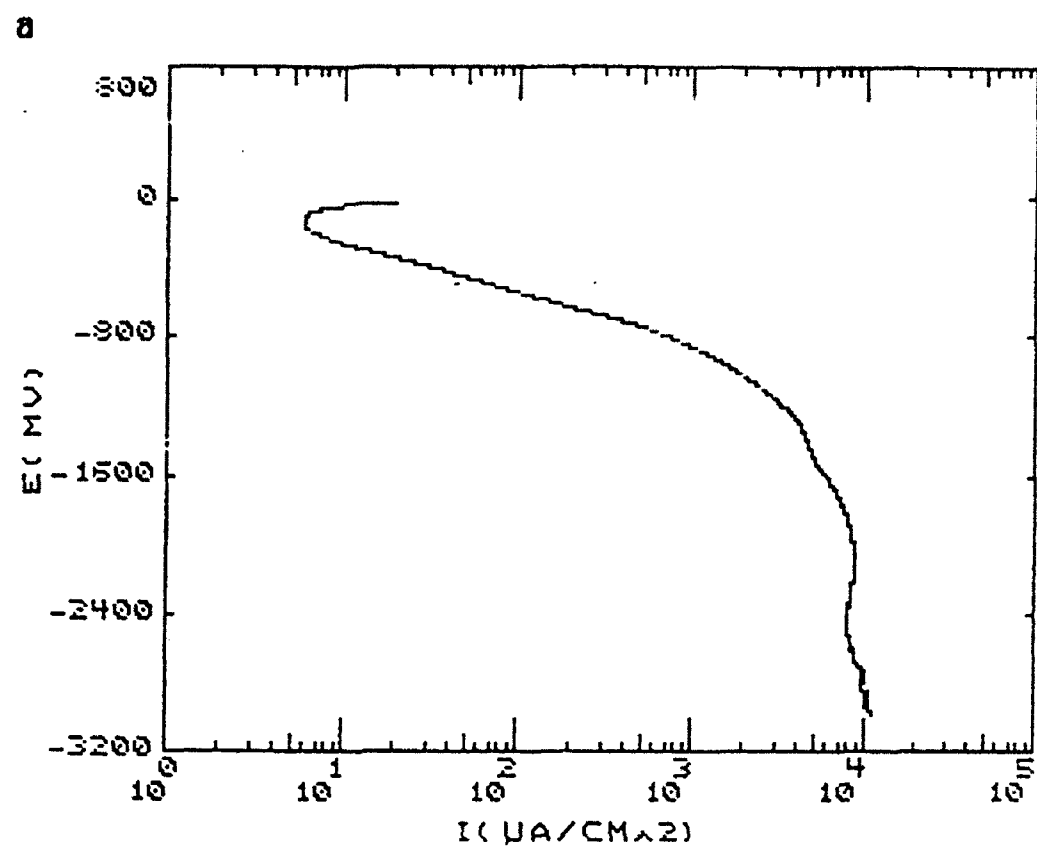


Fig 3

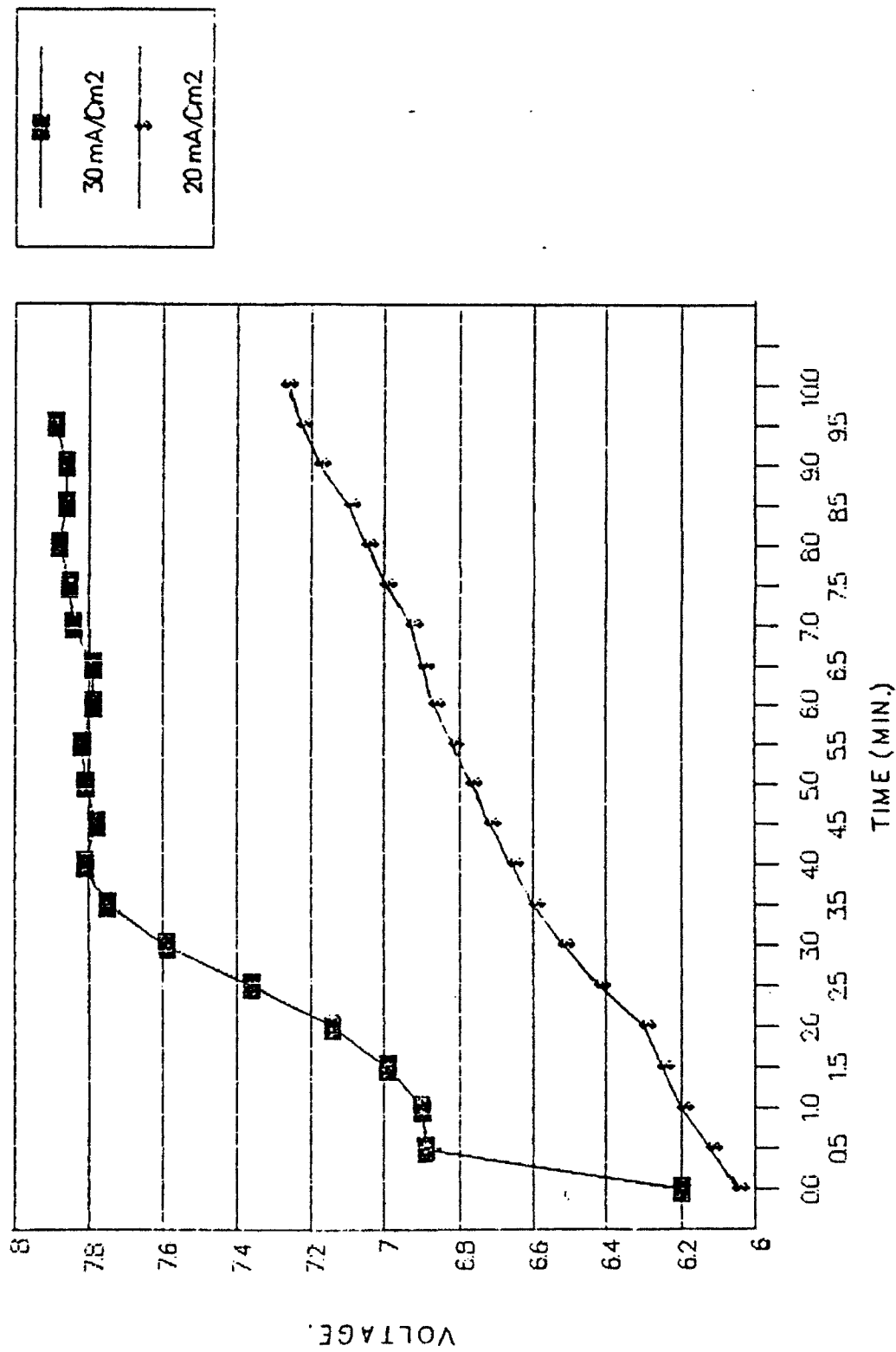


Fig 4

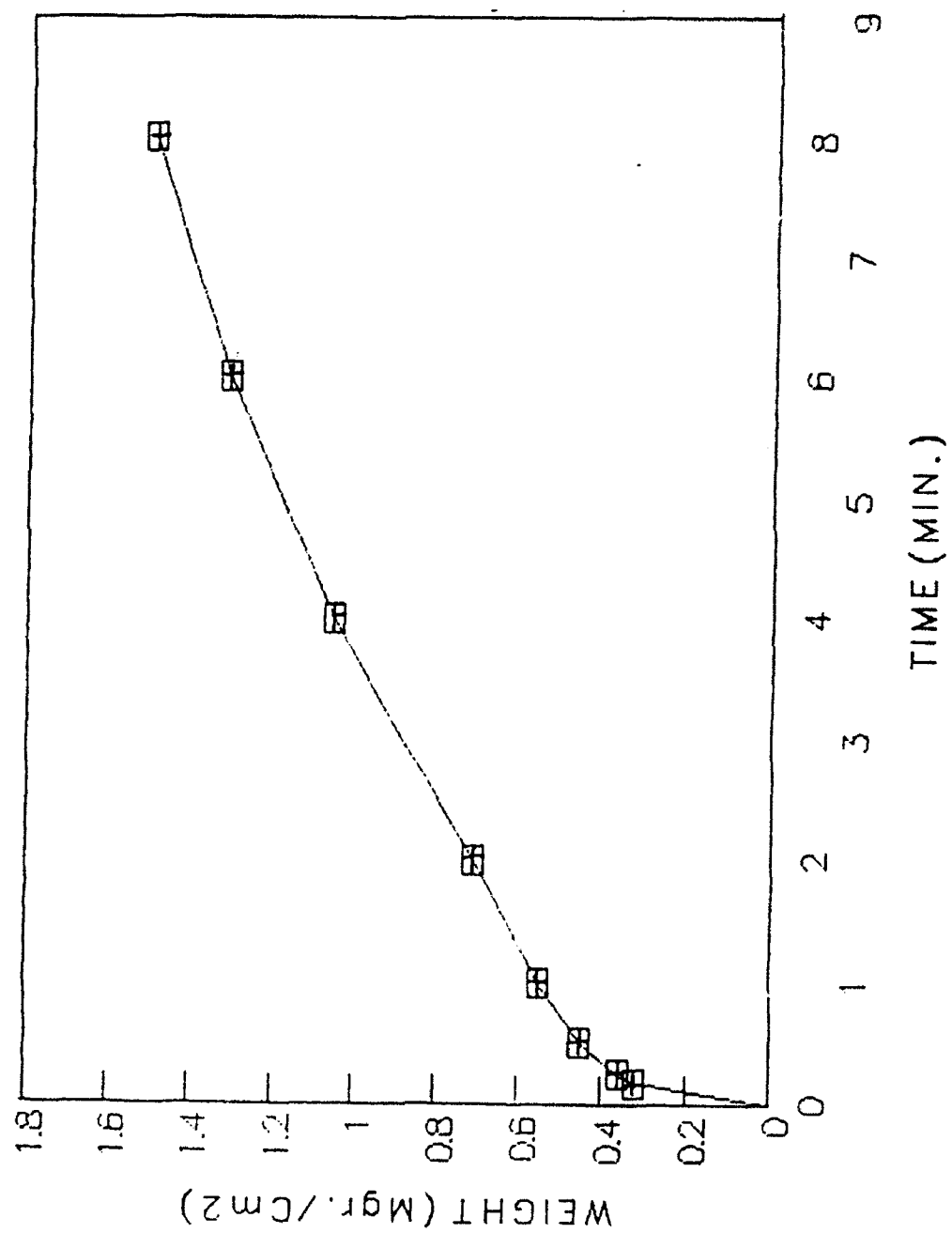


Fig 5



a



b

Fig. 6

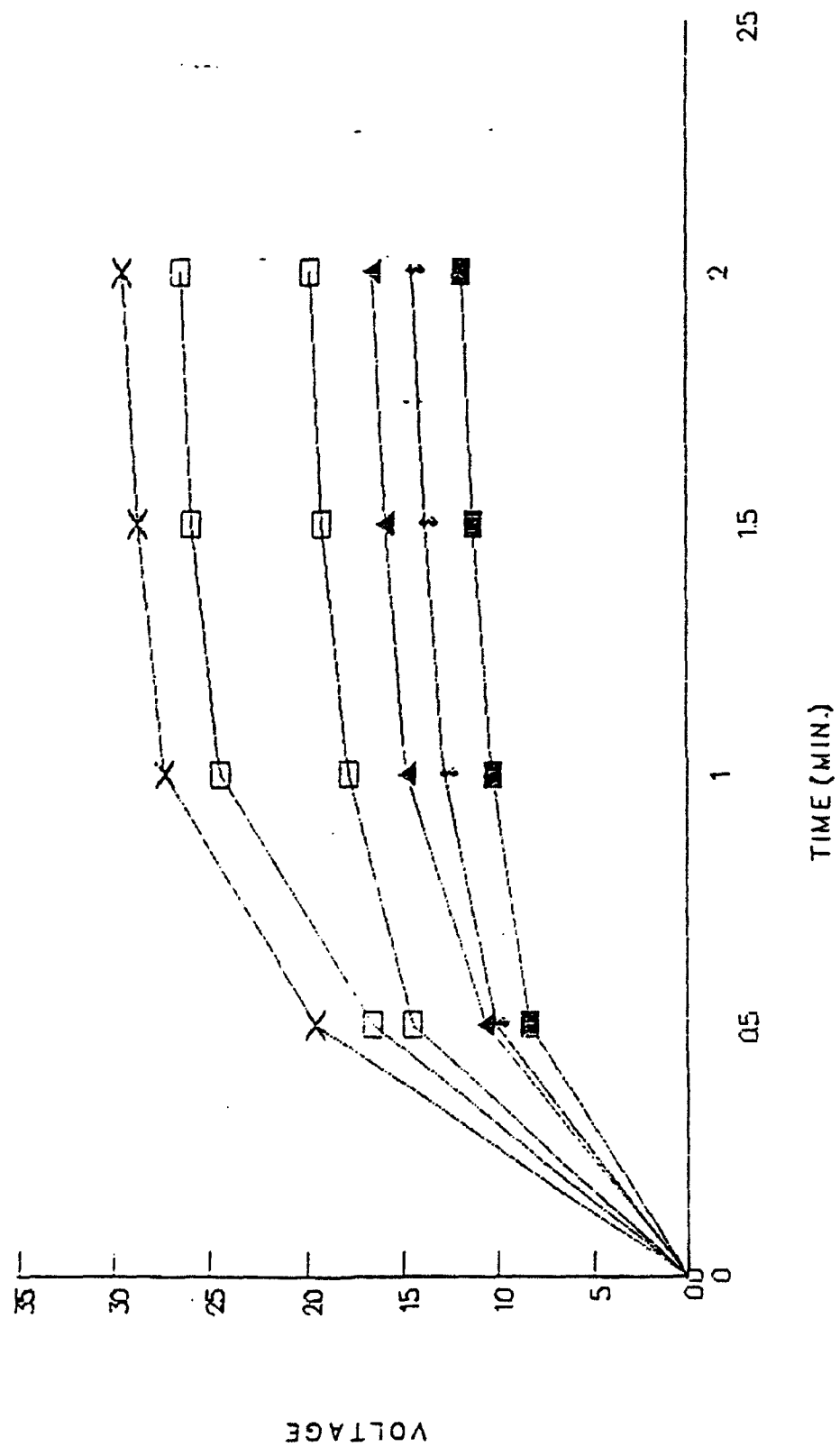


Fig 7

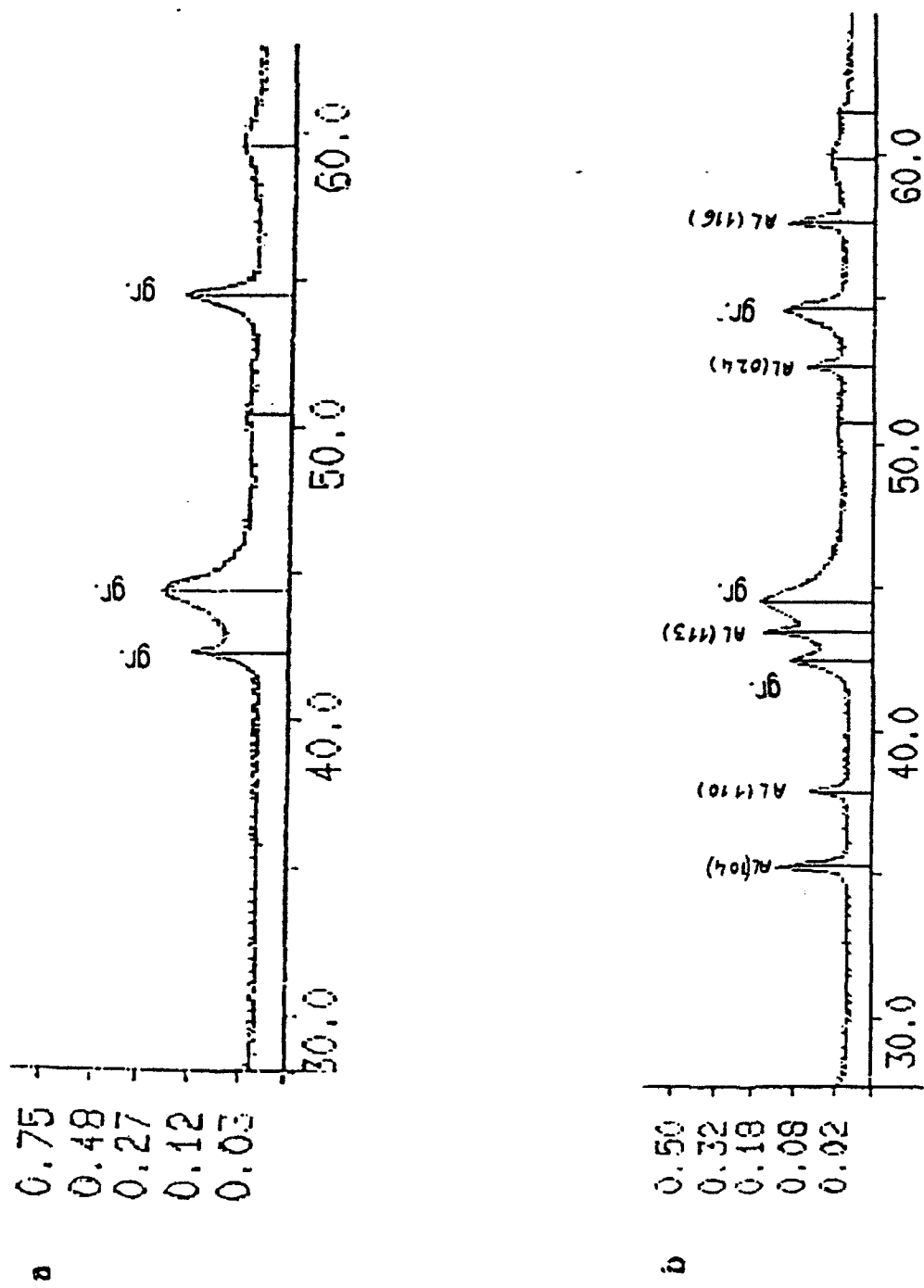
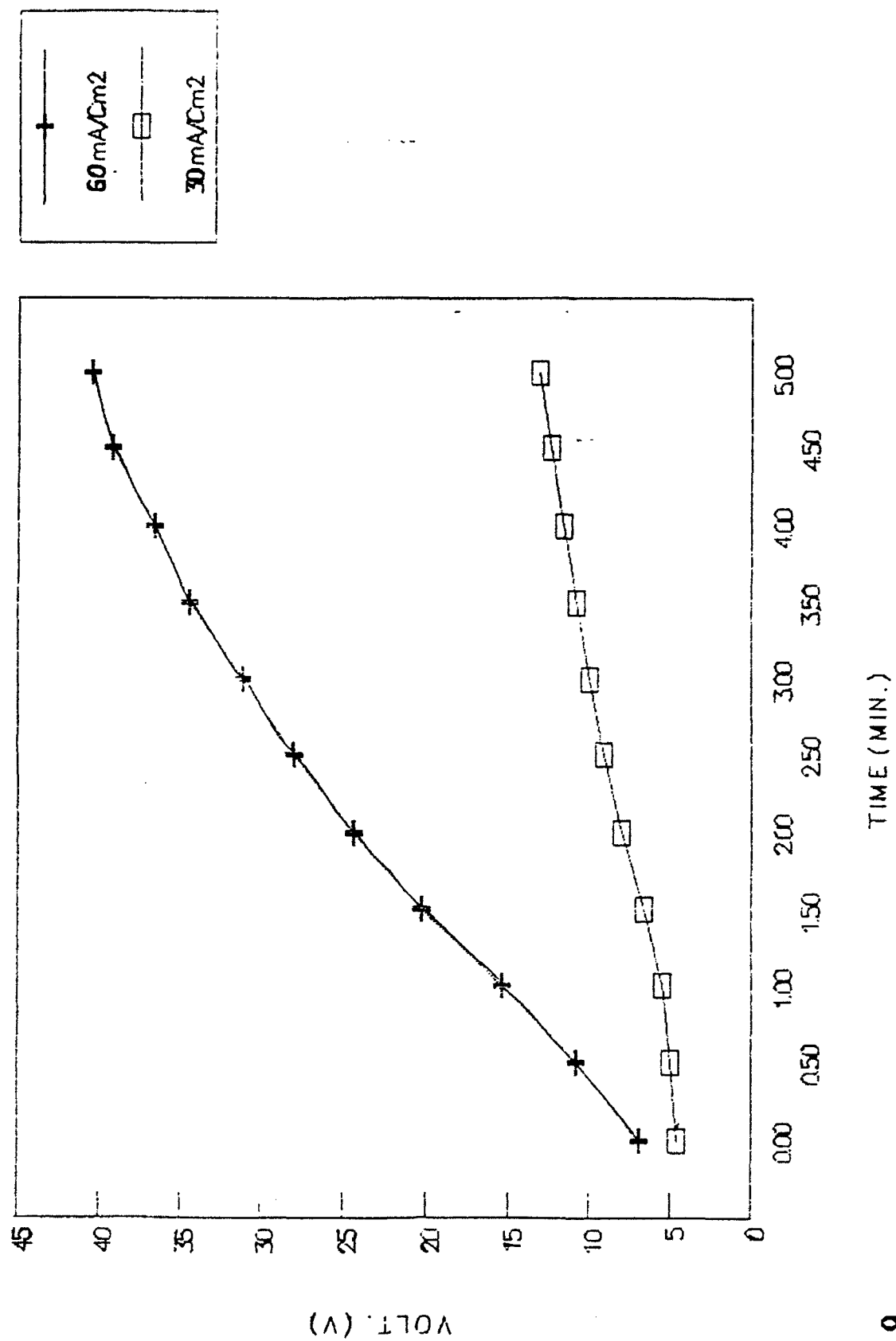


Fig 8



Deposition: $0.05 \text{ MAI (NO}_3)_3 + 0.05 \text{ MZrO}_3 \cdot (\text{NO}_3)_2$

$t = 10 \text{ min}$

$j = 25 \text{ mA/cm}^2$

Sintering: 1200°C

1hr

Ar

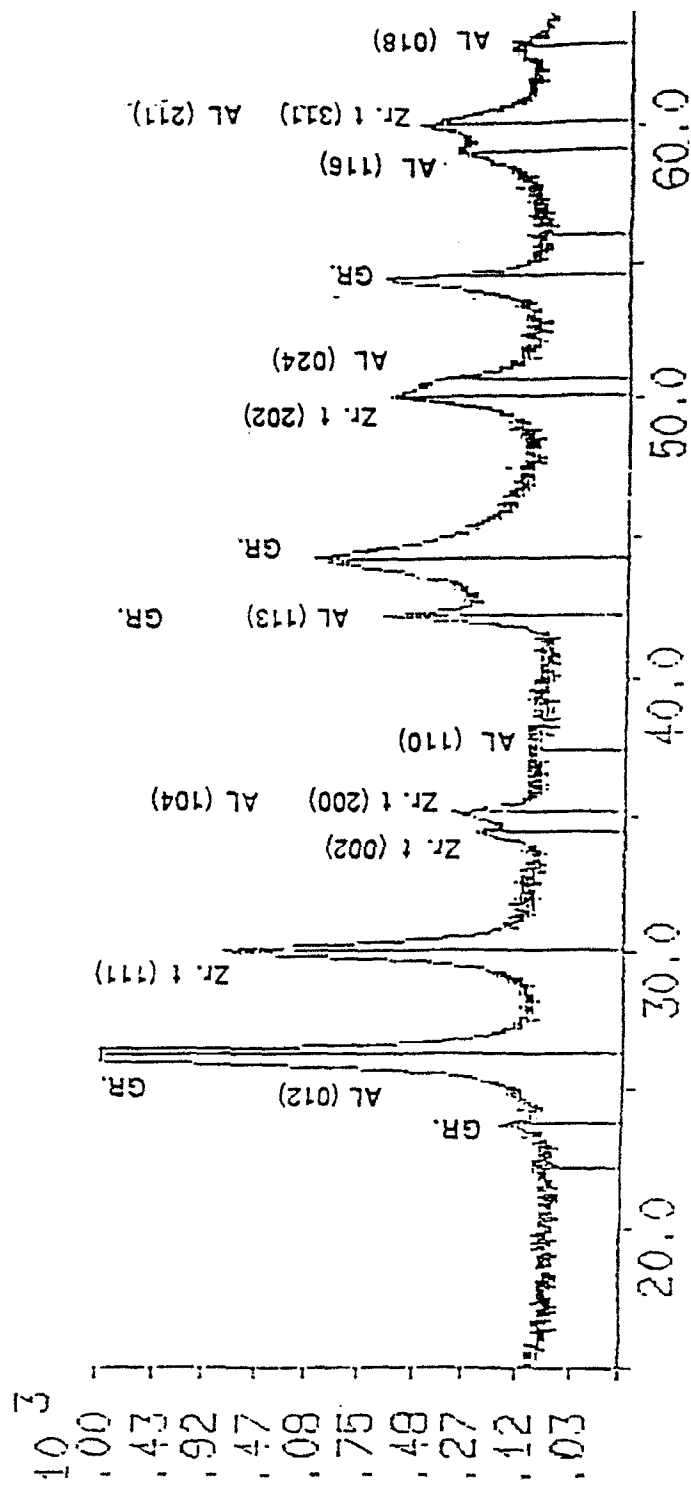


Fig 10

X-RAY: 0 - 20 keV
Live: 100s Preset: 100s Remaining:
Real: 117s , 15% Dead

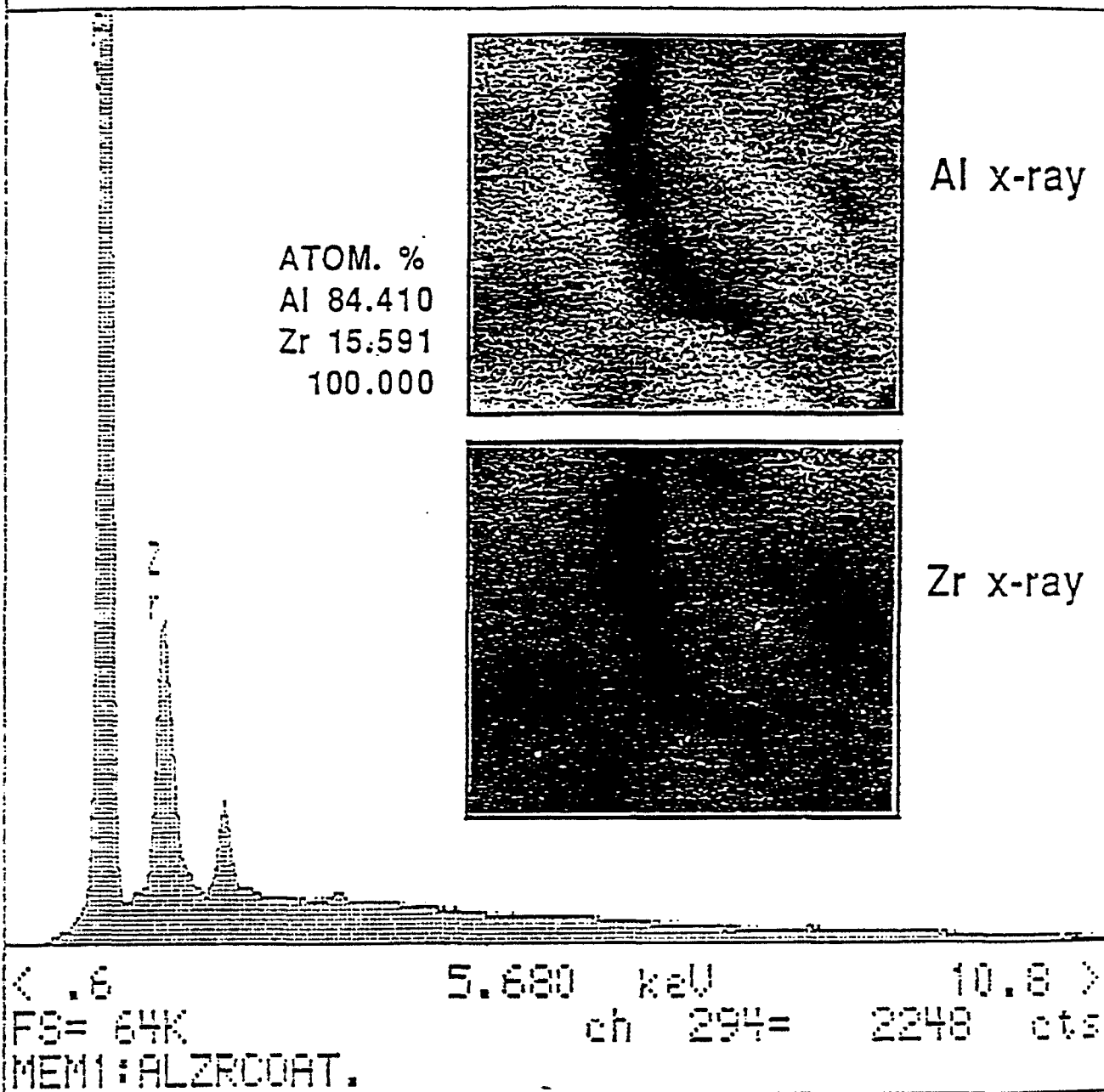


Fig 11

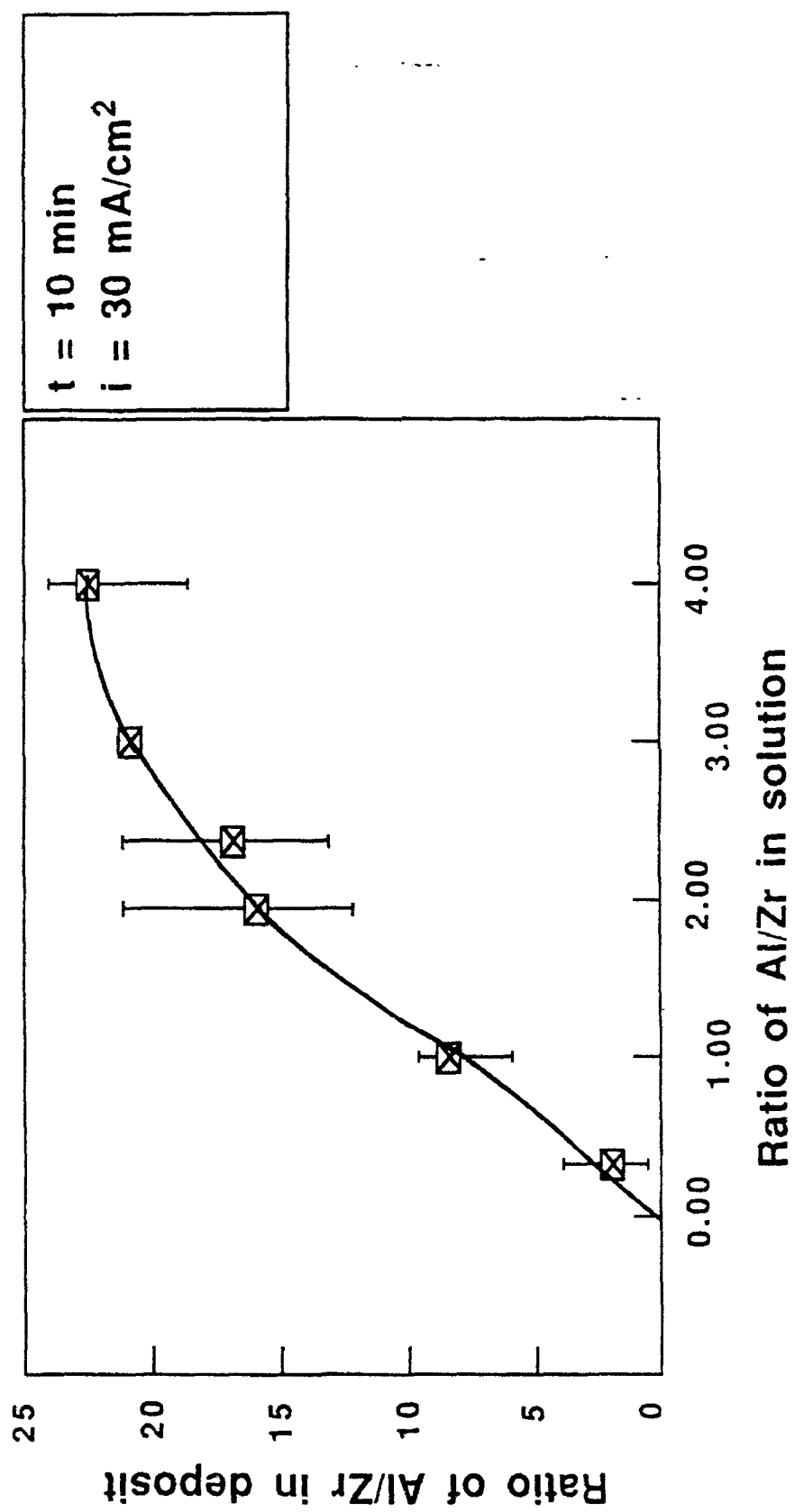


Fig 12

Deep Electrophoretic Penetration and Deposition of Ceramic Particles Inside Impermeable Porous Substrates.

1. ABSTRACT

The electrophoretic penetration of colloidal ceramic particles into an impermeable porous graphite substrate is investigated. The substrate is immersed in a suspension containing the particles and positioned between two electrodes. An electric potential gradient between the electrodes is used to drive the ceramic particles into the pores which are closed at the far end not allowing fluid permeation. Three driving mechanisms are identified: the hydrodynamic drag force exerted on the particles due to the electroosmotic flow of the solvent inside the pores, the electrophoretic force exerted on the particles and the stochastic Brownian force due to thermal fluctuations of the solvent molecules. While subjected to these forces, the particles may reach the walls of the pore and the short range van der Waals forces may cause their capturing and deposition onto the walls.

The objectives of this paper are: a) to predict the penetration depth of a single ceramic particle moving inside an impermeable porous substrate under the effect of an electric potential gradient, b) to derive the non-dimensional parameters characterizing the motion of the ceramic particles, and c) to gain a physical insight on the various mechanisms governing penetration.

Qualitatively, the results are that penetration depths are governed by a favorable (if large) Peclet number and unfavorable (if large) Damkohler number. However, the closed pore structure of the substrate causes diminished particle penetration if compared with an open pore structure, due to a less effective electroosmotic flow. Quantitative results for the mean penetration depths and the dispersion about the mean are also provided.

2. BACKGROUND

Deep penetration and deposition of inert species over the interstitial surfaces of a volatile porous substrate has been a major concern of the aero-space industry. Extremely strong, light and sometimes porous composites (such as carbon-carbon) may undergo undesired processes if exposed to a high temperature oxidizing environment. Chemical Vapor Deposition (CVD) of inert materials (such as Silica, Silicon-Carbide etc.) onto the walls of the pores, have been suggested in the past to protect the composites from oxidation. Alas, CVD has proven to be extremely slow and only shallow penetration has been detected. A rather new method to protect porous substrates by electrophoresis is studied and described in detail in our previous papers (1-2). In essence, an electric potential gradient is used to drive colloidal particles deep into the voids of the porous substrate. The analytical approach described in (2) considered an open porous structure. In this paper we focus our attention on the case where the substrate possesses small pores which are closed at one end and are impermeable to fluids. The purpose of this paper is: a) to suggest a theory and a mathematical model by which Deep Electrophoretic Deposition, can be analyzed and the non-dimensional parameters governing the process be obtained, and b) to predict the mean penetration depths and the dispersion of particles about the mean for the given set of parameters and structure of the porous substrate.

The motion of a single particle under the effect of electrophoretic forces has first been addressed by Smoluchowski (1918) and subsequently by many others (3-15). Smoluchowski predicted that a rigid spherical particle possessing an electric double layer and embedded in an unbounded flow field would be forced to move if subjected to an electrical potential gradient. The mobility of the particle depends linearly upon the dielectric constant of the fluid, the potential gradient, the zeta potential of the particle and is inversely proportional to the fluid viscosity. Wall effects were accounted for by Morrison & Stukel (1970) and Ken & Anderson (1985) for the case of a particle travelling in close proximity to the containing boundaries of the flow field. Keh & Anderson (1985) have shown that (if electroosmosis is disregarded) the particle would experience an increasing drag force and reduced mobility. It was also shown, that due to the electric field, the insulating rigid walls would induce an electroosmotic flow, its direction depending on the sign of the wall zeta

potential. For an open permeable structure the electroosmotic flow possesses a uniform velocity profile and a neutral particle immersed in the fluid would be dragged by the electroosmotic flow and move with almost identical velocity. However, for an impermeable structure though the induced electroosmotic flow still exists it is non uniform since a net zero mass flow must be observed inside the pores.(figure 1) Thus, the colloidal particle would be dragged by the electroosmotic flow and its motion determined by the *local* electroosmotic velocity. In case the particle is also subjected to an electrophoretic force, the particle would move *locally* with the combined electrophoretic and electroosmotic velocities. Superimposition is allowed due to the linearity of the governing low Reynolds number flow field equations. In addition, a sub-micron particle would experience an erratic Brownian motion due to the thermal fluctuations of the fluid molecules. Consequently, deterministic evaluation of the particle path under the combined effects of electroosmosis, electrophoresis and Brownian motion is invalid and a stochastic approach must be adopted (2).

The fluid motion inside a porous substrate under the effect of a *pressure gradient* (known as Darcy's law) has been addressed by many investigators. To devise the micro-pattern of the flow field, unit cell models (19-21) as well as more advanced finite elements approaches for spatially periodic structures (22-27) were applied. An equivalent treatment was proposed for the case of electroosmotic flow through an open porous structure (2), namely, the flow generated under the effect of an electric potential gradient. Since, a particle would be dragged by this interstitial electroosmotic flow, its evaluation is of foremost significance if one desires to calculate mean penetration depths of the ceramic particles. A general approach in which we modify Darcy's law so that it would incorporate electroosmotic effects is addressed in a separate paper (Haber (1990)). However, for the case of closed pores no similar treatment exists and a simple model is suggested in the following chapter.

The second effect to be accounted for is the direct electrophoretic force exerted on a particle travelling inside the small pores. Numerous treatments exist for the motion of a small rigid particle at low Reynolds numbers, wall effects excluded (29) and included (29-32). The fine structure of a porous substrate enveloping a particle was treated in various ways, for instance, a spherical particle travelling along an infinitely long cylinder of circular cross-section, a spherical particle embedded in a flow field which is bounded by a spherical envelope with pre-assumed free surface (or free vorticity) boundary conditions, and a small spherical particle moving inside a spatially-periodic lattice of pre-arranged large

spherical particles. Notwithstanding, all of the previous models assumed *no-slip* boundary conditions over the particle surface, whereas the electrophoretic force is applied via a unique *slip* boundary condition. Thus, the known approaches must be rectified accordingly.

The third effect, the random Brownian force due to the thermal fluctuations of the fluid, was treated by two different methods in the past. The first method applies a Lagrangian viewpoint of the problem utilizing Langevin's equation to evaluate mean particle velocity and dispersion (33,34). The second method applies an Eulerian approach where a Fokker-Planck equation is formulated and a moment method developed by Taylor-Aris is utilized to derive the pertinent means (35-37). Generally, it is accepted (and for linear cases can be proven (18)) that these methods would yield identical results and the choice between the methods is a matter of convenience.

In the next chapter we shall address the three foregoing mechanisms where we provide: a) a solution for the electroosmotic flow inside a long circular tube closed at the far end and a similar solution for a simpler 2D flow between two semi-infinite plates (a model simulating the electroosmotic flow in an impermeable porous structure), and b) a model for the stochastic behavior of the Brownian particle under the combined effect of electroosmosis and electrophoresis utilizing Fokker-Planck's equation.

3. METHOD OF SOLUTION

3a. Electroosmosis in Impermeable Porous Media

The flow through porous media generated by an electric potential gradient was analytically investigated by Kozak & Davis (1986,1989) using a unit cell model and by Haber (1990) using a simple approach based on the known solution of the flow field through a long open circular tube (in close similarity to one of the approaches used to analytically prove Darcy's law). Similar approaches for pressure driven flows were used to determine filtration efficiencies in porous substrates (39).

Tacitly, a permeable interconnected pore structure was assumed to exist in all the aforementioned treatise. In case the pores are not interconnected, no flow can penetrate the

porous structure and the net flow through it must be zero. Notwithstanding, microscopic flow can still exist inside the pores located close to the external boundaries of a substrate subjected to an external electric potential gradient. Normally, this flow is of no particular interest and can be totally ignored if macroscopic processes are investigated. However, if a coating of thickness very small compared with the substrate thickness is considered such flow is of utmost importance and may determine the penetration depth of the coating. Consequently, the first goal would be to determine this electroosmotic flow which is developed close to the boundaries of the substrate.

We proceed in a manner similar to the one we used in (2) and utilize a single long cylindrical tube to model the pore structure, only here the cylinder is closed at its far end.

The governing field equations for the flow through a tube induced by an electric potential gradient are based on Stokes' equations for low Reynolds number flows, i.e.

$$\eta \nabla^2 \mathbf{v} = \nabla p \quad \nabla \cdot \mathbf{v} = 0 \quad [1]$$

where \mathbf{v} and p are the velocity and pressure fields and η stands for the viscosity of the fluid.

The boundary conditions which the velocity field satisfies over the cylinder walls are (17):

$$v_z = -\frac{\epsilon \zeta_w}{4\pi\eta} \frac{\partial \phi}{\partial z}, \quad v_r = 0 \quad @ \quad r = b \quad [2]$$

where ϵ is the dielectric constant of the fluid, ζ_w is the zeta potential at the cylinder wall, ϕ stands for the electric potential, b is the radius of the tube and (r, z) are polar coordinates, the z coordinate coinciding with the cylinder axis. It should be noted that the no-slip condition can no longer be applied and in its place we use condition [2].

The general solution for \mathbf{v} is easily derived for a fully developed flow (i.e. $\partial v_z / \partial z = 0$.) namely,

$$v_z = -\frac{b^2 - r^2}{4\eta} \frac{\partial p}{\partial z} - \frac{\epsilon \zeta_w}{4\pi\eta} \frac{\partial \phi}{\partial z} \quad [3]$$

where the constant pressure gradient is yet to be determined. The auxiliary condition which must be used is that the net mass flow through the pore must vanish, i.e.

$$2\pi \int_0^b v_r r dr = 0 \quad [4]$$

Combining [3] and [4] determines the pressure gradient and yields the final form of the velocity field,

$$v_z = -\frac{\varepsilon \zeta_w}{4\pi\eta} \frac{\partial \phi}{\partial z} \left(2 \frac{r^2}{b^2} - 1\right) \quad [5]$$

Equation [5] represents a valid solution for a region not too close to the entrance of the pore or its dead end.

Similarly, it is easy to show that for a 2D case, where a pore is simulated by two flat plates $2b$ distant apart and closed at the far end, the velocity field is given by

$$v_z = -\frac{\varepsilon \zeta_w}{8\pi\eta} \frac{\partial \phi}{\partial z} \left(3 \frac{y^2}{b^2} - 1\right) \quad [6]$$

We shall use equation [6] rather than [5] in the following analysis due to the simpler mathematical handling of a 2D problem. We believe, however, that valid qualitative and quantitative predictions will be obtained for penetration depths of colloidal particles in an impermeable porous substrate. The full 3D problem based on equation [5] will be analyzed in the future and compared with the results provided in this paper.

We shall also henceforth assume that the velocity U' of a neutral particle suspended in the fluid depends upon its distance from the walls and equals the fluid velocity given by [6]. Thus, its z -component is .

$$U' = \frac{1}{2} U_w \left(3 \frac{y^2}{b^2} - 1\right) \quad [7]$$

where

$$U_w = -\frac{\epsilon \zeta_w}{4\pi\eta} \frac{\partial \phi}{\partial z} \quad [8]$$

Thus, a particle located at close proximity to the walls will be carried deeper into the pore due to electroosmosis while a particle located closer to the center will be retarded. This fact is the basic difference between this case and the case presented in (2) where the velocity field inside the pore due to electroosmosis has been shown to be uniform.

3b. Electrophoretic Motion of a Particle

The electrophoretic velocity U'' of a small rigid spherical particle suspended in an *unbounded* flow field of viscosity η and subjected to an external electric potential gradient $E = -\nabla \phi$ was first obtained by Smoluchowski,

$$U'' = -\frac{\epsilon \zeta_p}{4\pi\eta} \nabla \phi \quad [9]$$

where ζ_p is the zeta potential over the particle interface. Its z-component is given by

$$U_p = -\frac{\epsilon \zeta_p}{4\pi\eta} \frac{\partial \phi}{\partial z} \quad [10]$$

The basic assumptions made to derive [9] are that the Debye screening length is much smaller than the particle dimension and that the particle translates in an unbounded flow field.

If the particle translates at close proximity to a rigid surface, wall effects must be accounted for (e.g. Keh and Anderson(1985)). Norwithstanding, for particle dimensions which are more than ten times smaller than its distance to the wall, Smoluchowski's equation is an excellent approximation (given that no electroosmotic flow exists).

It is a well known result from the theory of low Reynolds number flows (40,41) that a particle approaching a rigid wall (subjected, for instance, to gravity forces) will experience a growing hydrodynamic resistance which at the limit of zero gap increases to infinity. However, the condition of slip velocity over the particle boundaries will cause that

resistance to grow in a slower manner up till a gap of the order of the Debye screening length. An exact treatment of this hydrodynamically singular behavior awaits exploration. However, over these very small distances one has to consider other surface (e.g. London-van der Waals) forces which eventually lead to the attraction of the particle to the walls. Thus, it seems reasonable to assume that Smoluchowski's equation can be used as a first order approximation for the mobility of a particle over the entire range of particle radius to wall-gap ratios.

Henceforth, we shall assume that equation [10] is applicable for the case of a single rigid particle immersed in a fluid of viscosity η and bounded by the walls of a long pore its axis pointing in the z-direction

3c The Probability Distribution for Particle Penetration Depths

3c.1 Statement of The Problem

Small sub-micron particles travelling inside the pores of a porous substrate are strongly affected by the thermal fluctuations of the fluid molecules and experience Brownian motion. This stochastic motion must be superimposed to the deterministic electrophoretic motion and electroosmotic induced velocity which are primarily parallel to the direction of the pore axis. The Brownian motion causes the particle to cross streamlines and sample all possible transverse positions which leads to the phenomenon known as Taylor dispersion.

Tracing down exactly the trajectory of a particle is therefore of no consequence. What we seek is the probability distribution that a particle entering the porous substrate would reach a given depth and not be deposited on the walls during its erratic motion inside the pores. In addition, the very complex and random structure of the porous substrate makes it impossible to obtain more than a formal representation of the equations and boundary conditions. The mathematical formulation must hinge on a simplified geometrical model for the porous structure which would be amenable to mathematical analysis. One of the very common approaches is to treat a single pore as a long circular tube of mean pore diameter its axis colinear with the local superficial velocity direction. Such a model is handicapped by the fact that no pronounced *lateral* dispersion of the particles across the

porous substrate is allowed. However, since only the mean *longitudinal* particle motion is sought such a model is expected to provide valid results on the main parameters affecting penetration depths. The fact that the pores are not interconnected but still of considerable length compared with their diameter allows us to treat the motion of the particle as unaffected *directly* by the presence of the dead end (although the existence of a closed end affects the electroosmotic velocity which in turn affects the motion of the particle). Figure 1 describes the basic geometrical and kinematical parameters applicable to the problem.

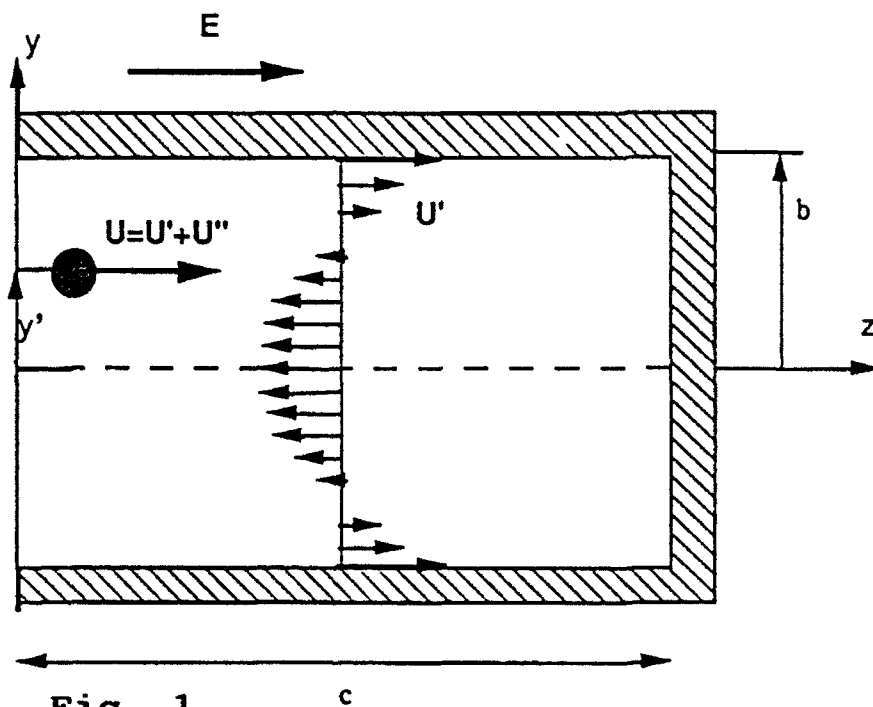


Fig. 1

The general differential equations governing the problem is Fokker-Planck's equation for the probability distribution. In our case it assumes the form,

$$\frac{\partial p}{\partial t} + \nabla_x \cdot \mathbf{J}_x + \nabla_y \cdot \mathbf{J}_y = \frac{1}{\chi_0} \delta(z) \delta(y - y_0) \delta(t) \quad [11]$$

where

$$J_z = Up - D_z \nabla_z p, \quad J_y = -D_y \nabla_y p,$$

$$D_z = kTM_z, \quad D_y = kTM_y, \quad [12]$$

$$U = U'(y, t) + U''(t)$$

Here $p(y, z, t / y_0, 0)$ stands for the conditional probability that a particle initially located at $(y_0, 0)$ reaches the infinitesimal volume around (y, z) after time t . The cartesian coordinate system (y, z) coincides with the pore midplane where y stands for the lateral distance from the pore midplane and z is the distance measured along the pore from the pore entrance. The symbol U stands for the deterministic part of the velocity of the particle, composed of its electrophoretic velocity and the electroosmotic velocity of the suspending field. It must be stressed that the interstitial flow due electroosmosis U' does not possess the commonly agreed upon parabolic (Poiseuille) form of velocity vanishing at the walls. It is very well approximated by the parabolic distribution shown in Figure 1 (equation [6]) for pore diameters larger than Debye's screening length (a condition normally met). Thus, U is a varying function with respect to the spatial coordinates. The flux J_z parallel to the axis of the pore depend on particle convection and diffusion along the pore axis, whereas the flux J_y arise from diffusion only. The diffusion coefficients D_z and D_y the first one parallel and the latter perpendicular to the pore axis, depend on the absolute temperature T of the liquid and the respective particle mobilities M_z and M_y . This generalized Stokes-Einstein relationship provided in [12] accounts for wall effects through the anisotropic form of the mobility tensor. From the physical point of view, it is obvious that the particle would experience unequal hydrodynamic resistance to its motion perpendicular and parallel to the pore axis. The mobility tensor components were approximately evaluated in Happel and Brenner (1973). It is shown that, for particles of radius a small compared with their distance to the wall, the mobilities M_z and M_y are approximately equal and possess the following form,

$$M_z = M_y = 1/(6\pi\eta a) . \quad [13]$$

The boundary conditions which the probability distribution p satisfies over the pore walls are first order diffusion-reaction rate equations ,

$$\mp D \frac{\partial p}{\partial y} = \kappa p \quad @ \quad y = \pm b \quad [14]$$

where κ is the local deposition rate and b stands for the pore mean radius.

The left hand side of [14] represents the diffusional flux of probability towards the pore walls whereas the right hand side represents the probability that a particle located at close proximity to the walls would indeed be deposited. The numerical value of κ depends on particle shape and dimension, electrostatic and hydrodynamic forces and the physical properties of the materials comprising the particles, the porous substrate and the suspending liquid. Indeed, it is extremely difficult to obtain κ from first principles. A feasible method to attain this end would be to devise an experiment in which one would utilize the given materials of the ceramic particles, porous substrate and liquid.

As for the downstream boundary condition, we assume that very far from the entrance p vanishes. This is in agreement with the assumption of very long pores or, in other words, that the particle is deposited on the walls long before it reaches the far end. A-priori, the solution would be used to formulate a condition for which this assumption can be justified. In addition, we would assume that the integral of p over the walls and the bulk of the fluid is unity for *all times* (this corresponds to assuming that a particle once it entered the pore is not allowed to escape or an upstream boundary condition of zero net flux). This last assumption can be justified if one recalls that the longitudinal dispersion is very small for the very short times the particle stays close to the entrance. In other words, the Brownian migration, which might cause the escape of the particle, is negligibly small compared with the longitudinal distances the particle travels due to convection for the short time it stays close to the entrance. Moreover, since the distribution function of p is very sharply peaked at the beginning of the process and then travels downstream, p itself can be assumed to approximately vanish at the entrance position.

3c.2 Analytical Solution and Results

It is very useful to state the non-dimensional parameters and time scales of the problem before we attempt to obtain an analytical or numerical solution of [11]. It is easy to

show that the pertinent time scale within which steady electroosmotic flow can be established is,

$$\tau_o = \frac{c}{U_w} \quad [15]$$

where U_w is the velocity adjacent to the walls and c is the length of the pore. This time scale would also provide a measure for the time it would take a particle adjacent to the walls to reach the far end of the pore due to electroosmosis.

Similarly, it can be shown from [11], [12] and [14] that additional three time scales exist for the penetration process of Brownian ceramic particles into the porous substrate. The first one τ_p is linked with the electrophoretic convective term of the Fokker-Planck equation,

$$\tau_p = \frac{c}{U_p} \quad [16]$$

which determines the time it would take a particle to reach the end of the pore due to electrophoretic forces.

The second time scale is related to the diffusive process, namely, the time it takes a Brownian particle to cross streamlines and sample all radial positions inside the tube,

$$\tau_D = \frac{b^2}{D} \quad [17]$$

The third time scale is obtained from boundary condition [12] and determines the deposition rate, namely,

$$\tau_R = \frac{b}{\kappa} \quad [18]$$

If we assume that the Brownian particles were introduced into the solution after electroosmotic steady state flow has been established, (U is time independent) non-dimensionalization of the Fokker-Planck equation and the associated boundary conditions result in three non-dimensional parameters which determine the solution completely. The first parameter can be identified as the Peclet number of the problem,

$$Pe = \frac{U_w b}{D} \quad [19]$$

which determines the relative significance of the convective electroosmotic process vis-a-vis the diffusive process. Recall that U_w is defined here as the electroosmotic velocity *adjacent* to the walls.

The second non-dimensional parameter is the Damkohler number which determines the ratio between the diffusion and the deposition time scales, namely,

$$\lambda = \frac{\tau_D}{\tau_R} = \frac{\kappa b}{D} \quad [20]$$

Thus, large values of λ mean that the deposition of particles on the walls is governed mainly by diffusion, whereas small values of λ mean that deposition is controlled by the local deposition rate.

The third non-dimensional parameter is the ratio between the electrophoretic and the electroosmotic velocities which also equals the ratio between the zeta potentials

$$\zeta = \frac{U_p}{U_w} = \frac{\zeta_p}{\zeta_w} \quad [21]$$

Its value is either negative or positive.

A general analytical solution of [11] is extremely difficult to obtain since U' depends on the lateral y -coordinate. We shall instead utilize a method devised by Aris and Taylor which makes it possible to derive the mean penetration distance and the dispersion about it. A detailed description of the general method is given in (). The reader is referred to

the appendix in which we describe how to apply it to the foregoing problem. A summary of the principal equations, outline of the solution procedure and the main results are now addressed.

Equation [11] rewritten in the 2D cartesian coordinate system (y,z) possesses the following form

$$\frac{\partial p}{\partial t} + U \frac{\partial p}{\partial z} = D \left(\frac{\partial^2 p}{\partial y^2} + \frac{\partial^2 p}{\partial z^2} \right) + \delta(t) \delta(z) \delta(y - y') \quad [22]$$

where

$$U = \frac{1}{2} U_w \left(3 \frac{y^2}{h^2} - 1 \right) + U_p \quad [23]$$

A cascade of partial differential equations can be derived from [22] all of which are independent of z and are easier to handle. The first three are

$$\frac{\partial p_0}{\partial t} = D \frac{\partial^2 p_0}{\partial y^2} + \delta(t) \delta(y - y') \quad [24]$$

$$\frac{\partial p_1}{\partial t} = D \frac{\partial^2 p_1}{\partial y^2} + U p_0 \quad [25]$$

$$\frac{\partial p_2}{\partial t} = D \frac{\partial^2 p_2}{\partial y^2} + 2D p_0 + 2U p_1 \quad [26]$$

where

$$p_0 = \int_0^{\infty} p \, dz, \quad p_1 = \int_0^{\infty} p z \, dz, \quad p_2 = \int_0^{\infty} p z^2 \, dz \quad [27]$$

The associated boundary conditions are

$$\mp D \frac{\partial p_i}{\partial y} = \pm \kappa p_i, \quad i = 1, 2, 3 \quad @ \quad y = \pm b \quad [28]$$

The solutions for p_1 and p_2 are required to determine the mean penetration and the dispersion about the mean. The solution for p_2 depends upon p_1 and it in turn depends upon p_0 . The solution of [24] for p_0 is straightforward

$$p_0(\eta|\eta', \tau) = h^{-1} \sum_1 \frac{\exp(-\delta_n^2 \tau)}{1 + \sin^2 \delta_n / \lambda} \cos(\delta_n \eta) \cos(\delta_n \eta') \quad [29]$$

where

$$\eta = \frac{y}{b}; \quad \eta' = \frac{y'}{b}; \quad \tau = \frac{Dt}{b^2} \quad [30]$$

and δ_n is a solution of the following algebraic equation

$$\delta_n \tan \delta_n = \lambda \quad [31]$$

which possesses an infinite number of roots. The n -th root lies in the region between $(n-1)\pi$ and $(n-.5)\pi$ and approaches $(n-1)\pi$ for large n 's.

the solution of [25] for p_1 is quite lengthy and results in the the expression

$$\begin{aligned} \frac{p_1}{p_0 \tau} = & \frac{1}{2} \sum_{n=1}^{\infty} \frac{\exp(-\delta_n^2 \tau) \cos \delta_n \eta \cos \delta_n \eta'}{(1 + \lambda^{-1} \sin^2 \delta_n)^2} \left(\frac{\sin 2\delta_n}{\delta_n} + \frac{3 \cos 2\delta_n}{2\delta_n^2} - \frac{3 \sin 2\delta_n}{4\delta_n^3} + 2\zeta(1 + \lambda^{-1} \sin^2 \delta_n) \right) + \\ & \frac{6}{\tau} \sum_{n=1}^{\infty} \sum_{m=1}^{\infty} \frac{[\exp(-\delta_n^2 \tau) - \exp(-\delta_m^2 \tau)] \cos \delta_n \eta \cos \delta_m \eta' \cos \delta_n \cos \delta_m}{(\delta_n^2 - \delta_m^2)^3 (1 + \lambda^{-1} \sin^2 \delta_n) (1 + \lambda^{-1} \sin^2 \delta_m)} \{ \delta_n^2 + \delta_m^2 + 2\lambda(\lambda + 1) \} \end{aligned} \quad [32]$$

The probability of a particle depositing per unit time per unit area over the pore walls is κp at $y=b$. Thus, the mean penetration depth, for particles entering the pore at arbitrary initial position is given by

$$\begin{aligned} \bar{z} = & 2\kappa \int_{t=0}^{\infty} \int_{y=-b}^b \int_{z=0}^{\infty} zp(z, y, t|y')|_{y=b} p(y') dz dy' dt = \\ & 2\kappa \int_{t=0}^{\infty} \int_{y=-b}^b p_1 p(y') dy' dt \end{aligned} \quad [33]$$

where $p(y')$ is the probability distribution of a particle entering the pore at time $t=0$ at position $y=y'$ and the factor 2 preceding the expression accounts for deposition on the wall at $y=-b$. An exact solution for the distribution would depend upon the solution for particle

concentration outside the porous substrate adjacent to its boundaries. This solution is not apriorily known. Instead, we shall assume a simple uniform distribution or, in other words, that all initial positions are equally likely. ,

Substitution of [34] and [32] into [33] yields,

$$\begin{aligned} \frac{\bar{z}}{P_0 b} = & \left(\sum_{n=1}^{\infty} \frac{\sin^2 \delta_n}{(1 + \lambda^{-1} \sin^2 \delta_n)^2} \left(\frac{\sin 2\delta_n}{\delta_n} + \frac{3 \cos 2\delta_n}{2\delta_n^2} - \frac{3 \sin 2\delta_n}{4\delta_n^3} + 2\zeta(1 + \lambda^{-1} \sin^2 \delta_n) \right) + \right. \\ & \left. 12 \sum_{n=1}^{\infty} \sum_{m=1}^{\infty} \frac{\cos^2 \delta_n \cos^2 \delta_m}{(\delta_n^2 - \delta_m^2)^2 \delta_n^2 \delta_m^2 (1 + \lambda^{-1} \sin^2 \delta_n) (1 + \lambda^{-1} \sin^2 \delta_m)} [\delta_n^2 + \delta_m^2 + 2\lambda(\lambda + 1)] \right) \end{aligned} \quad [34]$$

Figures 2 and 3 illustrates the dependence of the mean penetration depths upon the Damkohler number λ and the ratio between particle to wall zeta-potentials ζ , respectively. Deep penetration is affected mainly by two parameters, the Peclet number and the Damkohler number. The dependence upon Peclet number (either based on the electroosmotic or the electrophoretic velocities) is shown to be linear. The dependence upon the Damkohler number is mostly pronounced for values lower than 0.3. Small changes in this region would be manifested in large changes in penetration depths. High values of the Damkohler number would result in poor penetration depths. The third non-dimensional parameter, the zeta potential ratio, is of much lesser importance. The penetration depth increases slowly with a corresponding increase in the value of ζ .

The solution of [26] for p_2 is very lengthy and tedious and is based on the solutions for p_0 and p_1 given in [29] and [32]. Since we seek the dispersion about the mean penetration distance of particles deposited over the walls, we need to evaluate the integral

$$\begin{aligned} \sigma_z^2 = & 2\kappa \int_{t=0}^{\infty} \int_{y=-b}^b \int_{z=0}^{\infty} (z - \bar{z})^2 p(z, b, t|y) p(y) dz dy dt = \\ & 2\kappa \int_{y=-b}^b \int_{t=0}^{\infty} p_2(y = b, t|y) p(y) dy dt - \bar{z}^2 \end{aligned} \quad [35]$$

The integration of p_2 , albeit straightforward, is tedious and the final expression for σ_z^2 possesses the following form

$$\frac{\sigma_i^2}{P_i^2 b^2} = 2\lambda (S_1 + S_2 + S_3) - \left(\frac{\bar{z}}{P_i b} \right)^2 \quad [36]$$

where

$$S_1 = \frac{2}{P_i^2} \sum_{n=1}^{\infty} \frac{\sin \delta_n \cos \delta_n}{\delta_n^5 (1 + \lambda^{-1} \sin^2 \delta_n)} \quad [37]$$

$$\begin{aligned} S_2 = & \frac{1}{2} \sum_{n=1}^{\infty} \left(\frac{\sin 2\delta_n}{\delta_n} + \frac{3 \cos 2\delta_n}{2\delta_n^2} - \frac{3 \sin 2\delta_n}{4\delta_n^3} + 2\zeta(1 + \lambda^{-1} \sin^2 \delta_n) \right)^2 \times \\ & \frac{\sin \delta_n \cos \delta_n}{\delta_n^2 (1 + \lambda^{-1} \sin^2 \delta_n)^3} + \\ & 6 \sum_{n=1}^{\infty} \sum_{m=1}^{\infty} \left(\frac{\sin 2\delta_m}{\delta_m} + \frac{3 \cos 2\delta_m}{2\delta_m^2} - \frac{3 \sin 2\delta_m}{4\delta_m^3} + 2\zeta(1 + \lambda^{-1} \sin^2 \delta_m) \right) \times \\ & \frac{(\delta_n^2 + \delta_m^2 + 2\lambda^2 + 2\lambda) \cos^2 \delta_n \cos \delta_m \sin \delta_m}{\delta_n^2 \delta_m^5 (\delta_n^2 - \delta_m^2)^2 (1 + \lambda^{-1} \sin^2 \delta_n) (1 + \lambda^{-1} \sin^2 \delta_m)^2} \end{aligned} \quad [38]$$

and

$$\begin{aligned} S_3 = & 6 \sum_{n=1}^{\infty} \sum_{m=1}^{\infty} \left(\frac{\sin 2\delta_n}{\delta_n} + \frac{3 \cos 2\delta_n}{2\delta_n^2} - \frac{3 \sin 2\delta_n}{4\delta_n^3} + 2\zeta(1 + \lambda^{-1} \sin^2 \delta_n) \right) \times \\ & \frac{(\delta_n^2 + \delta_m^2 + 2\lambda^2 + 2\lambda) \cos^2 \delta_n \cos \delta_m \sin \delta_m}{\delta_n^4 \delta_m^3 (\delta_n^2 - \delta_m^2)^2 (1 + \lambda^{-1} \sin^2 \delta_m) (1 + \lambda^{-1} \sin^2 \delta_n)^2} + \\ & 72 \sum_{n=1}^{\infty} \sum_{m=1}^{\infty} \frac{\cos^3 \delta_m \sin \delta_m \cos^2 \delta_n (\delta_n^2 + \delta_m^2 + 2\lambda^2 + 2\lambda)^2}{\delta_m^5 \delta_n^2 (\delta_n^2 - \delta_m^2)^4 (1 + \lambda^{-1} \sin^2 \delta_n) (1 + \lambda^{-1} \sin^2 \delta_m)^2} + \\ & 72 \sum_{n=1}^{\infty} \sum_{m=1}^{\infty} \sum_{q=1}^{\infty} \frac{\cos^2 \delta_n \cos^2 \delta_q \cos \delta_m \sin \delta_m}{\delta_n^2 \delta_m^3 \delta_q^2 (\delta_n^2 - \delta_q^2)^2 (\delta_n^2 - \delta_m^2)^2} \times \\ & \frac{(\delta_n^2 + \delta_m^2 + 2\lambda^2 + 2\lambda) (\delta_n^2 + \delta_q^2 + 2\lambda^2 + 2\lambda)}{(1 + \lambda^{-1} \sin^2 \delta_n) (1 + \lambda^{-1} \sin^2 \delta_m) (1 + \lambda^{-1} \sin^2 \delta_q)} \end{aligned} \quad [39]$$

Figures 4 to 9 illustrate the long time dependence of the dispersion coefficient on the Damkohler number, on the zeta potential ratio and on the Peclet number.

Figures 4 and 5 illustrate the derived numerically computed values for the dispersion coefficient as function of the Damkohler number λ , for ζ values 0.1, 1 and 10 and Peclet numbers 0.1, 1 and 10, respectively. It can clearly be observed that high values of λ cause the dispersion coefficient to decay very fast. It means that most of the particles would deposit on the walls very close to the pore entrance and that the spread around the mean penetration distance is peaked. Small values of λ would result in deep penetration and a wide spread of particles (a desirable effect). For λ values smaller than 0.3, the dispersion coefficient is highly sensitive to λ variations. A decrease in λ by a factor of two may result in order of magnitude changes in the dispersion coefficient. Although the trend manifested in the figures is expected, the last mentioned result is not too obvious.

Figures 6 and 7 illustrate the values computed for the dispersion coefficient as function of the zeta potential ratio ζ , for λ values 0.1, 0.5 and 1 and Peclet numbers 0.1, 1 and 10, respectively. It manifests that the square of dispersion coefficient depends quadratically upon ζ . Its value increasing slowly with a corresponding increase in the zeta potential ratio. The reason for this behavior is not too clear. It may be due to the larger variations in the velocity profile across the pore, a fact which is known to enhance dispersion in similar flow systems.

Figures 8 and 9 illustrate the values computed for the dispersion coefficient as function of the Peclet number P_e for ζ values 0.1, 1 and 10 and λ values 0.1, 0.5 and 1, respectively. It manifests the important role of particle convection. For large P_e numbers, the dispersion coefficient increase almost linearly. The probability density drops significantly with the Peclet number P_e thus a more even distribution of particles is expected along the pore axis and deeper penetration is expected. In figure 5 the probability density is directly plotted vs. the local deposition parameter λ for Peclet values 0.1, 1.0 and 10 and two values of z , showing again the fast accumulation of particles near the pore entrance for small values of Peclet number.

4. CONCLUSIONS

Deep penetration and coating is feasible by electrophoretic methods. The figures elucidate the fact that deep penetration (more than hundred pore diameters) can be achieved only for small Damkohler numbers λ ($\lambda < 0.2$) and for high Peclet numbers ($Pe > 10$). Cases in which $\lambda = 0$ would obviously result in the largest value for the mean penetration. A small change in λ may cause order of magnitude changes in penetration depths. Introduction of a repelling force between the particles and the pore walls, stronger than van der Waals forces, may achieve this desired effect.

The dispersion around the mean penetration depth is large for small Damkohler numbers and grows almost linearly with Peclet number. Thus, an almost even spread can be achieved for the same values which will bring about deep penetration. This result is a very favorable outcome for electrophoretic coating methods.

An increase in the ratio ζ between the electrophoretic velocity of the particle and the electroosmotic velocity near the wall will cause only a mild increase in penetration depth and dispersion coefficient. Indeed, this parameter plays only a secondary role in the deep electrophoretic coating process. It is, however, preferable to increase the electrophoretic rather than the electroosmotic velocity.

Comparison with the results we obtained for the open pore structure of the substrate reveals that penetration depths for closed pores is smaller whereas dispersion in the latter is larger provided electroosmosis exists.

Validity of the analysis relies on the fact that particles do not reach the dead end position in the pore. Thus, the pore must be longer than the sum of the mean penetration distance and three times the value of the dispersion coefficient (this will account for more than 95% of the particles depositing on the walls prior to reaching the dead end).

The diffusion coefficient of the colloidal particles has a dual effect: 1) decreasing diffusion coefficient causes increasing Peclet number which has a favorable effect on penetration depth. 2) decreasing diffusion coefficient causes increasing deposition rate which has an unfavorable effect on penetration depth.

The process can be controlled by a judicious selection of particle size and concentration, solution properties, electric field intensity and its time protocol.

Acknowledgement

This research was supported by Air Force Office of scientific Research, Air Force Systems Command, USAF under Grant # 89-0474. The US Government is authorized to reproduce and distribute reprints for Governmental purposes notwithstanding any copyright notation thereon.

Figure Captions

figure 1: The definition of the coordinate system and the geometrical model for particle penetration .

figure 2: Mean penetration depth vs. The Damkohler number.

figure 3: Mean penetration depth vs. The ratio between electrophoretic and electroosmotic velocities (or particle to wall zeta potentials).

figure 4: The standard deviation vs. The Damkohler number (particle to wall zeta potential ratio is used as a parameter).

figure 5: The standard deviation vs. The Damkohler number (The Peclet number is used as a parameter).

figure 6: The standard deviation vs. The zeta potential ratio (The Damkohler number is used as a parameter).

figure 7: The standard deviation vs. The zeta potential ratio (The Peclet number is used as a parameter).

figure 8: The standard deviation vs. The Peclet number (The zeta potential ratio is used as a parameter).

figure 9: The standard deviation vs. The Peclet number (The Damkohler number is used as a parameter).

REFERENCES

1. L. Gal-Or and S. Haber, Deep Electrophoretic Penetration and Deposition of Ceramic Particles Inside Porous Substrates (Experimental). (1991 submitted)
2. S. Haber and L. Gal-Or, Deep Electrophoretic Penetration and Deposition of Ceramic Particles Inside Porous Substrates. An Analytical Model. (1991 submitted)
3. F.A. Morrison, *J. Coll. Interface Sci.*, **34**, 210 (1970).
4. R.W. O'Brein and L.R. White, *J. Chem. Soc. Faraday II*, **74**, 1607 (1978).
5. A. Delgado, F. Gonzalez-Caballero and G. Pardo, *J. Non-Equilibrium Therm.*, **10**, 251 (1985).
6. C.F. Zukoski and D.A. Saville, *J. Coll. Interface Sci.*, **115**, 422 (1987).
7. R. Natarajan and R.S. Schechter, *AIChE J.*, **33**, 1110 (1987).
8. R.W. O'Brein, *J. Coll. Interface Sci.*, **92**, 204 (1983).
9. R.W. O'Brein and R.J. Hunter, *Can. J. Chem.*, **59**, 1878 (1981).
10. T. Okubo, *J. Coll. Interface Sci.*, **125**, 380 (1988).
11. R.W. O'Brein and D.N. Ward, *J. Coll. Interface Sci.*, **121**, 402 (1988).
12. L. Benguigui and I.J. Lin, *Electrostatics*, **21**, 205 (1988).
13. J.G. Harfield and R.C. Bunker, *Filtration and Separation*, **25**, 412 (1988).
14. M.C. Fair and J.L. Anderson, *J. Coll. Interface Sci.*, **127**, 388 (1989).
15. M.W. Kozak and J. Davis, *J. Coll. Interface Sci.*, **127**, 497 (1989).
16. F.A. Morrison and J.J. Stukel, *J. Coll. Interface Sci.*, **33**, 88 (1970).
17. H.J. Keh and J.L. Anderson, *J. Fluid Mech.*, **153**, 417 (1985).
18. N.G. van Kampen, *Stochastic Processes in Physics and Chemistry*, North-Holland (1983).
19. J. Happel, *Trans. N.Y. Acad. Sci.*, **20**, 404 (1958).
20. B. Gal-Or and S. Waslo, *Chem. Eng. Sci.*, 1431 (1968).
21. S. Kuwabara, *J. Phys. Soc. Japan*, **14**, 527 (1959).
22. D. Edwards, M. Shapiro and H. Brenner, *Phys. Fluids A*, **2**, 45 (1990).
23. Zick and Homsy, *J. Fluid Mech.*, **115**, 13 (1982).
24. Sangani and A. Acrivos, *Int. J. Multiphase Flow*, **8**, 343 (1982).
25. Sorensen and Stewart, *Chem. Eng. Sci.*, **29**, 819 (1974).
26. Snyder and Stewart, *AIChE J.*, **12**, 167 (1966).
27. Karabellas, *Chem. Eng. Sci.*, **28**, 673 (1973).
28. S. Haber, Electroosmosis in Porous Media (submitted) (1990).

29. J. Happel and H. Brenner, *Low Reynolds Number Hydrodynamics*, Noordhoff (1973).
30. M.E. O'Neill, *Mathematica*, **11**, 67 (1964).
31. G. Hetsroni, S. Haber and E. Wacholder, *J. Fluid Mech.*, **41**, 689 (1970).
32. S.L. Goren, *J. Fluid Mech.*, **41**, 619 (1970).
33. S. Haber and R. Mauri, *J. Fluid Mech.*, **190**, 201 (1988).
34. R. Mauri and S. Haber, *SIAM*, **46**, 49 (1986).
35. L.H. Dill and H. Brenner, *PhysicoChem. Hydrodynam.*, **3**, 267 (1982).
36. S. Haber and H. Brenner, in *Recent Developments in Structural Continua*, edited by P.N. Kaloni and D. Dekee, Longman/Wiley, N.Y. (1986).
37. I. Frankel and H. Brenner, *J. Fluid Mech.*, **204**, 97 (1989).
38. M.W. Kozak and J. Davis, *J. Coll. Interface Sci.*, **112**, 403 (1986).
39. M. Shapiro and H. Brenner, *J. Aerosol Sci.*, **21**, 97 (1990).
40. M.E. O'Neill and S.R. Majumdar, *Z. Angew. Math. Phys.*, **21**, 164 (1970).
41. M.E. O'Neill and S.R. Majumdar, *Z. Angew. Math. Phys.*, **21**, 130 (1970).

Page missing

Fig 1

Fig. 2

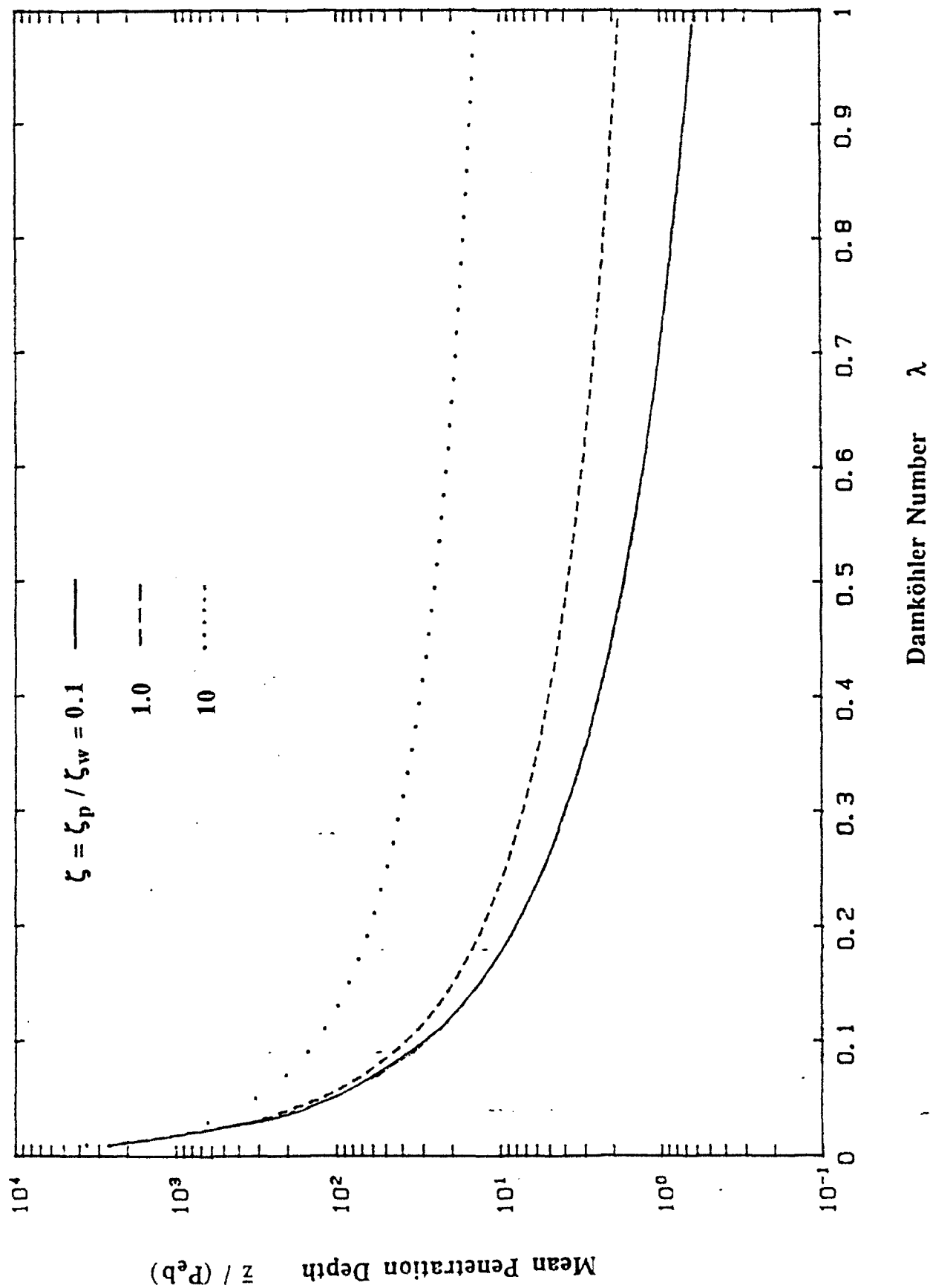
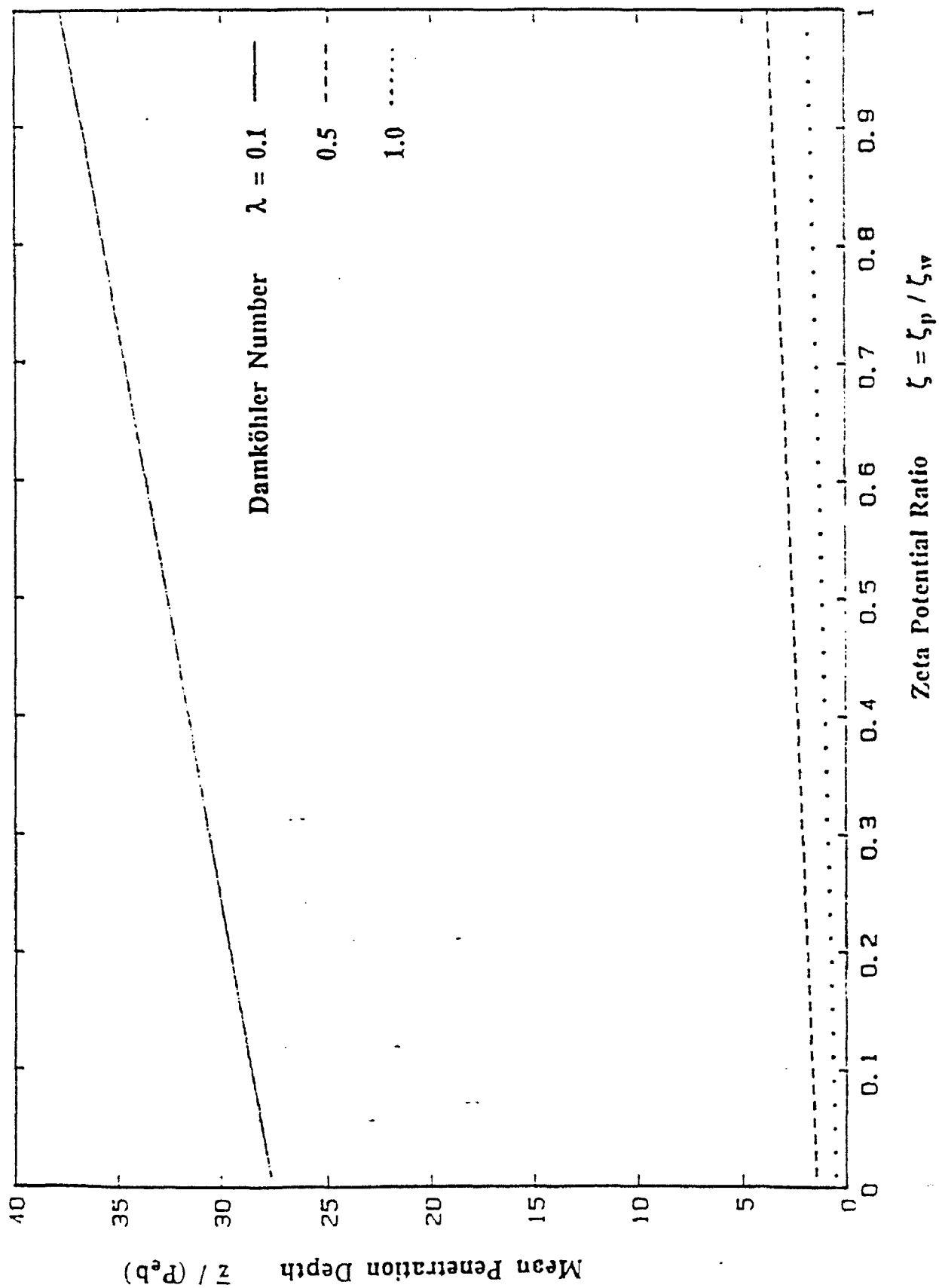


Fig 3



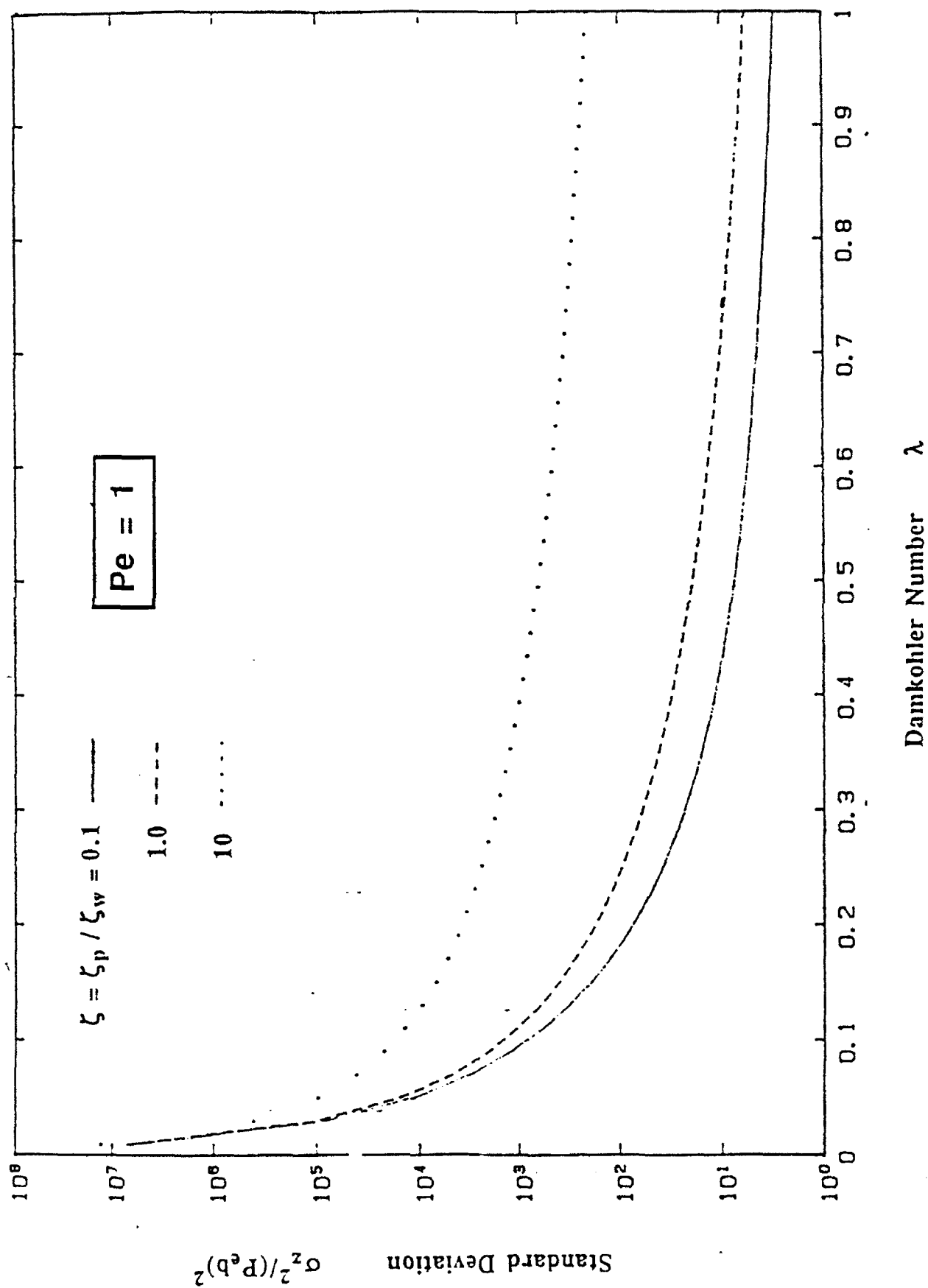
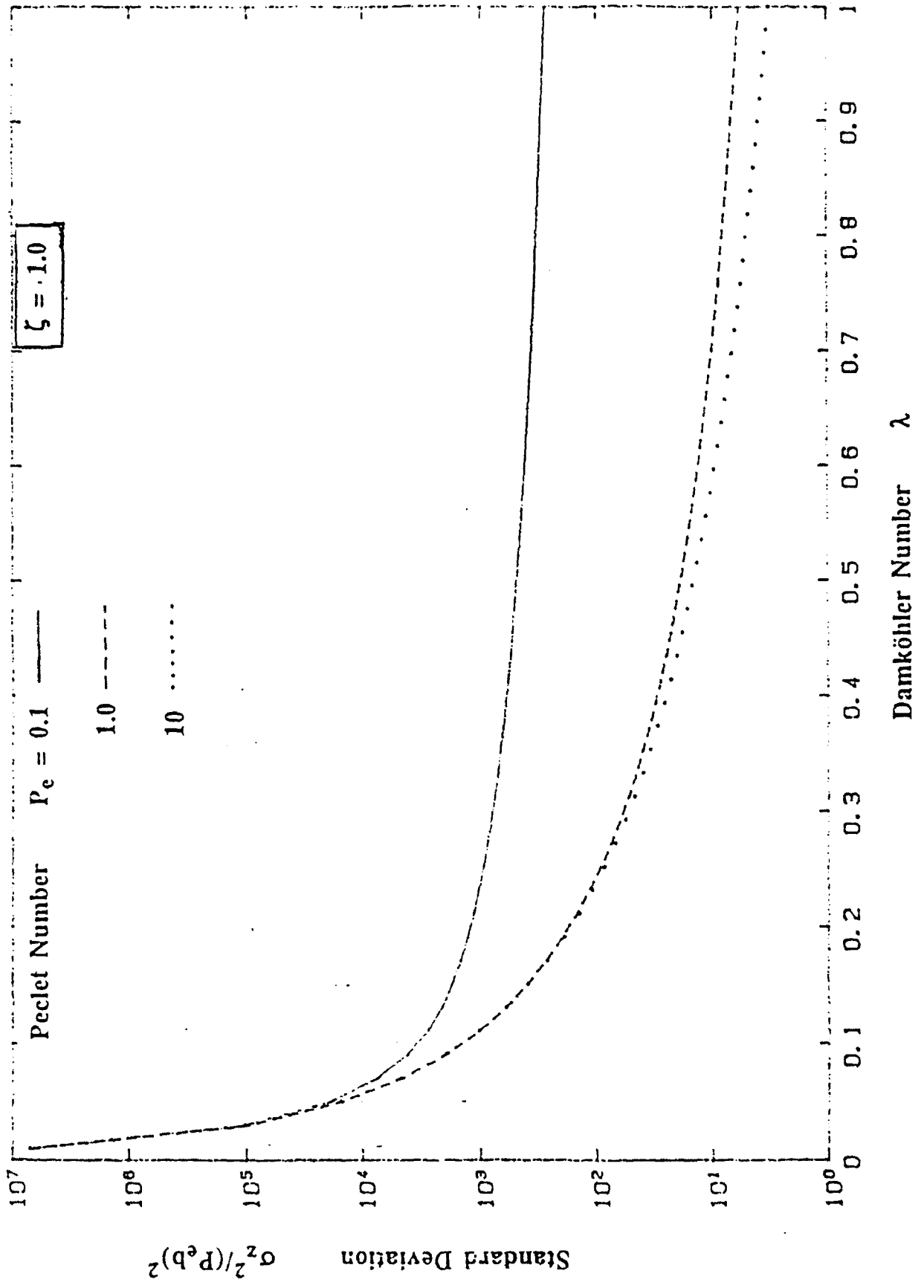


Fig 4



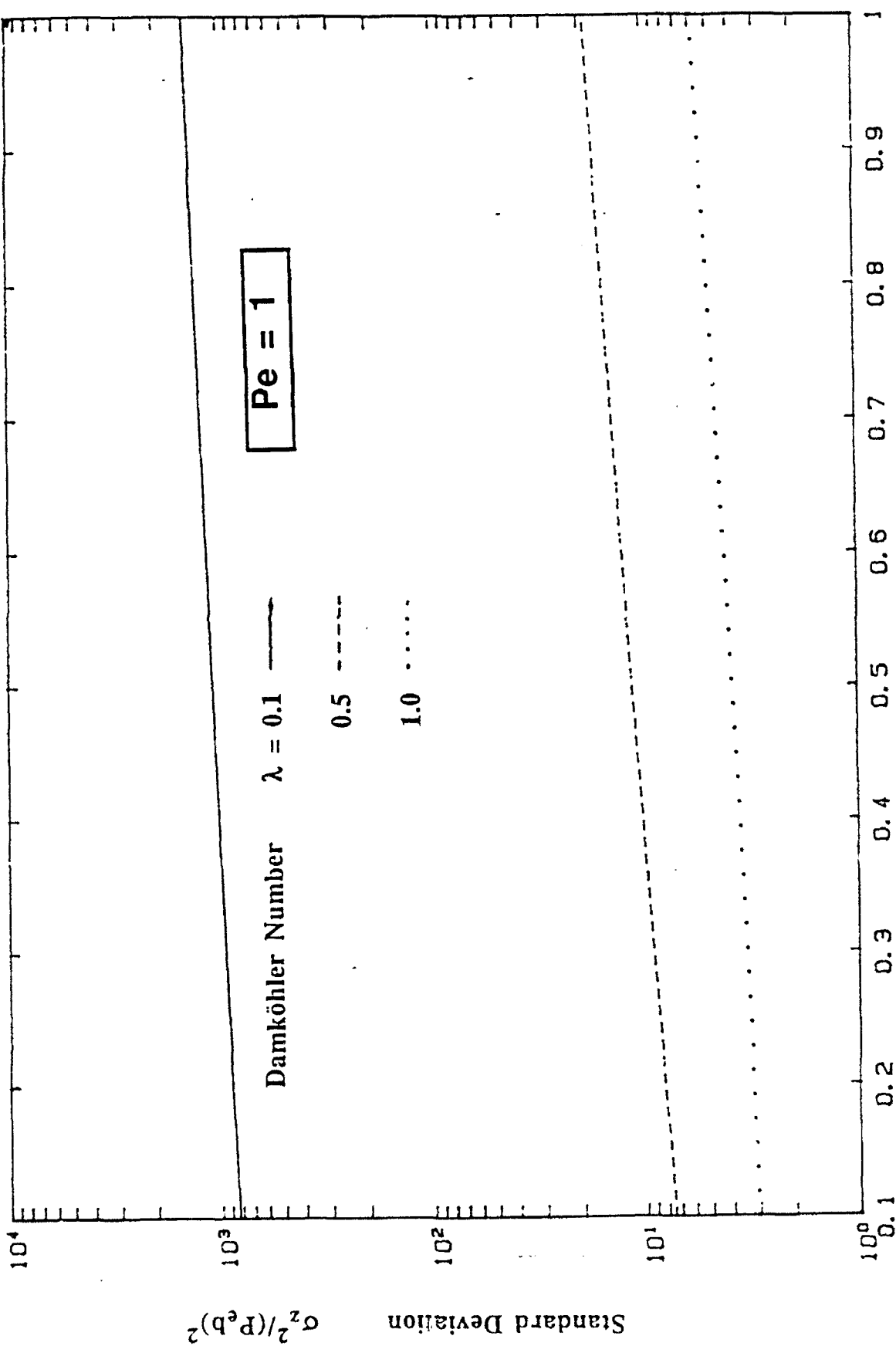


Fig. 6

Fig. 7

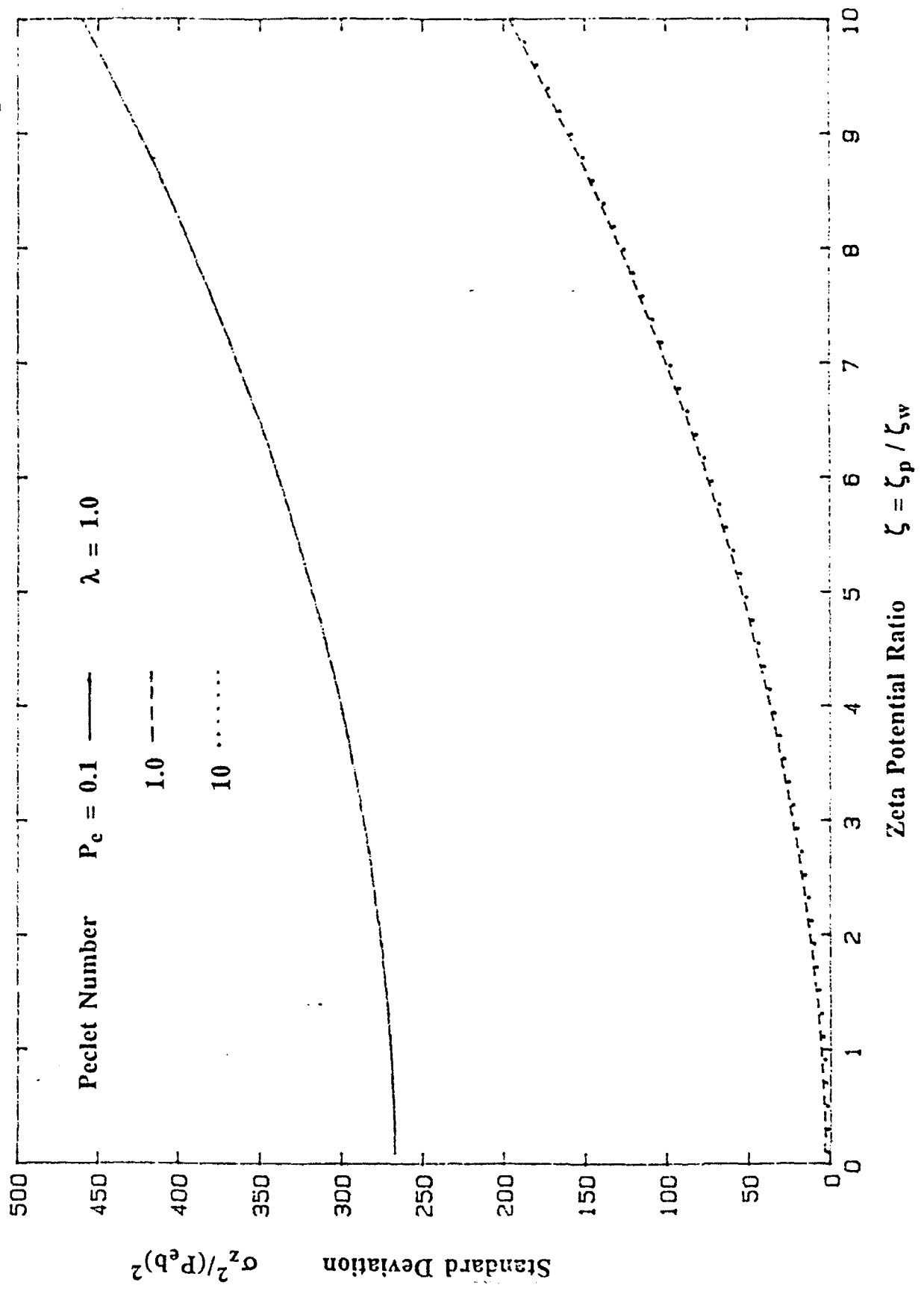


Fig. 8.

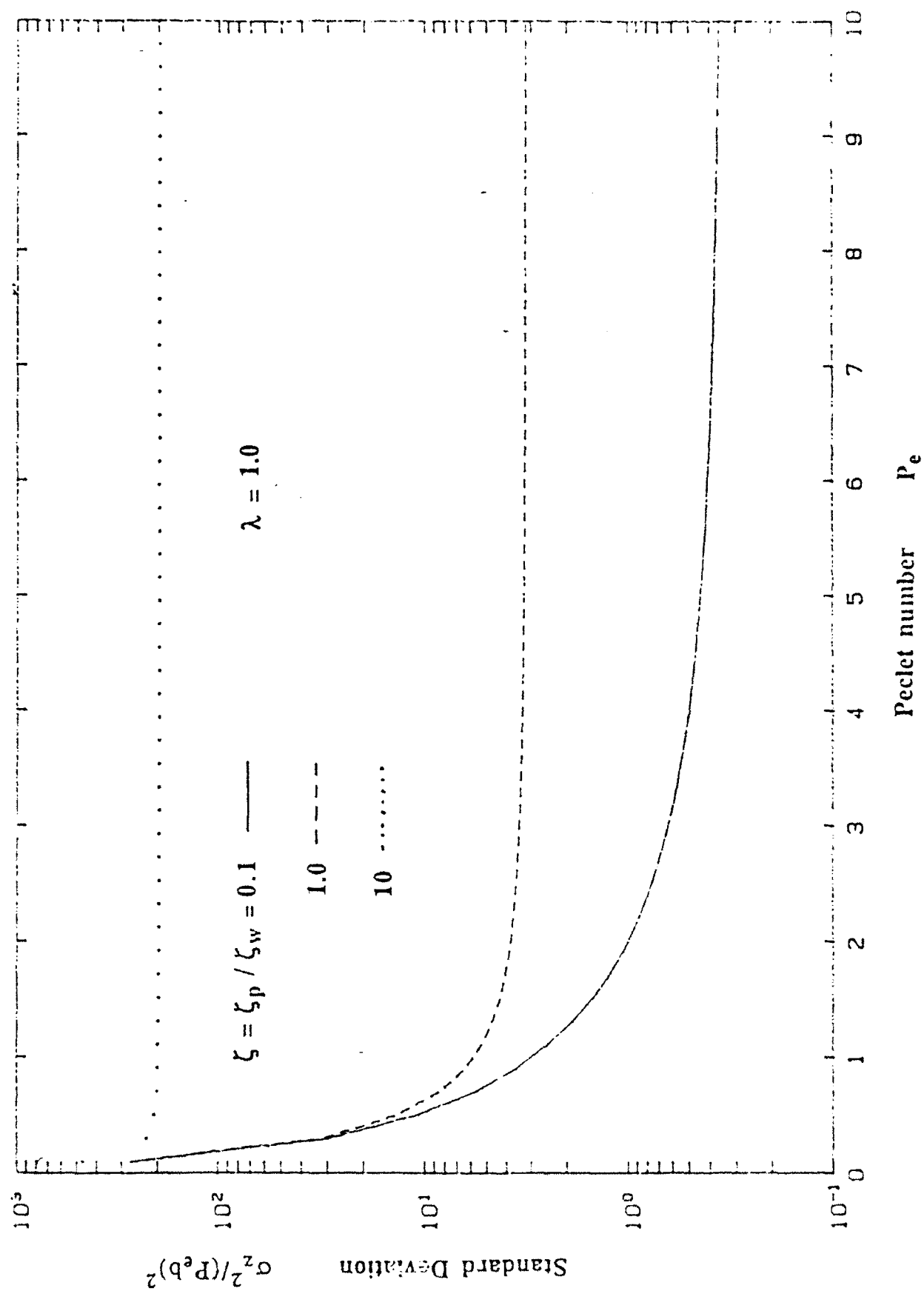
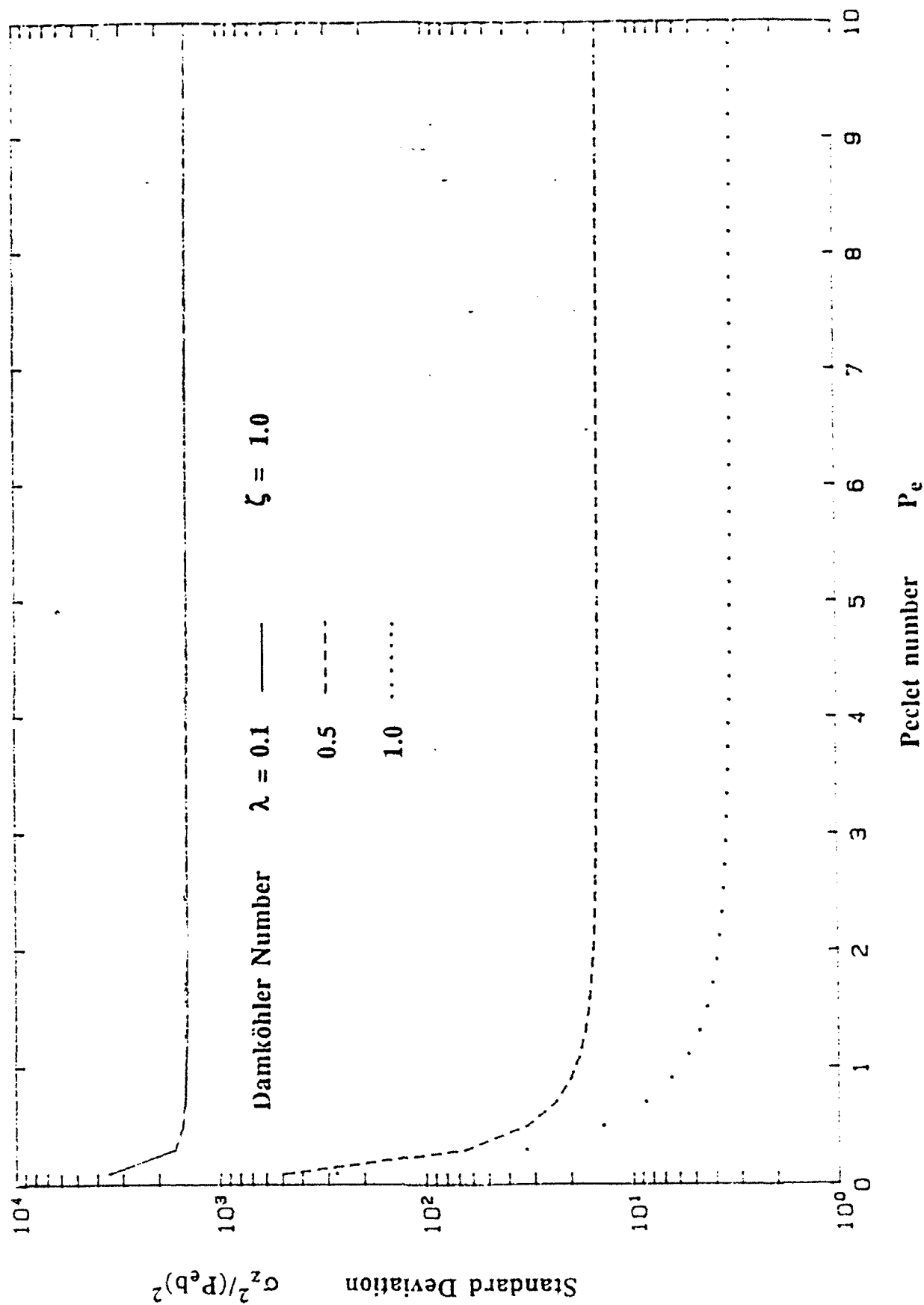


Fig. 9



Deep Electrophoretic Penetration and Deposition of Ceramic Particles inside Porous Substrates

I. Analytical Model

S. Haber and L. Gal-Or

Department of Mechanical Engineering and Institute of Metals,
Technion—Israel Institute of Technology, Haifa 32000, Israel

ABSTRACT

The electrophoretic penetration of colloidal silica particles into a carbon-carbon porous substrate is investigated. The carbon substrate is immersed in a solution containing the particles and positioned between two electrodes. An electric potential gradient between the electrodes is used to drive the solute (silica particles) into the pores. Three driving mechanisms are identified: the hydrodynamic drag force exerted on the particles due to the electroosmotic flow of the solvent inside the pores, the electrophoretic force exerted on the particles, and the stochastic Brownian force due to thermal fluctuations of the solvent molecules. While subjected to these forces, the particles may reach the walls of the pore and the short range van der Waals forces may cause their capturing and deposition onto the walls. The objectives of this paper are to predict the penetration depth of a single ceramic particle moving inside a porous substrate under the effect of an electric potential gradient, to derive the nondimensional parameters characterizing the motion of the ceramic particles, and to gain a physical insight on the various mechanisms governing penetration. Qualitatively, the results are that penetration depths are governed by a favorable (if large) Peclet number and unfavorable (if large) Damköhler number. Quantitative results are also provided.

Deep penetration and deposition of inert species over the interstitial surfaces of a volatile porous substrate has been a major concern of the aero-space industry. Extremely strong, light, and sometimes porous composites (such as carbon-carbon) may undergo undesired processes if exposed to a high temperature oxidizing environment. Chemical vapor deposition (CVD) of inert materials (such as silica, silicon-carbide, etc.) onto the walls of the pores, have been suggested in the past (1-2) to protect the composites from burning or deterioration. Alas, CVD has proven to be extremely slow and only shallow penetration has been detected. A new method to protect porous substrates by electrophoresis is carried out and described in detail in Part II. In essence, an electric potential gradient is used to drive colloidal particles deep into the voids of the porous substrate. The purpose of this paper (Part I) is to provide an overview of the existing theory and mathematical models closely related to deep electrophoretic deposition (DED), to suggest a theory and a mathematical model by which DED can be analyzed and the nondimensional parameters governing the process be obtained, and to predict penetration depths for the given set of parameters.

The motion of a single particle under the effect of electrophoretic forces has first been addressed by Smoluchowski (1918) and subsequently by many others (3-15). Smoluchowski predicted that a rigid spherical particle possessing an electric double layer and embedded in an unbounded flow field would be forced to move if subjected to an electrical potential gradient. The mobility of the particle depends linearly upon the dielectric constant of the fluid, the potential gradient, the zeta potential of the particle, and is inversely proportional to the fluid viscosity. Wall effects were accounted for by (16) and (17) for the case of a particle traveling in close proximity to the containing boundaries of the flow field. Keh and Anderson (17) have shown that if electroosmosis is disregarded the particle would experience an increasing drag force and reduced mobility. It was also shown that, due to the electric field, the insulating rigid walls would induce an electroosmotic flow, its direction depending on the sign of the wall zeta potential. Thus, a neutral particle immersed in the fluid would be dragged by the electroosmotic flow and move with almost identical velocity. In case the particle is also subjected to an electrophoretic force, the particle would move with the combined electrophoretic and electroosmotic velocities. Superposition is allowed due to the linearity of the governing low Reynolds number flow field equations. In addition, a submicron particle would experience an erratic Brownian motion due to the thermal fluctuations of the fluid molecules.

Consequently, deterministic evaluation of the particle path under the combined effects of electroosmosis, electrophoresis, and Brownian motion is invalid and a probabilistic approach must be adopted (18).

The fluid motion inside a porous substrate under the effect of a pressure gradient (known as Darcy's law) has been addressed by many investigators. To derive the micro-pattern of the flow field, unit cell models (19-21) as well as more advanced finite elements approaches for spatially periodic structures (22-27) were applied. However, no equivalent treatment exists for the case of electroosmotic flow through a porous structure, namely, the flow generated under the effect of an electric potential gradient. Since a particle would be dragged by this interstitial electroosmotic flow, its evaluation is of foremost significance if one desires to calculate mean penetration depths of the ceramic particles. A general approach in which Darcy's law is modified so that it would incorporate electroosmotic effects is addressed by us (28) and by others (29).

The second effect to be accounted for is the direct electrophoretic force exerted on a particle traveling inside the small pores. Numerous treatments exist for the low Reynolds number motion of small rigid uncharged particles (30), charged particles (17), wall effects excluded (30), and included (30-33). The fine structure of a porous substrate enveloping a particle was treated in various ways, for instance, a spherical particle traveling along an infinitely long cylinder of circular cross section, a spherical particle embedded in a flow field which is bounded by a spherical envelope with preassumed stress-free (or vorticity-free) boundary conditions, and a small spherical particle moving inside a spatially-periodic lattice of prearranged large spherical particles. Notwithstanding, all of the previous models assumed the no-slip boundary conditions which are correct for an uncharged particle surface, whereas the electrophoretic force is applied via a unique slip boundary condition. Thus, the known approaches must be altered to handle this new set of boundary conditions (17).

The third effect, the random Brownian force due to the thermal fluctuations of the fluid, has been treated by two different methods in the past. The first method applies a Lagrangian viewpoint of the problem utilizing Langevin's equation to evaluate mean particle velocity and dispersion (34, 35). The second method applies an Eulerian approach where a Fokker-Planck equation is formulated and a moment method developed by Taylor-Aris is utilized to derive the pertinent means (36-38). Generally, it is accepted (and for linear cases can be proven (18)) that these methods

would yield identical results and the choice between the methods is a matter of convenience.

In the next section we shall address the three foregoing mechanisms where we provide a short recapitulation of the basic equations governing electroosmotic flow in porous structures derived elsewhere (28), a model for the motion of a particle in a long cylindrical tube under the effect of an electric field, (a model simulating the motion of a particle in a porous structure), and a model for the stochastic behavior of the Brownian particle under the combined effect of electroosmosis and electrophoresis utilizing Fokker-Planck's equation.

Method of Solution

Electroosmosis in porous media.—The flow through porous media generated by an electric potential gradient was analytically investigated in (39) using a cell model and by (28) using a simple approach based on the known solution of the flow field through a long circular tube (in close similarity to one of the approaches used to analytically prove Darcy's law). Similar approaches for pressure driven flows were used to determine filtration efficiencies in porous substrates (40). For the sake of completeness we provide in the Appendix a short recapitulation of the basic assumptions and results presented in (28), a paper which was recently submitted for publication. We shall follow its symbol definition and use its main result (Eq. [A-10]) to evaluate the electroosmotic velocity developed inside a porous slab.

Assume the very simple case of an infinite slab of thickness c , which is subjected to an electric potential drop $\phi_2 - \phi_1$ and a zero pressure gradient (along, say, the z direction). The steady-state solutions of Eq. [A-10] for the electric potential inside the slab ϕ and the interstitial velocity v are simply

$$\phi = \phi_1 + (\phi_2 - \phi_1)z/c, \quad v = U' = -\gamma(\phi_2 - \phi_1)/c \mathbf{k} \quad [1]$$

where γ is the electroosmotic permeability defined in Eq. [A-6].

Thus, the electroosmotic velocity through the slab is uniform and constant. We adopt the symbol U' for the velocity solution of this simple case and shall apply it later in the paper.

Electrophoretic motion of a particle.—The electrophoretic velocity U' of a small rigid spherical particle suspended in an unbounded flow field of viscosity η and subjected to an external electric potential gradient $E = -\nabla\phi$ was first obtained by Smoluchowski

$$U' = -\frac{\epsilon\zeta_p}{4\pi\eta} \nabla\phi \quad [2]$$

where ζ_p is the zeta potential over the particle interface and ϵ is the dielectric constant of the fluid. The basic assumptions made to derive Eq. [2] are that the Debye screening length is much smaller than the particle dimension and that the particle translates in an unbounded flow field.

If the particle translates at close proximity to a rigid surface, wall effects must be accounted for (17). Notwithstanding, for particle dimensions which are more than ten times smaller than its distance to the wall, Smoluchowski's equation is an excellent approximation (if no electroosmotic flow exists).

It is a well known result from the theory of low Reynolds number flows (41, 42) that a particle approaching a rigid wall (subjected, for instance, to gravity forces) will experience a growing hydrodynamic resistance which at the limit of zero gap increases to infinity. However, the condition of slip velocity over the particle boundaries will cause that resistance to grow in a slower manner up till a gap of the order of the Debye screening length. An exact treatment of this hydrodynamically singular behavior awaits exploration. However, over these very small distances one has to consider other surface forces (e.g. London-van der Waals) which eventually lead to the attraction of the particle to the walls. Thus, it seems reasonable to assume that Smoluchowski's equation can be used as a first order ap-

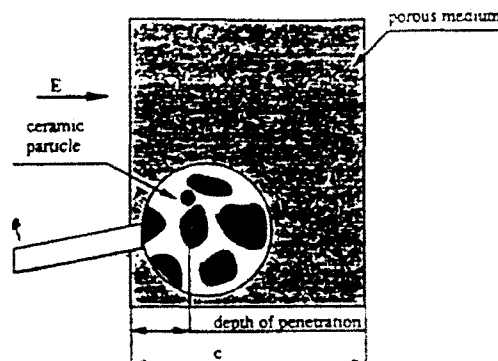


Fig. 1. A slab of porous substrate of thickness c .

proximation for the mobility of a particle over the entire range of particle-wall gaps.

Henceforth, we shall assume that Eq. [2] is applicable for the case of a single rigid particle immersed in a fluid of viscosity η and bounded by the walls of a long tube.

The probability distribution for particle penetration depths.—*Statement of the problem.*—Small submicron particles traveling inside the pores of a porous substrate (see Fig. 1) are strongly affected by the thermal fluctuations of the fluid molecules and experience Brownian motion. This stochastic motion must be superimposed to the deterministic electrophoretic motion and electroosmotic induced velocity which are primarily parallel to the direction of the pore axis. The Brownian motion causes the particle to cross streamlines and sample all possible transverse positions which leads to the phenomenon known as Taylor dispersion.

Tracing down exactly the trajectory of a particle is therefore of no consequence. What we seek is the probability distribution that a particle entering the porous substrate would reach a given depth and not be deposited on the walls during its erratic motion inside the pores. In addition, the very complex and random structure of the porous substrate makes it impossible to obtain more than a formal representation of the equations and boundary conditions. The mathematical formulation must hinge on a simplified geometrical model for the porous structure which would be amenable to mathematical analysis. One of the very common approaches is to treat a single pore as a long circular tube of mean pore diameter, its axis colinear with the local superficial velocity direction. Such a model is handicapped by the fact that no pronounced lateral dispersion of the particles across the porous substrate is allowed. However, since only the mean longitudinal particle motion is sought, such a model is expected to provide valid results on the main parameters affecting penetration depths. Figure 2 describes the basic geometrical and kinematical parameters applicable to the problem.

The general differential equations governing the problem is Fokker-Planck's equation for the probability distribution. In our case it assumes the form

$$\frac{\partial p}{\partial t} + \nabla_z \cdot \mathbf{J}_z + \nabla_r \cdot \mathbf{J}_r + \nabla_\theta \cdot \mathbf{J}_\theta = \frac{1}{\tau_0} \delta(z) \delta(r - r_0) \delta(\theta - \theta_0) \delta(t) \quad [3]$$

where

$$\begin{aligned} \mathbf{J}_z &= U_p - D_z \nabla_z p, \quad \mathbf{J}_r = -D_r \nabla_r p, \quad \mathbf{J}_\theta = -D_\theta \nabla_\theta p \\ D_z &= kTM, \quad D_r = kTM, \quad D_\theta = kTM, \end{aligned} \quad [4]$$

$$U = U'(t) + U''(t)$$

Here $p(r, z, \theta, t/\tau_0, 0, \theta_0)$ stands for the conditional probability that a particle initially located at $(r_0, 0, \theta_0)$ reaches the infinitesimal volume around (r, z, θ) after time t . The polar

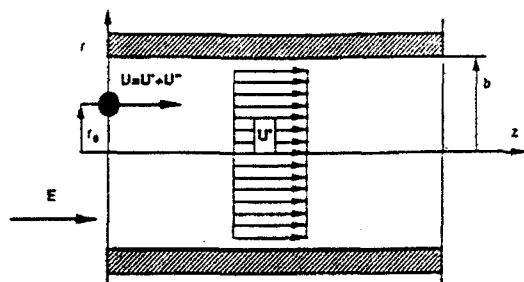


Fig. 2. The definition of the coordinate system and the geometrical model for particle penetration.

coordinate system (r, z, θ) coincides with the pore axis where r stands for the radial distance from the pore axis, z is the distance measured along the pore axis from the pore entrance, and θ is the azimuthal angle. The symbol U stands for the deterministic part of the velocity of the particle, composed of its electrophoretic velocity and the electroosmotic velocity of the suspending field. It must be stressed that the interstitial flow due electroosmosis U^* does not possess the commonly agreed upon parabolic (Poiseuille) form (29). It is very well approximated by plug flow (as shown in Fig. 2) for pore diameters larger than Debye's screening length (a condition normally met). Thus, U is a uniform function with respect to the spatial coordinates as long as the particle diameter is at least ten times smaller than the pore diameter. The flux J_z parallel to the axis of the pore depend on particle convection and diffusion along the pore axis, whereas the fluxes J_r and J_θ arise from diffusion only. The diffusion coefficients D_r , D_θ , and D_z , the first one parallel and the latter perpendicular to the pore axis, depend on the absolute temperature T of the liquid and the respective particle mobilities M_r , M_θ , and M_z . This generalized Stokes-Einstein relationship provided in Eq. [4] accounts for wall effects through the anisotropic form of the mobility tensor. From the physical point of view, it is obvious that the particle would experience unequal hydrodynamic resistance to its motion perpendicular and parallel to the pore axis. The mobility tensor components were approximately evaluated in (30). It is shown that, for particles of radius a small compared to their distance to the wall, the mobilities M_r , M_θ , and M_z are approximately equal and possess the following form

$$M_r = M_\theta = M_z = 1/(6\pi\eta a) \quad [5]$$

The boundary condition which must be satisfied by the probability distribution p is

$$-D \frac{\partial p}{\partial r} = \kappa p \quad \text{at } r = b \quad [6]$$

where κ is the local deposition rate and b stands for the pore mean radius.

The left hand side of [6] represents the diffusional flux of probability towards the pore walls whereas the right hand side represents the probability that a particle located at close proximity to the walls would indeed be deposited. The numerical value of κ depends on particle shape and dimension, electrostatic, and hydrodynamic forces and the physical properties of the materials comprising the particles, the porous substrate, and the suspending liquid. Indeed, it is extremely difficult to obtain κ from first principles. A feasible method to attain this end would be to devise an experiment in which one would utilize the given materials of the ceramic particles, porous substrate, and liquid.

As for the downstream boundary condition, we assume that very far from the entrance p vanishes. This is in agreement with the assumption of very long pores or, in other words, that the particle is deposited on the walls long before it reaches the far end. A-posteriori, the solution would provide the condition for which this assumption can be justified. In addition, we would assume that the in-

tegral of p over the walls and the bulk of the fluid is unity for all times (this corresponds to assuming that a particle once it entered the pore is not allowed to escape). This condition which is normally applied for Lagrangian formulation of the problem, is also used here. It replaces the traditional Danckwerts' (43, 44) upstream boundary condition which is normally applied for an Eulerian representation of a similar problem. It can be justified if one recalls that the longitudinal dispersion is very small for the very short times the particle stays close to the entrance. In other words, the Brownian migration, which might cause the escape of the particle, is negligibly small compared with the longitudinal distances the particle travels due to convection during the short times it stays close to the entrance.

Analytical solution and results.—It is very useful to state the nondimensional parameters and time scales of the problem before we attempt to obtain an analytical or numerical solution of Eq. [3]. It is easy to show from Eq. [1] that the pertinent time scale within which steady electroosmotic flow can be established is

$$\tau_M = \frac{c}{\gamma E} \quad [7]$$

where E is the externally applied electric field.

Similarly, it can be shown from Eq. [3], [4], and [6] that three time scales exist for the penetration process of Brownian ceramic particles into the porous substrate. The first time scale is linked with the convective term of the Fokker-Planck equation, namely

$$\tau_c = \frac{c}{U} \quad [8]$$

which determines the time it would take the particle to cross the porous slab.

The second time scale is related to the diffusive process, namely, the time it takes a Brownian particle to cross streamlines and sample all radial positions inside the tube

$$\tau_D = \frac{b^2}{D} \quad [9]$$

The third time scale is obtained from boundary condition [6] and determines the deposition rate, namely

$$\tau_R = \frac{b}{\kappa} \quad [10]$$

If we assume that the Brownian particles were introduced into the solution after electroosmotic steady state flow has been established, (U is time independent) nondimensionalization of the Fokker-Planck equation and the associated boundary conditions results in two nondimensional parameters which determine the solution completely. The first parameter can be identified as the Peclet number of the problem

$$Pe = \frac{Ub}{D} = \frac{(U^* + U^*)b}{D} \quad [11]$$

which determines the relative significance of the convective process vis-a-vis the diffusive process.

The second nondimensional parameter, the Damköhler-number, determines the ratio between the diffusion and the deposition time scales, namely

$$\lambda = \frac{\tau_D}{\tau_R} = \frac{\kappa b}{D} \quad [12]$$

Thus, large values of λ mean that the deposition of particles on the cylinder walls is governed mainly by diffusion, whereas small values of λ mean that deposition is controlled by the local deposition rate.

An analytical solution of Eq. [3] (in its nondimensional form) can readily be obtained for the case in which U is inde-

pendent of the radial coordinate r . Since U' and U'' are indeed devoid of radial coordinate dependence for small particle radius to pore diameter ratios, a general solution for p can be obtained. However, the exact initial location of the Brownian particle is of no consequence if particles penetrate the pore at equally probable radial positions and azimuthal angles. It is, therefore, reasonable to define a new unconditional probability distribution function P based on the conditional probability function p as follows

$$P(\eta, \zeta, \tau) = b^2 \int_{A_0} p(\eta, \zeta, \theta, \tau | \eta_0, 0, \theta_0) P(\eta_0, \theta_0) dA \quad [13]$$

where we assume that $P(\eta_0, \theta_0) = 1/A_0$ is the uniform probability distribution of finding a particle at time $t = 0$ at any arbitrary location at the pore entrance and $A_0 = \pi R_0^2$ is the cross-section area of the pore.

The expression for the probability distribution P , as defined by Eq. [13], is independent of the initial azimuthal angle θ_0 and radial position r_0 and though lengthy and tedious manipulations are required it is easier to derive

$$P(\eta, \zeta, \tau) = \frac{1}{\sqrt{\pi\tau}} e^{-\frac{a-Pe\tau^2}{4\tau}} \sum_{n=1}^{\infty} \left(\int_0^1 \eta' J_0(\alpha_n \eta') d\eta' \right) \frac{\alpha_n^2 J_0(\alpha_n \eta)}{(\lambda^2 + \alpha_n^2) J_0^2(\alpha_n)} e^{-\alpha_n^2 \tau} \quad [14]$$

Here

$$\eta = \frac{r}{b}; \quad \zeta = \frac{z}{b}; \quad \tau = \frac{Dt}{b^2} \quad [15]$$

and J_0 is the Bessel function of zero order.

The α_n parameters are determined by the following indicial equation

$$\alpha_n J_1(\alpha_n) = \lambda J_0(\alpha_n) \quad [16]$$

which has a countable number of roots α_n ($n = 1, 2, \dots$).

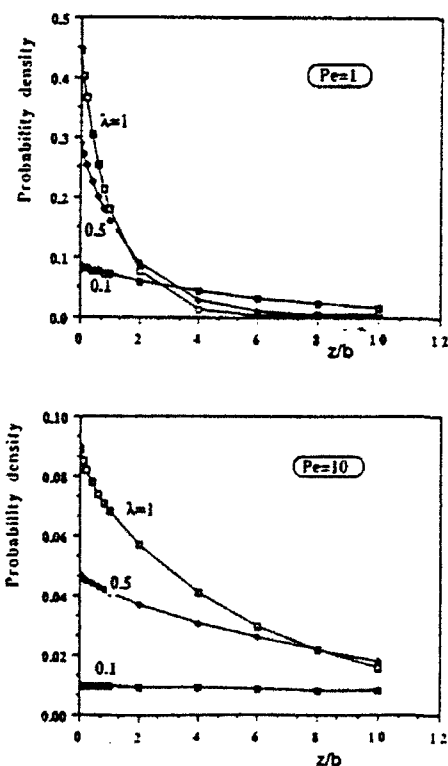


Fig. 3. The probability density P_z vs. the downstream nondimensional distance z/b .

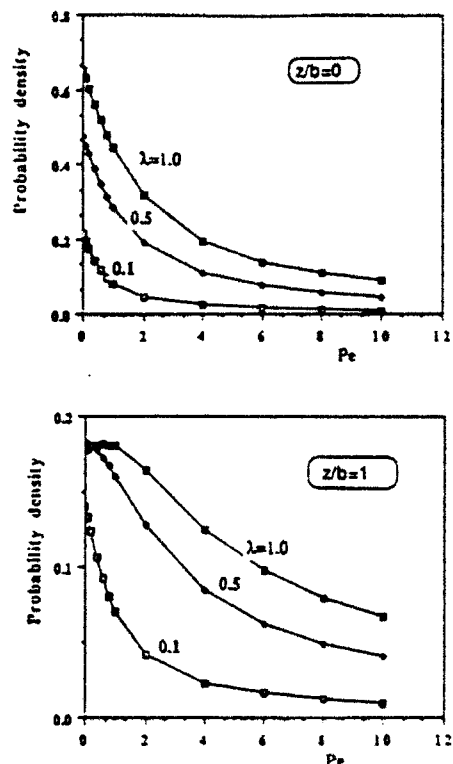


Fig. 4. The probability density P_z vs. the electrophoretic Peclet number.

It is interesting to note that P is independent of θ due to the inherent axial symmetry of the problem.

Equations [14] and [16] can now be utilized to numerically compute more physically meaningful probabilities. For example, if we are to inquire what is the probability per unit length that a particle has deposited over the pore

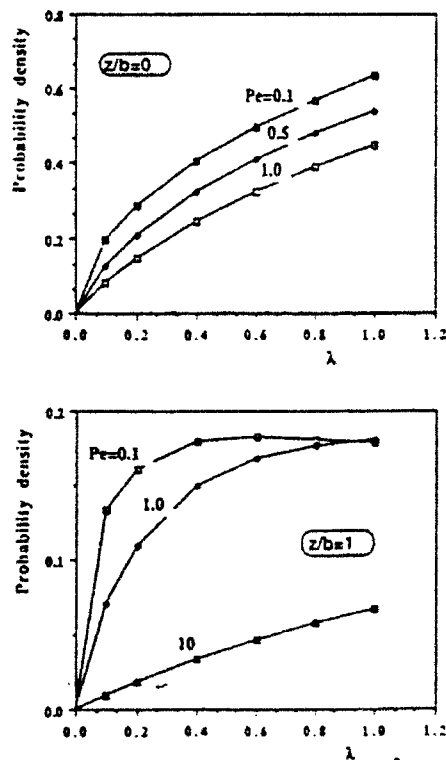
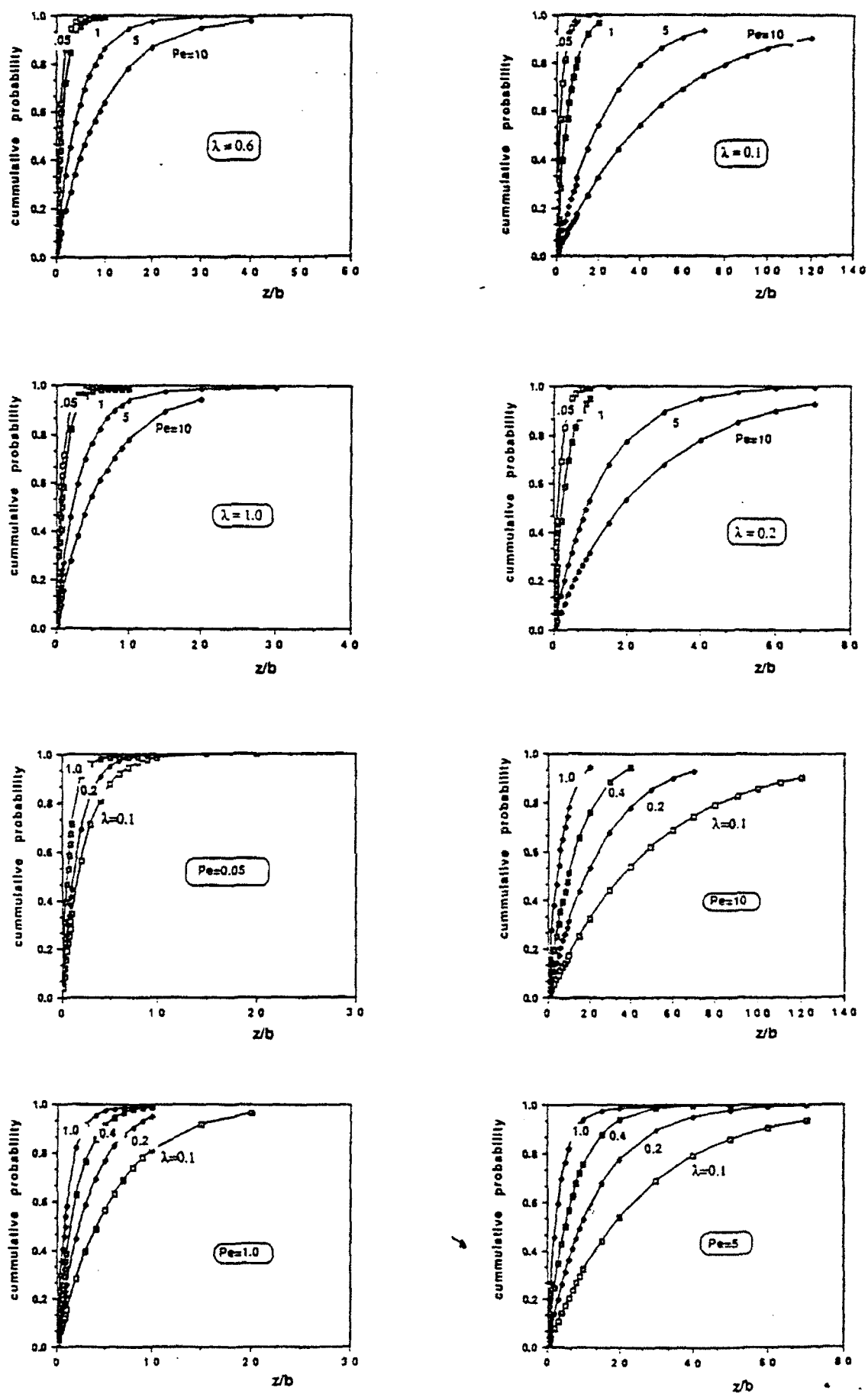


Fig. 5. The probability density P_z vs. the Damkohler number.

Fig. 6. The cumulative probability P_c vs. the downstream nondimensional distance z/b .

walls, a very long time after it has been introduced into the system, we simply calculate

$$P_d(z; P_e, \lambda) = - \int_0^z \left[\frac{\partial P}{\partial \eta} \right]_{\eta=1} d\tau = \lambda \int_0^z [P]_{\eta=1} d\tau \quad [17]$$

where the right hand side equality stems from boundary condition [6]. It is easy to show that

$$P_d(z; P_e, \lambda) = 4\lambda \sum_{n=1}^{\infty} \left(\int_0^1 \eta' J_0(\alpha_n \eta') d\eta' \right) \frac{\alpha_n^2}{(\lambda^2 + \alpha_n^2) J_0(\alpha_n) \sqrt{P_e^2 + 4\alpha_n^2} + 4\alpha_n^2 (\sqrt{P_e^2 + 4\alpha_n^2} - P_e)} \quad [18]$$

Figure 3 illustrates the numerically computed values of P_d as a function of z for Peclet numbers 1 and 10 and λ values 0.1, 0.5, and 1. The trend is very clear. High values of λ cause the probability density to decay very fast with z . This means that most of the particles would deposit on the walls very close to the pore entrance and deep penetration cannot be achieved. Figure 4 illustrates P_d as a function of Peclet number P_e for λ values 0.1, 0.5, and 1 and for given pore depths ($z = 0$ and 1). It manifests the very important role of particle convection. The probability density drops significantly with the Peclet number P_e , thus a more even distribution of particles is expected along the pore axis and deeper penetration is expected. In Fig. 5 the probability density is directly plotted vs. the Damköhler number λ for Peclet values 0.1, 1.0, and 10 and two values of z , showing again the fast accumulation of particles near the pore entrance for small values of Peclet number.

Figure 6 illustrates the foregoing conclusions vividly. Based on the probability density P_d we can define a new cumulative probability

$$P_c = \int_0^z P_d d\zeta \quad [19]$$

which can physically be interpreted as the long time ratio between the number of particles deposited over the pore walls up to pore depth z/b and the total number of particles introduced at $z = 0$ and $t = 0$. The figures elucidate the fact that deep penetration (more than hundred pore diameters) can be achieved only for very low Damköhler numbers ($\lambda < 0.1$) and for very high Peclet numbers ($Pe > 100$). Cases in which $\lambda = 0$ would obviously result in the deepest penetration. It might be achieved by introducing a repelling force between the particles and the pore walls, stronger than van der Waals forces. The asymptotic value of the cumulative probability for large values of z is always unity, since after a long time the probability that a particle has been deposited anywhere over the pore walls is unity (the particle cannot disappear).

Figure 7 summarizes the foregoing results. We define the penetration depth as the z/b value for which $P_c = 0.9$. In other words, 10% of the particles would penetrate deeper than the value shown in the figure for a given set of parameters, the Damköhler number λ and the Peclet number P_e . Obviously, the 0.9 numerical value chosen for P_c is quite arbitrary and a lower or a higher percentage could have been chosen. The basic interpretation of the results, however, would remain unaltered. It is obvious from Fig. 7 that the penetration depth for a given value of λ grows almost linearly with the Peclet number (which is not at all surprising). The slope of the curves depends strongly on λ ; the smaller the λ value the deeper the particle penetration.

Conclusions

The following general conclusions can be drawn from the foregoing analysis. Deep penetration and coating is feasible by electrophoretic processes. Enhanced penetration is obtained for large electrophoretic Peclet numbers and small Damköhler numbers. Electroosmosis (directly dependent on the electroosmotic permeability γ and thus on the sign of the wall zeta potential) increases the Peclet number and thus penetration only if the electroosmotic

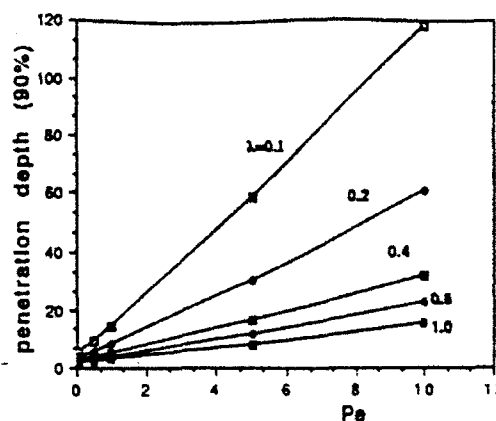


Fig. 7. Penetration depth (defined as the downstream value of z/b for which there is 90% probability that the particle has deposited after a very long time) vs. the electrophoretic Peclet number (the Damköhler number is used as a parameter).

and electrophoretic velocities coincide in direction, i.e. ζ_w and ζ_p possess the same signs. The diffusion coefficient of the colloidal particles has a dual effect: Decreasing diffusion coefficient causes increasing Peclet number which has a favorable effect on penetration depth. Decreasing diffusion coefficient causes increasing deposition rate which has an unfavorable effect on penetration depth. The process can be controlled by a judicious selection of particle size and concentration, solution properties, electric field intensity and its time protocol.

Quantitative comparison with experimental results that we presented in Part II is not yet possible since only global results of total mass deposition inside the pores was measured and not how mass is distributed inside the porous slab (which is the main result we presented in this paper). Further experimental work is required to analyze this very important feature of deep electrophoretic deposition, which will determine its advantage over other coating processes. On the other hand, the total of mass deposited inside the porous slab depends on the ratio between the flux of particles depositing over the exterior surface of the slab and flux of particles penetrating it. Thus, further theoretical work is required to determine this ratio dependence on the process parameters before comparison can be made with the experiments conducted in Part II.

Notwithstanding, several recommendations based on the theoretical results were made and found in qualitative agreement with experiment, e.g. the electroosmotic permeability depends linearly on the ratio ϵ/η which depends solely on solvent properties. Enhancement of penetration is predicted to occur if this ratio is high. Several liquids were examined (water, isopropanol, ethanol, and pentanol) and water possessing the highest ratio has shown the best results (Fig. 9 in Part II). A rather limited quantitative comparison with Fig. 9 in Part II can be made. We calculate the ratio of SiO_2 percentile of particles deposited inside porous graphite and migrating in a certain solvent to SiO_2 percentile of particles migrating in a given solvent, say, water.

solvent	$\gamma(\text{theory})$	$\gamma(\text{experiment})$
Pentanol	0.052	0.078
Propanol	0.112	0.29
Ethanol	0.283	0.42

where

$$\gamma = \frac{\% \text{SiO}_2(\text{solvent})}{\% \text{SiO}_2(\text{water})}$$

The foregoing table reveals that the trend predicted in this paper is definitely correct and there is a fixed bias which can be attributed to inaccuracies in measurements (difficulty in removing the deposit over the exterior sur-

face of the graphite slab), variations in zeta potentials and mathematical model simplifications.

Acknowledgment

Research sponsored by the Air Force Office of Scientific Research Air Force Systems Command U.S.A.F. under Grant No. AFSOR 89-0474. The U.S. Government is Authorized to reproduce and distribute reprints for Governmental purposes notwithstanding any copyright notation thereon.

Manuscript submitted Feb. 15, 1991; revised manuscript received Oct. 17, 1991.

APPENDIX

The flow through porous media generated by an electric potential gradient is discussed in (28) and is briefly recapitulated.

The governing field equations for the flow through a long circular tube induced by an electric potential gradient are based on Stokes' equations for low Reynolds number flows, i.e.

$$\eta \nabla^2 \mathbf{v} = \nabla p, \quad \nabla \cdot \mathbf{v} = 0 \quad [\text{A-1}]$$

where \mathbf{v} and p are the velocity and pressure fields and η stands for the viscosity of the fluid. The boundary conditions which the velocity field satisfies over the cylinder walls are (17)

$$v_r = \frac{\epsilon \zeta_w}{4\pi\eta} \frac{\partial \phi}{\partial z}, \quad v_z = 0 \quad \text{at } r = b \quad [\text{A-2}]$$

where ϵ is the dielectric constant of the fluid, ζ_w is the zeta potential at the cylinder wall, ϕ stands for the electric potential, b is the radius of the tube and (r, z) are polar coordinates, the z coordinate coinciding with the cylinder axis. It should be noted that the no-slip condition can no longer be applied and in its place we use condition [A-2].

The solution for \mathbf{v} is easily derived for a fully developed flow, namely, $\partial v_r / \partial z = 0$. It is a simple superposition of the effects of the pressure gradient and the electric potential gradient. Integrating over the tube cross section, the mean intersitial velocity is obtained

$$\bar{v}_z = -\frac{b^2}{8\eta} \frac{\partial p}{\partial z} - \frac{\epsilon \zeta_w}{4\pi\eta} \frac{\partial \phi}{\partial z} \quad [\text{A-3}]$$

Integrating over the entire cross section of the porous medium the superficial velocity is

$$v_z = -\frac{\epsilon_p \langle b^4 \rangle / \langle b^2 \rangle}{8\eta} \frac{\partial p}{\partial z} - \frac{\epsilon_p \epsilon \zeta_w}{4\pi\eta} \frac{\partial \phi}{\partial z} \quad [\text{A-4}]$$

where ϵ_p stands for the medium porosity.

Since a homogeneous porous medium contains pores in all possible directions, a similar procedure can be applied for pores oriented along the x and y directions. Expressions similar to [A-4] can be obtained for v_x and v_y and further generalized to derive the following expression for \mathbf{v} in vectorial notation

$$\mathbf{v} = -\Gamma \nabla p - \gamma \nabla \phi \quad [\text{A-5}]$$

where

$$\Gamma = \frac{\epsilon_p \langle b^4 \rangle / \langle b^2 \rangle}{8\eta}, \quad \gamma = \frac{\epsilon_p \epsilon \zeta_w}{4\pi\eta} \quad [\text{A-6}]$$

Here Γ and γ can be viewed as the hydrodynamic and electric permeabilities, respectively. Equation [A-5] can be viewed as a generalization of Darcy's law for the case where an electrical potential gradient as well as a pressure gradient is imposed over a porous medium. It is obvious that these two forces are decoupled and a potential gradient alone can induce electroosmotic flow inside a porous structure. Increasing the electrical permeability, γ , would cause an increase in the electroosmotic flow. Thus, an increase in medium porosity, fluid dielectric constant, and zeta-potential of the pore walls and decrease in fluid viscosity would cause enhanced flow through a porous structure for a given potential gradient.

In addition, one must satisfy mass conservation which results in the following continuity equation for incompressible fluid

$$\nabla \cdot \mathbf{v} = 0 \quad [\text{A-7}]$$

Equations [A-5] and [A-7] and the appropriate boundary conditions on ϕ and p do not constitute a complete set by which the velocity, pressure, and potential fields can be evaluated. An additional relation between the flux of the electric charge \mathbf{j} and the electric potential and pressure gradient can be established in a manner similar to the derivation of Eq. [A-5]

$$\mathbf{j} = -\gamma \nabla p - K \nabla \phi \quad [\text{A-8}]$$

where K is the electric conductivity. It is interesting to note that γ appears both in Eq. [A-5] and Eq. [A-8] in full agreement with Onsager's reciprocal rule. The exact evaluation of K is of no interest at the moment and will not be addressed. Similar to Eq. [A-7] we obtain

$$\nabla \cdot \mathbf{j} = 0 \quad [\text{A-9}]$$

which is simply Kirchhoff's law applied to a porous medium.

Utilizing Eq. [A-5], [A-7], [A-8], and [A-9] it is easy to show that ϕ and p can be decoupled and satisfy the following equations for a homogeneous medium

$$\nabla^2 \phi = \nabla^2 p = 0 \quad [\text{A-10}]$$

i.e., ϕ and p are harmonic functions which can easily be derived for a given set of boundary conditions.

Equations [A-5], [A-8] and [A-10] constitute the main results of (28).

REFERENCES

1. F. Christin, R. Naslain, and C. Bernard, in "Chemical Vapor Deposition/1979," T. Sedgewick and H. Lydtin, Editors, PV 79-3, p. 499, The Electrochemical Society Softbound Proceedings Series, Princeton, NJ (1979).
2. F. Christin, L. Heraud, J. Choury, R. Naslain, and P. Hagenmuller, in "Proc. 3rd European CVD Conf.," Neuchatel (1980).
3. F. A. Morrison, *J. Coll. Interface Sci.*, **34**, 210 (1970).
4. R. W. O'Brien and L. R. White, *J. Chem. Soc. Faraday II*, **74**, 1607 (1978).
5. A. Delgado, F. Gonzalez-Caballero, and G. Pardo, *J. Non-Equilibrium Therm.*, **10**, 251 (1985).
6. C. F. Zukoski and D. A. Saville, *J. Coll. Interface Sci.*, **115**, 422 (1987).
7. R. Natarajan and R. S. Schechter, *AIChE J.*, **33**, 1110 (1987).
8. R. W. O'Brien, *J. Coll. Interface Sci.*, **92**, 204 (1983).
9. R. W. O'Brien and R. J. Hunter, *Can. J. Chem.*, **59**, 1878 (1981).
10. T. Okubo, *J. Coll. Interface Sci.*, **125**, 380 (1988).
11. R. W. O'Brien and D. N. Ward, *ibid.*, **121**, 402 (1988).
12. L. Benguigui and I. J. Lin, *Electrostatics*, **21**, 205 (1988).
13. J. G. Harfield and R. C. Bunker, *Filtration and Separation*, **25**, 412 (1988).
14. M. C. Fair and J. L. Anderson, *J. Coll. Interface Sci.*, **127**, 388 (1989).
15. M. W. Kozak and J. Davis, *ibid.*, **127**, 497 (1989).
16. F. A. Morrison and J. J. Stukel, *ibid.*, **33**, 88 (1970).
17. H. J. Keh and J. L. Anderson, *J. Fluid Mech.*, **153**, 417 (1985).
18. N. G. van Kampen, "Stochastic Processes in Physics and Chemistry," North-Holland (1983).
19. J. Happel, *Trans. N.Y. Acad. Sci.*, **20**, 404 (1958).
20. B. Gal-Or and S. Waslo, *Chem. Eng. Sci.*, **23**, 1431 (1968).
21. S. Kuwabara, *J. Phys. Soc. Japan*, **14**, 527 (1959).
22. D. Edwards, M. Shapiro, and H. Brenner, *Phys. Fluids A*, **2**, 45 (1990).
23. A. A. Zick and G. M. Homsy, *J. Fluid Mech.*, **115**, 13 (1982).
24. A. S. Sangani and A. Acrivos, *Int. J. Multiphase Flow*, **8**, 343 (1982).
25. J. P. Sorensen and W. E. Stewart, *Chem. Eng. Sci.*, **29**, 819 (1974).
26. L. J. Snyder and W. E. Stewart, *AIChE J.*, **12**, 167 (1966).
27. A. J. Karabellas, T. H. Wegener, and T. J. Hanratty, *Chem. Eng. Sci.*, **28**, 673 (1973).
28. S. Haber, *Electroosmosis in Porous Media* (submitted) (1990).
29. R. Datta and V. R. Kotamarthi, *AIChE J.*, **36**, 916 (1990).
30. J. Happel and H. Brenner, "Low Reynolds Number

- Hydrodynamics," Noordhoff (1973).
31. M. E. O'Neill, *Mathematica*, 11, 67 (1964).
 32. G. Hetsroni, S. Haber, and E. Wacholder, *J. Fluid Mech.*, 41, 689 (1970).
 33. S. L. Goren, *J. Fluid Mech.*, 41, 619 (1970).
 34. S. Haber and R. Mauri, *ibid.*, 190, 201 (1988).
 35. R. Mauri and S. Haber, *SIAM*, 46, 49 (1986).
 36. L. H. Dill and H. Brenner, *PhysicoChem. Hydrodynam.*, 3, 267 (1982).
 37. S. Haber and H. Brenner, in "Recent Developments in Structural Continua," P. N. Kaloni and D. Dekee, Editors, Longman/Wiley, New York (1986).
 38. I. Frankel and H. Brenner, *J. Fluid Mech.*, 204, 97 (1989).
 39. M. W. Kozak and J. Davis, *J. Coll. Interface Sci.*, 112, 403 (1986).
 40. M. Shapiro and H. Brenner, *J. Aerosol Sci.*, 21, 97 (1990).
 41. M. E. O'Neill and S. R. Majumdar, *Z. Angew. Math. Phys.*, 21, 164 (1970).
 42. M. E. O'Neill and S. R. Majumdar, *ibid.*, 21, 180 (1970).
 43. P. V. Danckwerts, *Chem. Engng. Sci.*, 2, 1 (1953).
 44. R. A. Novy, H. T. Davis, and L. E. Scriven, *ibid.*, 45, 1515 (1990).

Deep Electrophoretic Penetration and Deposition of Ceramic Particles Inside Porous Substrates

II. Experimental Model

L. Gal-Or, S. Liubovich, and S. Haber

Department of Mechanical Engineering and Institute of Metals Technion,
Israel Institute of Technology, Haifa 32000, Israel

ABSTRACT

The objective of the present study was to experimentally evaluate the feasibility of depositing ceramic particles on the surface of a porous substrate and inducing them into it by electrophoresis. It was demonstrated that it is possible to charge and electrophoretically deposit both oxide (fused and colloidal SiO_2) and nonoxide (SiC and SiN) ceramics on a conductive graphite substrate. It was also shown that ceramic particles are induced into porous graphite, and that under optimal conditions the whole cross section of the specimens was penetrated. The amount of induced material was found to increase with the ratio of dielectric constant to viscosity (ϵ/η) of the solvent, as well as with particle concentration and field intensity. However, due to simultaneous buildup of an overlying deposit, penetration as a function of deposition time reaches a plateau prior to the filling of the whole pore volume.

Electrophoretic deposition is obtained via migration of nonconductive electrically charged particles in an electric field towards one of the electrodes.

Two different charging modes are attributed to ceramic particles (1); a dissociation mode, such as the dissociation of silanol groups present in silica: $\text{SiOH} + \text{OH}^- \rightarrow \text{SiO}^- + \text{H}_2\text{O}$ (negatively charged particles), and an absorption mode, such as the absorption of H^+ from water or from weak acids: $n\text{Al}(\text{OH})_3 + \text{HNO}_3 \rightarrow [\text{Al}(\text{OH})_3]_n^+ + n\text{H}^+ + n\text{NO}_3^-$ (positively charged particles).

Usually the polarity of the particles has to be determined experimentally, as the charge is acquired spontaneously on mixing the particles with the solvent, and it may be reversed upon addition of ionic compounds.

The surface charge, once formed, is then balanced by ions of an opposite charge derived from the solution, and thus a double layer is formed around it.

According to the model proposed by Stern, this double layer consists of a rigid part with a linear potential gradient, and a diffuse part with a nonlinear potential gradient termed "zeta potential" (2).

When an electric field is applied to a charged particle, the latter tends to migrate towards the electrode with the opposite charge. Its velocity, however, is slowed down by the drag action of the surrounding double layer, which is pulled in the opposite direction by the field.

The mobility of the particle in an unbounded fluid is derived by equating the electric force with the frictional resistance and the relaxation force. Consequently, the mobility u is given by

$$u = E\epsilon/4\pi\eta [1 + f(kr)]$$

where u = mobility, E = field strength, ϵ = dielectric constant of fluid, ζ = zeta potential of particles, η = viscosity of fluid, $k = 1/\text{double layer thickness}$, and r = radius of particle.

$f(kr)$, which varies between 0 and 1 for small and large values of kr , respectively, represents the relaxation phe-

nomenon, for $k \ll r$, the above expression reduces to the Smolucnowski equation, namely

$$u = (E \times \epsilon \times \zeta) / 4\pi\eta$$

u varies between 0 and 20×10^4 cm/s/v/cm.

The electrophoretic yield is given by

$$y = a \int u E C S dt$$

where a = yield constant, c = conc. of particles, S = area of electrode, and t = time.

In the equations above it is assumed that the contribution of the hydrodynamic velocity to deposition is negligible; its role being confined to maintenance of the suspension. As for the phenomena that take place at the electrode, once the particles reach it, three possibilities are considered.

One hypothesis is that the particles undergo an electrode reaction which neutralizes them. This, however, does not account for the fact that deposits were obtained on a polymeric diaphragm located between two electrodes (4).

The second hypothesis states that the particles are brought to the electrode by a field which exerts sufficient force to overcome their mutual repulsion, thus allowing them to come close enough for the London-van der Waals forces of attraction to predominate (5). According to the Verwey and Overbeek (5), the minimal field strength necessary for this purpose (calculated from the energy of particles interaction) is

$$E = 2F/3\epsilon\zeta r$$

A third hypothesis assumes that secondary processes taking place at the electrode can produce ions which coagulate the particles by discharging them, or produce hydroxides which polymerize and adsorb on particles, thus holding them together (6).

In the previous discussion the assumption was that the particle is suspended in an unbounded fluid. When electro-

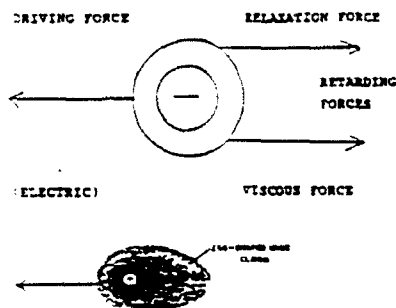


Fig. 1. Egg-shaped ionic cloud and forces acting on a moving particle.

phoresis in porous structures is considered, the presence of rigid boundaries affects both the electric field and the velocity of the particles. According to Anderson (7-9) the effect of the pore wall on particle velocity is threefold: the applied electric field exerts a force on the d.l. at the pore wall if the latter is charged. Electroosmotic flow of the fluid is thus produced, which either augments or opposes the electrophoretic velocity of the particle, depending on the polarity of ζ_p vs. ζ_w ; the pore wall distorts the electric flux around the particle, thereby intensifying the local electric field so that particle velocity is augmented; and the pore wall creates additional viscous stresses in the fluid which slow down the particle. A more detailed analysis of electrophoretic penetration is given in another report on this study (10).

Parameters which affect electrophoretic deposition and penetration are zeta potential of the particles, particle size, particle concentration, dielectric constant and viscosity of solvent, electric field strength, and time.

In this work the feasibility of electrophoretic deposition of several kinds of ceramic particles was first evaluated, after which the effect of several deposition parameters on the amount of colloidal SiO_2 induced into the pores of the substrate was studied.

Experimental Procedure

The deposition and impregnation experiments were carried out on porous graphite substrates. The graphite was UCAR Grade 45, with 48% volume porosity and an average pore size of 60μ . Specimens of $20 \times 20 \times 7$ mm were most often used. The ceramic powders deposited were: colloidal SiO_2 , Pyrogenic Aerosil, submicron with a specific area of $450 \text{ m}^2/\text{g}$; fused SiO_2 - $1-40\mu$; SiC - $<40\mu$; and SiN - $0.2-1.0\mu$. The ceramic particles were suspended in water, isopropanol, ethanol, and pentanol. The particle concentrations were 3, 13, and 30 g/l.

Deposition was carried out at constant voltage, with the current decreasing with time. Electric field strength was varied between 5 and 150 V/cm and deposition time between 5 and 120 min.

Prior to deposition, specimens were rinsed with acetone for 5 min in an ultrasonic bath. After deposition they were dried in air for 24 h before examination. For quantitative determination of the impregnated material (colloidal SiO_2 only) specimens were weighed before and after deposition to an accuracy of 0.1 mg. In this case the external deposit was removed physically before weighing. As a cross-check, the amount of SiO_2 induced into the porous structure was determined by weighing the residue after burn-off of the graphite at 950°C for 20 h.

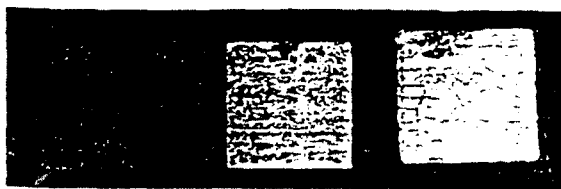


Fig. 2. "Green" deposits of SiC , SiN , and fused SiO_2 (from left to right) on graphite.



Fig. 3. Colloidal SiO_2 deposit on graphite.

The specimens were examined by optical and electron microscopy both on the surface and in cross section. The cross sections were obtained by fracturing the specimen after removal of the external deposit.

Results

A macroscopic view of deposits of SiC , SiN , and fused SiO_2 is seen in Fig. 2. The deposits were in a "green" state (unsintered), and since no special precautions had been taken, the deposits cracked during drying. The colloidal SiO_2 formed a transparent deposit and is therefore presented at larger magnification in the SEM (Fig. 3), which shows a fluffy feather-like substance.

The presence of colloidal SiO_2 in the pores of the graphite was demonstrated by examining the cross section of a specimen by SEM (Fig. 4) and mapping the Si (Fig. 5) on the same area. Clusters of colloidal SiO_2 are seen inside the cross section, the distribution of elemental Si coinciding with the clusters.

Figure 6 shows the skeleton of SiO_2 which remained after burn-off of the graphite at 900°C for 2 h. Presence of the SiO_2 in the cross section of the skeleton is seen in Fig. 7.

Quantitative data of the penetrated SiO_2 as function of solvent properties and deposition parameters, are given in Fig. 8-11. The amount of SiO_2 is expressed as weight percent of the specimen.

The amount of penetrated SiO_2 as a function of the ratio between dielectric constant and viscosity of the solvent is shown in Fig. 8 for constant field. SiO_2 concentration in

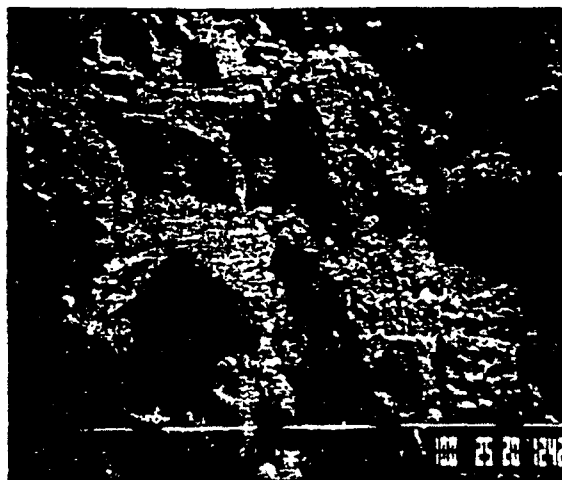


Fig. 4. Colloidal SiO_2 cluster inside the porous graphite (view of a cross section).

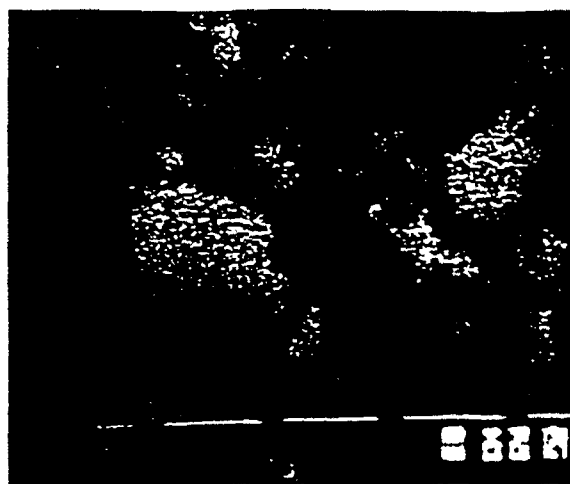


Fig. 5. X-ray mapping for Si on area in Fig. 4.



Fig. 7. Cross section of skeleton in Fig. 6.

solvent, and deposition time. A strong influence of the solvent properties is revealed.

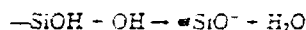
The dependence on the field intensity for three different SiO_2 concentrations in water and for two concentrations in propanol is given in Fig. 9. To each concentration, there corresponds an optimal field. The SiO_2 concentration in the solvent affects the amount of penetrated SiO_2 for otherwise identical conditions; this is seen in Fig. 10 for deposition from water and from propanol.

The effect of deposition time on the amount of penetrated SiO_2 is shown in Fig. 11 again for deposition from water and from propanol.

Discussion

The feasibility of depositing oxide and nonoxide ceramics on an electrically conductive substrate by electrophoresis is demonstrated in Fig. 1.

Charging of the SiO_2 particles is probably the consequence of dissociation of silanol groups in the silica

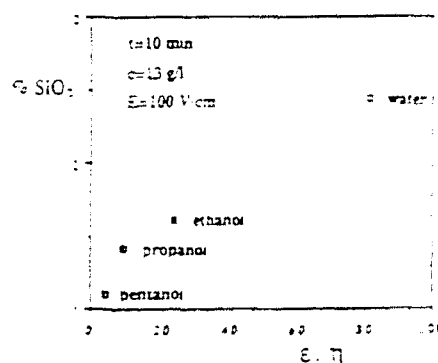
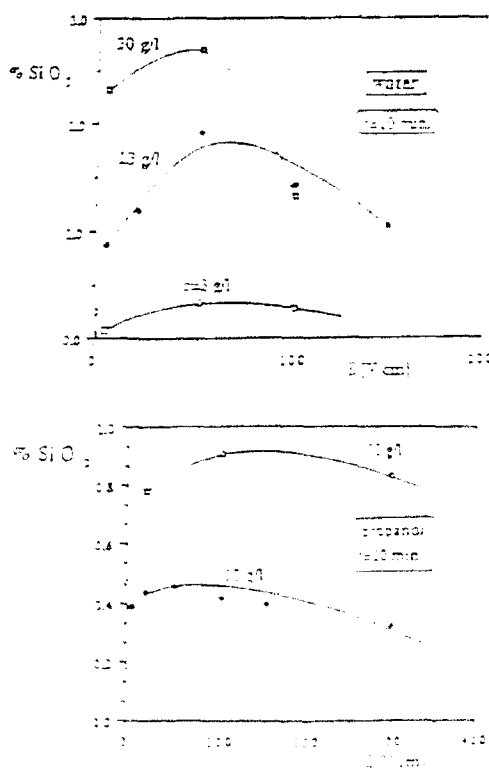
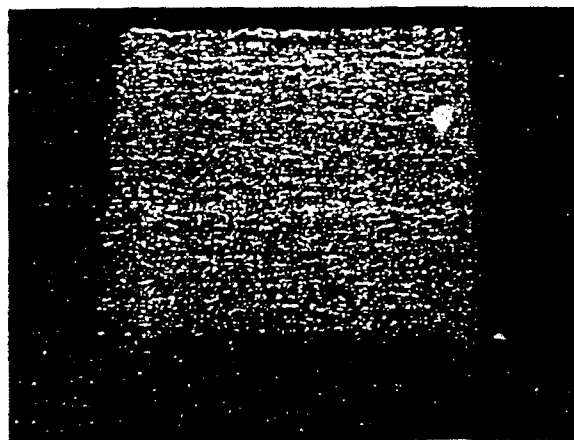


The charge, thus obtained, is negative and, in fact, the particles migrate towards the anode in the electric circuit. Charging of nonoxide ceramics takes place probably via an adsorption mechanism, with SiC acquiring a negative charge and depositing on the anode, and SiN acquiring a positive charge and depositing on the cathode.

The cracks in the coating formed during drying as a result of shrinkage. A study is currently under way to modify the drying procedure so that contraction stresses will be minimized and cracking prevented.

In order to verify the possibility of the induction of ceramic particles into the pores, cross sections of coated

graphite were prepared by fracturing the specimens. The presence of SiO_2 clusters in the cross section is evidenced both morphologically in Fig. 3 and by microanalysis in Fig. 4. The clusters vary in size, possibly reflecting the vari-

Fig. 8. Amount of SiO_2 that penetrated the porous graphite from various solvents.Fig. 9. Amount of penetrated SiO_2 as a function of electric field intensity.Fig. 6. SiO_2 skeleton that remains after graphite burn-off.

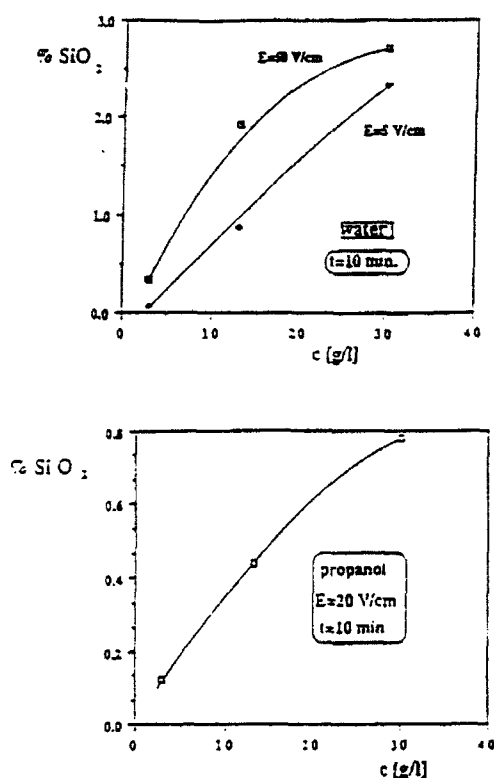


Fig. 10. Amount of penetrated SiO_2 as a function of its concentration in the solvent.

ation of pore size. The distribution of elemental Si coincides, as expected, with cluster locations.

A most interesting result was obtained during quantitative determination of the impregnated SiO_2 . It was found that in specimens in which the induced SiO_2 was at the higher levels (such as 0.6–2.5%) a SiO_2 skeleton of the same shape and dimensions as the original specimen remained after removal of the graphite. Moreover, the presence of the SiO_2 throughout the cross section of the skeleton indicates impregnation of the whole cross section of the specimen.

The effect of solvent properties on penetration can be predicted from the theoretical analysis in Ref. (10). Penetration is enhanced at large Peclet numbers

$$\text{Pe} = \frac{Ub}{D}$$

where U is the particle velocity, b the mean pore radius, and D the diffusion coefficient of the particle. The electrophoretic velocity is proportional to ϵ/η of the solvent. Four solvents were tested with ϵ/η ratios ranging from 4.2 for pentanol to 81 for water. As predicted, the amount of penetrated SiO_2 increased with this ratio (Fig. 7).

The electric field has a dual effect on the extent of particle penetration. Due to increase of the particle velocity and Peclet number with field strength, penetration is enhanced by it. However, the field also enhances the buildup of an external deposit on the substrate, which blocks penetration. Therefore, there exists an optimal field strength (Fig. 8), its value decreasing with increased particle concentration, because of faster buildup of the external coating at higher concentrations.

Penetration increases with particle concentration both in water and propanol. At low field strengths (5 V/cm) the relationship is linear for the range of concentrations studied (Fig. 9).

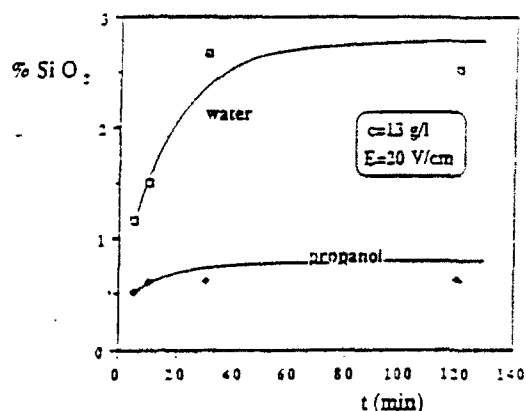


Fig. 11. Effect of deposition time on amount of penetrated SiO_2 .

Penetration increases with deposition time, but reaches a plateau after a period which depends on solvent concentration and field strength. The fact that the plateau is reached before full impregnation of the pores is probably due to the blockage by the external coating. Thus, the extent of penetration could be increased if a way is found to prevent surface deposition.

Conclusions

A variety of ceramic materials, both oxides and nonoxides, were deposited electrophoretically on a porous graphite substrate. In addition to the formation of surface deposits, electrophoretic induction of ceramic particles into the porous substrate was demonstrated.

Quantitative studies of the amount of penetrated material as a function of deposition parameters were carried out for colloidal SiO_2 . It was shown that penetration is enhanced by a high dielectric constant and low viscosity of the solvent, by particle concentration, and by field strength. Due to simultaneous buildup of an external deposit, a plateau is reached in the extent of penetration as a function of time, prior to the filling of the whole pore volume. Prevention or inhibition of surface deposition would favor an increased extent of penetration.

Acknowledgment

Research sponsored by the Air Force Office of Scientific Research, Air Force Systems Command, U.S.A.F. under Grant No. AFOSR 89-0474. The U.S. Government is authorized to reproduce and distribute reprints for Governmental purposes, notwithstanding any copyright notation thereon.

Manuscript submitted Feb. 15, 1991; revised manuscript received Oct. 17, 1991.

REFERENCES

1. J. Davies, *J. Coll. Interface Sci.*, **63**, 480 (1978).
2. Y. S. Moya, *Ceramic Bull.*, **59**, 1198 (1980).
3. J. O'M. Bockris and K. N. Reddy, "Modern Electrochemistry," Vol. 1, p. 832, Plenum Press, New York (1970).
4. D. R. Brown and F. W. Salt, *J. Appl. Chem.*, **15**, 40 (1965).
5. E. J. W. Verwey and J. Overbeek, "Theory of the Stability of Lyophobic Colloids," Elsevier, Amsterdam (1948).
6. P. Benson, *Electrochim. Acta.*, **9**, 275 (1964).
7. J. L. Anderson, in "The Chemistry and Physics of Composite Media," M. Tomkiewicz and P. N. Sen, Editors, PV 85-8, p. 103, The Electrochemical Society Softbound Proceedings Series, Pennington, NJ (1985).
8. H. Y. Keh and J. L. Anderson, *J. Fluid Mech.*, **153**, 417 (1985).
9. J. L. Anderson, *J. Coll. Interface Sci.*, **105**, 45 (1985).
10. S. Haber and L. Gal-Or, *This Journal*, **139**, 1071 (1992).

1. T. C. Reiman and R. H. Sabersky, *ibid.*, 11, 1083 (1968).
2. E. L. Jarrett and T. L. Sweeney, *AIChE J.*, 13, 797 (1967).
3. J. W. Evans, *This Journal*, 135, 1999 (1988).
4. R. C. Alkire, H. Deligianni, and J.-B. Ju, *ibid.*, 137, 818 (1990).
5. C. E. Shin and D. J. Economou, *ibid.*, 136, 1997 (1989).
6. R. Alkire and H. Deligianni, *ibid.*, 135, 1093 (1988).
7. J. Newman, "Electrochemical Systems," p. 210, Prentice Hall, Inc., Englewood Cliffs, NJ (1973).
8. K. G. Jordan, Ph.D. Thesis, University of California, Berkeley (1990).

Electrolytic ZrO₂ Coatings

I. Electrochemical Aspects

L. Gal-Or, I. Silberman, and R. Chaim

Israel Institute of Metals and Department of Materials Engineering, Technion-Israel Institute of Technology, Haifa, 32000, Israel

ABSTRACT

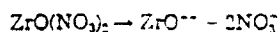
ZrO₂ coatings were deposited on graphite and titanium from an aqueous solution based on a water-soluble precursor. A two-step mechanism is suggested for the ZrO₂ formation: generation of hydroxyl ions (OH⁻) at the cathodic substrate by reduction of NO₃⁻ and dissolved O₂, and then reaction of the hydroxyl ions with zirconyl ions present in the solution to form the hydroxide Zr(OH)₄, which in turn decomposes on drying to yield zirconia (ZrO₂). Faradaic efficiencies of 26-50% were found, attributable to reduction reactions that do not produce hydroxyl ions, as well as to formation of the hydroxide at sites removed from the cathodic substrate due to diffusion of the hydroxyl ions. The effects of current density, time, and hydrodynamic conditions on coating weight, cell voltage, temperature, and pH of the solution were studied.

Ceramic coatings are currently of much interest for applications in high-temperature and severely corrosive environments. A variety of methods are available for their production, including plasma spraying (1,2), chemical vapor deposition (CVD) and sputtering (3), and sol-gel processes (3-5).

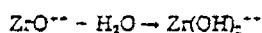
Formation of ceramic coatings by electrochemical means is a relatively new technique and has been described by Switzer (6,7) in application to synthesis of ceramic films and powders. It presents several advantages over alternative coating techniques: the thickness and morphology of the deposit can be controlled by the electrochemical parameters; relatively uniform deposits are obtainable on complex shapes; the deposition rate is higher than for most other methods, and the equipment is of low cost (8). Oxides and hydroxides (6-10) were deposited by a redox change reaction induced on the anode. Formation of a ceramic oxide through cathodic reactions was demonstrated only recently by Switzer with CeO₂ and ZrO₂ coatings (6,7).

In the present work, deposition of zirconia (ZrO₂) from an aqueous solution of zirconyl nitrate [ZrO(NO₃)₂] was studied. The sequence of reactions leading to oxide formation is expected to be the following:

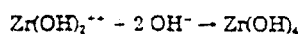
(i) dissociation of the zirconyl salt (11)



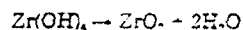
(ii) hydrolysis of the zirconyl ion



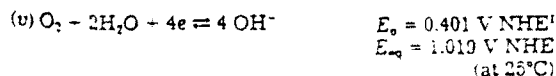
(iii) interaction of the hydrated cation with OH⁻ ions generated at the cathode by reduction reactions described further on



(iv) dehydration of the hydroxide



The cathodic reactions that generate OH⁻ and their standard and equilibrium potentials calculated with the aid of the Nernst equation are

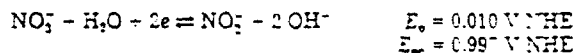


¹ Normal hydrogen electrode.

(assuming a concentration of 8 mg/liter of O₂)



(vi) reduction of the NO₃⁻ ions

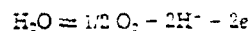


(At a 0.1M concentration of nitrate; the concentration of NO₃⁻ is assumed to be half of that of OH⁻ derived from the pH of the solution.)

(vii) reduction of H₂O



The anodic reaction which occurs simultaneously is



Thus, the hydroxide may form in two successive steps: electrochemical generation of OH⁻, and a chemical reaction between the latter and the zirconyl cations. The present paper describes the effects of the electrochemical deposition parameters on the formation rate of the ZrO₂ coatings.

Experimental Procedure

The deposits were obtained on two different substrates, prepared in the form of 2 × 10 × 20 mm specimens: (i) porous graphite (UC grade 45) and (ii) commercially pure titanium (ASTM B-265-58T). The graphite specimens were polished with a 1000 grit SiC abrasive paper, and the Ti plates machined and then polished with 180 grit paper. All specimens were then rinsed with ethanol in an ultrasonic bath, then washed with distilled water and dried in air.

The electrolyte used was a 0.1M aqueous solution of ZrO(NO₃)₂ · nH₂O, with an initial pH value of 2.3.

A power supply, Hipotronics 801-1A, was used, and cell voltage and current were measured with Avometers. Polarization curves were obtained with a PAR Model 270 potentiostat. Deposits were obtained at current densities ranging from 15 to 100 mA/cm², and durations of 10-60 min. in the course of which the cell voltage, the pH, and temperature of the solution were measured. Most ex-

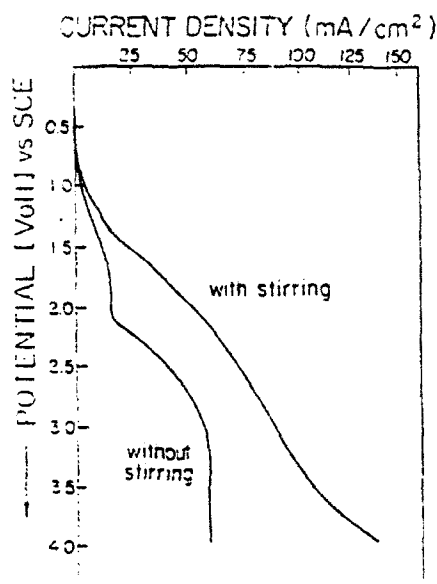


Fig. 1. Cathodic polarization curves for graphite in 0.1M $\text{ZrO}(\text{NO}_3)_2 \cdot n\text{H}_2\text{O}$, at 2 mV/s scan. Stirred vs. unstirred solution.

periments were performed without stirring, some with stirring.

The deposits were dried in air at room temperature. Coating weights were determined by weighing the specimens before and after deposition, within an accuracy of ± 0.05 mg. Some of the deposits were submitted to sintering treatments, for microstructural studies reported in Part II of this series (12).

Results and Discussion

The results described below refer only to the graphite specimens. Cathodic polarization curves for the graphite vs. saturated calomel electrode (SCE) in 0.1M $\text{ZrO}(\text{NO}_3)_2$ are shown in Fig. 1.

For the unstirred solution, two polarization regions were observed, representing reduction reaction associated with activation- and concentration-type polarization regimes, respectively. Due to the limitations of the potentiostat (limited to -4 V), the maximal current density (c.d.) achieved was limited to 55 mA/cm^2 . The curve obtained for the stirred solution does not show domains of limited c.d.

In keeping with the order of the electrochemical potentials of the various reduction reactions, the first reaction in the polarization curve is probably a reduction of dissolved

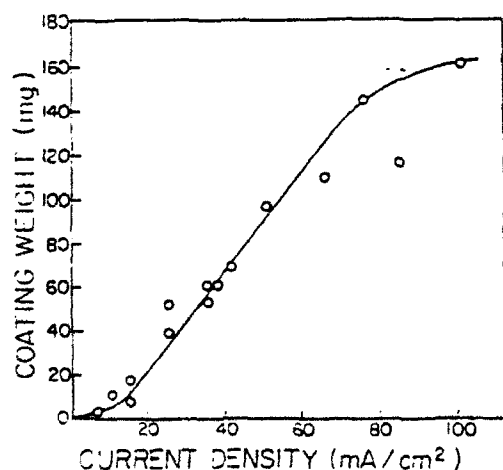


Fig. 2. Coating weight as function of current density for constant deposition time at 60 min.

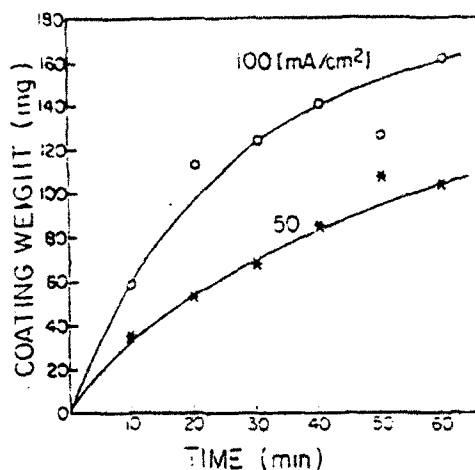


Fig. 3. Coating weight as function of deposition time for various current densities.

O_2 , overlapping partially the second reaction, which is reduction of the NO_3^- ions. The third reaction taking place at c.d.'s above 55 mA/cm^2 is expected to be reduction of H^+ . The discrepancy between the theoretical potentials and the values in the polarization curves are attributed by overpotentials inherent to the substrate and ohmic overpotentials due to hydroxide deposit.

The dependence of coating weight on the c.d. for a constant deposition time of 60 min is shown in Fig. 2. As could be expected, weight increases with current density, and the observed three modes of dependence, apparently reflect the three cathodic reactions.

The first part of the curve (low c.d.'s of $0-15 \text{ mA/cm}^2$) is characterized by a relatively moderate (low deposition rate) slope ($0.7 \text{ mg} \cdot \text{cm}^2/\text{mA}$), associated with a low generation rate of OH^- from reduction of O_2 (see Fig. 1). The steeper slope in the second part ($15-75 \text{ mA/cm}^2$) represents a higher rate of deposit formation, associated with a high rate of OH^- generation from the reduction of NO_3^- . The third part ($75-100 \text{ mA/cm}^2$) is again associated with a relatively moderate slope, due in this case to onset of reduction of H^+ ions to form H_2 , a reaction that does not produce OH^- ions, and hence does not contribute to deposit formation.

The dependence of coating weight on deposition time for two different c.d.'s is shown in Fig. 3. Coating weight increases with time in a decelerating manner. Stirring is seen to cause a significant reduction in the deposition rate (Fig. 4), probably by facilitating migration of OH^- from the

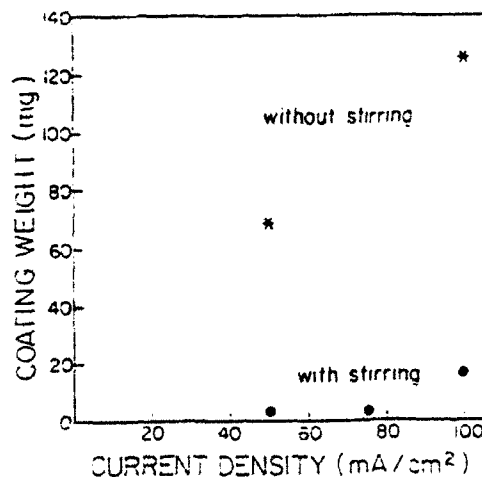


Fig. 4. Coating weight as function of current density, stirred vs. unstirred solution.

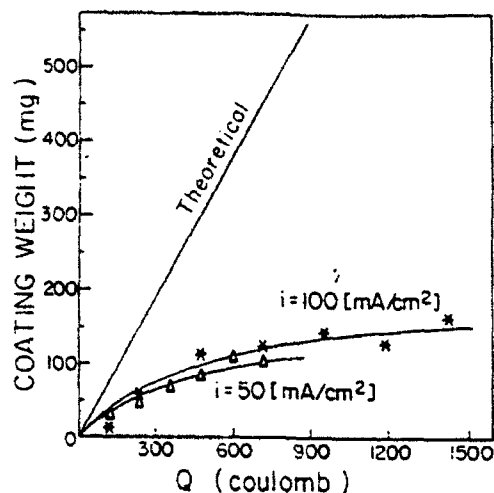


Fig. 5. Coating weight as function of electric charge. Theoretical vs. experimental results.

cathode into the bulk of the solution, so that the hydroxide formed does not accumulate on the cathode.

At high c.d.'s (above 75 mA/cm^2), "strings" of gas bubbles were observed after a certain time, emerging from the surface of the coated substrate and demonstrating the reduction of H^+ to H_2 .

The faradaic efficiency is relatively low and is presented in Fig. 5 as the actual coating weight compared with the theoretical weight, assuming that the electric charge served exclusively for generation of OH^- ions. It was also assumed that all electrosynthesized ZrO_2 deposited on the substrate. The deviation of the actual coating efficiency from the theoretical values may be attributed due to the following possible phenomena: (i) Charge-transfer reactions that do not produce OH^- ions. (ii) Consumption of OH^- by H^+ ions present in the original solution and generated at the anode. (iii) Undeposited Zr(OH)_2 formed in the bulk of the solution.

The dependence of cell voltage on deposition time for different c.d.'s is shown in Fig. 6. The voltage is seen to increase with c.d. for a constant deposition time. At higher current densities, the voltage stabilizes at shorter times. This behavior is related to the mechanism of the coating formation. In the initial stage of the coating process, the cathodic substrate is conductive and OH^- ions are generated over its entire surface. Due to the porosity of the substrate, a porous coating is initially formed. As the coating process progresses, the deposit becomes denser and

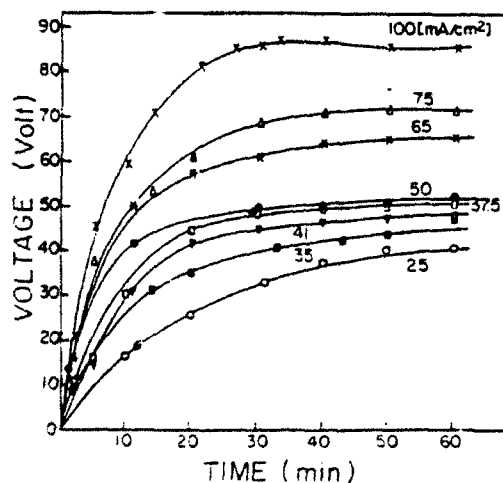


Fig. 6. Cell voltage as function of deposition time for various current densities.

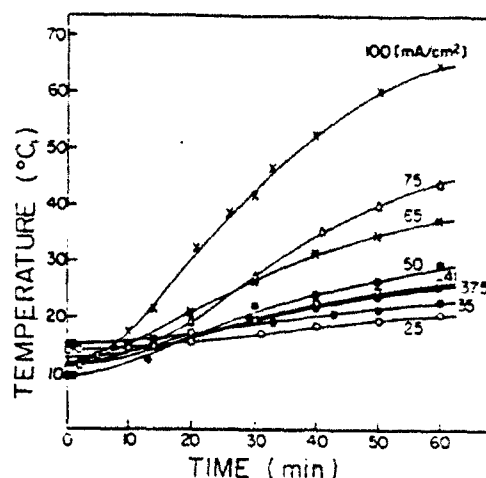


Fig. 7. Solution temperature as function of deposition time for various current densities.

thicker, and its electrical resistance increases, with the attendant increase in both cell voltage and solution temperature. The change in electric resistance is responsible in part for the accentuated limiting c.d.'s and the relatively high potentials observed in the cathodic polarization curve of the unstirred solution (Fig. 1). After a certain time, the cell voltage reaches a maximum, but the deposit continues to form while undergoing local breakdowns manifested in "strings" of gas bubbles. These breakdowns create sites of stronger reduction currents, which in turn enable the deposit process to continue without further increase in the cell voltage. The deposit thus consists of two layers [see Fig. 1 in Ref. (12)]: a thin dense layer formed in the first stage and a relatively thicker one formed in the second. The morphology of the deposit is in agreement with the proposed mechanism for formation of thick coatings.

The dependence of solution temperature on deposition time is shown in Fig. 7, at various c.d.'s. It is seen that initially (for the first 10 min or so), the temperature level varies within a fairly narrow range, irrespective of the c.d.; but in the longer run it rises drastically—the higher the c.d., the steeper the rise. This thermal effect is due to the increase in electric resistance, caused by formation of the deposit.

The temperature increase may affect the diffusion rate of OH^- away from the cathode and that of Zr(OH)_2 toward it. Thus, it would be desirable to control the temperature during the coating experiments by stirring the solution.

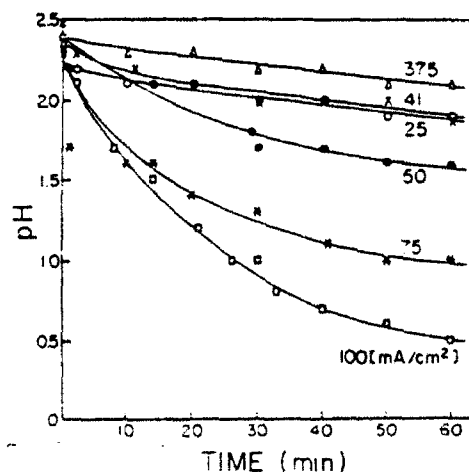


Fig. 8. pH of solution as function of deposition time for various current densities.

This, however, would interfere with deposit accumulation on the cathode. Coating weight of nickel hydroxide was reported (13) to be unaffected by moderate agitation of the concentrated solution. In this regard, coating weight is expected to be influenced when low-concentration solutions and severe stirring conditions are used.

The time pattern of the pH level of the solution is shown in Fig. 8. Below 40 mA/cm², the pH varied little, but at higher c.d.'s significant decreases were observed already from the outset. It should be mentioned that the pH was measured in the bulk of the unstirred solution; local readings at the cathode may show an increase in pH due to the OH⁻ ions. The explanation may be that the pH as measured was governed by the H⁺ ions generated at the anode, since the OH⁻ ions formed at the cathode were used up in deposit formation without contributing to the resultant pH of the bulk solution.

The present work demonstrated the potentialities of the electrolytic method for producing ZrO₂ coatings, with relatively easy control of their thickness. However, it is necessary to control the drying stage in order to achieve sound and crack-free coatings. Optimal conditions for the formation of ZrO₂ coatings are low current densities and short coating times, in view of the nonconductive nature of this oxide.

Acknowledgment

Research sponsored by the Air Force Office of Scientific Research, Air Force Systems Command, U.S.A.F., under Grant No. AFOSR 89-0474. The U.S. Government is au-

thorized to reproduce and distribute reprints for Governmental purposes notwithstanding any copyright notation thereon.

Manuscript submitted Aug. 6, 1990; revised manuscript received Dec. 17, 1990.

REFERENCES

1. T. E. Schmid and R. Y. Hecht, *Ceram. Eng. Sci. Proc.*, 9, 1089 (1988).
2. A. Kobayashi, N. Hasegawa, and H. Namikawa, *Trans. J.W.R.I.*, 18, 13 (1989).
3. M. Shane and M. L. Mecartney, *J. Mater. Sci.*, 25, 1537 (1990).
4. W. J. Dalzell and D. E. Clark, Department of Materials Science and Engineering, University of Florida, Gainesville, FL (1988).
5. D. E. Clark, W. J. Dalzell, and D. C. Folz, *Ceram. Eng. Sci. Proc.*, 9, 1111 (1988).
6. J. A. Switzer, *Am. Ceram. Soc. Bull.*, 66, 1521 (1987).
7. J. A. Switzer and R. J. Phillips, in "Better Ceramics Through Chemistry III," C. J. Brunker, D. E. Clark, and D. R. Ulrich, Editors, Vol. 121, pp. 111-114, Materials Research Society Proceedings (1988).
8. G. E. F. Brewer, *Am. Ceram. Soc. Bull.*, 51, 216 (1972).
9. D. Tench and L. Warren, *This Journal*, 130, 869 (1983).
10. M. Sakai, T. Sekine, and Y. Yamayaki, *ibid.*, 130, 1631 (1983).
11. M. J. Sienko, and R. A. Plane, "Chemistry," 2nd ed., Chap. 20, McGraw Hill, Inc., New York (1961).
12. R. Chaim, I. Silberman, and L. Gal-Or, *This Journal*, 138, 1942 (1991).
13. K.-C. Ho, *ibid.*, 134, 52C (1987).

Electrolytic ZrO₂ Coatings

II. Microstructural Aspects

R. Chaim, I. Silberman, and L. Gal-Or

Department of Materials Engineering and Israel Institute of Metals, Technion-Israel Institute of Technology, Haifa, 32000, Israel

ABSTRACT

Zirconia coatings were formed on graphite and titanium substrates by electrodeposition. The as-deposited coatings were amorphous and cracked during the drying stage. Sintering of the coatings on the graphite substrates caused crystallization, with formation of a variety of mixtures of the tetragonal and monoclinic ZrO₂ polymorphs having nanosize crystallites. Oxidation of the Ti substrate and reaction with zirconia during the heat-treatment resulted in addition to a microstructure resembling ceramic composite coatings.

Ceramic functional coatings on metallic and ceramic substrates are currently under extensive investigations. An electrochemical route based on an electrophoretic process has been applied largely for ceramic coatings (1-4). Since this technique makes use of a ceramic powder suspension, the final microstructure of the coating is strongly influenced by the powder characteristics. The thin-film Sol-Gel technique (5) and electrolytic deposition of ceramic coatings directly from an aqueous solution, developed recently (6-10), enable control of coating composition and microstructure through the chemical, electrochemical, and firing process parameters.

The present paper deals with microstructural evolution of the electrolytically formed zirconia coatings on two types of substrates: graphite and titanium. Although from the technological point of view these substrates were considered to be equally important, their chemical reactions with the zirconia coating are expected to differ significantly, and thus evolve various microstructures within the fired coating.

Experimental Procedure

The details of the substrate materials, chemical solution, and the electrochemical coating parameters were described in Part I of this series (11).

The deposits formed on the substrates were dried in air at room temperature. Firing was carried out at 400 and 600°C in air, and at 900°C in argon for 1 h for the graphite substrates. The coated titanium substrates were fired at 780°C for 1 h in air.

The microstructure and composition of the zirconia coatings were characterized after the different stages of the process, using optical and scanning electron microscopy (SEM) (Model JSM-840), equipped with energy-dispersive spectroscopy (EDS). The phase content and the crystallite size were determined by x-ray diffraction (XRD) with a diffractometer (Model PW-1820) operated at 40 kV and 40 mA, using monochromatized Cu K α radiation, at a scanning speed of 0.4 (degree/min).

Results and Discussion

The as-deposited coatings appeared as a transparent viscous fluid, especially at high current densities and long coating durations, where thick deposits were visually observable. *In situ* microscopical observations showed development of cracks within the coating layer on graphite during the drying process. The wet deposit contained many bubbles. During drying some of the bubbles coalesced to form larger ones, while others were expelled from the deposit and migrated to its surface. The bubbles

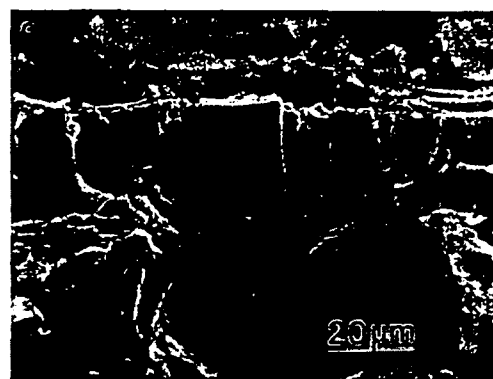
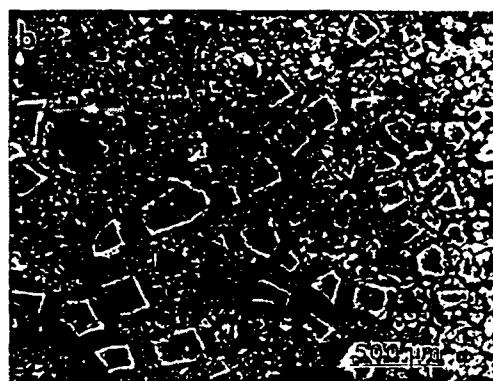
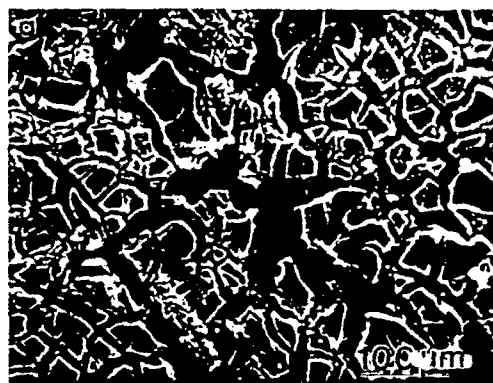


Fig. 1. SEM images of dried zirconia coatings on graphite resemble a "cracked-mud" morphology both for (a) thin coating (25 mA/cm² for 15 min) and (b) thick coating (25 mA/cm² for 75 min). Thick coatings are often composed of two layers. (c) Cross section shows penetration of the coating into pores of the graphite.

resulting from the drying process were observed only for graphite substrates and presumably result from entrapped gases within pores, which are not present in Ti substrates. During the drying process discontinuities formed within the coating, which became deep cracks toward the end of the process. The resultant coating layer had a "cracked-mud" appearance (as shown in Fig. 1 and 2), irrespective of the substrate material. In both systems, the nonuniform contraction of the wet coating was attributed to these surface microcracks.

The coating weight and thus its thickness was found to increase with increase (up to certain values) of the current density and the coating duration. Thicker coatings showed larger islands in the cracked-mud morphology.

Thick coatings (over 50 μm) on the graphite substrates often consisted of two layers, the upper layer being thicker and composed of coarser islands (Fig. 1b). These layers are believed to form during different stages of the coating pro-



Fig. 2. SEM images of dried zirconia coatings on Ti showing the "cracked-mud" morphology. This featureless surface morphology is characteristic of the amorphous nature of the coating. (b) At higher magnifications, no drying pools are visible in coatings on Ti.

cess, as discussed in Ref. (11). SEM observation of the coating cross sections have clearly shown the coating build-up at the surface porosity (Fig. 1c).

X-ray diffraction patterns of the dry as-deposited coatings and of the fired coatings are shown in Fig. 3 and 4 for the graphite and titanium substrates, respectively. The coating layers before firing have the typical pattern of

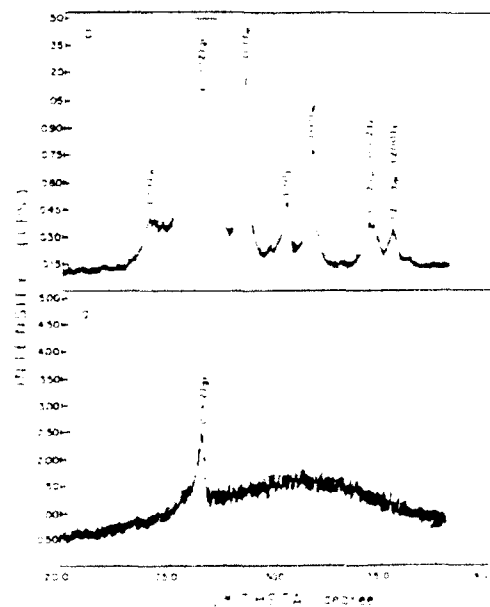


Fig. 3. X-ray diffraction pattern of zirconia coatings on graphite. (a) Amorphous-type broadened peak from the as-deposited coating and the sharp peak from the graphite (a) substrate. (b) Reflections from the tetragonal (t) and monoclinic (m) polymorphs are characteristic of the ZrO₂ coatings, sintered at 600°C for 1 h.

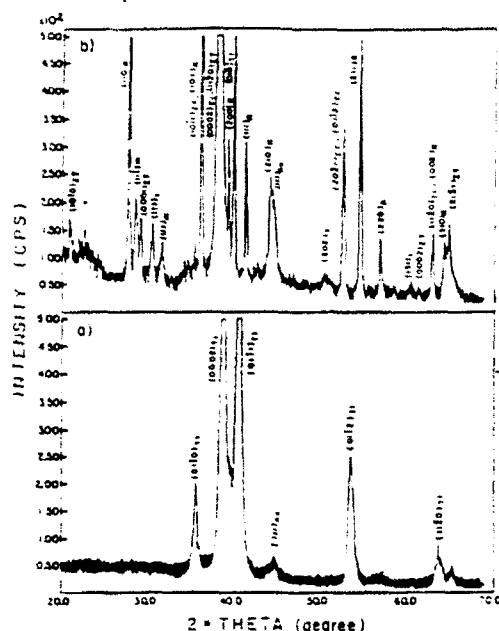


Fig. 4. X-ray diffraction pattern of zirconia coatings on Ti. (a) Absence of sharp reflections from a deposited coating indicates on its amorphous nature. (b) Typical reflections from α -Ti, TiO_2 (rutile-R), ZrO_2 (tetragonal-t and monoclinic-m) and various zirconium titanates (ZT) are seen for coatings sintered at 780°C for 1 h.

amorphous zirconia, in which a broadened amorphous-type peak appears around the angle $2\theta \sim 30$ degrees (Fig. 3a and 4a), irrespective of the substrate material. This finding is consistent with the relatively smooth and featureless morphology of the as-deposited coating surfaces (Fig. 1 and 2).

Firing induced a different phase evolution and morphology in these substrate/coating systems as was expected, and the resulting fired coatings were opaque. The microstructure of the coating on the graphite substrate was characterized by fine equiaxed submicron particles (Fig. 5). These particles were identified as a mixture of tetragonal (t) and monoclinic (m) polymorphs of zirconia (Fig. 3b), based on the $\{111\}$ and $\{400\}$ -type reflections. The line broadening of the $\{111\}$ -type reflections was used to calculate the crystallite size of the polymorphs with the aid of the Scherrer equation (12), assuming no strain effects due to the substrates. (This assumption was based on the similar line broadenings in XRD, which have resulted from the same zirconia coating before and after spallation from the graphite substrates.) The volume fractions of the two phases (t and m) were determined through the "polymorph" equation as corrected by Porter and Heuer (13).

The crystallite size was found to be 2 and 12 nm for the 400 and 600°C treatments, respectively, with the polymorphs indistinguishable. By contrast, treatment at 900°C for 1 h in argon resulted in crystallite sizes of 25 and 20 nm for the tetragonal and monoclinic phases, with volume fractions of 15 and 85%, respectively. These size data indicate that the SEM image (Fig. 5) represents zirconia aggregates.

Firing of the zirconia coatings on graphite substrates at the various temperatures led only to crystallization of the amorphous coating. According to the Ellingham diagram (14), graphite oxidizes under the present firing conditions to form CO gas, but no reaction with the zirconia is expected to occur. Formation of undoped zirconia via solution by different techniques and crystallization of the low-temperature polymorphs of zirconia by firing at the relatively low temperature are well documented in the literature (15-17). The presence of the t polymorph is related primarily to the crystallite size effect (18, 19), by which the tetragonal phase may be retained metastably at room temperature. The crystallite sizes of the tetragonal phase pres-

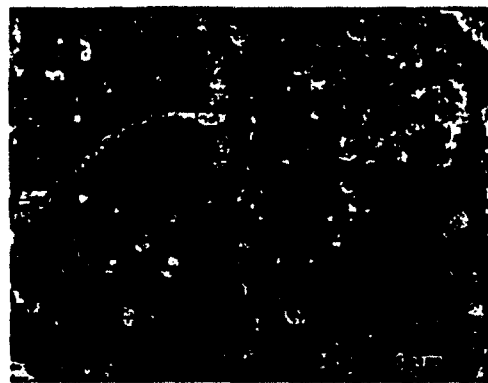


Fig. 5. SEM image of sintered ($600^\circ\text{C}/1$ h) zirconia coating on graphite. The submicron particles represent aggregates constituting a mixture of tetragonal and monoclinic polymorphs of zirconia.

ent within the coating (12-25 nm) matched well with the reported particle sizes for similar calcination treatments (14-28 nm) (16), the range within which this polymorph exists.

The zirconia coating on the Ti substrates exhibited a totally different inner microstructure after firing. Oxidation of the metallic titanium during firing resulted in the original spaces between the cracks in the coating layer being filled by the growing titanium oxide (Fig. 6). Microchemical EDS analyses of the various features of the coating (see Table I), and elemental mapping for Ti (Fig. 6d) confirmed the Ti-rich nature of the polycrystalline phase between the zirconia islands. An appropriate x-ray diffraction pattern from this specimen (Fig. 4b) contained reflections of TiO_2 in the form of rutile, ZrO_2 with the tetragonal and monoclinic phases, and additional reflections coincident with those of the $\text{Zr}_2\text{Ti}_3\text{O}_{11}$, $\text{Zr}_2\text{Ti}_2\text{O}_{10}$, and $\text{Zr}_2\text{Ti}_3\text{O}_{11}$ hexagonal phases (20). In this case at a firing temperature of 780°C , stable titanium oxide grows due to oxidation of a parabolic type (21, 22). Furthermore, oxidation of Ti at this temperature occurs mainly by diffusion of Ti rather than that of oxygen through the growing oxide layer, a circumstance which favors formation of the low-oxygen titanium zirconate phases. The volume fractions of the tetragonal and monoclinic phases in these coatings were calculated to be 37 and 63%, and their crystallite sizes 26 and 25 nm, respectively.

Although the pH of the mother solution was intentionally adjusted for work in the cathodic regime, it also affects the relative stability of the zirconia polymorphs. In this regard, the ratio of the t/m phase content after calcination at 400 - 600°C was reported (23) to increase at pH values above 10 and below 6 for the zirconyl nitrate solution from which the zirconia gel was precipitated. Again,

Table I. EDS composition results for ceramic coating on Ti substrates.^a

Microstructural feature	Chemical composition (mole percent)		Remarks ^b
	Zr	Ti	
Zirconia	48.0	52.0	P1 in Fig. 6e
island center	59.0	41.0	
(reacted regions)	65.0	35.0	
	69.0	31.0	
	76.0	24.0	
Zirconia	73.0	27.0	P2 in Fig. 6e
island periphery	85.0	15.0	
(nonreacted regions)	87.0	13.0	
Oxidized regions	9.0	91.0	P3 in Fig. 6e
between zirconia	0.0	100.0	
islands	0.0	100.0	

^a Fired at 780°C for 1 h in air.

^b Examples for the analyzed regions.

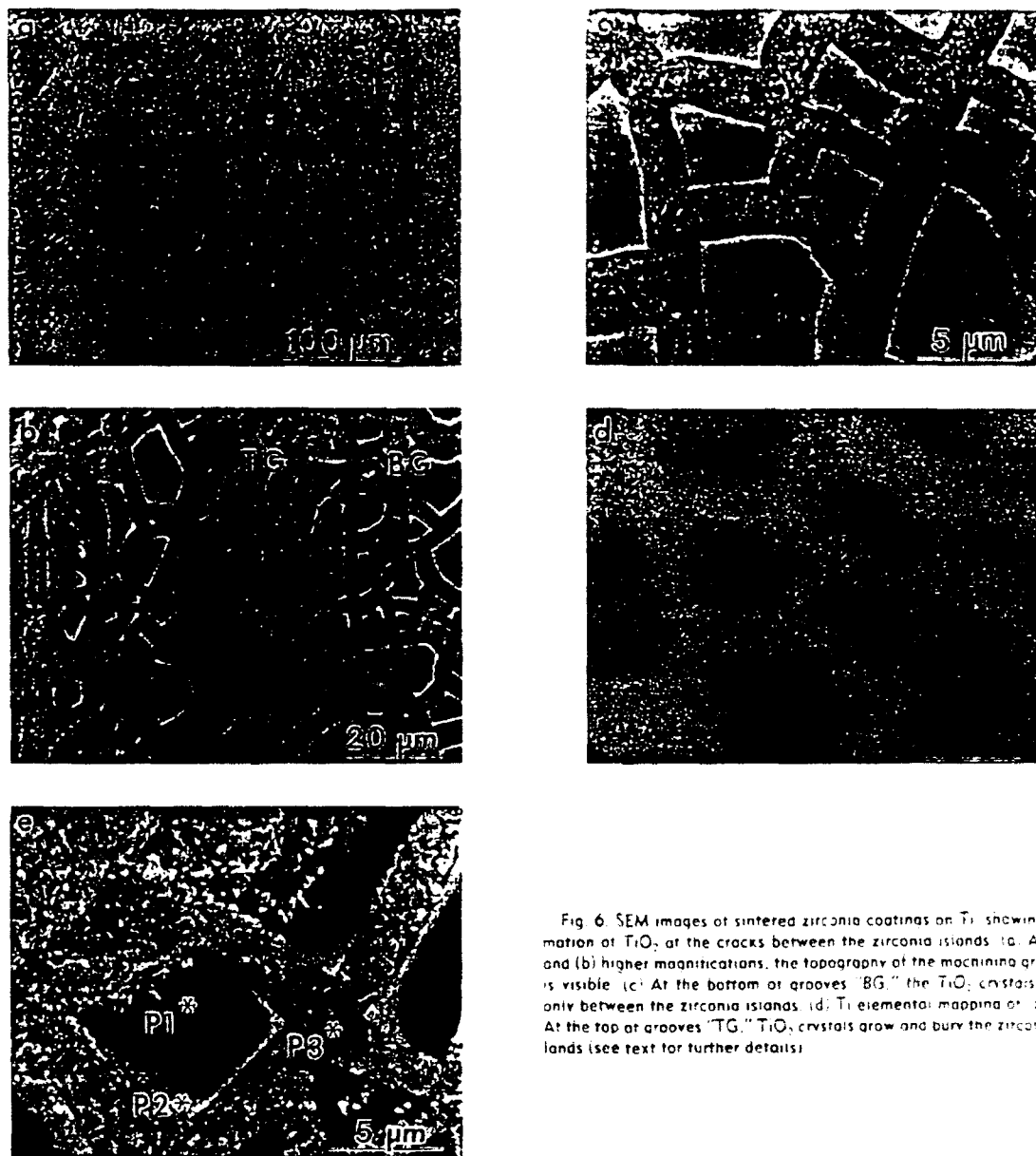


Fig. 6. SEM images of sintered zirconia coatings on Ti showing formation of TiO_2 at the cracks between the zirconia islands. (a) At low and (b) higher magnifications, the topography of the machining grooves is visible. (c) At the bottom of grooves "BG," the TiO_2 crystals grew only between the zirconia islands. (d) Ti elemental mapping of (c). (e) At the top of grooves "TG," TiO_2 crystals grow and bury the zirconia islands (see text for further details).

where comparison is possible, the measured crystallite size (26 nm) and the t:m phase ratio (37/63) have showed good match to the reported values (22 nm and 40/60, respectively) (24) in a similar solution (pH = 5.0) and calcination condition (650°C). The effect of pH on stabilization of the zirconia polymorphs was speculated to be both by replacement of the incorporated anions by either OH^- or Cl^- and pH-dependent transformations of hydroxyl ligands to bridging hydroxyl groups to bridging oxide ions (7).

The surface microstructure of the coating layer on Ti substrates was dependent on the coating thickness prior to firing. At locations with greater coating thicknesses (i.e., at the bottom of the machining grooves), titanium oxide growth was confined to the gaps between the zirconia islands (Fig. 6c). However, at locations with smaller coating thicknesses (i.e., at the top of the machining grooves), the oxide grew to the extent that it partially buried the zirconia islands (Fig. 6e). In both cases, the centers of the islands are stated to have reacted with the titanium substrate (see also Fig. 6d) and were thus partially incorporated into the t:m phase. The phase ratio of the fired films, which depend on the firing temperature, is similar to that reported for the sintered zirconia films, which were mentioned by NOD

(Fig. 4b). Thus, direct oxidation of the crack surfaces, together with crystallization and chemical reaction of the coating with the metallic matrix at the island-substrate interface,

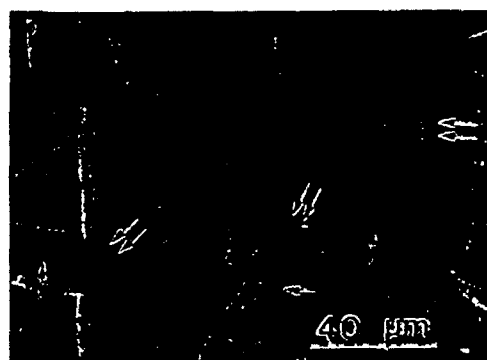


Fig. 7. SEM image showing the line traces of the zirconia island contours prior to sintering (single arrows) and after sintering (double arrows). From which the sintering shrinkage may be deduced.

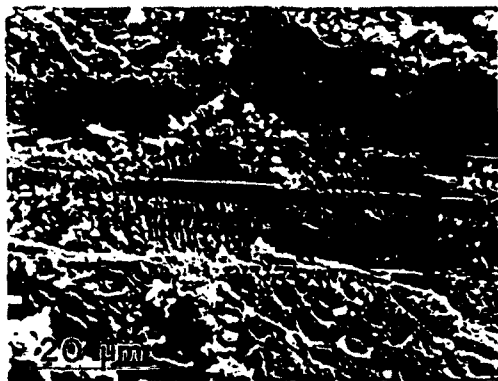


Fig. 8. SEM image of the scratch trace, showing high density of microcracks at the smeared regions, perpendicular to the scratch direction.

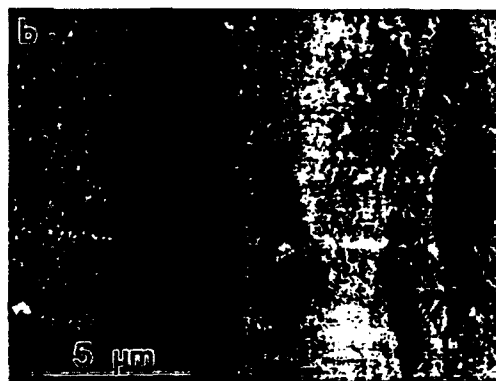


Fig. 9. SEM images showing: (a) Typical coating cross section where fine TiO_2 crystals grew around the zirconia islands, accompanied by shrinkage and bending. (b) Debonding at the coating/substrate interface results in dimpled fracture surfaces.

interfaces, form the composite morphology of the zirconia islands embedded in the TiO_2 matrix.

In many cases, traces parallel to the periphery of the zirconia islands were observed on the titanium oxide layer, as shown by the single arrows in Fig. 7. [These traces could be identified as the original contours of the zirconia islands prior to firing, since some broken pieces from the edges of the original islands were buried and left at these locations (double arrows in Fig. 7).] By this means, the firing shrinkage of the coating was estimated to be of the order of ~20%, assuming a similar percent shrinkage for the third dimension of the coating thickness.

The diamond Vickers microhardness of the coating on the Ti substrates has an average value of 520 kg/mm^2 . Scratches were applied manually to the coating surface with a diamond indenter in order to qualitatively charac-

terize the adherence and brittleness of the composite coating layer. A typical trace of one of these scratches is shown in Fig. 8; it exhibits a high density of microcracks perpendicular to the scratch direction. The presence of these microcracks in the smeared region indicates heavy deformation of the material by the indenter. Moreover, some regions of the coating near the scratch trace were debonded from the substrate (Fig. 9). This debonding occurred by crack propagation either through the coating or at the substrate/coating interface. In the latter case, the fractured surface was composed of very fine dimples, indicating some ductility at the interface.

Finally, the qualitative scratch test of the coating and its debonding behavior indicate relatively good adhesion to the Ti substrate. In this regard, the chemical reactions between substrate, coating, and atmosphere determine the microstructural evolution within the coating. The characteristic microstructure which resulted from these reactions is similar to those of transformation toughened zirconia composites, and may be considered for design of wear-resistant, oxidation-resistant and thermal barrier coating applications.

Acknowledgment

Research sponsored by the Air Force Office of Scientific Research, Air Force Systems Command, USAF, under Grant No. AFOSR 89-0474. The U.S. Government is authorized to reproduce and distribute reprints for governmental purposes, notwithstanding any copyright notation thereon.

Manuscript submitted Aug. 6, 1990; revised manuscript received Jan. 4, 1991.

REFERENCES

- G. E. F. Brewer, *Am. Ceram. Soc. Bull.*, **51**, 216 (1972).
- D. E. Clark, W. J. Dalzell, and D. C. Folz, *Ceram. Eng. Sci. Proc.*, **9**, 1111 (1988).
- D. R. Brown and F. W. Salt, *J. Appl. Chem.*, **15**, 40 (1965).
- L. Gal-Or and S. Liubovich, Report AFOSR Grant No. 88-0097, March (1989).
- E. Kato, M. Ezoe, and K. Daimon, in "Advances in Ceramics, Vol. 24: Science and Technology of Zirconia III," S. Somiya, N. Yamamoto, and H. Hanagida, Editors, American Chemical Society, Washington, DC (1988).
- D. Tench and L. Warren, *This Journal*, **130**, 869 (1983).
- M. Sakai, T. Sekine, and Y. Yamazaki, *ibid.*, **130**, 1631 (1983).
- J. A. Switzer, *ibid.*, **133**, 722 (1986).
- J. A. Switzer, *Am. Ceram. Soc. Bull.*, **66**, 1521 (1987).
- J. A. Switzer and R. J. Phillips, in "Better Ceramics Through Chemistry III," C. J. Brunker, D. E. Clark, and D. R. Ulrich, Proceedings of the Materials Research Society, Vol. 121, pp. 111-114 (1988).
- L. Gal-Or, I. Silberman, and R. Chaim, *This Journal*, **138**, 1939 (1991).
- B. D. Cullity, "Elements of X-Ray Diffraction," p. 284, Addison-Wesley Publishing Co., Reading, MA (1978).
- D. L. Porter and A. H. Heuer, *J. Am. Ceram. Soc.*, **62**, 298 (1979).
- L. S. Darken and R. W. Gurry, "Physical Chemistry of Metals," p. 349, McGraw-Hill Book Co., New York (1953).
- E. Tani, M. Yoshimura, and S. Somiya, *J. Am. Ceram. Soc.*, **66**, 11 (1983).
- P. Singh and S. K. Date, *J. Mater. Sci. Lett.*, **6**, 621 (1987).
- R. Srinivasan, R. De Angelis, and B. H. Davis, *J. Mater. Res.*, **1**, 583 (1986).
- R. G. Garvie, *J. Phys. Chem.*, **69**, 1238 (1965).
- M. V. Swain, *J. Mater. Sci. Lett.*, **3**, 1159 (1986).
- L. E. Fykin, V. V. Vavilova, I. I. Kornilova, R. P. Ozerov, and S. P. Solov'ev, *Dokl. Phys. Chem.*, **194**, 823 (1970).
- P. H. Morton and W. M. Baldwin, *Trans. ASM*, **44**, 1004 (1952).
- P. Kofstad, K. Hauffe, and H. Ljolllesdal, *Acta Chem. Scand.*, **12**, 239 (1958).
- B. H. Davis, *J. Am. Ceram. Soc.*, **67**, C-168 (1984).
- S. S. Jada and N. G. Peletis, *J. Mater. Sci. Lett.*, **8**, 143 (1989).

COATING AND IMPREGNATION OF CARBON-CARBON COMPOSITES
WITH CERAMICS BY ELECTROPHORETIC DEPOSITION

L. Gal-Or, S. Liubovich

Israel Institute of Metals

AFOSR Grant 88-0097

Technion No. 5045-06

Interim Scientific Report

March 1, 1988 - February 28, 1989

Prepared for

EOARD - England, London

AFOSR - Bolling, Washington D.C., 20332, U.S.A.

REPORT DOCUMENTATION PAGE

1a. REPORT SECURITY CLASSIFICATION Unclassified		1b. RESTRICTIVE MARKINGS	
2a. SECURITY CLASSIFICATION AUTHORITY		3. DISTRIBUTION / AVAILABILITY OF REPORT Approved for public release; Distribution unlimited	
2b. DECLASSIFICATION / DOWNGRADING SCHEDULE			
4. PERFORMING ORGANIZATION REPORT NUMBER(S)		5. MONITORING ORGANIZATION REPORT NUMBER(S)	
6a. NAME OF PERFORMING ORGANIZATION Israel Institute of Metals	6b. OFFICE SYMBOL (if applicable)	7a. NAME OF MONITORING ORGANIZATION European Office of Aerospace and Development	
6c. ADDRESS (City, State, and ZIP Code) Technion Research and Development Foundation Technion City Haifa 32000, Israel		7b. ADDRESS (City, State, and ZIP Code) Box 1 FPO New York 09510 00	
8a. NAME OF FUNDING / SPONSORING ORGANIZATION Air Force Office of Scientific Research	8b. OFFICE SYMBOL (if applicable) NE	9. PROCUREMENT INSTRUMENT IDENTIFICATION NUMBER AFOSR 88-00	
8c. ADDRESS (City, State, and ZIP Code) Bolling AFB, DC 20332-6448		10. SOURCE OF FUNDING NUMBERS PROGRAM ELEMENT NO. 611027 SUBJECT NO. 2306 TASK NO. A2 WORK UNIT ACCESSION NO.	
11. TITLE (Include Security Classification) Coating and Impregnation Carbon-Carbon Composites with Ceramics by Electrophoretic Deposition.			
12. PERSONAL AUTHOR(S) L. Gal-Or, S. Liubovich			
13a. TYPE OF REPORT Interim	13b. TIME COVERED FROM 5/1/88 TO 2/28/89	14. DATE OF REPORT (Year, Month, Day) April 1989	15. PAGE COUNT 85
16. SUPPLEMENTARY NOTATION			
17. COSATI CODES FIELD GROUP SUB-GROUP		18. SUBJECT TERMS (Continue on reverse if necessary and identify by block number) Electrophoretic Deposition, Electrodeposition, Carbon-Carbon Composites, Coating, Impregnation.	
19. ABSTRACT (Continue on reverse if necessary and identify by block number) Electrophoretic deposition of ceramic coatings on porous graphite and on a 2D C-C composite was studied using colloidal and fused SiO ₂ , SiC and SiN. It was shown that all these ceramic materials acquire an electric charge and hence deposit under the influence of the electric field. In addition to the formation of a surface deposit, the induction of particles into the pores of porous graphite was demonstrated. The effects of deposition voltage, solvent properties and particle concentration on penetration were studied by examination of cross-sections in the SEM and by quantitative analysis of induced SiO ₂ . Ceramic deposits of CeO ₂ , ZrO ₂ and Al ₂ O ₃ were formed on graphite and 2D C-C by an electrochemical reduction of aqueous solutions containing inorganic salts of the appropriate metals.			
20. DISTRIBUTION / AVAILABILITY OF ABSTRACT <input checked="" type="checkbox"/> UNCLASSIFIED/UNLIMITED <input type="checkbox"/> SAME AS RPT. <input type="checkbox"/> OTIC USERS		21. ABSTRACT SECURITY CLASSIFICATION Unclassified	
22a. NAME OF RESPONSIBLE INDIVIDUAL Dr. Alan H. Rosenstein		22b. TELEPHONE (Include Area Code) (202) 767-4984	22c. OFFICE SYMBOL AFOSR/NE

TABLE OF CONTENTS

	<u>Page</u>
CHAPTER 1 - INTRODUCTION	1
CHAPTER 2 - LITERATURE SURVEY	3
2.1 Electrophoretic Deposition of Ceramic Particles...	3
2.2 Electrophoresis in Porous Structures	11
2.3 Electrochemical Deposition of Ceramic Films	13
2.4 Electrochemical Reactions in Porous Electrodes....	14
CHAPTER 3 - EXPERIMENTAL - METHODS AND MATERIALS	19
CHAPTER 4 - RESULTS OF EXPERIMENTS	24
4.1 Electrophoretic Deposits	24
4.1.1 Surface Morphology	24
4.1.2 Morphology and Composition of Cross- Sections	24
4.1.3 The electroosmotic effect	53
4.1.4 Electrophoretic impregnation of a porous substrate with ceramic particles	53
4.1.5 Morphology of induced SiO ₂	60
4.1.6 Relevant solvent properties	60
4.2 Electrodeposition of Ceramic Films	62
4.2.1 CeO ₂ deposition	62
4.2.2 ZrO ₂ deposition	67
4.2.3 Al ₂ O ₃ deposition	68
CHAPTER 5 - DISCUSSION OF RESULTS	73
CHAPTER 6 - CONCLUDING REMARKS	77
BIBLIOGRAPHY	79

CHAPTER 1 - INTRODUCTION

The present report summarizes the work performed in the first stage of the project.

The final objective of this project is to develop a method for coating and impregnation of carbon-carbon composites with ceramic materials so as to enable their application in oxidising atmospheres at elevated temperatures.

The basic concept of the program is to utilize the phenomenon of electrophoresis, which has been so far applied extensively in biological systems, for the displacement of ceramic particles and their deposition on the C-C substrate. The electric conductivity of the C-C enables its functioning as an electrode in an electric circuit in which a high strength field is applied generating the motion of the charged ceramic particles. Moreover, it is expected that the high strength field will facilitate the penetration of the fine ceramic particles into residual pores and cracks of the substrate.

The scope of the project was later expanded so as to include a new method of deposition, in addition to electrophoresis - electroreduction. By this method ceramic oxides are synthesized from an ionic aqueous solution following an electrochemical reaction.

In the present stage most experiments were performed on a model material for C-C - porous graphite. The main reasons for the use of this model material are its more accurate characterization and hence better reproducibility, in addition to more ready availability.

As part of the general scope described above the following objectives were put forward for this stage:

- To investigate the possibility to charge, and hence deposit under the influence of the electric field, a number of ceramic materials which can potentially protect C-C in high-temperature oxidizing environments (colloidal and fused SiO_2 , SiN and SiC).
- To investigate the possibility to deposit ceramic coatings on graphite and C-C from aqueous ionic solutions by electroreduction (the coatings studied were CeO_2 , ZrO_2 and Al_2O_3).
- To prove the concept that ceramic particles can be induced into a porous substrate due to the effect of the electric field.
- To verify the possibility to obtain ceramic deposits in the pores of a porous substrate by electroreduction of a suitable ionic solution.

CHAPTER 2 - LITERATURE SURVEY

2.1 ELECTROPHORETIC DEPOSITION OF CERAMIC PARTICLES

Electrophoretic deposition of ceramic coatings has two main advantages when compared to other coating methods:

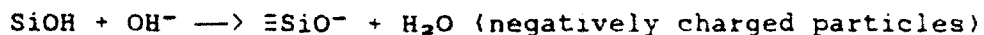
- more rigid control of coating thickness;
- better "throwing power" which enables efficient coating of complex shapes.

As related to our specific interest a third advantage seems attainable: the induction of the ceramic coating into the pores of a porous substrate under the influence of the electric field.

Electrophoretic deposition is obtained by the movement of non-conductive but electrically charged particles in an electric field to one of the electrodes.

Two different charging modes are attributed to ceramic particles [1]:

- a) dissociation mode, such as the dissociation of silanol groups present in silica:



- b) adsorption mode, such as the adsorption of H^+ from water or from weak acids: $n \text{ Al(OH)}_3 + n \text{ HNO}_3 \longrightarrow [\text{Al(OH)}_3]_n \cdot n \text{ H}^+ + n \text{ NO}_3^-$ (positively charged particles).

The surface charge once formed is then balanced by ions of an opposite charge derived from the solution and thus a double layer is formed.

Usually the polarity of the particles has to be determined experimentally because the particles acquire the charge spontaneously when mixed with the solvent. Further, this charge may be reversed upon addition of ionic compounds.

According to the model proposed by Stern the double layer constitutes of a rigid part with a linear potential gradient,

and a diffuse part with a non-linear potential gradient termed "Zeta potential".

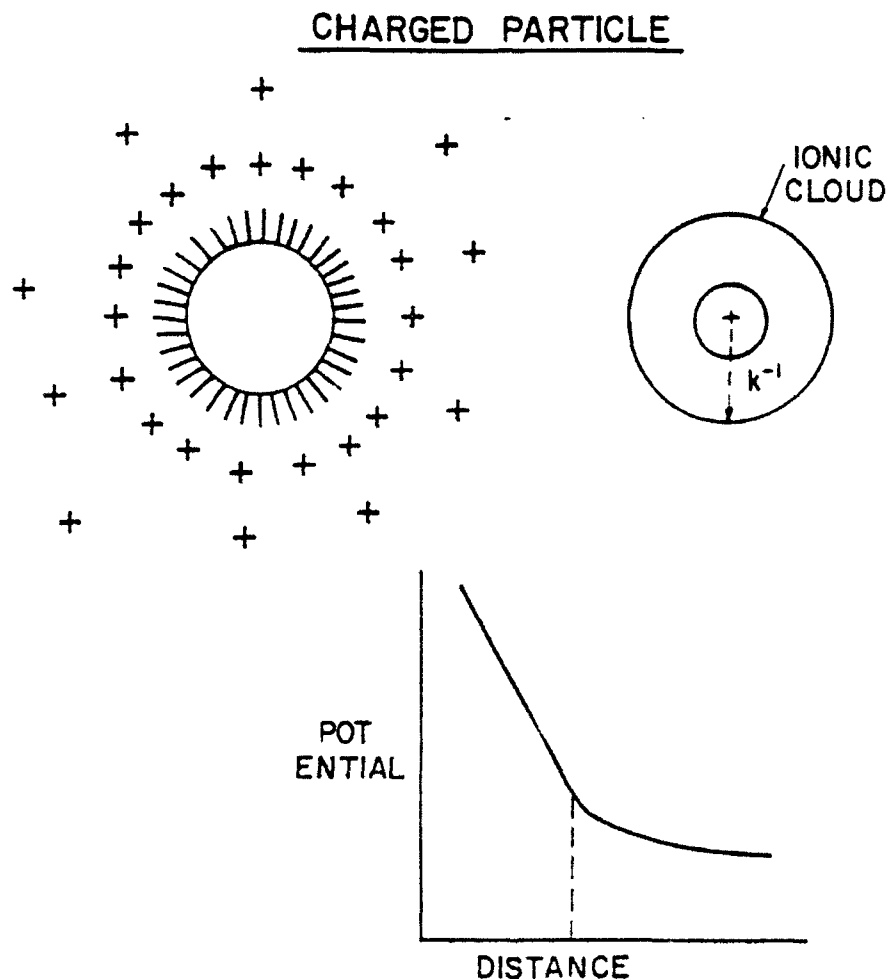


Fig. 1: The double layer and potential gradient surrounding a charged particle.

The Zeta potential can be determined by two main methods: microscopic determination of the velocity of individual particles using the Smoluchovski equation or in the Burton cell where a pure filtrate of solvent is poured on the suspension, a field is applied and the movement of the sharp boundary is monitored [2].

When an electric field is applied to a charged particle it will

move to the electrode with the opposite charge. However, the diffuse double layer around the particle interferes with its movement. The diffuse charge tends to move with the particle to which it is attached but on the other hand it is influenced by the electric field which pulls it in the opposite direction. The particle apparently wins. It moves through the liquid with a diffuse egg-shaped double layer surrounding it (although it is not actually carrying the oppositely charged ionic atmosphere but is rather leaving part of it behind and rebuilding it in front as it moves along). The tendency of the ions in the diffuse d.l. to move in the direction opposite to the movement of the particle has an effect on the velocity. It produces a "drag" which slows down its movement (see Fig. 2) [3]:

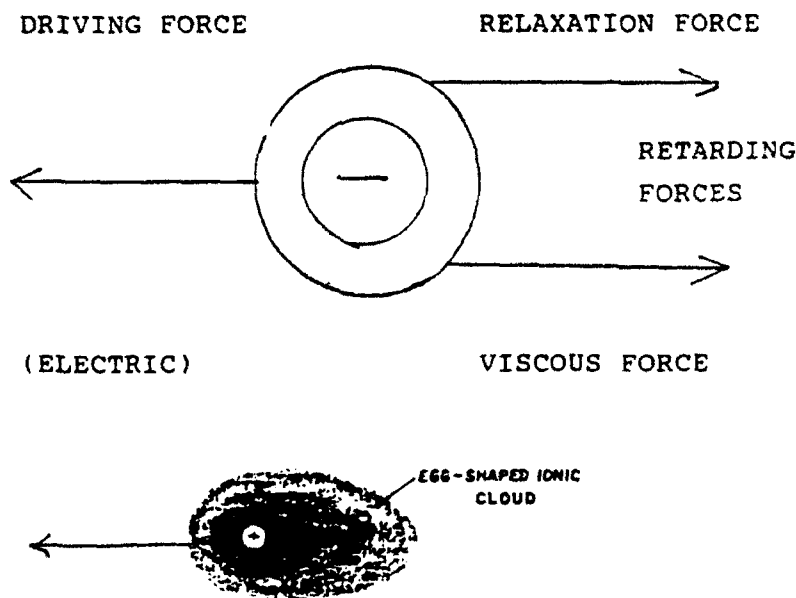


Fig. 2: Egg-shaped ionic cloud and forces acting on a moving particle.

The mobility of the particle is derived by equating the electric force with the frictional resistance and the relaxation force. Thus the mobility μ is given by:

$$\mu = E\epsilon\zeta/4\pi\eta K[1+f(kr)] \text{ where:}$$

μ - mobility
 E - field strength
 ϵ - dielectric constant of fluid
 ζ - zeta potential of particles
 η - viscosity of fluid
 K - $1/\text{double layer thickness}$
 r - radius of particle

$f(kr)$ varies between 0 and 1 for small and large values of kr respectively.

$f(kr)$ represents the relaxation phenomenon, if $k \ll r$ then:

The Smoluchowski equation is obtained and:

$$\mu = (E \cdot \epsilon \cdot \zeta) / 4\pi\eta$$

Values of μ vary between $0-20 \times 10^{-4}$ cm/sec/1V/cm. The electrophoretic yield is given by:

$$y = a \int \mu E C S dt \text{ where } C - \text{conc. of particles.}$$

S - area of electrode
 t - time

In the above equations it is assumed that the contribution of the hydrodynamic velocity to deposition can be neglected and its importance lies in maintenance of the suspension.

What happens once the particles have reached the electrode? Three theories exist on this subject:

One theory assumes that the particles that reach the electrode undergo an electrode reaction which neutralizes them. This will not explain the fact that MgO deposits are obtained on a

polymeric diaphragm located between two electrodes [4].

The second theory states that the particles are brought to the electrode by a field which exerts sufficient force to overcome the repulsion between them allowing them to come close enough for the London-Van der Waals forces of attraction to predominate [5].

According to the Varwey & Overbeek theory [5] the minimal field strength necessary to overcome the repulsion between particles is calculated from the energy of interaction between particles.

The energy of repulsion between two spherical particles V_R is:

$$V_R = \frac{\epsilon a \zeta^2}{2} \ln(1 + e^{\chi H_0}) \quad \chi = \sqrt{\frac{4\pi e^2 n_1 z_1^2}{\epsilon kT}}$$

The energy of attraction - V_A is: $p = \frac{2\pi H_0}{\lambda}$

$$V_A = \frac{Aa\alpha}{12H_0} \quad \text{if } 0.5 < p < \infty \quad \alpha = \frac{-2.45}{5p} + \frac{2.17}{15p^2} + \dots$$

$$V = V_R - V_A \quad \text{if } 0 < p < 2 \quad \alpha = \frac{1}{1 + 1.77p}$$

a - radius of particle.

H_0 - distance between surfaces of particles.

χ - $1/\text{distance of the diffuse d.l.}$

n - No of ions per unit volume.

A - London van der Waals const.

e - electronic charge.

α - finite time of propagation of electromagnetic waves when particle separation is large.

λ - wavelength of intrinsic electronic oscillations of e.

From these equations the field strength, E , necessary to overcome repulsion between particles can be calculated from:

$$E = 2F/3\epsilon a \zeta$$

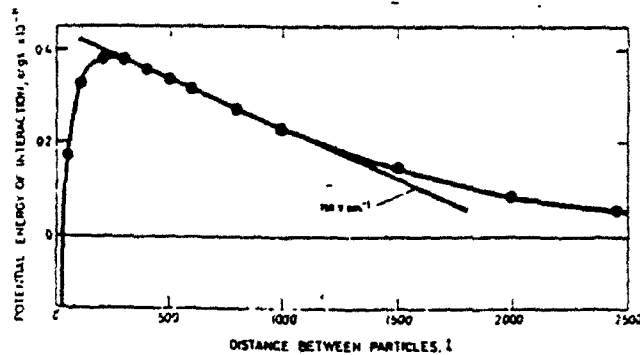


Fig. 3: Energy of interaction between charged particles as function of distance.

A third theory presumes that secondary processes which take place at the electrode can produce ions which coagulate the particles by discharging them or produce hydroxides which polymerize and adsorb on particles holding them together [6].

Parameters which affect electrophoretic deposition are the following:

- Particle charge
- Particle size distribution
- Particle concentration
- Dielectric constant of solvent
- Deposition voltage
- Time

There is an optimum value for the dielectric constant (ϵ). Solvents with too low ϵ do not possess the necessary dissociating power to obtain a charging effect on the particles. Yet too high ϵ leads to high conductivity and low deposition efficiency due to parasitic electrochemical reactions. Thus deposition from an aqueous solution will result in high energy losses and formation of voids due to gas evolution. In previous studies it was found that optimal deposition is obtained in solvents with $\epsilon \approx 14$ [7]. (See Fig. 4

ζ can be measured also by passing a solution under pressure P through a packed bed of particles and measuring E across the bed.

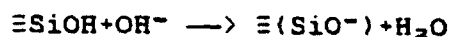
$$\zeta = 4\pi\eta\lambda E/\epsilon P$$

η - viscosity.

λ - specific cond.

ϵ - dielectric constant

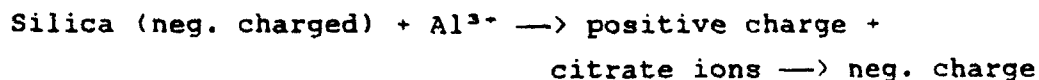
Most silicas have a certain population of silanol groups ($\equiv\text{Si-OH}$) which can dissociate:



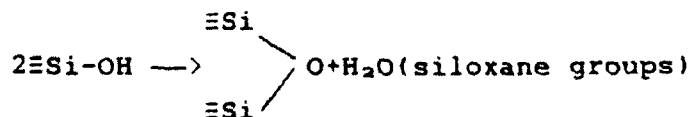
Thus a negative charge forms on the surface.

Certain ions such as Al^{3+} can be adsorbed and change the sign of the ζ potential. On top of them citrate ions can be adsorbed to change again to $-\zeta$ [9].

Consecutive transformation of charge is possible such as in the following events [10]:



Various degrees of hydration are possible. Thus silica particles prepared by precipitation in water or long ageing in it have surfaces entirely covered with $\equiv\text{SiOH}$ groups. If heated at $>400^\circ\text{C}$ the following happens:



At 1200°C only siloxane remains and hydration is slow.

on the solvent. Therefore, the coated electrode must be determined experimentally for each material since the particles acquire the charge spontaneously when mixed with the solvent. Further this charge may be reversed upon addition of ions.

2.2 ELECTROPHORESIS IN POROUS STRUCTURES

In the previous sections the assumption was made that the particle is suspended in an infinite fluid. When electrophoresis in porous structures is considered the presence of rigid boundaries will affect both the electric field and the velocity of the particles.

According to J. Anderson [11,12,13] the pore wall produces three effects on the particle velocity:

- The applied electric field exerts a force on the d.l. of the pore wall if the wall is charged (ζ_w). An electrosmotic flow of the fluid is thus produced which either augments or opposes the electrophoretic velocity of the particle depending on the polarity of ζ_w vs. ζ_p .
- The pore wall distorts the electric flux (current lines) around the particle thereby intensifying the local electric field so that the particle velocity is enhanced.
- The pore wall creates additional viscous stresses in the fluid which retard the particle velocity.

Anderson analyzed the effect of the presence of a pore when the particle is located in the centerline of a long pore. Particle interaction is neglected. Two geometries are considered: a cylindrical one $x=a/R$ (a - particle radius, (R - pore radius) and a slit $x=a/B$ (B - half width).

The basic equations which apply to this system are:

$$\begin{aligned} \nabla \cdot \mathbf{E} &= 0 && \text{(conservation of charge)} \\ \eta \nabla^2 \mathbf{V} - \nabla p &= 0 && \text{(Stokes eq., velocity dominated by} \\ &&& \text{viscous stresses).} \\ \nabla \cdot \mathbf{V} &= 0 && \text{(conservation of mass)} \end{aligned}$$

Solving these equations one obtains:

$$U_p = [1 - 1.2899\lambda^3 + 1.8963\lambda^5 - 1.0278\lambda^7 + 0(\lambda^9)] \times \frac{\varepsilon(\zeta_p - \zeta_w)E_\infty}{4\pi\eta}$$

for a cylindrical configuration, and:

$$U_p = [1 - 0.2677\lambda^3 + 0.3383\lambda^5 - 0.0402\lambda^7 + 0(\lambda^9)] \times \frac{\varepsilon(\zeta_p - \zeta_w)E_\infty}{4\pi\eta}$$

for a slit configuration

It should be noted that the pore size effect enters first at λ^3 . Therefore λ has a weak effect. This is because of a fast decay of electrical and velocity disturbances from a particle moving in an unbounded field.

The disturbance to the electric field is given by:

$$E_p = \frac{1}{2} \left(\frac{a}{r} \right)^3 \left[1 - \frac{3\kappa a}{r^2} \right] E_\infty$$

$$V_p = -\frac{1}{2} \left(\frac{a}{r} \right)^3 \left[1 - \frac{3\kappa a}{r^2} \right] U_0 \quad U_0 = \frac{\varepsilon(\zeta_p - \zeta_w)E_\infty}{4\pi\eta}$$

Both fall off with λ^3 .

The pore wall intensifies the electric field moving the particle faster but the effect on the hydrodynamics leads to a larger retardation, thus overall the velocity is reduced as the pore size decreases.

In a closed system the average flow of solution through the porous medium is zero and a macroscopic pressure gradient develops to oppose the electroosmotic flow produced by the electric field. The cross-section available for the particle is $(1-\lambda)^2$ for a cylinder and $(1-\lambda)$ for a slit.

cylinder:

$$U_p = \frac{\varepsilon\zeta_p}{4\pi\eta} E_\infty \left[1 + \left(\frac{\zeta_w}{\zeta_p} \right) \left(2\lambda - \frac{7}{5}\lambda^2 \right) - \left(1 - \frac{\zeta_w}{\zeta_p} \right) \times 1.289\lambda^3 \right]$$

slit:

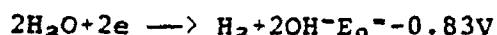
$$U_p = \frac{\varepsilon\zeta_p}{4\pi\eta} E_\infty \left[1 + \left(\frac{\zeta_w}{\zeta_p} \right) (\lambda - \lambda^2) - \left(1 - \frac{\zeta_w}{\zeta_p} \right) \cdot 0.2677\lambda^3 \right]$$

Here the electrophoretic effect comes in at Δ and is weak while the pressure flow has a contribution dependent on Δ and has therefore a stronger contribution.

It is to be stressed that in the above analysis the pore walls were considered to be non-conductive.

2.3 ELECTROCHEMICAL DEPOSITION OF CERAMIC FILMS

It has recently [14] been described in literature that it is possible to synthesize ceramic films from water soluble ceramic precursors by an electrochemical method. The method is based on cathodic reduction of water or another anion as NO_3^- , to generate OH^- . A secondary reaction between the OH^- and an appropriate metal ion present in the solution can result in formation of the hydroxide and oxide of that metal. Thus, Switzer [14] has synthesized CeO_2 in a system where the catholyte was 1.0M cerous ammonium nitrate and the anolyte contained 1.0M NaNO_3 . The cathodic reactions which took place on a platinum cathode at c.d. of 50mA/cm² were:



The mechanism of the secondary reaction is not clear yet but it may be:



The powder deposited on the cathode was identified by X-ray diffraction to be ceric oxide with a cubic lattice constant of 0.5409nm and a crystallite size of 7.0nm. After ultrasonic dispersion the material was found to have a narrow particle size distribution with an average particle size of 1.8 μ . The

morphology of the ceramic film will depend mainly on the electric conductivity of the oxide formed. Thus highly conductive materials can form thick dense films or powders.

It is possible to synthesize oxides by an anodic reaction. This is based on the oxidation of a metal ion to an oxidation state at which it undergoes hydrolysis to an hydroxide or oxide. Switzer [14] has deposited thallic oxide films from a solution of a 0.5M thallous acetate in 1.0M NaOH on silicon substrates. By similar reactions oxides of Ni, Cu, Co, Fe and Mn were deposited by Tend and Warren [15] while Sakai et al. [16] have deposited a mixed Pb-Ti oxide film.

The methods described above differ from the electrophoretic deposition of colloidal ceramic particles. However, we believe that they can become powerful methods for coating flat and complex shapes as well as for impregnation of porous structures with ceramic materials.

2.4 ELECTROCHEMICAL REACTIONS IN POROUS ELECTRODES

Electrochemical reactions in porous electrodes have been studied in two systems mainly:
in fuel cell electrodes and in electrochemical reactors used for processes such as metal ions removal from waste water.

Two groups of electrodes exist: forced flow through and diffusion porous electrodes. Theoretical analysis of reaction kinetics in such systems have been performed by numerous researchers [17,18,19,20].

One of the models used in the analysis of diffusion electrodes is the "straight pore" model (see Fig. 5).

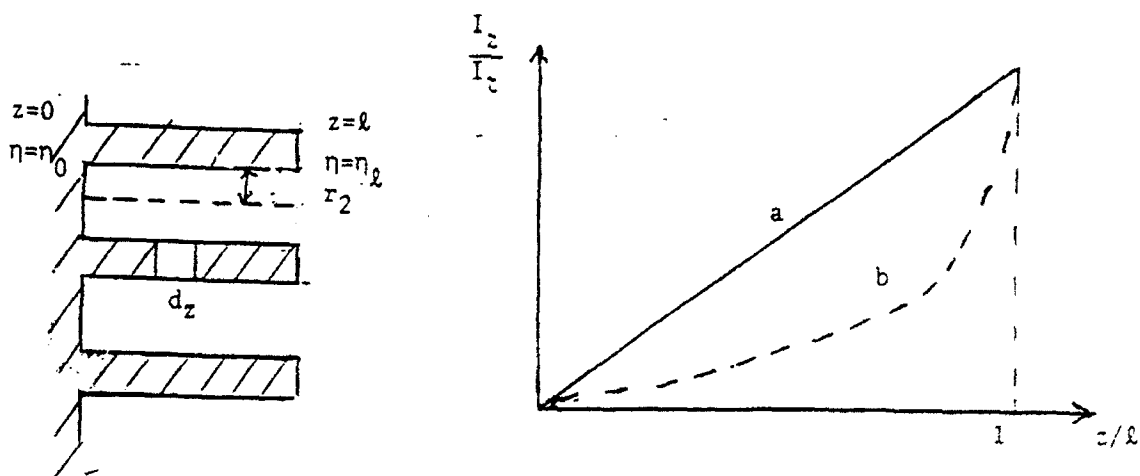


Fig. 5: The straight pore model for diffusion electrodes and the current distribution.

This model assumes that the electrode consists of a number of identical, straight, nonintersecting, cylindrical pores running through the entire length of a conductive matrix.

The basic assumptions in this model are that the pores are filled with electrolyte, no potential drop exists in the solid electrode so that potential gradients are in the solution only, the concentration of reactants is high so that no mass transfer limits exist.

The potential distribution in such a system is:

$$\eta_z - \eta_0 = \frac{4RT}{F}$$

The current, up to point Z-I_z, and the total pore current - I_t is:

$$I_z = \tan\left[\frac{a^{\frac{1}{2}}}{2}\right] \left(\frac{y_0}{2}\right)$$

$$I_t = k\pi r_2^2 \times \frac{2RT}{\ell F} a^{\frac{1}{2}} \exp\left(\frac{y_0}{2}\right) \tan\left[\left(\frac{a^{\frac{1}{2}}}{2}\right) \exp\left(\frac{y_0}{2}\right)\right]$$

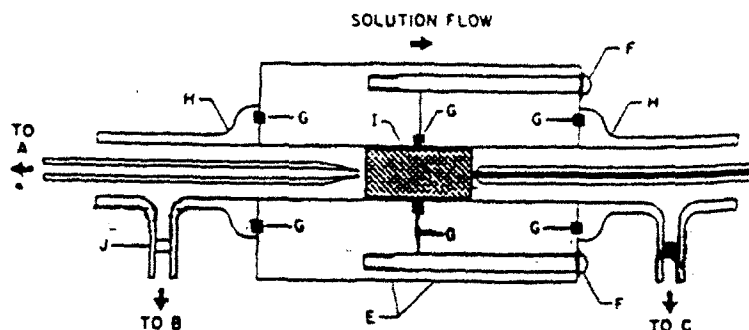
$$k = \frac{1}{\cosh \frac{y_0}{2}} \quad a = \frac{2i_0 \ell^2 F}{K \cdot R \cdot Tr_2} \quad y = \frac{\eta F}{2RT}$$

where

i_0 - exchange current

η - overpotential

The current distribution will depend mainly on i_0 and k - conductivity of the solution. For $i_0 < 10^{-9} \text{ A/cm}^2$ and $k > 10 \text{ ohm}^{-1} \text{ cm}^{-1}$, there is no potential variation in the pore and the current distribution is linear. If for example $i_0 = 10^{-6} \text{ A/cm}^2$, $k = 0.1 \text{ ohm}^{-1} \text{ cm}^{-1}$ and $r_2 = 5 \times 10^{-4} \text{ cm}$, then 10% of the current are generated at the first half of the pore when $\eta = 0.3 \text{ V}$. Flow-through porous systems have been analyzed through several models. We shall mention the macroscopic model [18] described in Fig. 6.



Schematic diagram of cell assembly. A, upstream electrode (SCE); B, counterelectrode; C, downstream reference electrode (SCE); D, platinum contact rod (glass-covered); E, Kel body; F, assembly bolt; G, O-ring seal; H, glass tube with joint; I, porous graphite electrode inside heat-shrinkable J, glass frit.

Fig. 6: Flow-through porous reactor.

In this model no detailed description of pore geometry is attempted, the electrode being characterized by the void fraction (ϵ) and the surface per unit volume only (a). The electrode is considered to be isotropic with the matrix conductivity being higher than that of the filled pores so that the potential difference is due to the solution only. The electrolyte flows through the electrode due to a pressure gradient. The potential gradient ($\Delta\phi_s$) and the collection efficiency (CE) of the cathodic reduction of metallic ions is given by:

At high flow rates:

$$-\frac{\Delta\phi_s}{I_{\max}} \sim \frac{R_s}{2} \frac{p}{U^{2/3}}$$

while at low flow rates:

$$\frac{\Delta\phi_s}{I_{\max}} \sim R_s \frac{U^{2/3}}{p} \quad \frac{\Delta\phi_s}{I_{\max}} = R_s \left\{ \frac{U}{ak_m AL} [1 - \exp(-\frac{ak_m AL}{U})] - \exp(-\frac{ak_m AL}{U}) \right\}$$

where:

- a - specific interfacial area
- A - cross-section of electrode
- k_m - average mass transfer coeff.
- L - length
- U - volume flow rate
- R_s - resistance of solution filled pores = L
- σ - conductivity of electrolyte
- P - pressure gradient

The process of sintering, the compatibility of substrate coating and the evaluation of the oxidation resistance will be discussed in a future report.

CHAPTER 3 - METHODS AND MATERIALS

a) Substrates

Two kinds of substrates were used, a porous graphite and a carbon-carbon composite:

- Porous Graphite UCAR Grade 45
Porosity - 48%
Average pore size - 60 μ
- 2D Carbon-Carbon (received from Edwards Base, no further details available).

b) Ceramic Materials

Electrophoresis

- Colloidal SiO₂ - Pyrogenic Aerosil
(submicron 460 m²/gr)
- Fused SiO₂ (1-40 μ)
- Glass Ceramic (borosilicate matrix with SiO₂ and ZrO₂ crystalline phases)
(ave. size 5-6 μ).
- SiC (600 mesh <40 μ)
- SiN (0.2-1.0 μ).

Electrodeposits

CeO₂, ZrO₂, Al₂O₃ were deposited.

c) Specimens

12-25mm diameter, 5-7mm thick or 20x20x7mm.

d) Deposition parameters

Electrophoresis was carried out from suspensions of

respective particles in non-aqueous solvents. Stirring was applied during deposition. Deposition was carried out at constant voltage with current varying due to deposit formation. Electrodeposition was carried out from aqueous solutions in a two-compartment system with anolyte and catholyte of different compositions. Figs. 7 and 8 describe the experiment set-ups.

Electrophoresis

Deposition voltage - 30-450V

Particle conc. - 3-33 g/l

Solvents - isopropanol, ethanol, hexanol

Temp. - room

Current density - 100-5 mA/cm² (c.d. fell during experiments due to build up of deposit).

Deposition time - for most specimens it was 2 hrs but in cases when thick deposits formed rapidly deposition was stopped when the c.d. fell to 5 mA/cm².

Counter electrodes - stainless steel.

Distance between electrodes - 18mm.

Electrodeposition

Catholytes: 1M Ce (NO₃)₃, 1M Al(NO₃)₃, 1M ZrO(NO₃)₂

Anolyte: 1M NaNO₃

Deposition voltage: 5-40V

Current density - 10-50 mA/cm²

Temp. - 25-55°C

Deposition time - 3-120 min

Counter electrode - Pt

Specimen preparation

Ultrasonic cleaning in acetone for 5 min prior to coating and air drying for 24 hrs after deposition prior to examination of deposit. In case of quantitative determination of impregnated SiO₂ the external deposit was removed physically.

e) Testing of deposits

Specimens were examined in the SEM for morphology. Mapping and line scans were applied for analysis of coating. The SEM used was Jeol T-200.

Examinations were performed on the surface and on cross-sections. The cross-section was obtained by breaking the specimen after removal of the external coating with compressed air. X-ray diffraction was made on the deposits obtained by electro-reduction as received and in some cases after thermal treatment. Quantitative determination of SiO_2 induced into the porous structure of graphite at varying deposition parameters was made by analyzing the SiO_2 residue after burn-off of the carbon at 950°C for 20 hrs. The white residue was treated with $\text{HNO}_3 + \text{HF}$ forming volatile HF_3Si . Weight differences were determined in both stages.

f) Electroosmotic flow

This effect was studied on graphite specimens that were cleaned and weighed prior to immersion in isopropanol and water for defined intervals with and without an electric field (50V/cm). The specimens were weighed again after immersion. On basis of weight gain, dimensions and percentage of porosity, the percentage of filled pores was calculated.

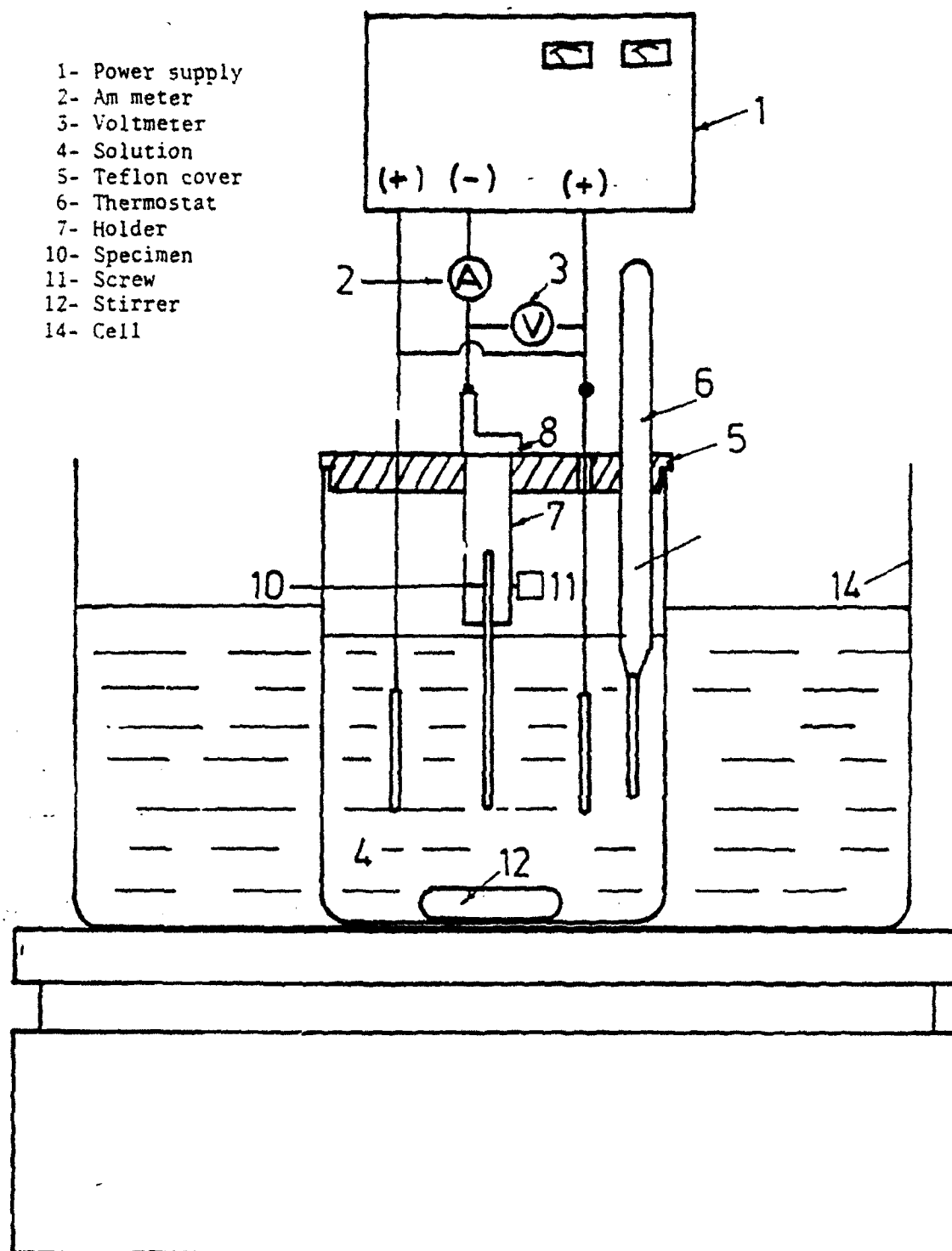
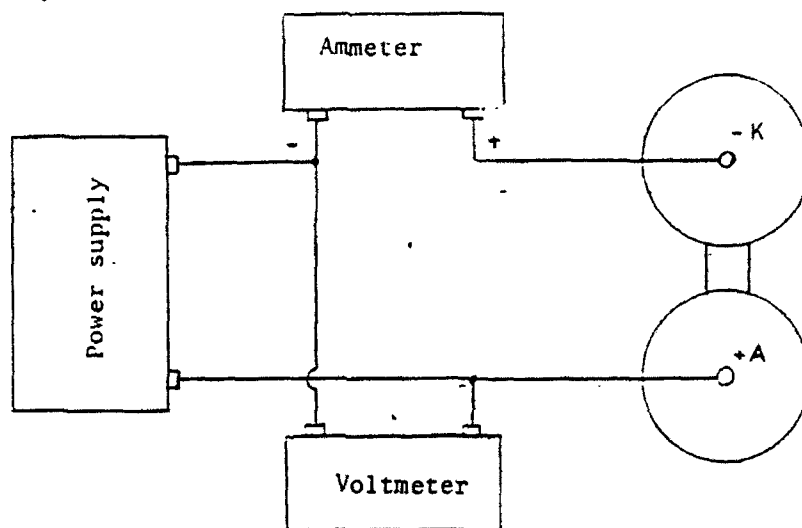


Fig. 7: Experimental set-up for electrophoresis.



Electrochemical cell:
anodic & cathodic
compartments

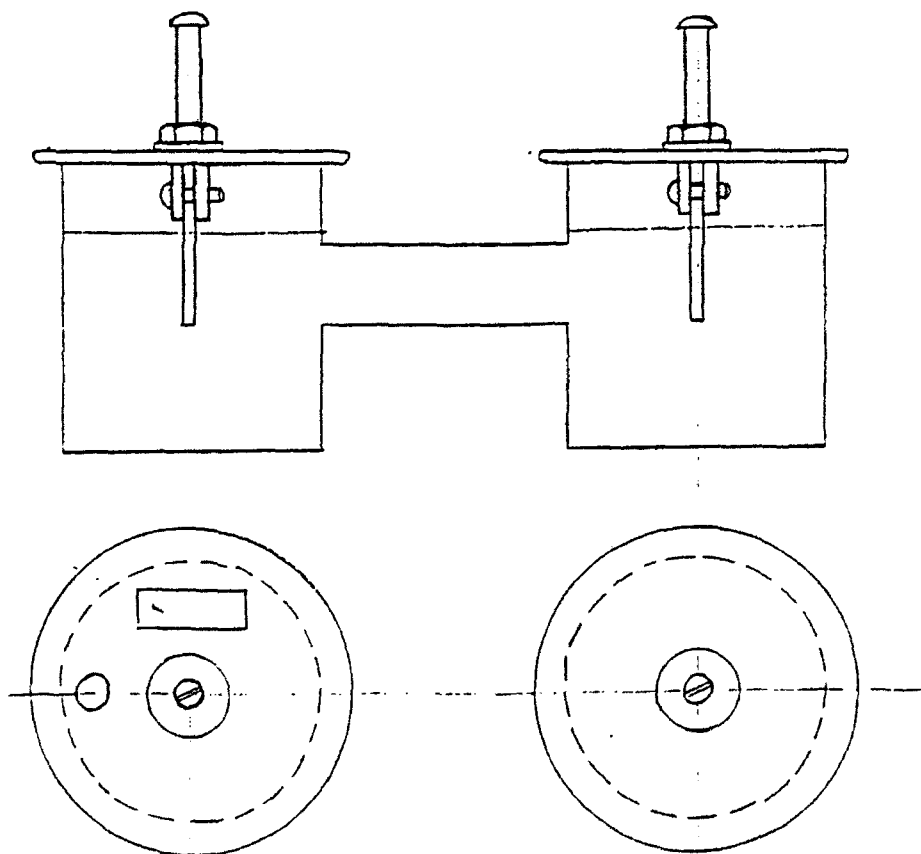


Fig. 8: Experimental set-up for electrodeposition.

CHAPTER 4 - RESULTS

4.1 Electrophoretic deposits

4.1.1 Surface morphology

The surface morphology of the "green" deposits, both on graphite and C-C specimens, was examined by optical and electron microscopy. Figs 9-13 represent the macroscopic view of the various deposits excluding colloidal SiO_2 which resulted in a transparent coating. The surface view of the SiO_2 deposit is seen in SEM micrographs (Figs. 14,15) including a x-ray mapping (Fig. 16).

4.1.2 Morphology and composition of cross-sections

In order to verify the possibility of induction of ceramic particles into the porous substrate cross-sections of coated specimens of graphite and in a few cases of C-C, were prepared (following removal of external coating) and studied in the SEM. At this stage, the study concentrated on the colloidal SiO_2 deposit (Figs. 24-44) with only initial examinations of the SiC , SiN and fused SiO_2 (Figs. 17-23). For the colloidal SiO_2 , the cross-sections of specimens obtained under varying deposition parameters were examined at locations differing in distance from surface so as to study the "in depth" distribution of SiO_2 . However, only two locations are shown here, one close to the surface (about 0.5mm from surface and termed "edge") and one in the middle of the cross-section (3.5mm from edge termed "center") (see Figs. 29-44). For specimens 8 & 9 no center photo is shown since there was no SiO_2 found. Prior to the systematic study; the existence of SiO_2 in the cross-section was established without specific notice of the distance from surface (Figs. 24-28). The deposition parameters for the colloidal SiO_2 specimen seen in Figs. 29-44 are described in Table 1. For reference a cross-section of an uncoated graphite specimen was examined also (Fig. 44).

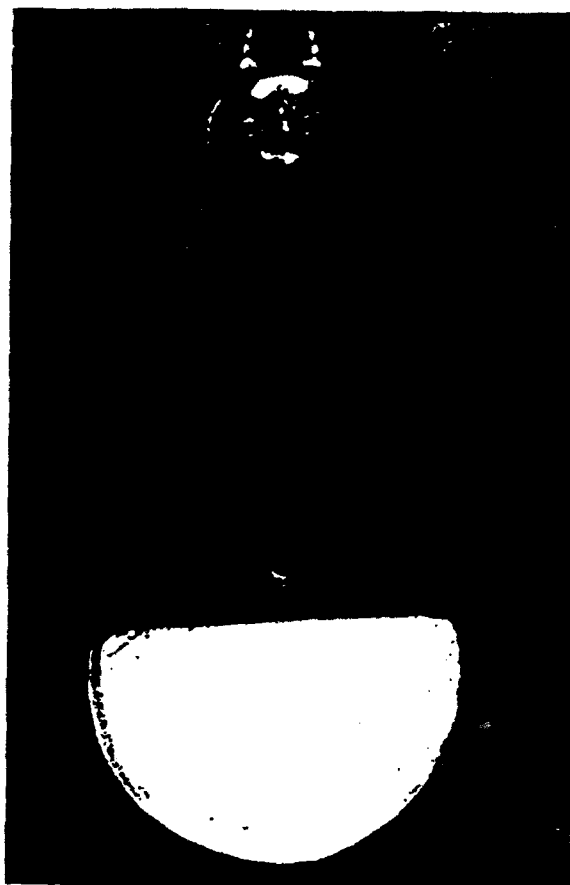


Fig. 9: Glass ceramic on graphite (electrophoresis).

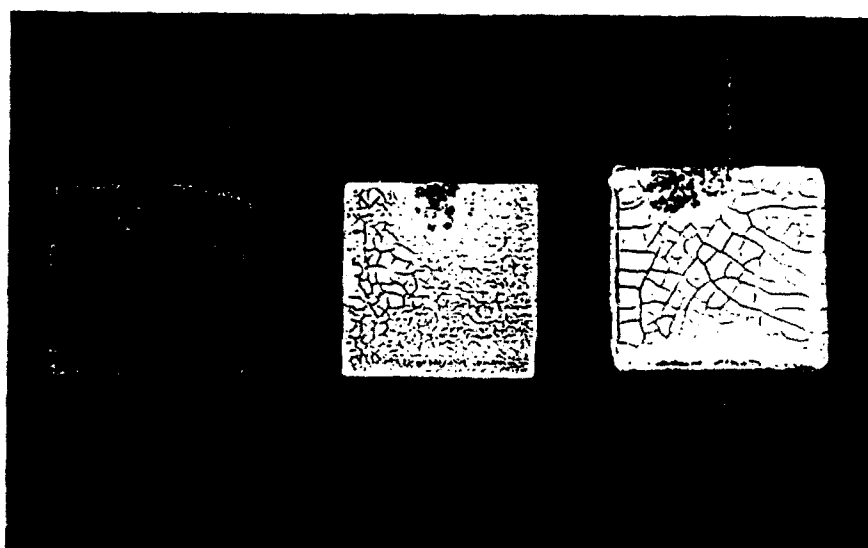


Fig. 10: SiC, SiN and fused SiO₂ on graphite (electrophoresis).

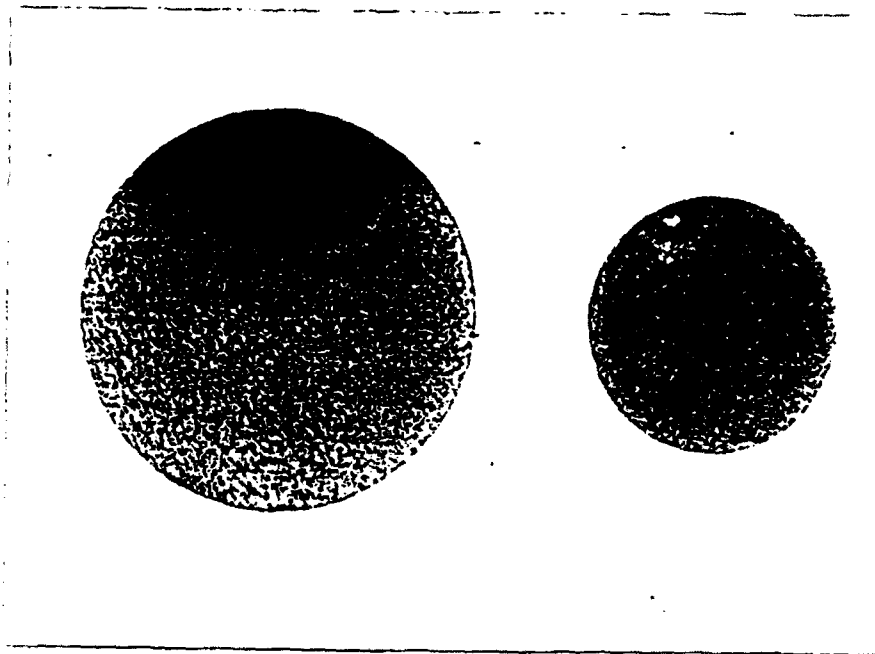


Fig. 11: SiC on C-C composite (left perpendicular direction to fiber cloth, right parallel to cloth) - electrophoresis.



Fig. 12: Fused SiO₂ on C-C composite (left perpendicular, right parallel) - electrophoresis.



Fig. 13: SiN on C-C composite - electrophoresis.

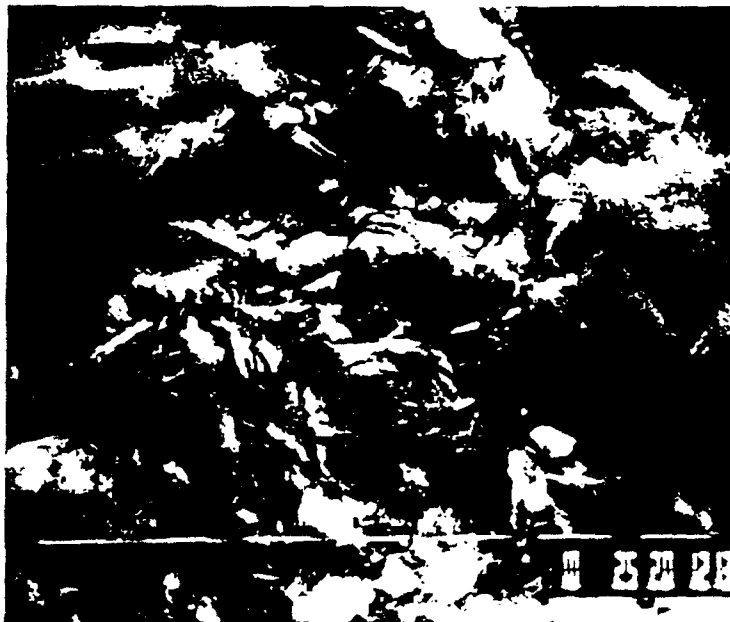


Fig. 14: Colloidal SiO₂ on graphite (electrophoresis).

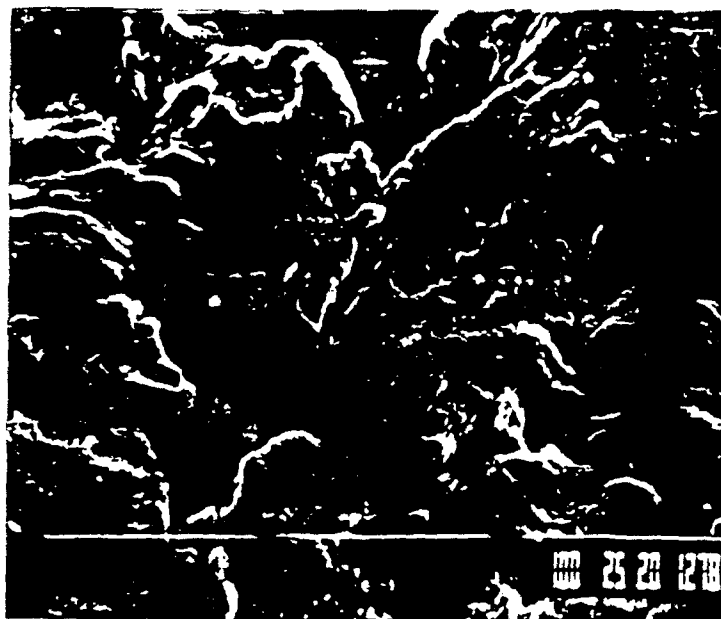


Fig. 15: as in Fig. 14 but another specimen.

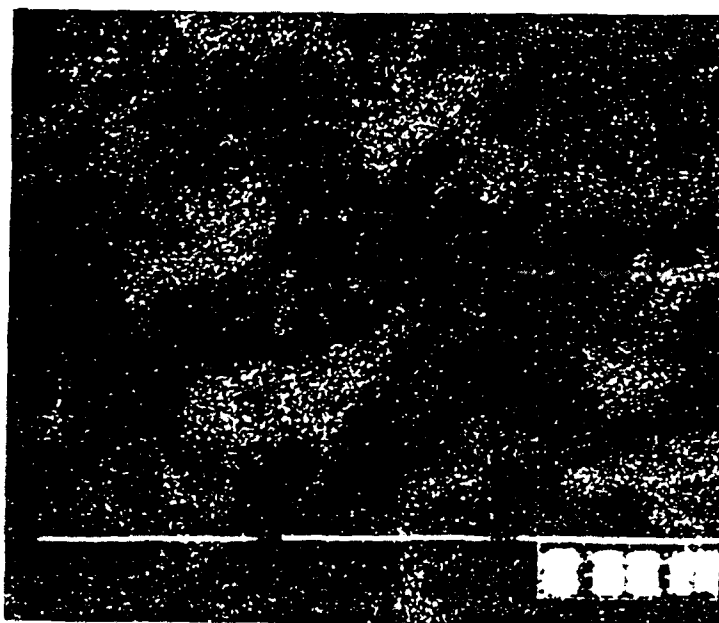


Fig. 16: X-ray mapping of Si on area seen in Fig. 15.

Table 1: Deposition parameters for specimens examined in the SEM (Figs. 29-44) (Deposition time - 2 hrs).

Specimen No.	Solvent	SiO ₂ concn. (g/l)	Deposition Voltage (V)
1	Isopropanol	13	30
2	"	"	150
3	"	"	450
4	"	"	300
5*	"	"	300
6	Ethanol	3	30
7	"	"	150
8	"	"	300
9	"	"	450
10	Pentanol	"	30
11	"	"	150
12	"	"	300
13	"	"	450
14	Isopropanol	3 g/l SiN	30
15 Blank	-	-	-

* Exposure to solvent for 5 min prior to deposition.



Fig. 17: Cross-section of graphite specimen coated with fused SiO₂. (Morphology + x-ray mapping of Si).



Fig. 18: Cross-section of graphite specimen coated with SiC.



Fig. 19: X-ray mapping of Si on area seen in Fig. 18.

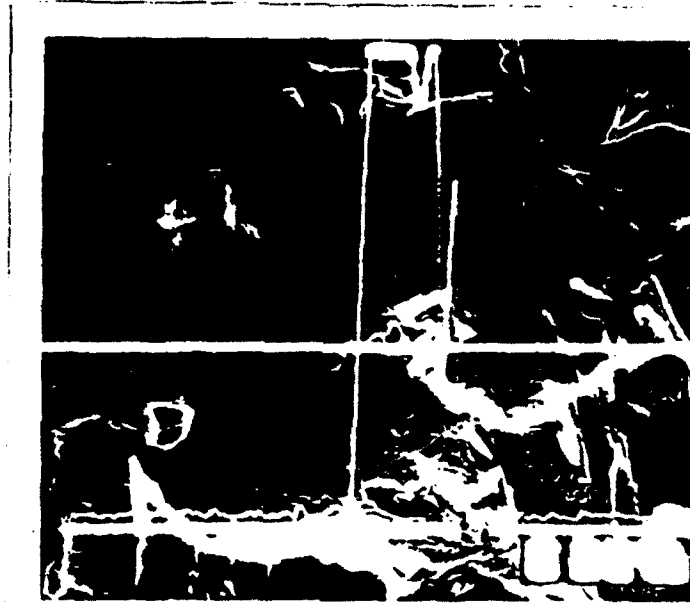


Fig. 20: SiC particle in C-C section.

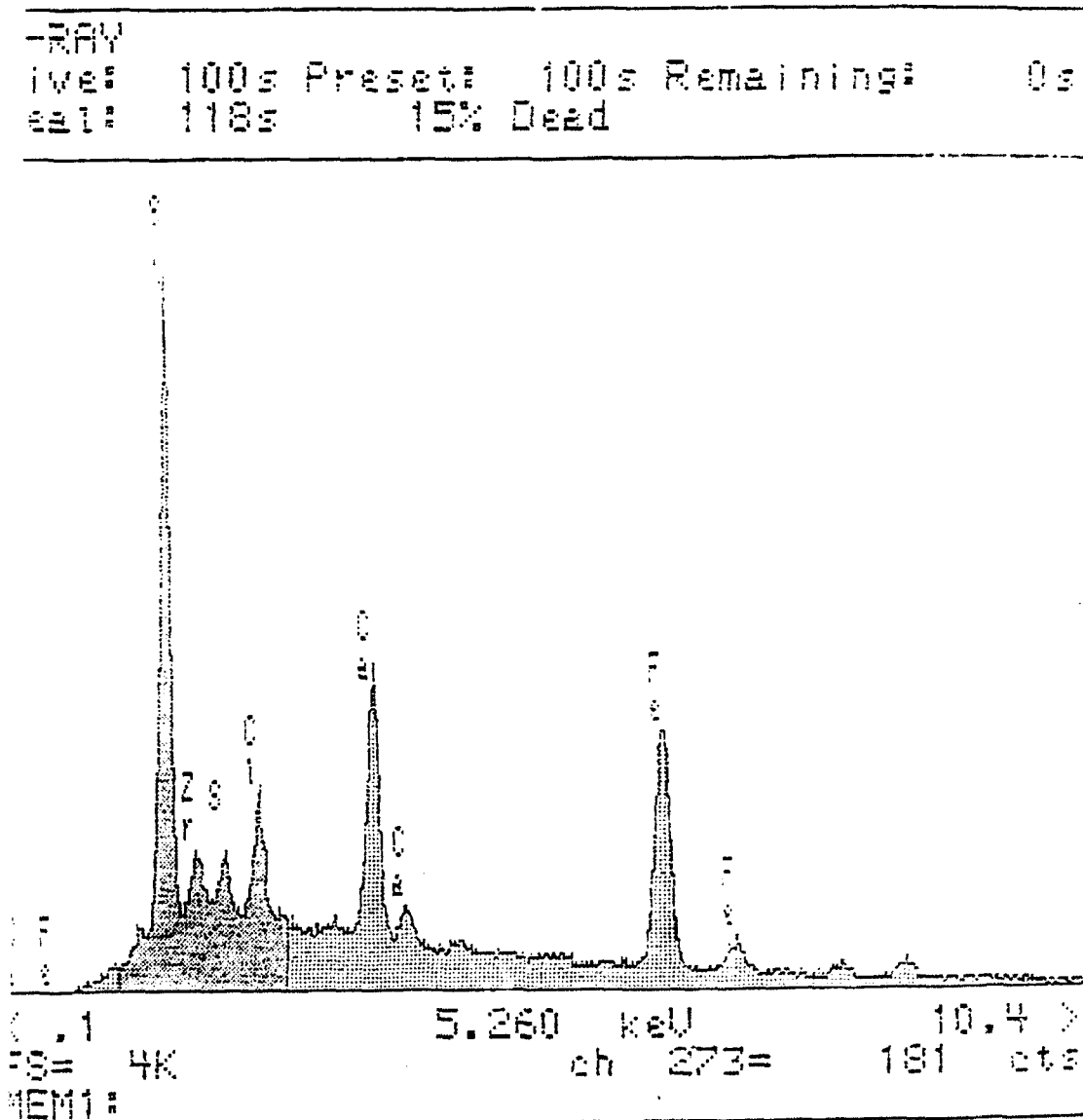


Fig. 21: EDS spectrum of particle seen Fig. 20.



Fig. 22: SiN particle in C-C composite section.

X-RAY
 Live: 65s Preset: 100s Remaining: 35s
 Real: 77s 16% Dead

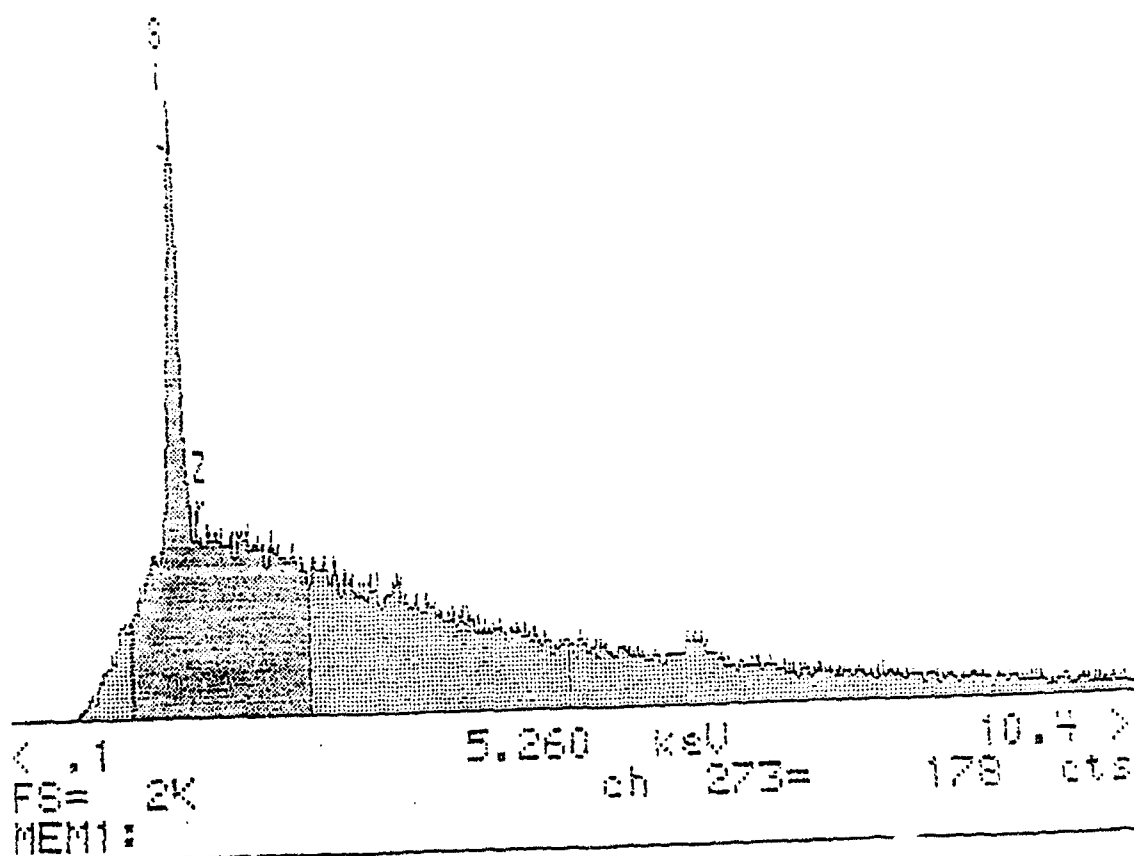


Fig. 23: EDS spectrum of particle seen in Fig. 22.

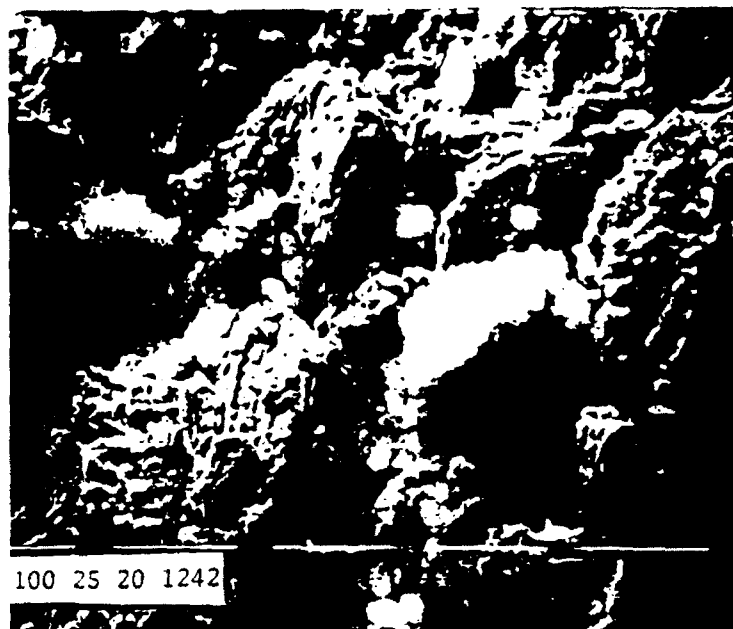


Fig. 24: Cross-section of graphite specimen coated with colloidal SiO_2 .

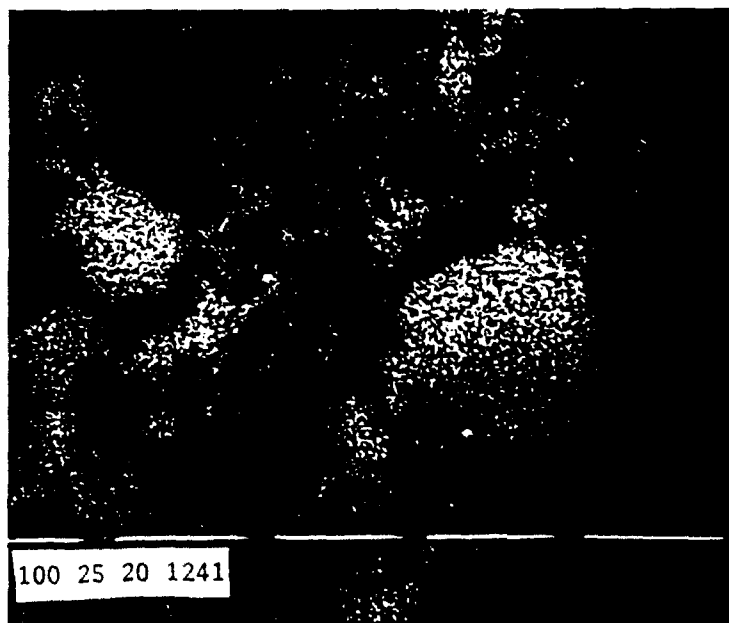


Fig. 25: X-ray mapping for Si on area seen in Fig. 24.

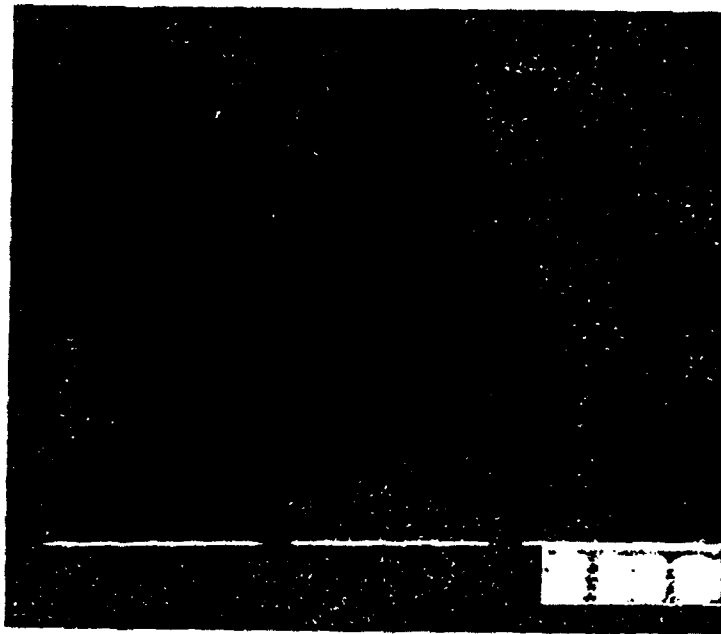


Fig. 26: X-ray mapping for Si on another area seen of cross-section.

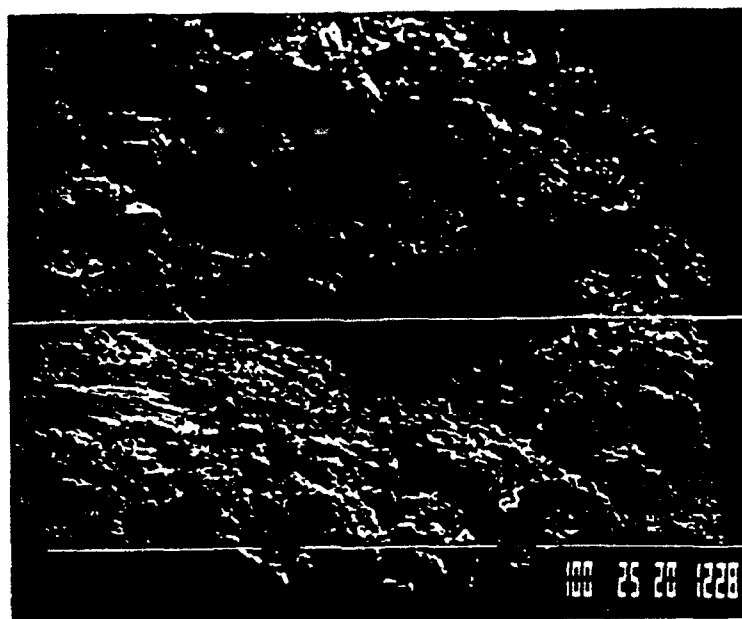


Fig. 27: As in Fig. 24.

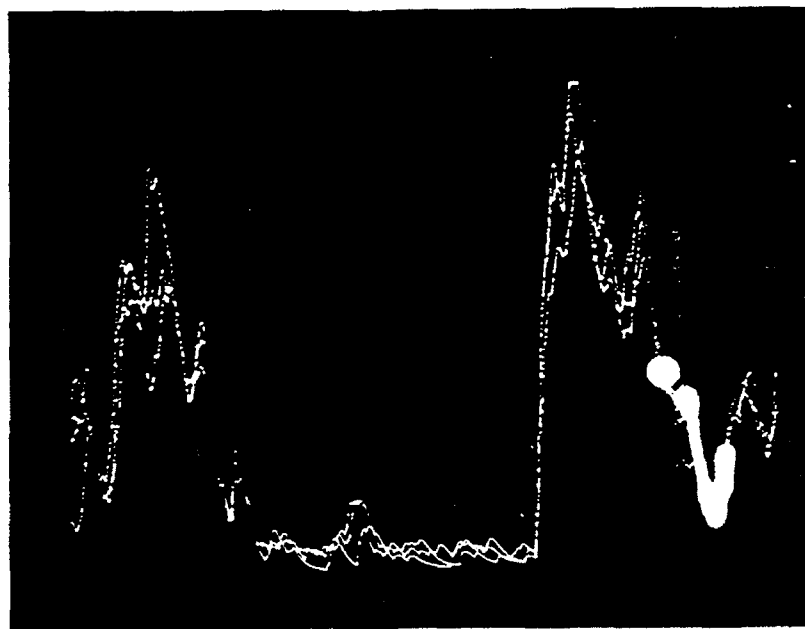


Fig. 28: Line scan for Si along the line seen in Fig. 27.

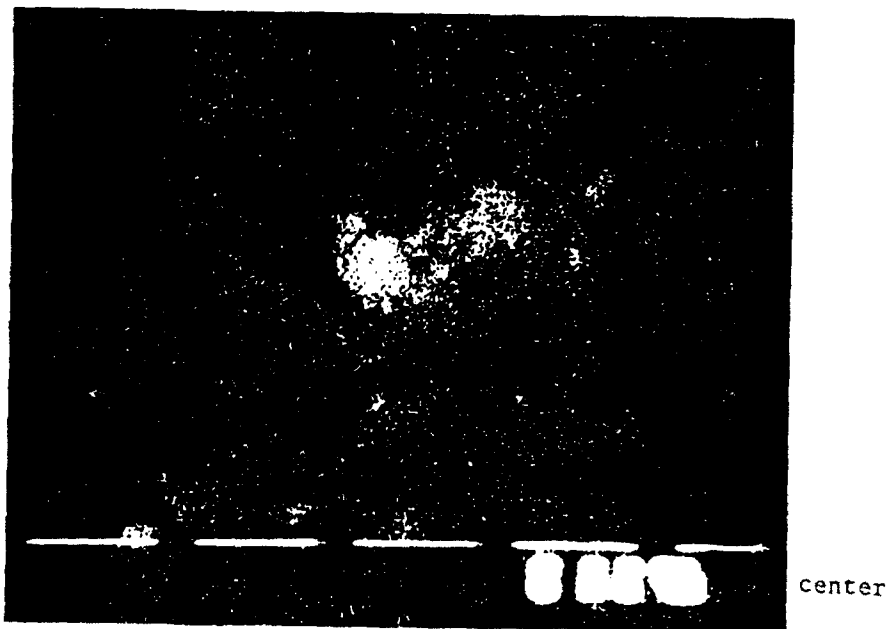
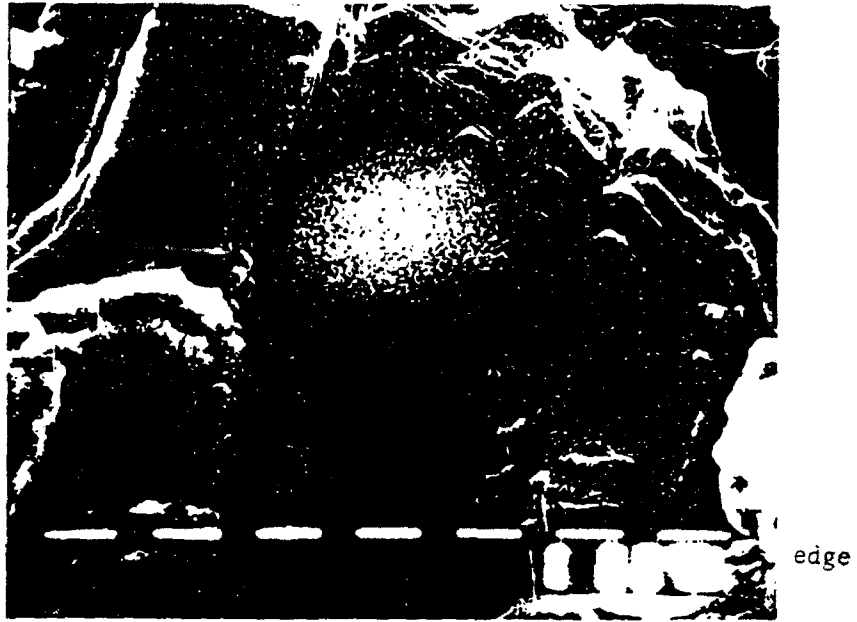


Fig. 29: Cross-section of specimen No. 1 -
Si mapping.

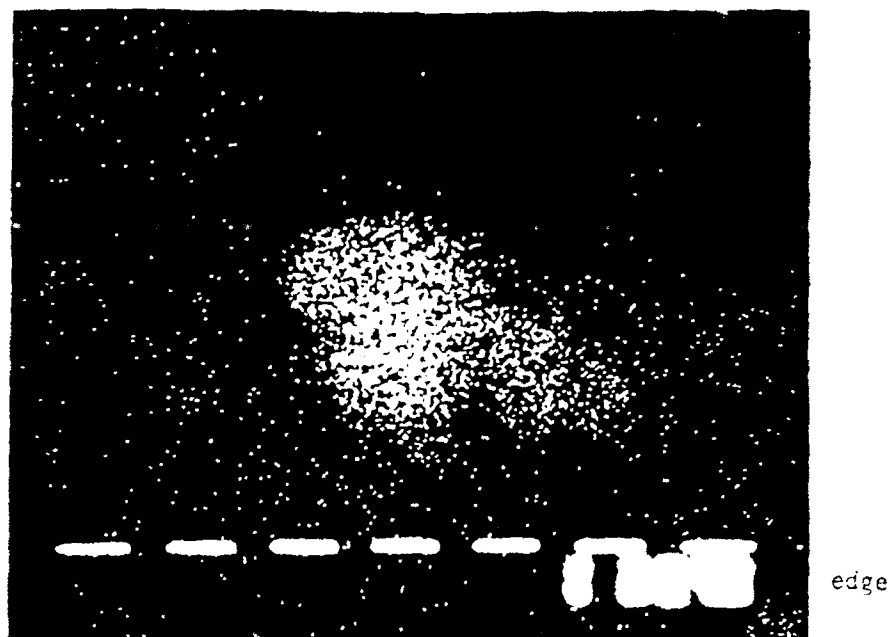


Fig. 30: Cross-section of specimen No. 2 -
Si mapping.

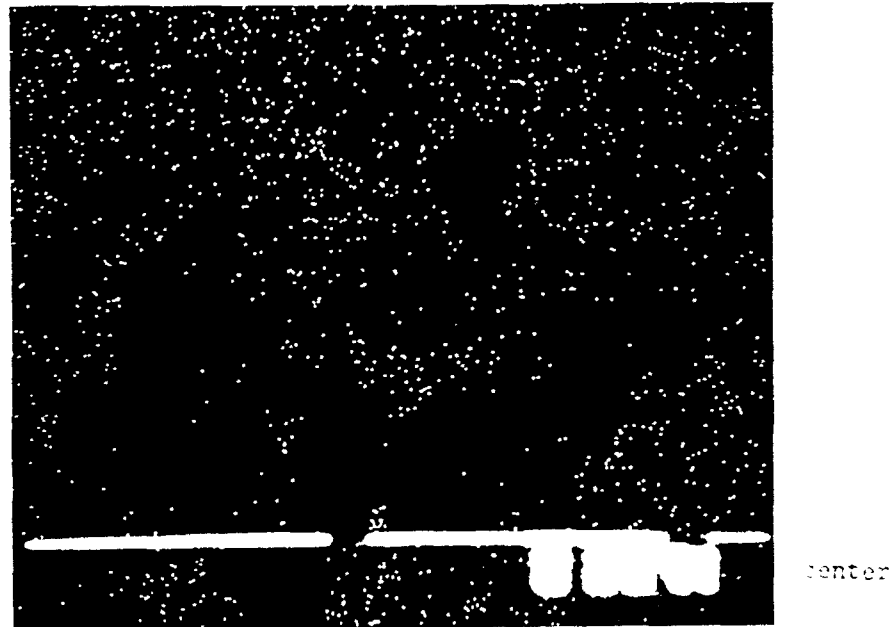
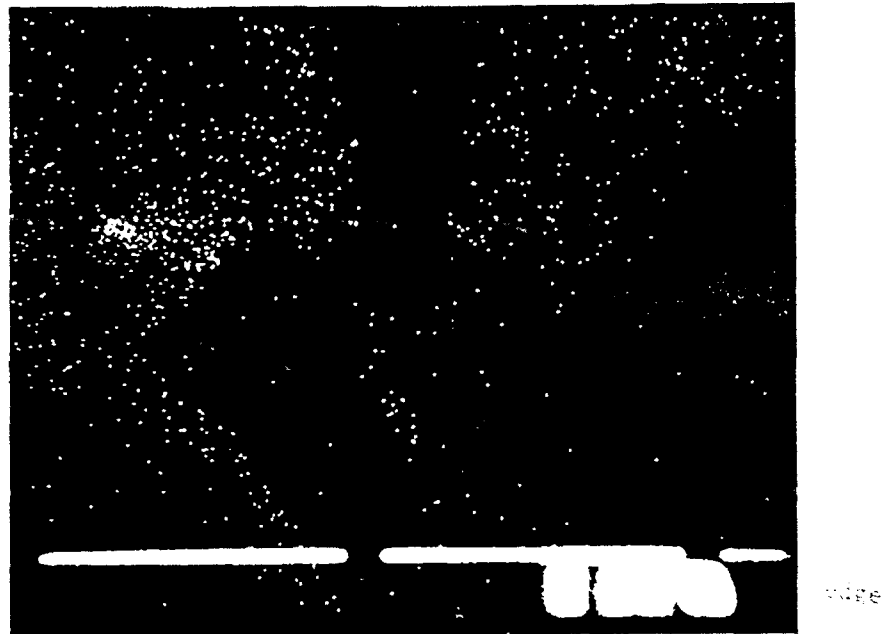


Fig. 31: Cross-section of specimen No. 3 -
Si mapping.

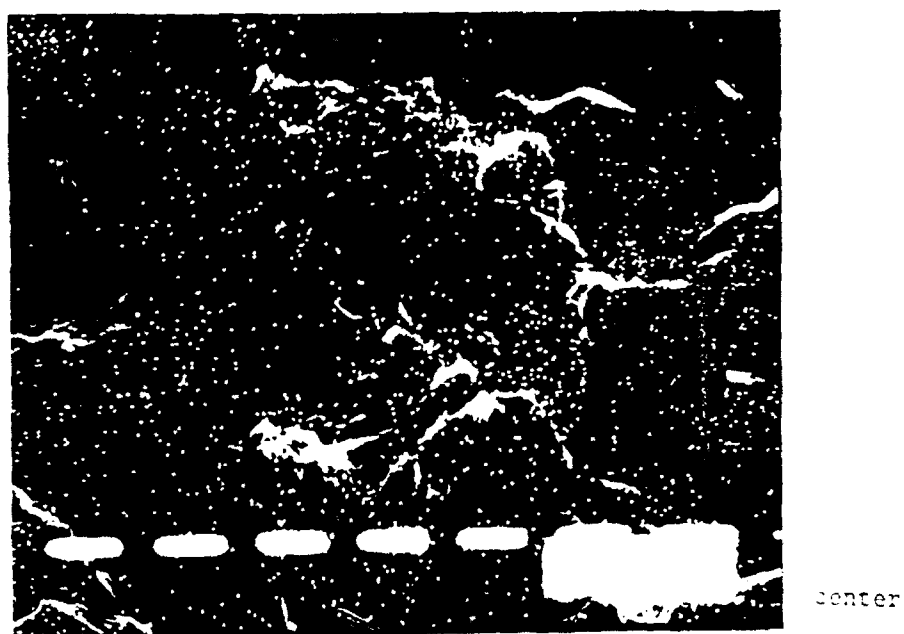
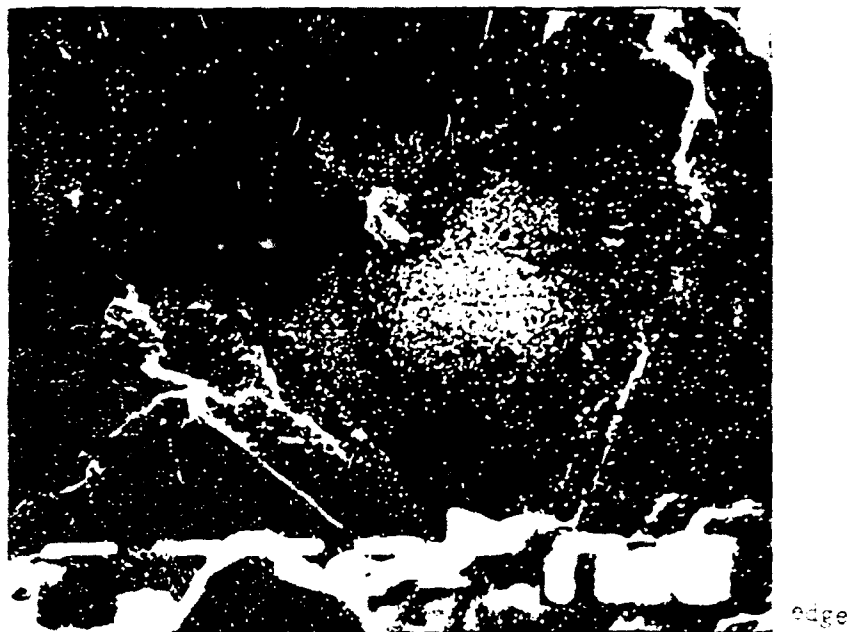


Fig. 32: Cross-section of specimen No. 4 -
Si mapping.

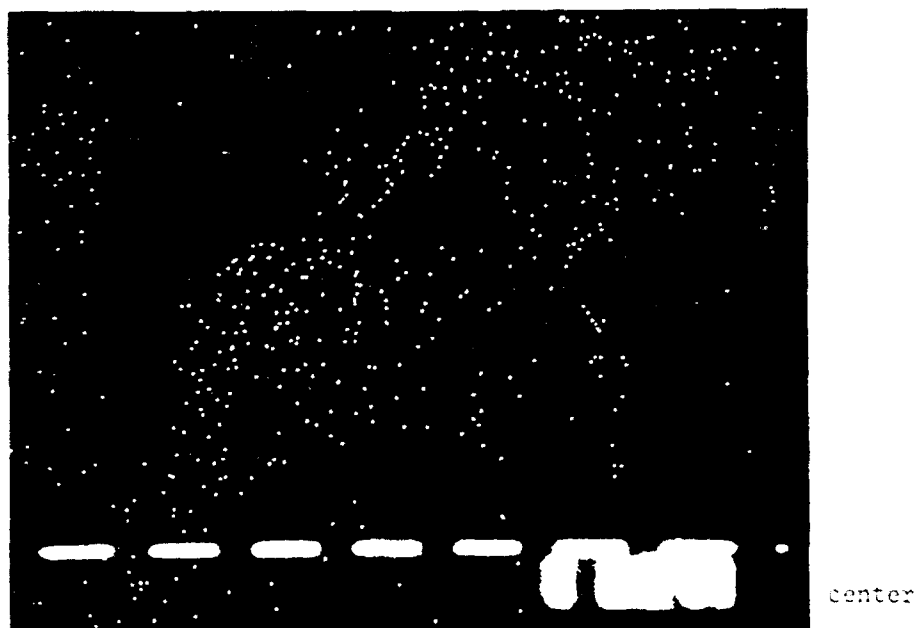
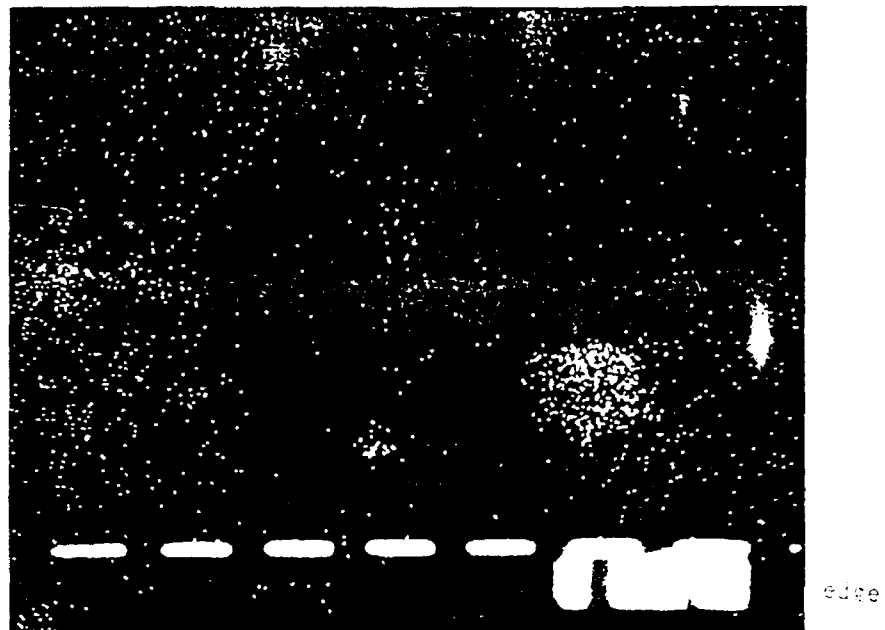


Fig. 33: Cross-section of specimen No. 5 -
Si mapping.

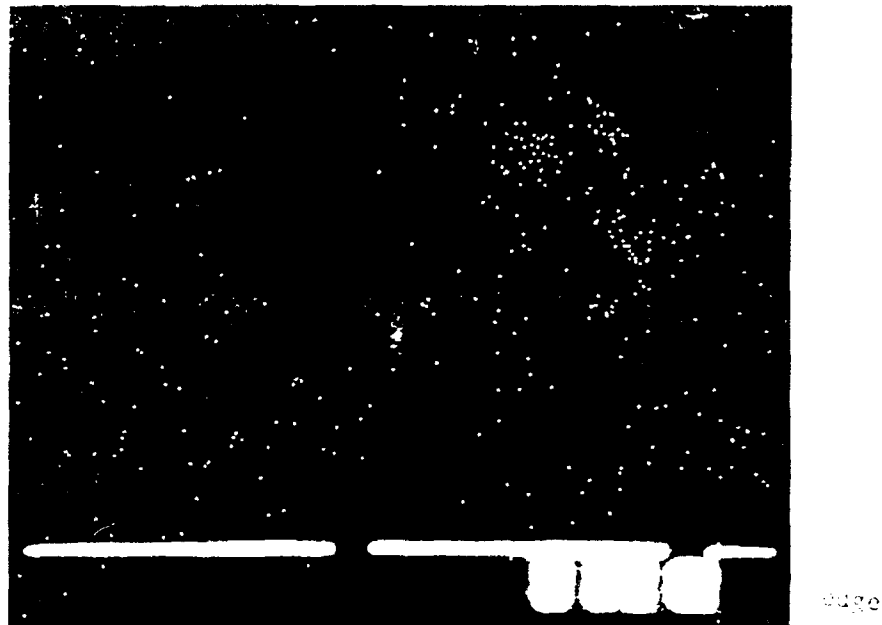
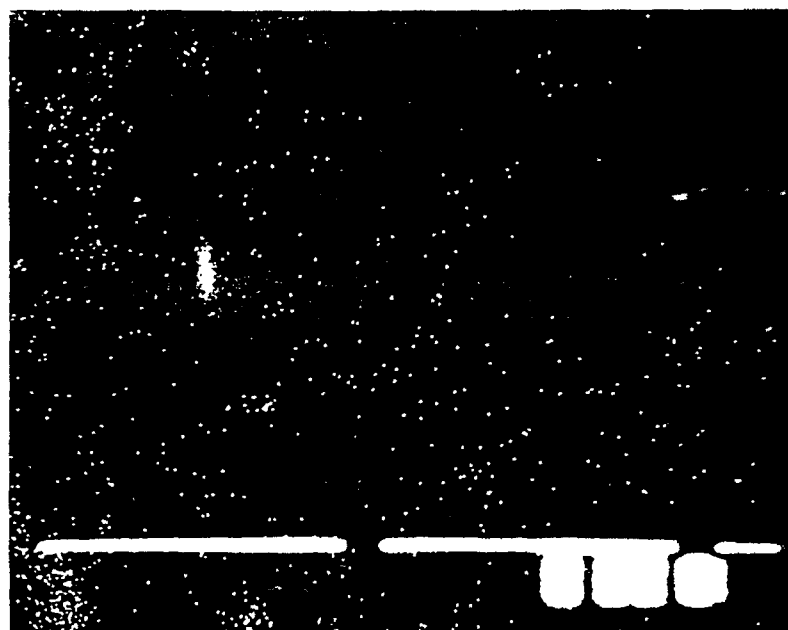
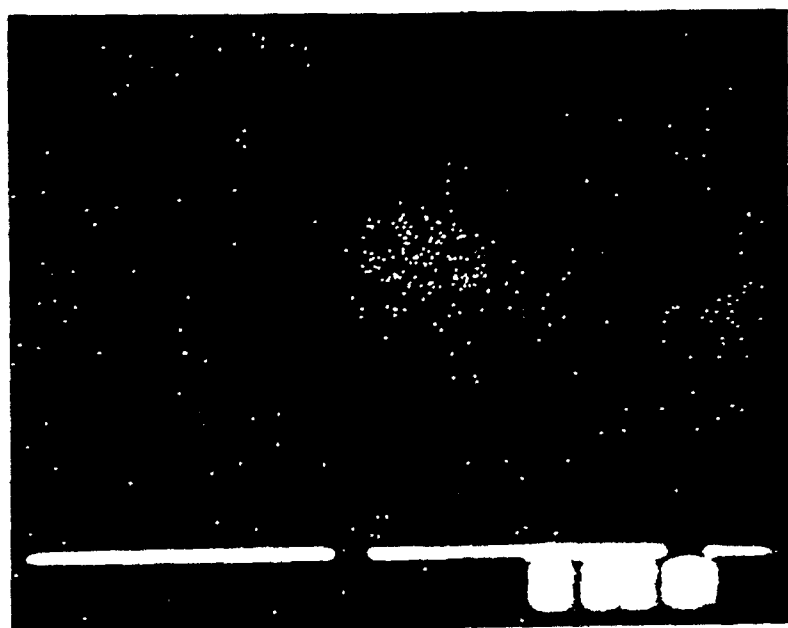


Fig. 34: Cross-section of specimen No. 6 -
Si mapping.



edge



center

Fig. 35: Cross-section of specimen No. 7 -
Si mapping.

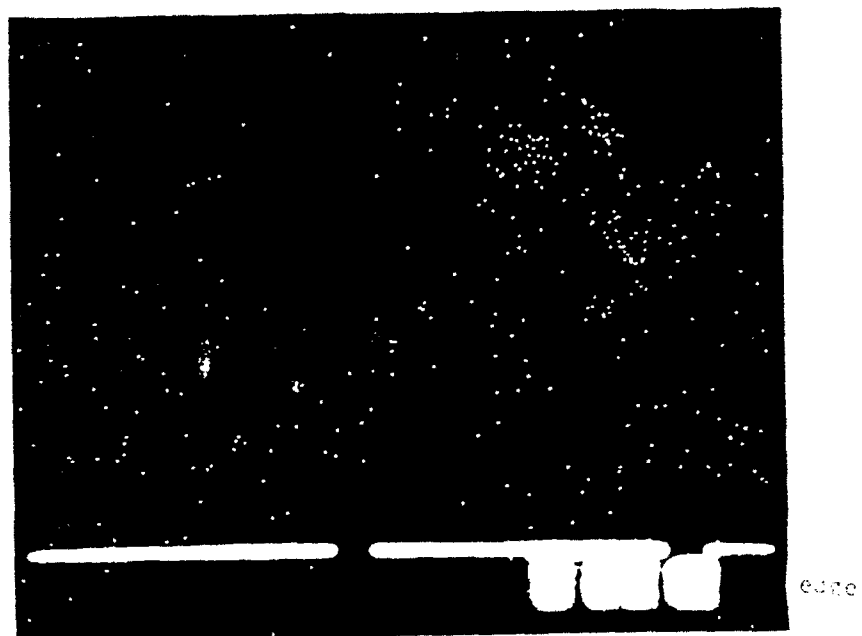


Fig. 36: Cross-section of specimen No. 8 -
Si mapping.

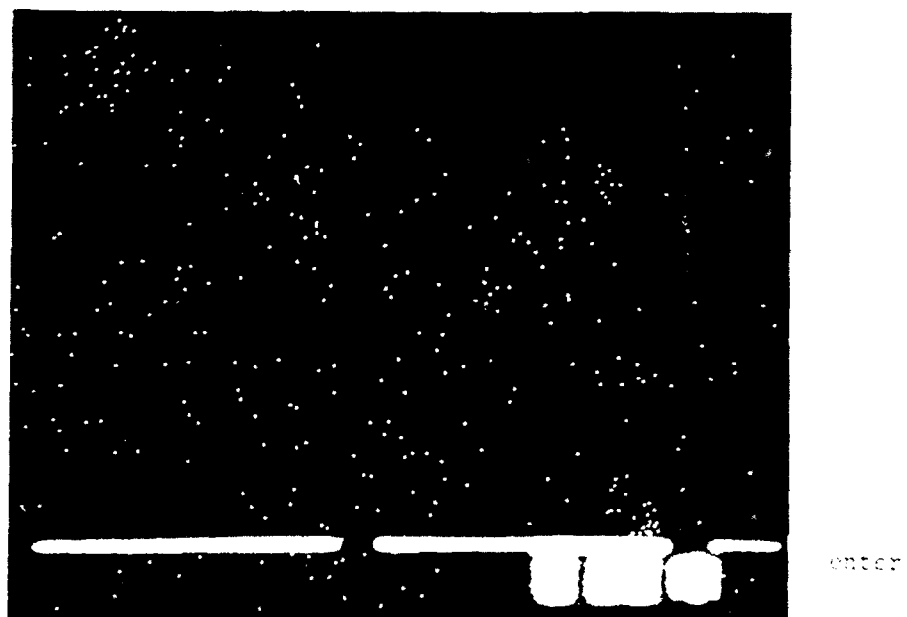
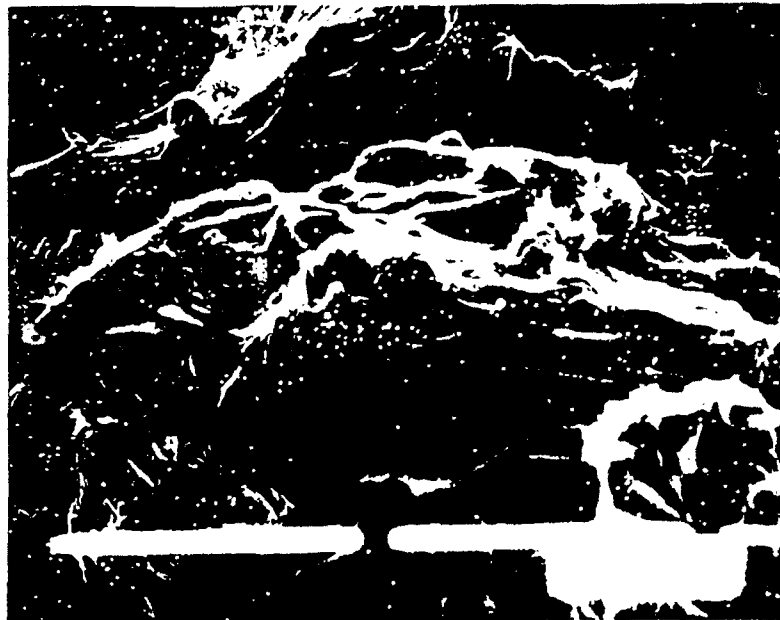


Fig. 37: Cross-section of specimen No. 9 -
Si mapping.



edge



center

Fig. 38: Cross-section of specimen No. 10 -
Si mapping.

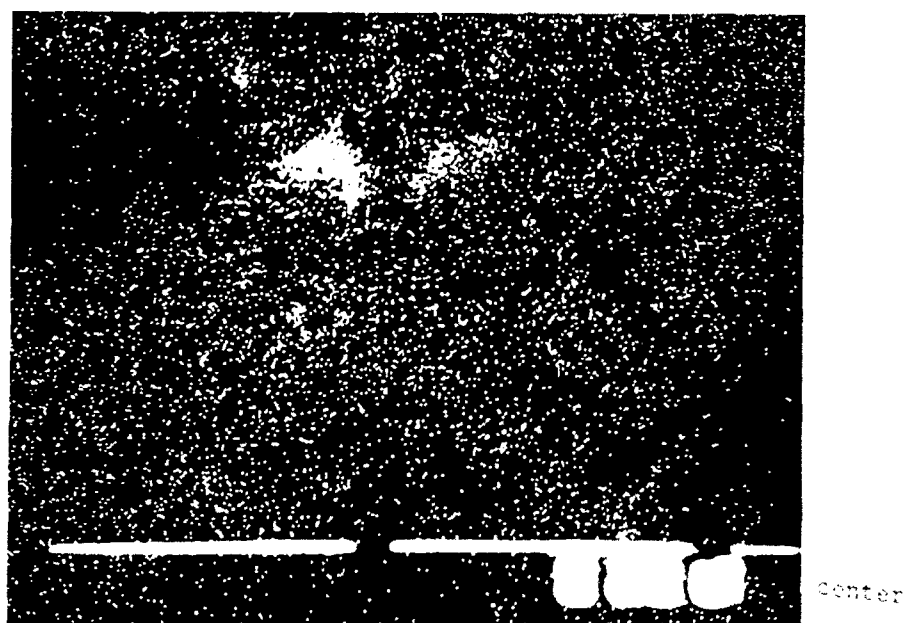
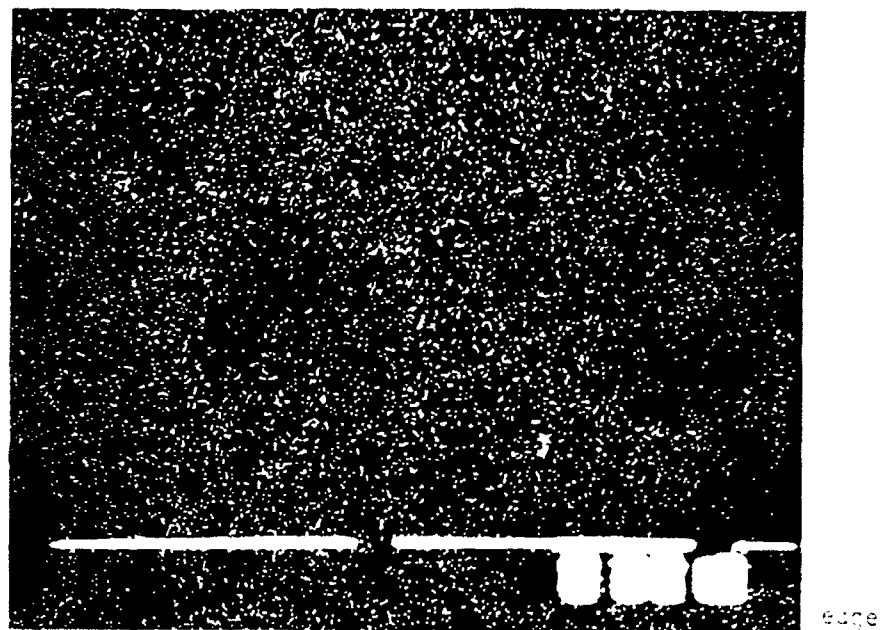


Fig. 39: Cross-section of specimen No. 11 -
Si mapping.

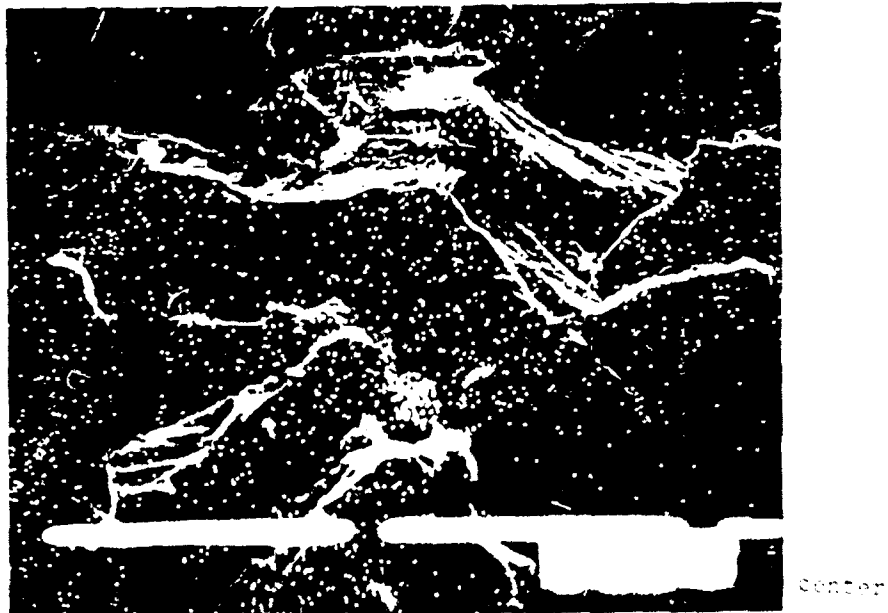


Fig. 40: Cross-section of specimen No. 12 -
Si mapping.



edge



center

Fig. 41: Cross-section of specimen No. 13 -
Si mapping.



Fig. 42: Si - line scan of cross-section of specimen 13.



Fig. 43: Cross-section of specimen No. 14 -
Si mapping.



Fig. 44: Cross-section of uncoated specimen -
Si mapping.

4.1.3 The electroosmotic effect

According to J. Anderson [11] when a porous medium is brought in contact with a solvent an applied electric field will cause an electroosmotic flow of the solvent into the pores provided the pore walls are charged. To verify the existence of this effect the following experiments were carried out:

Specimens of porous graphite (20x20x7mm) were immersed in distilled water (pH=5.5) and in isopropanol. The weight gain as function of immersion time with and without the existence of an electric field (50V/cm) was determined. Based on pore volume and solvent density the percentage of pores filled was determined (see Table 2 and Fig. 45 next page).

4.1.4 Electrophoretic impregnation of a porous substrate with ceramic particles

The amount of colloidal SiO_2 induced into porous graphite at varying deposition parameters was determined. The determination was performed by analyzing quantitatively the amount of SiO_2 in the specimen after physical removal of the external coating and graphite layer. The analytical method is described in chapter 3. The amount of SiO_2 was expressed in weight percents as related to the graphite specimen. A blank specimen (uncoated) was tested too and a background value of 0.03% was found. Table 3 describes the deposition parameters and results obtained. From these results the dependence of degree of impregnation on deposition voltage, particle concentration and type of solvent was offered and presented in Figs. 46-48.

Table 2: Influence of electric field on pore filling
50V/cm

I-Propanol										W a t e r				Time of Ex- posure min				
Field					No Field					Field					No Field			
Wt- Wo/gr	Wt/gr	Wo/gr	Wt- Wo/gr	Wt/gr	Wo/gr	Wt- Wo/gr	Wt/gr	Wo/gr	Wt- Wo/gr	Wt/gr	Wo/gr	Wt- Wo/gr	Wt/gr		Wo/gr			
0.8341 80%	5.3050	4.4709	0.3966 38%	4.8107	4.4141	0.4612 34%	5.0810	4.6198	0.1585 12%	4.8485	4.6900				5			
0.8810 84%	5.2963	4.4153	0.7932 75%	5.2583	4.4651	1.071 79%	5.5957	4.5247	0.1585 12%	4.6408	4.4823				15			
0.8594 82%	5.3634	4.5040	0.7877 72%	5.2286	4.4409	1.0582 78.9%	5.5897	4.5315	0.1479	4.6295	4.4816				30			
			0.7228	5.1349	4.3421										45			
			0.8660	5.2982	4.4322										60			

Wo - Original weight

Wt - Weight at end of exposure

Results in % - % of pore volume filled.

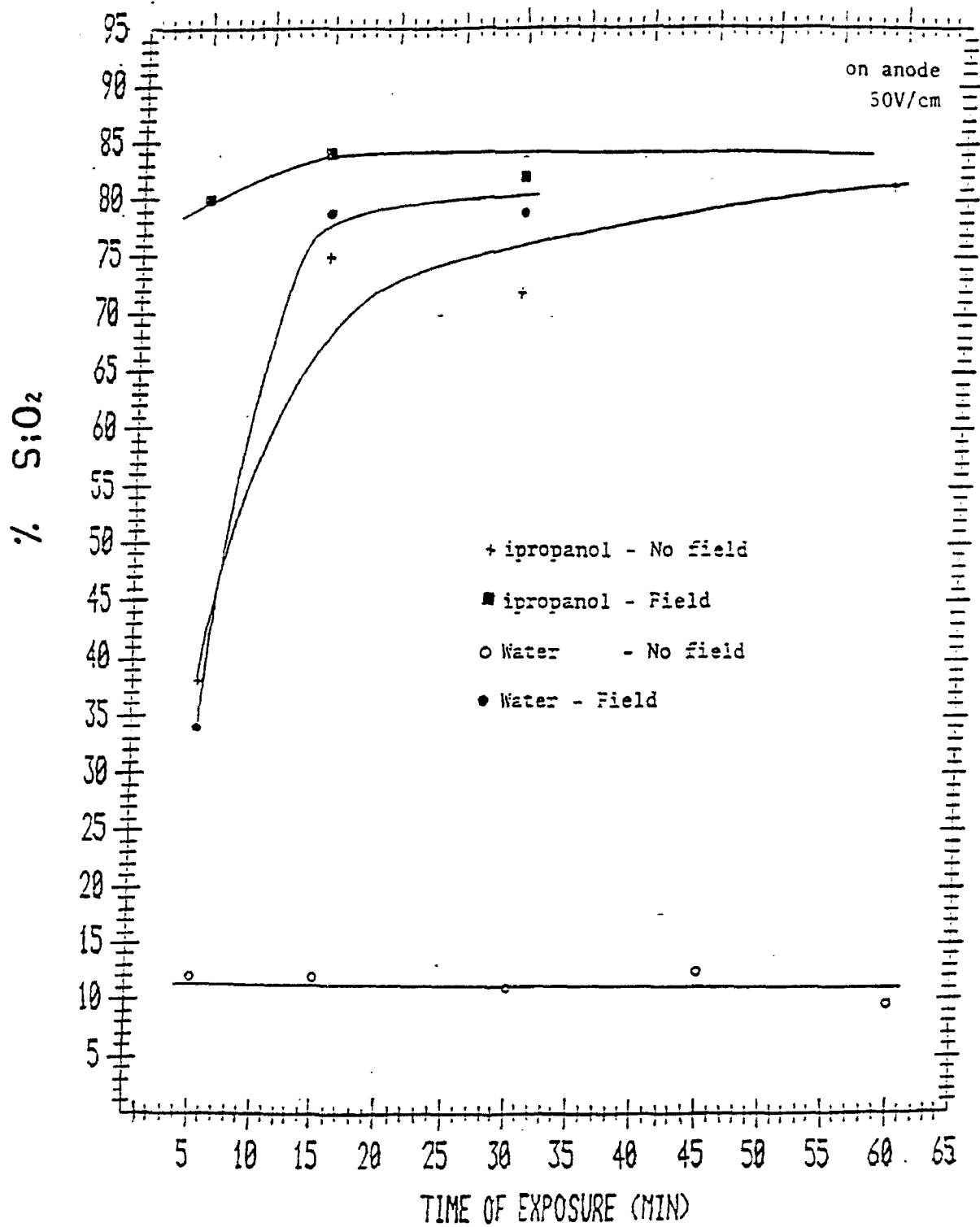


Fig. 45: Percentage pores volume filled as function of exposure time.

Table 3: Weight percentage of SiO_2 in graphite specimens as determined by chemical analysis. (Deposition time - 2 hrs).

Specimen No.	Solvent	Concen. SiO_2 g/l	Deposition voltage (V)	% SiO_2
1	Isopropanol	3	30	0.16
2	"	"	150	0.23
3	"	"	300	0.26
4	"	"	450	0.18
5	"	13	30	0.35
6	"	"	150	0.18
7	"	"	300	0.30
8	"	"	450	0.11
9*	"	"	150	0.61 (wet milling)
10	"	30	30	0.4
11**	"	13	30	0.68
12	Pentanol	3	30	0.1
13	"	"	100	0.1
14	"	"	150	0.2
15	"	"	200	0.1
16	"	13	150	0.1
17	Hexanol	3	150	0.07
Blank				0.03

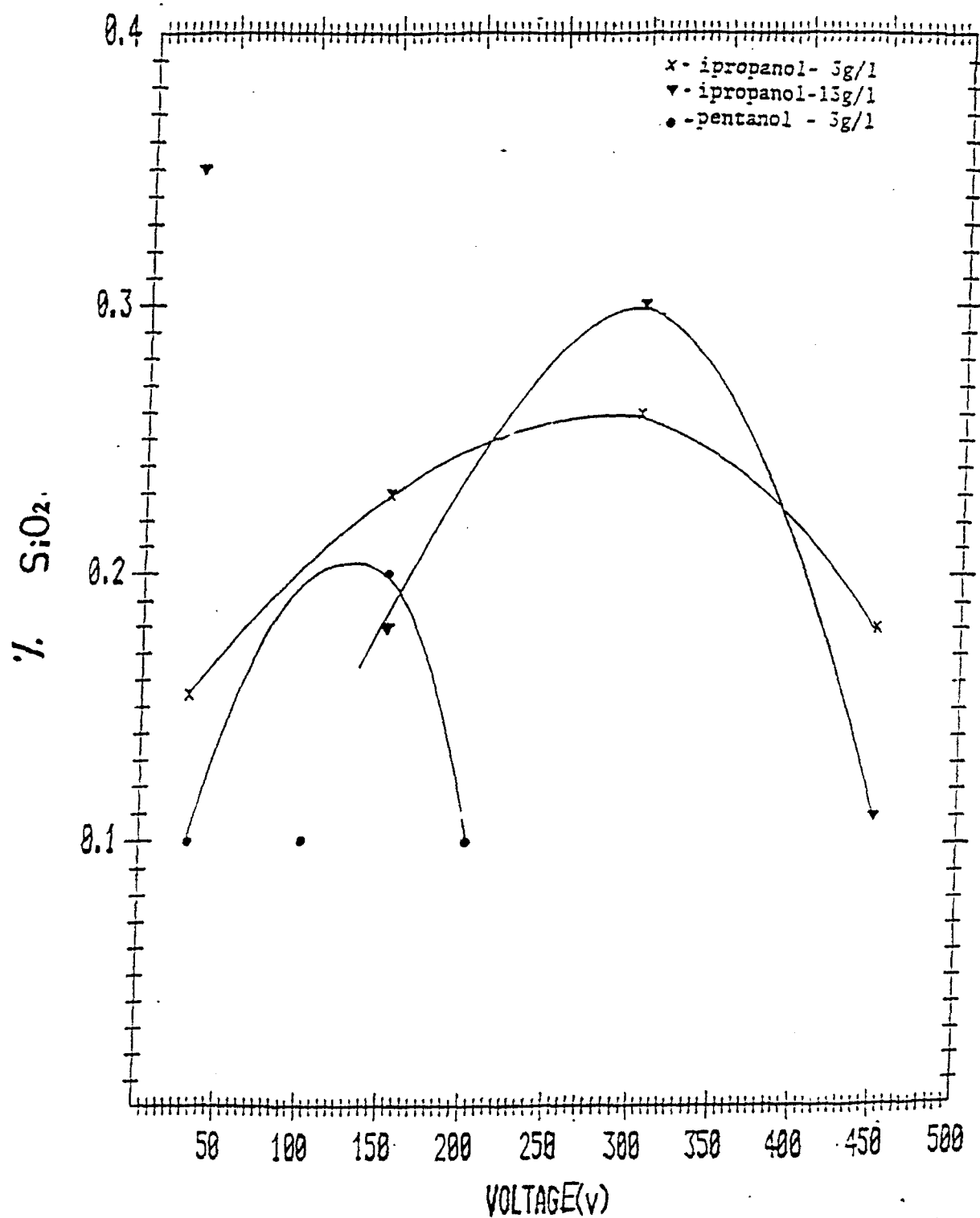


Fig. 46: % SiO_2 induced as function of deposition voltage.

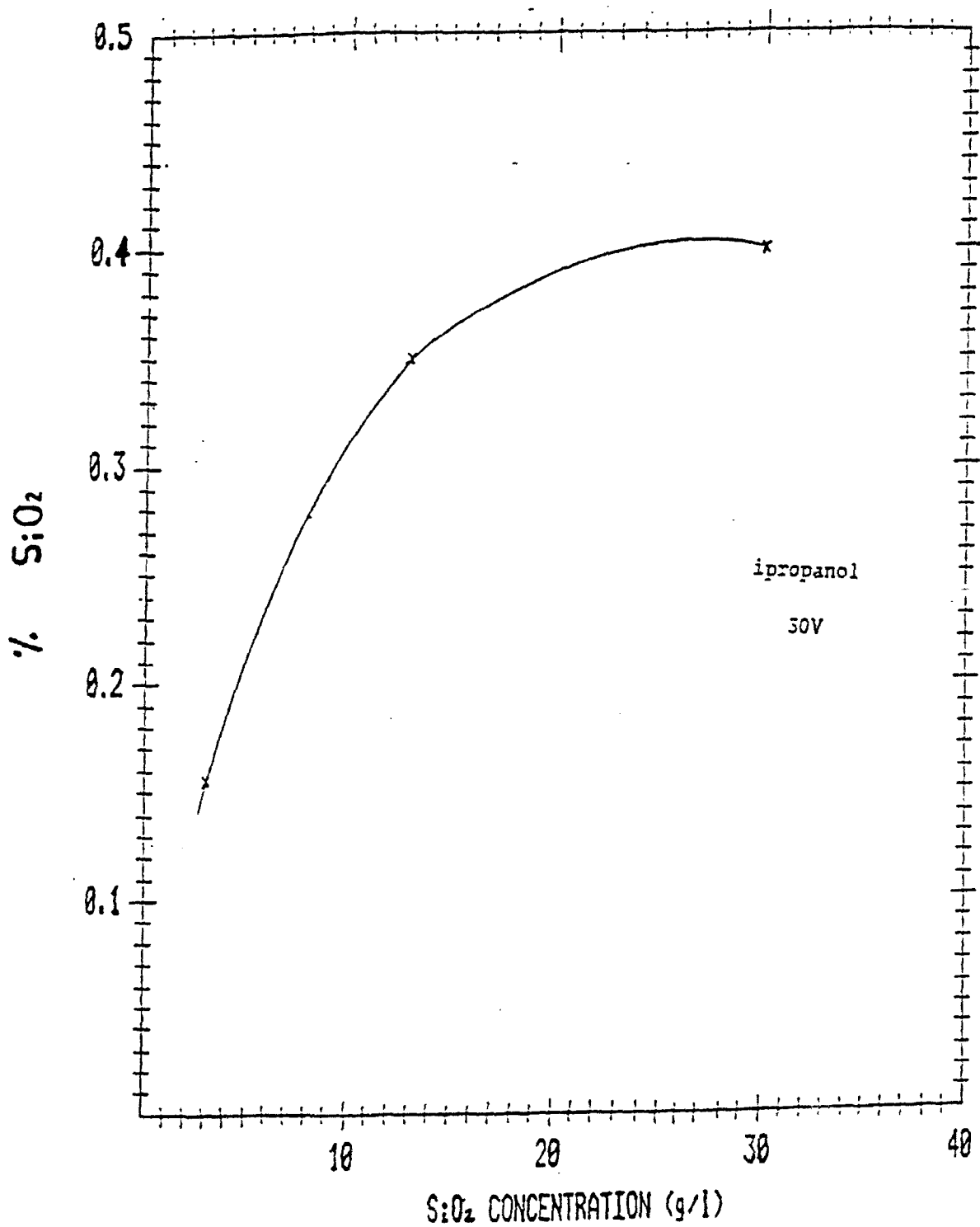


Fig. 47: % SiO_2 induced as function of particle concentration.

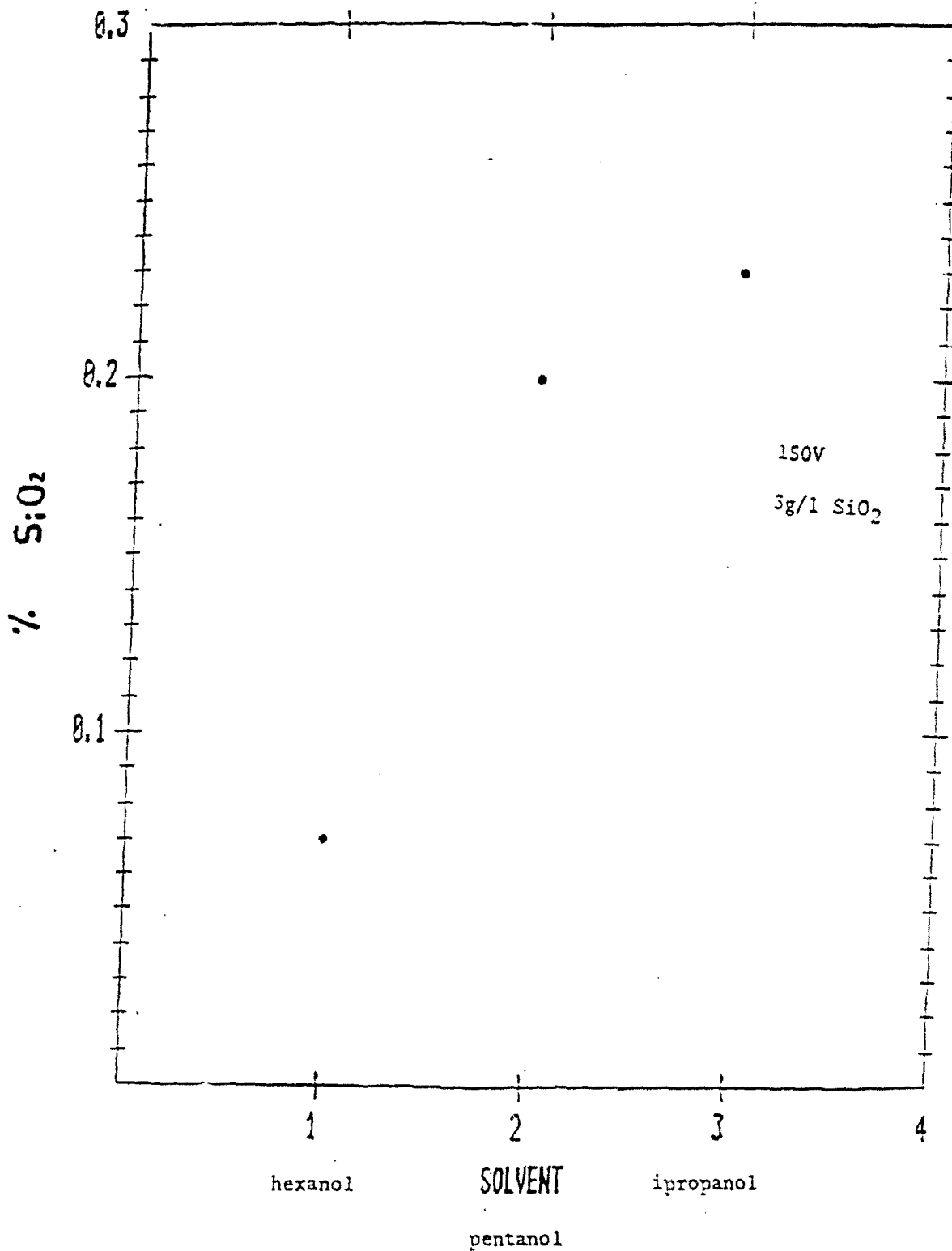


Fig. 48: % SiO₂ induced as function of type of solvent.

4.1.5 Morphology of induced SiO₂

A most interesting phenomenon was observed during the quantitative determination of the SiO₂ induced in porous graphite. As mentioned before, the first stage in the determination is the removal of the graphite by its oxidation at 950°C. In specimens with a higher content of SiO₂ (0.68%), after the carbon volatilization a skeleton of SiO₂ in the exact form and volume of the original graphite specimen was seen (see Figs. 49,50).

4.1.6 Relevant solvent properties

Two solvent properties relevant to electrophoretic deposition are presented in Table 4 based on data from literature. In addition the viscosity of two SiO₂ suspensions in isopropanol and one in pentanol were measured using an Epprecht Rheomat 15 instrument. Measurements of shear stress as dependent on shear rate were performed on suspensions which have been stirred for 30 min.

Table 4: solvent properties (at 25°C)

Solvent	Dielectric Constant	SiO ₂ conc. g/l	Viscosity (cp)
Ethanol	24.3	-	1.04
Isopro-			
panol	18.3	-	2
"	-	13	4.37
"	-	30	5.74
Pentanol	13.9	-	3.31
"	-	13	5.21
Hexanol	13.3	-	-



Fig. 49: Induced SiO_2 skeleton remaining after porous graphite volatilization (0.68% SiO_2) specimen in Table 3.

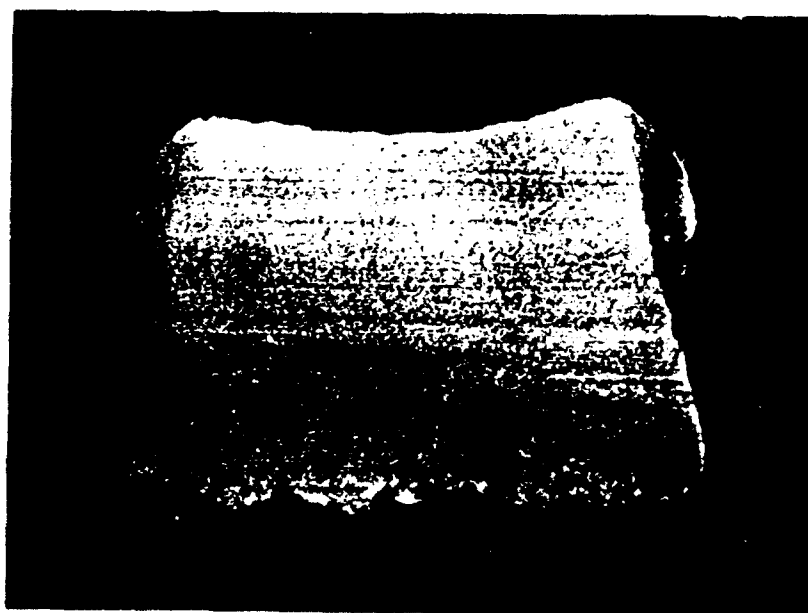


Fig. 50: Cross-section of skeleton seen in Fig. 49.

4.2 Electrodeposition of ceramic films

Three types of oxides (CeO_2 , ZrO_2 and Al_2O_3) were deposited from aqueous solutions containing $\text{Ce}(\text{NO}_3)_4$, $\text{Al}(\text{NO}_3)_3$ and $\text{ZrO}(\text{NO}_3)_2$ respectively through an electrochemical reaction. The deposits were formed both on graphite and on C-C specimens which functioned as cathodes in an electrochemical cell.

4.2.1 CeO_2 deposition

The CeO_2 was deposited from a catholyte of 1M $\text{Ce}(\text{NO}_3)_4$ with an initial pH of 2.2. The anolyte, separated by a glass frit, was 1M NaNO_3 . The graphite and C-C specimens were cleaned with acetone and then kept in the solution for 20 min in an ultrasonic bath to facilitate penetration of the solution into pores. Surface deposits were obtained at 20V (initial c.d. of $30\text{mA}/\text{cm}^2$) at 30°C for 10 min. In impregnation experiments the voltage and c.d. were lowered (5V, $5\text{mA}/\text{cm}^2$) and the temperature raised to 55°C . The experiment duration was prolonged too to 30 min. The surface deposit was examined with the SEM and also by X-ray diffraction. Fig. 51 shows the deposit on C-C specimen, while Figs. 52, 53 show the deposit on graphite as seen in the SEM and by mapping of Ce. The results of X-ray diffraction of the deposit and the diffraction of a known CeO_2 powder are given in Table 5.

The formation of CeO_2 deposits inside the matrix of a C-C specimen is shown in Figs. 54-56.

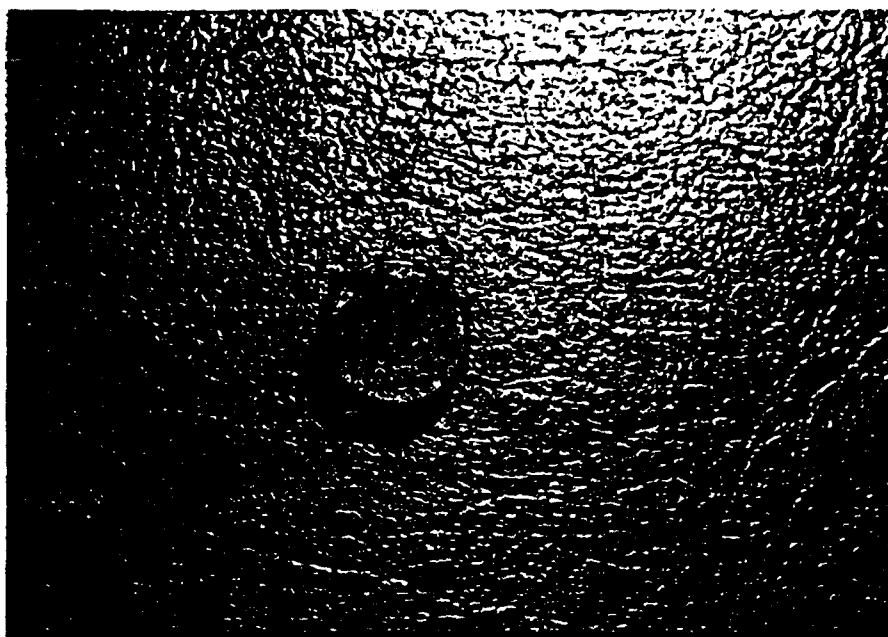


Fig. 51: CeO_2 on C-C composite (electrodeposition).



Fig. 52: CeO_2 on graphite (electrodeposition).

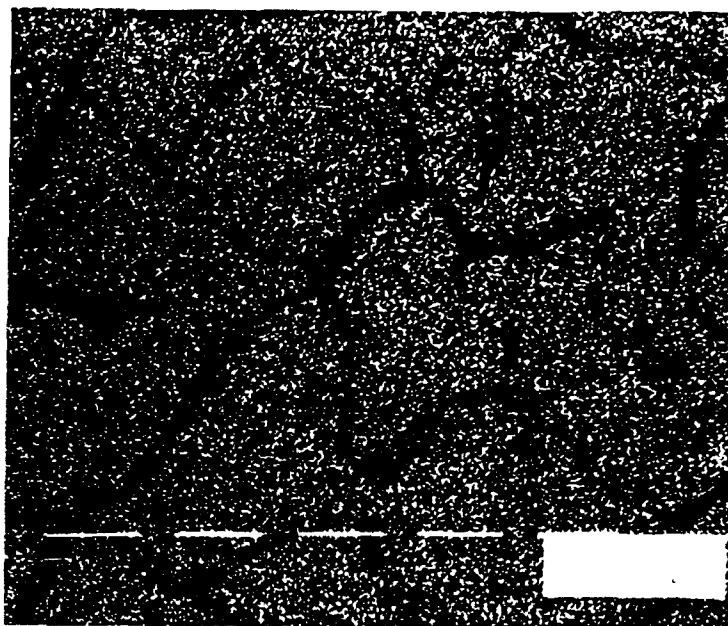


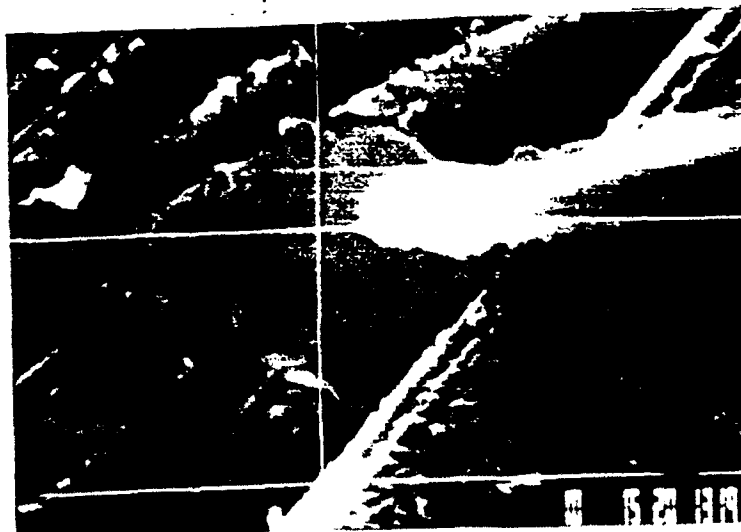
Fig. 53: X-ray mapping of Ce on area seen in Fig. 52.

Table 5: X-ray diffraction characteristic of CeO_2

Peak no	Angle (deg)	Tip width (deg)	Peak (cts)	Backg (cts)	D spac (Ang)	I/Imax (%)	Type			Sign.
							A1	A2	Ot	
1	28.7000	0.60	1739.	96.	3.1080	100.00	X			7.24
2	33.1625	0.60	576.	100.	2.6993	33.12	X			2.24
3	47.5875	0.60	1406.	62.	1.9093	80.67	X			4.37
4	56.4075	1.20	635.	19.	1.6299	36.52	X			4.90
5	59.1650	0.60	376.	0.	1.5603	21.64	X			2.51
6	69.5300	0.60	166.	30.	1.3509	9.57	X			1.66
7	76.6475	0.60	751.	37.	1.2423	43.17	X			4.37
8	79.2000	0.40	681.	0.	1.2085	39.17	X			19.05
9	88.6000	0.40	824.	29.	1.1029	47.37	X			1.86
10	95.6000	0.40	767.	23.	1.0398	44.12	X			2.40

X-ray diffraction characteristic of CeO_2 powder.

Peak no	Angle (deg)	Tip width (deg)	Peak (cts)	Backg (cts)	D spac (Ang)	I/Imax (%)	Type		
							A1	A2	Ot
1	28.3800	1.20	912.	250.	3.1423	100.00	X		
2	32.7775	1.00	156.	259.	2.7301	17.13	X		
3	47.2100	1.20	713.	243.	1.9237	78.16	X		
4	56.0175	1.40	449.	204.	1.6403	49.28	X		
5	69.1525	1.20	86.	77.	1.3574	9.49	X		
6	75.9500	1.20	202.	88.	1.2533	22.11	X		
7	88.4075	1.40	67.	166.	1.1048	7.37	X		
8	94.8450	2.00	76.	132.	1.0461	8.30	X		
9	106.4325	1.20	61.	62.	0.9618	6.67	X		
10	113.6350	2.00	110.	137.	0.9204	12.09	X		
11	116.2000	0.40	45.	231.	0.9073	4.92	X		

Fig. 54: CeO_2 particles in C-C composite section.

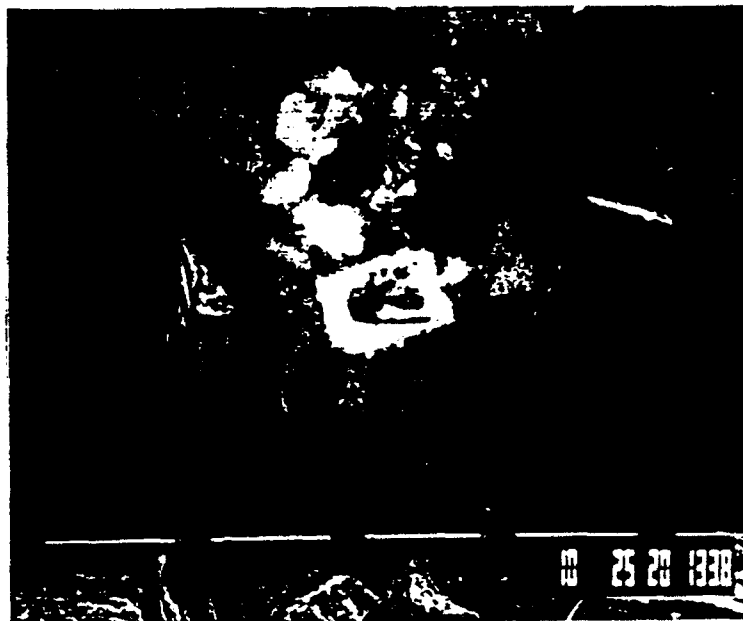


Fig. 55: Like Fig. 54.

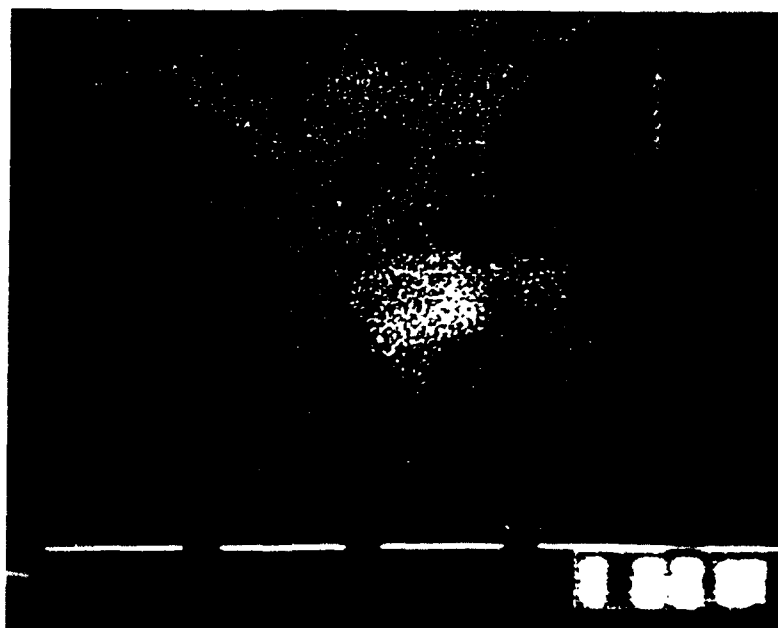


Fig. 56: X-ray mapping of Ce on area seen in Fig. 55.

4.2.2 ZrO₂ deposition

The ZrO₂ deposit was obtained from a solution of 1M ZrO(NO₃)₂·4H₂O in the cathodic section and an anolyte of 1M NaNO₃. The deposit was obtained on a graphite cathode with a platinum foil acting as the anode. The deposition was performed at a constant c.d. of 25 mA/cm² (nominal) which corresponded to a voltage of 5V. The initial pH of the solution was 1.1. Deposition time was 60 min. At the end of the experiment a thin white deposit was evenly distributed on the surface of the graphite. Fig. 57 shows the surface deposit, while Fig. 58 shows the x-ray mapping of Zr on the same area. At a smaller magnification relatively large crystals are seen (see Fig. 59) in some locations. A cross-section through the coated specimen was prepared (by cutting with a diamond saw) and is seen at 2 magnifications in Fig. 60. Microanalysis of the deposit was performed in locations of smaller and larger crystallites and the results, corresponding to the atomic ratio in ZrO₂, are shown in Figs. 61. X-ray diffraction of the deposit as received indicates an amorphous structure. Further experiments at higher c.ds. and duration showed the possibility to obtain heavy and thick deposits. Calcination experiments are underway and they indicate a crystallization process of the deposit (detailed results will be reported at a later stage).



Fig. 57: ZrO₂ on graphite (electrodeposition).



Fig. 58: X-ray mapping of Zr on area seen in Fig. 57.

4.2.3 Al₂O₃ deposition

The possibility to obtain thin white aluminum oxide deposits on graphite was demonstrated in experiments performed with 1M Al(NO₃)₃ as catholyte and 1M NaNO₃ as anolyte at a c.d. of 50mA/cm² corresponding to 30V for 15 min. Initial pH=2.6.

Fig. 62 shows a general view of the deposit on graphite specimen and Figs. 63.64 show a microscopic view and a x-ray mapping of Al of the same deposit.

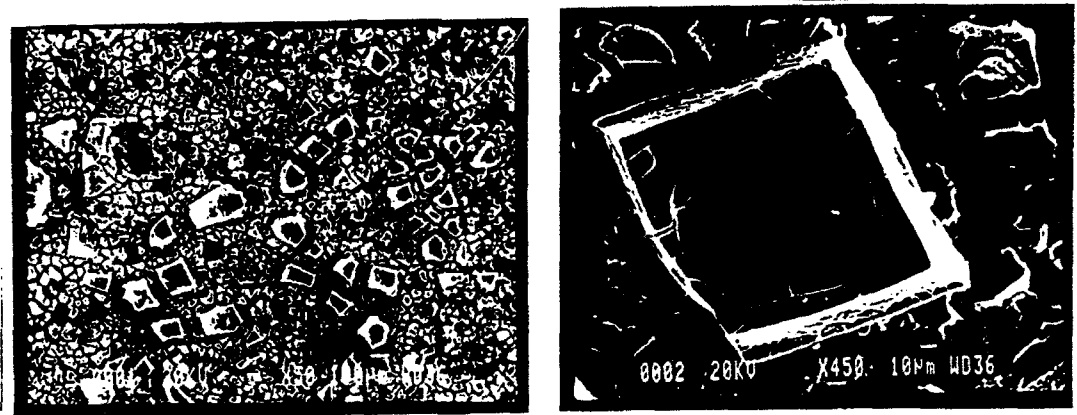


Fig. 59: ZrO₂ on graphite.



Fig. 60: Cross-section through ZrO₂ deposit.

LIVETIME(spec.)= 100

ENERGY RES AREA
 - 5.7 106.61 65709
 TOTAL AREA= 198051

.....
 Peak at 1.02 keV omitted?
 Peak at 15.74 keV omitted?
 Peak at 17.64 keV omitted?
 FIT INDEX= 2.50

ELMT APP.CONC ERROR(WT%)
 ZrL : 1 55.260 .411
 CaK : 1 .793 .074
 ..E 2 ZAF'SJ

20.00 kV TILT= .00 ELEV=40.00 AZIM= .00 COSINE=1.000

Spectrum:

Last elmt by STOICH.,NORMALISED

ELMT	ZAF	%ELMT	ATOM.%	%OXIDE	FORMULA
ZrL : 1	.919	73.083	32.789	Zr102 78.720	.992
CaK : 1	.904	1.067	1.089	Ca201 1.280	.033
O K : 0	.000	25.850	66.122		2.000
TOTAL		100.000	100.000	100.000	1.025

Fig. 61: Microanalysis of ZrO₂ deposit.



Fig. 62: Al_2O_3 on graphite (electrodeposition).



Fig. 63: Al_2O_3 graphite (electrodeposition).



Fig. 64: X-ray mapping of Al on area seen in Fig. 63.

CHAPTER 5 - DISCUSSION OF RESULTS

Surface deposits of all the ceramic materials studied (colloidal and fused SiO_2 , SiC and SiN) were obtained both on graphite and C-C substrates by electrophoresis. SiO_2 and SiC deposits formed on the anode indicating the presence of a negative charge on the particles, while SiN deposited on the cathode. The charging mechanism of SiO_2 takes place as indicated in literature, by the ionization of silanol groups present on the surface of silica which has been in contact with water for prolonged periods.



The charging of SiC and SiN can be envisaged through an adsorption mechanism with SiC adsorbing negative ions and SiN adsorbing positive ones. In the systems we studied the available ions are OH^- and H^+ deriving from small concentrations of water present in the solvent. The dielectric constant of the solvent (isopropanol) is at an appropriate level so as to enable charging of the particles and yet to prevent electrochemical decomposition of the fluid and evolution of gas.

Under the influence of the electric field the particles move to the electrode with the opposite charge forming a relatively dense and adherent "green coating" the thickness of which depends on the deposition time (Figs. 9-13).

In thick coatings cracking is evident in the green state. This has been encountered in previous work and eliminated by increase of particle surface energy. In the coatings on the C-C composite, a non-uniformity in coverage is observed due to the texture of the carbon fiber cloth and local variations in conductivity (Figs. 11,12). All together the composite is, as expected, sufficiently conductive electronically so as to enable its functioning as an electrode in the electrochemical system.

In addition to the formation of surface deposits, the induction of the particles into the pores of a porous substrate was demonstrated both qualitatively and quantitatively. The qualitative studies were performed on cross-sections of coated

porous graphite in the SEM. Clusters of colloidal SiO_2 are seen inside the cross-sectional (Fig. 24) while in the case of larger particles and as in the case of SiC and fused SiO_2 , single discrete particles are seen in graphite (Figs. 17,18) and in C-C (Fig. 20). X-ray mappings of the exposed cross-sections for the Si showed the presence of this element in the clusters and particles. A line scan for Si (Fig. 28) showed variations in its concentration indicating its localization in the induced particles. In some cases the presence of Si in the particle was shown by obtaining its spectrum with peaks characteristic of Si (Fig. 21).

In order to evaluate the degree of penetration of the ceramic particles as function of depth, locations at varying distance from the surface were mapped for Si. This was done for colloidal SiO_2 deposits. Only two locations are shown in this report, one close to the surface and one in the center of the cross-section (Figs. 29-44).

It is very difficult to deduce comparative evaluations from these experiments. Those are much more rigorously obtained from following quantitative determinations of SiO_2 . However, one trend is quite clear: the decrease in SiO_2 concentration with depth of specimens.

Quantitative evaluation of the amount of SiO_2 induced into the pores was made by determining the amount of SiO_2 in the porous specimen after removal of the external deposit. Since no sintering of the SiO_2 was performed, it was possible to remove the graphite completely by its gasification at 950°C . The value obtained for SiO_2 in a blank graphite specimen was only 0.03%. The tests were performed for deposits obtained in three solvents at varying deposition voltages and particle concentrations. The choice of solvents was based on their dielectric constant and viscosity. We decided to test in addition to isopropanol a solvent with higher dielectric constant and lower viscosity - ethanol, and two with lower ϵ but higher viscosity - pentanol and hexanol (see table 4). A lower viscosity is expected to facilitate particle penetration due to reduction in viscous

stresses. Powers [7] claims that electrophoretic deposition is obtainable only in a definite range of dielectric constants (d.c.) ($\epsilon=12-25$). It was of interest to experiment with solvents with lower (pentanol, hexanol) and higher d.c. (ethanol). However, it was impossible to differentiate between the effects of the d.c. and that of the viscosity since both varied independently in the various solvents. Fig. 48 shows that at identical voltage and particle concentration the order of impregnation efficiency is:

isopropanol > pentanol > hexanol

(negligible impregnation was found in the SEM for ethanol and therefore no quantitative tests were performed).

It can be deduced therefore that lowering of d.c. and increase in viscosity retards particle impregnation. It should also be pointed out that the presence of ceramic particles raises the viscosity appreciably, the value increases with increase in particle concentration (see Table 4). The effect of deposition voltage on impregnation is seen in Fig. 46. A maximum at around 300V is seen for propanol at two concentrations. This can be explained by the ambivalent effect of the voltage. On one hand its increase will enhance penetration due to increase of the electric field but at the same time the build-up of the external coating which will be enhanced too will block further impregnation. Indeed at 450V a very fast build-up of external coating was observed.

The effect of concentration is seen in Fig. 47 for isopropanol at 30V. The impregnation increases with concentration with a diminishing rate.

A most interesting result was obtained during the quantitative SiO_2 determination. It was found that in those specimens where the SiO_2 concentration was at higher levels (such as 0.6%), a SiO_2 skeleton of the same shape and dimensions as the original specimen remained after the gasification of the graphite (Fig. 49). Moreover, the cross-section of the skeleton contained SiO_2 (Fig. 50) indicating impregnation of the whole cross-section of

the graphite specimen. Thus the induction of the colloidal SiO_2 into the porous matrix under the influence of the electric field was proven.

The electroosmotic effect which enhances the filling of pores as a result of the presence of an electric field was shown in the experiments described in 4.1.3, Table 2 and Fig. 45.

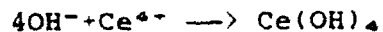
The presence of an electric field has a strong influence on the penetration of water into the pores of graphite. Only 12% of the pores were filled in absence of a field, while about 80% were filled after over 5 min. but less than 15 min. of exposure, when a field of 30V/cm was applied. In the case of isopropanol 80% of filling was attained both with and without the electric field. However, the rate of filling was higher with the electric field.

Deposits of CeO_2 , ZrO_2 and Al_2O_3 were obtained by cathodic reduction reactions that form OH^- followed by the interaction of the OH^- with the appropriate cation:

- electroreduction of H_2O and NO_3^- :



- interaction between the OH^- and the cation:



- Dehydration of the hydroxide to form CeO_2 , Al_2O_3 and ZrO_2 .

A crystallographic analysis was made for the cerium containing deposit only so far confirming the CeO_2 composition.

A similar preliminary analysis of the Zr containing deposit indicates the as-deposited material to be amorphous and to transform into the crystalline form by calcination. Thick deposits of CeO_2 and ZrO_2 could be formed by increasing c.d.s. and deposition time. However, in the case of Al_2O_3 only very

thin films were obtained. This might be due to differences in the electric conductivity of the three compounds.

CHAPTER 6 - CONCLUDING REMARKS

The final objective of this research project is the development of a method for coating and impregnation of carbon-carbon composites with ceramic materials.

During this stage of the project the fundamental concepts underlying the approach, based on the phenomena of electrophoresis and electrodeposition, were tested.

Most experiments were performed, at this stage, on a model material for C-C: porous graphite.

The results obtained can be summarized as follows:

- Electrophoretic deposition of the ceramic materials, studied so far (colloidal and fused SiO_2 , SiC and SiN), on graphite and C-C takes place following charging of the particles and their displacement under the influence of the electric field. The SiO_2 and SiC particles acquire a negative charge therefore are deposited on the anode, while the SiN is deposited on the cathode.
- In addition to the formation of surface deposits the induction of the ceramic particles into a porous substrate was demonstrated qualitatively for all ceramics and was studied quantitatively for colloidal SiO_2 . The extent of penetration was studied on cross-sections of coated porous graphite in the SEM and by quantitative determination of the SiO_2 content in specimens obtained at various deposition conditions.

- It is shown that an optimal value exists for the deposition voltage resulting from its ambivalent effect on particle penetration. This value was found to be around 300V (180 V/cm).
- The effect of the solvents studied on impregnation efficiency in decreasing order is:
propanol > pentanol > hexanol > ethanol
- Increase of particle concentration enhances impregnation up to about 30 g/l for colloidal SiO_2 .
- Although the weight percentages of impregnated SiO_2 are low, it is shown that the whole cross-section of the porous graphite was impregnated. This is demonstrated by the SiO_2 skeleton left behind after gasification of the graphite.
- Further optimization of deposition parameters will lead to increase of extent of impregnation.
- The electroosmotic flow of isopropanol and of water into the pores was demonstrated.
- Ceramic coatings of CeO_2 , ZrO_2 and Al_2O_3 were deposited on graphite and C-C by electroreduction of aqueous solutions containing inorganic salts of the appropriate metals. Clusters of CeO_2 were obtained in the skeleton of C-C by this method.

BIBLIOGRAPHY

1. J. Davies et al., J. Coll. Interf. Sci., 63(3), 480, 1978.
2. Y.S. Moya et al., Ceramic Bull. 59 (12) 1980.
3. O.M. Bockris, K.N. Reddy, "Modern Electrochemistry", Vol. I, 1970.
4. D.R. Brown, F.W. Salt, J. Appl. Chem. 15, 40, 1965.
5. E.J.W. Verwey, J. Th. Overbeek, "Theory of the Stability of Lyophobic Colloids", 1948, Elsevier.
6. P. Benson et al. Electrochimica Acta, 9, 275(1964).
7. P.W. Powers, J. Electrochem. Soc., 122(4)490, 1975.
8. R.I. Nelson, Thin Solid Films, 81, 329(1981).
9. J.M. Horn, G.Y. Onoda, J. Am. Cer. Soc., 61(11-12), 523(1978).
10. D.U. Krishna, Rao, E.C. Subbarao, Ceramic Bull. 58(4), 467, 1979.
11. J.L. Anderson, Proc. Electrochem. Soc., 1985, p. 103.
12. H.Y. Keh, J.L. Anderson, J. Fluid. Mech. 153, 417(1985).
13. J.L. Anderson, J. Coll. Interf. Sci. 105(1), 45(1985).
14. J.A. Switzer, Am. Ceram. Soc. Bull. 66(10), 1521(1987).
15. D. Tend, L.F. Warren, J. Electrochem. Soc. 130, (4), 869(1983).
16. M. Sakai et al. ibid, 130(7), 1631 (1983).

17. S. Srinivasan, H.D. Hurwitz, J.O.M. Bockris, J. Chem. Phys. 46, 3108(1967).
18. G.M. Brown, F.A. Posey, J. Electrochem. Soc. 128, (2), 306 (1981).
19. B.G. Ateya, L.G. Austin, *ibid*, 124(11), 1590(1977).
20. J.A. Trainham, J. Newman, *ibid*, 124(10), 1528 (1977).